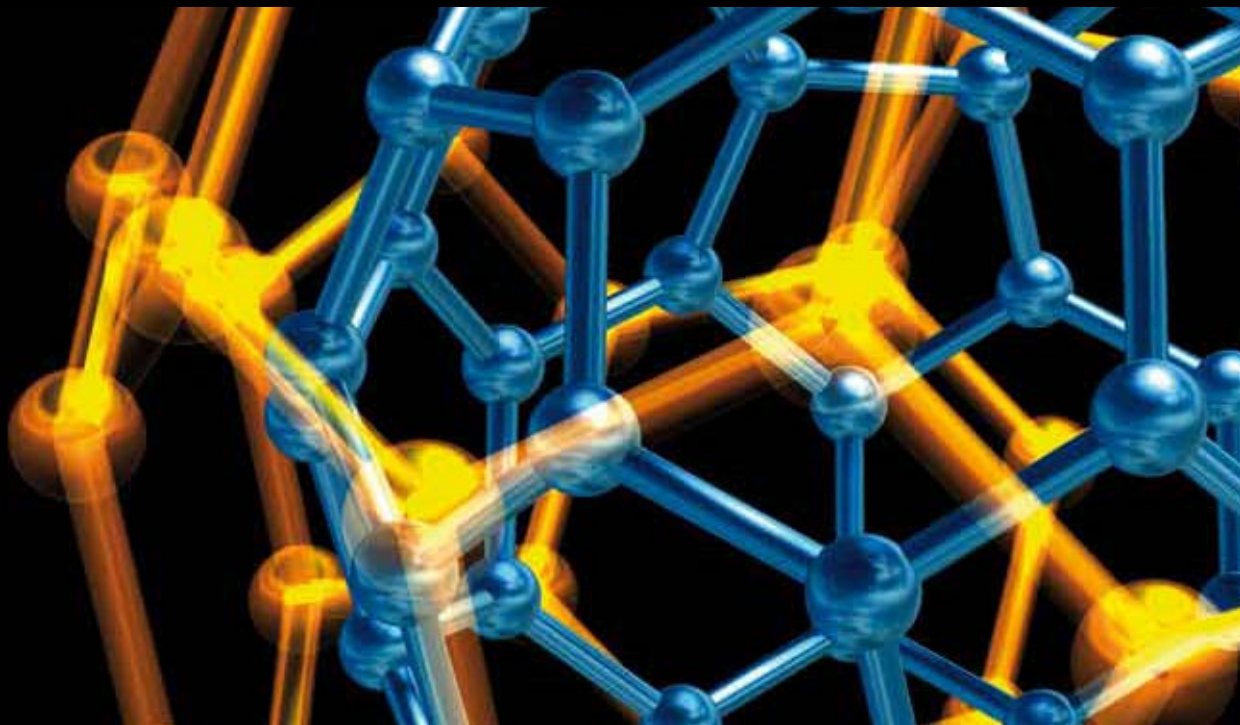


NANOCOMPOSITES 2012

GUEST EDITORS: GUIFU ZOU, HONGMEI LUO, BAOQUAN SUN, MENKA JAIN,
AND HUIHENG PENG





Nanocomposites 2012

Journal of Nanotechnology

Nanocomposites 2012

Guest Editors: Guifu Zou, Hongmei Luo, Baoquan Sun,
Menka Jain, and Huisheng Peng



Copyright © 2012 Hindawi Publishing Corporation. All rights reserved.

This is a special issue published in "Journal of Nanotechnology." All articles are open access articles distributed under the Creative Commons Attribution License, which permits unrestricted use, distribution, and reproduction in any medium, provided the original work is properly cited.

Editorial Board

Simon Joseph Antony, UK
Yoshio Bando, Japan
B. Bhushan, USA
Felix A. Buot, USA
Carlos R. Cabrera, Puerto Rico
John A. Capobianco, Canada
Franco Cerrina, USA
Gan Moog Chow, Singapore
Jeffery L. Coffey, USA
Dmitriy A. Dikin, USA
Dimitris Drikakis, UK
H. D. Espinosa, USA
John S. Foord, UK
E. Goldys, Australia
Lambertus Hesselink, USA
Joseph Irudayaraj, USA
Niraj K. Jha, USA

Miguel Jose-Yacamán, USA
Valery Khabashesku, USA
Yoke Khin Yap, USA
Sakhrat Khizroev, USA
Andrei Kolmakov, USA
Charles M. Lieber, USA
Charles M. Lukehart, USA
A. Salam H. Makhlof, Germany
Constantinos Mavroidis, USA
Vincent Meunier, USA
Paolo Milani, Italy
Oded Millo, Israel
Oussama Moutanabbir, Canada
M. Grant Norton, USA
R. Lee Penn, USA
S. N. Piramanayagam, Singapore
A. M. Rao, USA

Paresh Chandra Ray, USA
Benjaram M. Reddy, India
Federico Rosei, Canada
Mehmet Sarikaya, USA
Jorge M. Seminario, USA
V. Shalaev, USA
Mahi R. Singh, Canada
Bobby G. Sumpter, USA
Xiao Wei Sun, Singapore
Weihong Tan, USA
O. K. Tan, Singapore
Thomas Thundat, USA
Boris I. Yakobson, USA
Nan Yao, USA
Chuan Jian Zhong, USA

Contents

Nanocomposites 2012, Guifu Zou, Hongmei Luo, Baoquan Sun, Menka Jain, and Huisheng Peng
Volume 2012, Article ID 267135, 2 pages

FOLDNA, a Web Server for Self-Assembled DNA Nanostructure Autoscaffolds and Autostaples,
Chensheng Zhou, Heng Luo, Xiaolu Feng, Xingwang Li, Jie Zhu, Lin He, and Can Li
Volume 2012, Article ID 453953, 5 pages

Preparation and Properties of PTFE-PMMA Core-Shell Nanoparticles and Nanocomposites,
Diego Antonioli, Michele Laus, Giampaolo Zuccheri, Valerj Kapeliouchko, Maria Cristina Righetti,
Luca Boarino, and Katia Sparnacci
Volume 2012, Article ID 875815, 10 pages

**Ultrafine Magnetite Nanopowder: Synthesis, Characterization, and Preliminary Use as Filler of
Polymethylmethacrylate Nanocomposites**, Pietro Russo, Domenico Acierno, Mariano Palomba,
Gianfranco Carotenuto, Roberto Rosa, Antonino Rizzuti, and Cristina Leonelli
Volume 2012, Article ID 728326, 8 pages

**Self-Organization of K^+ -Crown Ether Derivatives into Double-Columnar Arrays Controlled by
Supramolecular Isomers of Hydrogen-Bonded Anionic Biimidazolate Ni Complexes**, Makoto Tadokoro,
Kyosuke Isoda, Yasuko Tanaka, Yuko Kaneko, Syoko Yamamoto, Tomoaki Sugaya, and Kazuhiro Nakasuji
Volume 2012, Article ID 216050, 10 pages

**Wear-Resistant Ultrahigh-Molecular-Weight Polyethylene-Based Nano- and Microcomposites for
Implants**, S. V. Panin, L. A. Kornienko, N. Sonjaitham, M. V. Tchaikina, V. P. Sergeev, L. R. Ivanova,
and S. V. Shilko
Volume 2012, Article ID 729756, 7 pages

Nanotechnological Strategies for Biofabrication of Human Organs, Rodrigo A. Rezende, Fábio de Souza
Azevedo, Frederico David Pereira, Vladimir Kasyanov, Xuejun Wen, Jorge Vicente Lopes de Silva,
and Vladimir Mironov
Volume 2012, Article ID 149264, 10 pages

**The Optimum Dispersion of Carbon Nanotubes for Epoxy Nanocomposites: Evolution of the Particle
Size Distribution by Ultrasonic Treatment**, Tomas Roll Frømyr, Finn Knut Hansen, and Torbjørn Olsen
Volume 2012, Article ID 545930, 14 pages

Exfoliated Graphite Reinforced PMMA Composite: A Study on Nanoindentation and Scratch Behavior,
Himel Chakraborty, Arijit Sinha, Nillohit Mukherjee, and Partha Protim Chattopadhyay
Volume 2012, Article ID 940516, 5 pages

Preparation of Mesoporous Silica-Supported Palladium Catalysts for Biofuel Upgrade, Ling Fei,
Harvind Kumar Reddy, Joshua Hill, Qianglu Lin, Bin Yuan, Yun Xu, Peter Dailey, Shuguang Deng,
and Hongmei Luo
Volume 2012, Article ID 309093, 6 pages



Mechanical and Thermal Characteristics of Bio-Nanocomposites Consisting of Poly-L-lactic Acid and Self-Assembling Siloxane Nanoparticles with Three Phases, Masatoshi Iji and Naoki Morishita

Volume 2012, Article ID 137614, 8 pages

The Overall Effects of AlN Nanoparticle Addition to Hybrid Magnesium Alloy AZ91/ZK60A,

Muralidharan Paramsothy, Jimmy Chan, Richard Kwok, and Manoj Gupta

Volume 2012, Article ID 687306, 8 pages

Editorial

Nanocomposites 2012

Guifu Zou,¹ Hongmei Luo,² Baoquan Sun,³ Menka Jain,⁴ and Huisheng Peng⁵

¹ School of Energy, Soochow University, Suzhou, Jiangsu 215000, China

² Department of Chemical Engineering, New Mexico State University, Las Cruces, NM 88003, USA

³ Center for Soft Matter, Soochow University, Suzhou, Jiangsu 215015, China

⁴ Department of Physics, University of Connecticut, Storrs, Mansfield, CT 06269, USA

⁵ Macromolecular Science Department, Fudan University, Shanghai 200433, China

Correspondence should be addressed to Guifu Zou, zougufu@suda.edu.cn

Received 3 December 2012; Accepted 3 December 2012

Copyright © 2012 Guifu Zou et al. This is an open access article distributed under the Creative Commons Attribution License, which permits unrestricted use, distribution, and reproduction in any medium, provided the original work is properly cited.

Composite materials that traditionally incorporate micron-scale reinforcements in a bulk matrix offer opportunities to tailor material properties such as hardness, tensile strength, ductility, density, thermal and electrical conductivity, and wear resistance. With the advent of nanomaterials, nanocomposites are multiphase materials where one of the phases has at least one dimension of less than 100 nm. The properties of nanocomposite materials depend not only on the properties of the building components but also on their morphologies and interfacial characteristics. There is also the possibility of producing improved or multifunctionalities and/or new properties due to the coupling between the two components, which may not be found for each component at a pure state. The published works are briefly addressed as follows.

The paper by Shanghai Jiao Tong University, China, reports a web server, FOLDNA, which can automatically design two-dimensional (2D) self-assembled DNA nanostructures according to custom pictures and scaffold sequences provided by the users. Self-assembled DNA is built by a long single strand scaffold DNA and a lot of short single strand DNA known as staples. Self-assembled DNA nanostructures are increasingly valuable in nanomaterial and biosensing applications. A paper from Italy investigates the preparation and mechanical properties of polytetrafluoroethylene-poly(methyl methacrylate) (PTFE-PMMA) core-shell particles by a seeded emulsion polymerization method. Compact nanocomposites were prepared by annealing the core-shell particles at a temperature higher than the glass transition temperature of PMMA. Another paper also from Italy is about microwave-assisted hydrothermal synthesis to

magnetite (Fe_3O_4) nanoparticles with a monodispersed crystallite structure with particles size around 15–20 nm, which were used as filler for a commercial polymethylmethacrylate resin.

Altra paper from Japan is about the self-assembled supramolecular architectures. Anionic tris (biimidazolate) nickelate (II) ($[\text{Ni}(\text{Hbim})_3]^-$), a hydrogen-bonding (H-bonding) molecular building block, undergoes self-organization into honeycomb-sheet superstructures connected by complementary intermolecular H-bonds. The crystal obtained from the stacking of these sheets is assembled into channel frameworks, approximately 2 nm wide, that clathrate two cationic K^+ -crown ether derivatives organized into one-dimensional (1D) double-columnar arrays. In this paper, the authors showed that all five cationic guest-included crystals form nanochannel structures that clathrate the 1D double-columnar arrays of one of the four types of K^+ -crown ether derivatives, one of which induces a polymorph. The paper from Russia, studies the influence of modification by hydroxyapatite (HA) nano- and microparticles on tribotechnical properties of ultrahigh-molecular-weight polyethylene (UHMWPE) to develop polymer implants for endoprostheses. It was concluded that nanofilling of UHMWPE by 0.1–0.5 wt% HA increases its wear resistance in 3.5 times compared to the pure polymer. High-energy treatment by N^+ ion beam brings structural rearrangement and cross linking of macromolecules in the polymer surface layers resulting in an increase of its wear resistance. The authors expected that the high-energy treatment of UHMWPE-based composites can be used in combination with filling by

HA nanoparticles as a method of sterilization of products for medical applications (orthopaedic implants). Another paper is a collaborative study from Brazil, Latvia, and USA. This paper focuses on demonstrating how nanomaterials with nanolevel size can contribute to the development of 3D human tissues and organs which have macrolevel organization. The authors presented several examples of novel tissue and organ biofabrication technologies based on using novel nanomaterials and described a robotic device for fabrication of compliant composite electrospun vascular graft.

A paper from Norway is a study of the optimum dispersion of multiwalled carbon nanotubes (MWCNTs) for epoxy nanocomposites. The particle size distributions were characterized by the means of a disc centrifuge, and the effect of dispersion time, power density, and total energy input, for both bath and circulation probe ultrasonic dispersing equipment was investigated. The eighth paper from India aims to compare the scratch hardness (H_s) with the indentation hardness (H_{IT}) obtained from nanoindentation measurements of exfoliated graphite/poly (methyl methacrylate) (EG/PMMA) composites produced by in situ melt mixing method. It was found out that there is a good correlation between the scratch hardness and the indentation hardness at low indentation depths, with a linear relationship between hardness and the reinforcement content of exfoliated graphite. A paper is contributed by one of our guest editors in USA. The paper reports the preparation of two hydrocracking catalysts Pd/CoMoO₄/silica and Pd/CNTs/CoMoO₄/silica (CNTs, carbon nanotubes) and reports the catalyst activity measured in a Parr reactor with camelina fatty acid methyl esters (FAMES) as the feed. The results showed that the Pd nanoparticles have been incorporated onto mesoporous silica in Pd/CoMoO₄/silica or on the CNTs surface in Pd/CNTs/CoMoO₄/silica catalysts. The two catalysts both show high conversion and selectivity in a hydrocracking catalytic reaction. The different combinations of metals and supports have selective control cracking on heavy hydrocarbons due to synergism between metals and different reaction sites where the catalysts were loaded.

A paper from Japan is a study of mechanical and thermal characteristics of biopolymer nanocomposites consisting of poly-L-lactic acid (PLLA) and self-assembling siloxane nanoparticles with three phases. A high-density siloxane phase (plural cores), an elastomeric silicone phase, and a caprolactone oligomer phase were developed to increase the mechanical properties of PLLA. The nanoparticles, average size of 13 nm, were self-assembled by aggregation and condensation of an organosiloxane with three units: [isocyanatepropyltrimethoxysilane] (IPTS), [polymethylpropylloxysiloxane] (PMPS), and a caprolactone oligomer (CLO), which form each phase. Bending and tensile testing showed that the use of these nanoparticles (5 wt% in PLLA) greatly increases the tenacity (breaking strain) of PLLA while maintaining its relatively high breaking (maximum) strength. The elongation of the nanocomposite was more than twice that of PLLA while the elasticity modulus and breaking (maximum) strength were comparable to those of PLLA. The nanoparticles also increased the impact strength of PLLA. From

these results, the bionanocomposite using the three-phased nanoparticles is expected to be used in durable product applications and other new applications. These nanoparticles can also be applied to various other brittle polymers by modifying the structure of the outside phase to achieve a high affinity with these polymers. A paper in this issue is contributed from Singapore. A hybrid magnesium alloy nanocomposite containing AlN nanoparticle reinforcement was fabricated using solidification processing followed by hot extrusion. The nanocomposite exhibited similar grain size to the monolithic hybrid alloy, reasonable AlN and intermetallic nanoparticle distribution, nondominant (0002) texture in the longitudinal direction, and 17% higher hardness than the monolithic hybrid alloy. Compared to the monolithic hybrid alloy, the nanocomposite exhibited higher tensile yield strength (0.2% TYS) and ultimate tensile strength (UTS) without significant compromise in failure strain and energy absorbed until fracture (EA) (+5%, +5%, -14%, and -10%, resp.). Compared to the monolithic hybrid alloy, the nanocomposite exhibited unchanged compressive yield strength (0.2% CYS) and higher ultimate compressive strength (UCS), failure strain, and EA (+1%, +6%, +24%, and +6%, resp.).

*Guifu Zou
Hongmei Luo
Baoquan Sun
Menka Jain
Huisheng Peng*

Research Article

FOLDNA, a Web Server for Self-Assembled DNA Nanostructure Autoscaffolds and Autostaples

Chensheng Zhou, Heng Luo, Xiaolu Feng, Xingwang Li, Jie Zhu, Lin He, and Can Li

Bio-X Institutes, Shanghai Jiao Tong University, 1954 Huashan Road, Shanghai 200240, China

Correspondence should be addressed to Can Li, lican@sjtu.edu.cn

Received 3 April 2012; Revised 23 July 2012; Accepted 10 August 2012

Academic Editor: Menka Jain

Copyright © 2012 Chensheng Zhou et al. This is an open access article distributed under the Creative Commons Attribution License, which permits unrestricted use, distribution, and reproduction in any medium, provided the original work is properly cited.

DNA self-assembly is a nanotechnology that folds DNA into desired shapes. Self-assembled DNA nanostructures, also known as origami, are increasingly valuable in nanomaterial and biosensing applications. Two ways to use DNA nanostructures in medicine are to form nanoarrays, and to work as vehicles in drug delivery. The DNA nanostructures perform well as a biomaterial in these areas because they have spatially addressable and size controllable properties. However, manually designing complementary DNA sequences for self-assembly is a technically demanding and time consuming task, which makes it advantageous for computers to do this job instead. We have developed a web server, FOLDNA, which can automatically design 2D self-assembled DNA nanostructures according to custom pictures and scaffold sequences provided by the users. It is the first web server to provide an entirely automatic design of self-assembled DNA nanostructure, and it takes merely a second to generate comprehensive information for molecular experiments including: scaffold DNA pathways, staple DNA directions, and staple DNA sequences. This program could save as much as several hours in the designing step for each DNA nanostructure. We randomly selected some shapes and corresponding outputs from our server and validated its performance in molecular experiments.

1. Introduction

When Watson and Crick discovered the nucleic acid pairing rules in 1953, the theoretical foundation of self-assembled DNA was established. In 1982, Seeman laid the foundation of “structural DNA Nanotechnology” by folding DNA into lattices [1]. Later in 2006, Rothmund initiated spatially restricted 2D self-assembled DNA structure by using a bottom-up method, which is also known as DNA origami [2, 3]. In the same year, asymmetric self-assembled DNA nanostructure was folded by Qian et al. [4]. Since then, applications of DNA nanostructures in research and diagnosis have been continuously developed, such as methods to examine single nucleotide polymorphism on flat DNA origami, to attach antibodies onto tiles and to perform RNA hybridization assays [5–8].

Self-assembled DNA is built by a long single strand scaffold DNA and a lot of short single strand DNA known as staples. The number of staples is decided by the length of the scaffold DNA, which is typically 7 kilobase-long.

Using bottom-up fabrication methods, the scaffold DNA is folded to form the shape of the nanostructure, while the staple DNA fix the scaffold DNA, thus forming the two-dimensional DNA nanostructure. With the development of DNA nanotechnology, software for computer-aided design of nucleic acids was developed to help with the calculation of DNA nanostructure [9–15]. By using the software, the efficiency of designing self-assembled DNA nanostructure has been dramatically increased. However, there are still several manual steps for designing the nanostructure, including modification of border staples and calculation scaffold DNA length in each line, which require a full understanding of the DNA origami technical details. Hence an automatic design tool which provides a more easy access to apply the DNA nanofabrication tools to researchers in related areas, for instance, nanoparticle base drug delivery, will introduce self-assembled DNA technology to more interdisciplinary areas [16].

In our server FOLDNA, the pathway of the scaffold is automatically generated according to the shape of a



FIGURE 1: Screenshot from FOLDNA home page. In the web server FOLDNA, users can upload a monochrome image and a scaffold DNA sequence. Then the server will automatically design the whole nanostructure. Here we have a default scaffold DNA sequence (M13mp18) provided. It can be customized to any desired sequence.

given picture. Then the staple DNA strands, typically 32 nucleotides (nt) each, are generated to pair with the scaffold. We fill in the staple DNA according to the DNA helix torque angle, ensuring the final nanostructure is flat according to Rothmund's method [2]. With the help of FOLDNA, the entire process of DNA nanostructure design is simplified to image preparation, checking the results, and ordering oligonucleotides to carry out experiments. This open server is available at <http://www.bio-x.cn/foldna/>.

2. Results

2.1. Server Results. The web server FOLDNA offers a user-friendly interface (Figure 1). An example scaffold DNA (M13mp18), which can be customized by the user, is provided for a quick test. By submitting a desired shape of DNA nanostructure as a monochrome picture, along with the scaffold DNA sequence, users can obtain complete sequences of staple DNA which can hybridize onto the scaffold DNA to form the desired shape. No matter what the size the given picture is, the program will automatically adjust the picture so that the long scaffold DNA can be optimally filled into it. The results displayed in FOLDNA contain the pathway and sequence of the folded scaffold DNA and staple DNA, which can be directly used in the experiments. Finally, wet-lab experiments are conducted to validate the results from the program (Figure 2).

3. Interpretation of Results Displayed in Web Server

3.1. Digitized Image. A digitized image is displayed together with the uploaded image. The digitized image outline indicates how the image is filled by the scaffold DNA. Each number in the digitized image stands for one basic building brick (brick for abbreviation). Here, the width of each brick is equal to 8 bases of nucleic acid, while the height is equal to 2 rows. When rectangular bricks are filled into the monochrome image, bricks around the border lines will be either picked or abandoned. We try to make the best use of the scaffold sequence and avoid left single strand to form mismatches. Here, we use a floating point value system to evaluate the percentage of the black-colored area and determine whether or not a border brick should be picked.

This percentage cannot be set as a fixed value because a rigid value does not work well for all images. Therefore, a floating point is calculated according to each image, under the precondition that there are enough scaffold DNA to fill them, thereby ensuring the maximum number of border bricks are included. As a result, the left length of the scaffold DNA in the web page is normally no more than 50 bases.

3.2. Scaffold Structure. In our program, the default long single stand DNA that acts as scaffold is M13mp18, a 7 kb single strand DNA from bacteriophage M13. However, if a different scaffold is desired, users can customize their own sequence. Depending on the length of the uploaded sequence, the program zooms the image in or out to fit the uploaded template before generating the scaffold pathway. FOLDNA is able to process complicated images such as images with holes, or images with erratic borders.

To maximize the function of our web server, we have worked out a program that can deal with any continual image. Our program accepts shapes with holes or indentations at any location. The bottom-up designing method is specially written to ensure all complicated shapes can be reasonably filled up by the scaffold sequences.

3.3. Staple Structure. Since scaffold DNA mainly goes crabwise, it needs something vertical to fix it. Staple DNA exactly binds the neighboring scaffold strands. According to Rothmund's paper [2], staples were first designed to bind neighboring upper and lower scaffold DNA, with about 8 bases on the upper one and another 8 bases on the lower one. Then, to make it more stable, adjacent staples are linked, which increases the average staple length to about 32 bases. On the top and bottom edges, staples are prolonged or cut by the program to ensure the edge is completely paired. The shortest staple DNA generated by the server is 24 bases, while the longest staple is 40 bases. This range ensures a reasonable melting temperature and a reasonable length for synthesis and purification.

With user determined scaffold DNA length, sequence, and desired shape, the staple DNA sequences are calculated automatically.

3.4. Staple Sequences. On the web server, the staple DNA sequence can be downloaded as an isolated file. When closing the webpage, the digitized image will expire, but the link to the staple sequence will still be valid until the server space has been filled, at which point old files will be replaced.

4. Experimental Results

Designing results from FOLDNA are validated by molecular experiments. They are tested by uploading a simple image of a hexagon and complex images with concavity and holes, along with the example scaffold DNA (M13mp18), to examine the capability of our server. We ordered staple DNA according to its output and performed the self-assembly experiments of hybridizing the staple DNA onto the scaffold DNA. The shapes of assembled DNA nanostructures

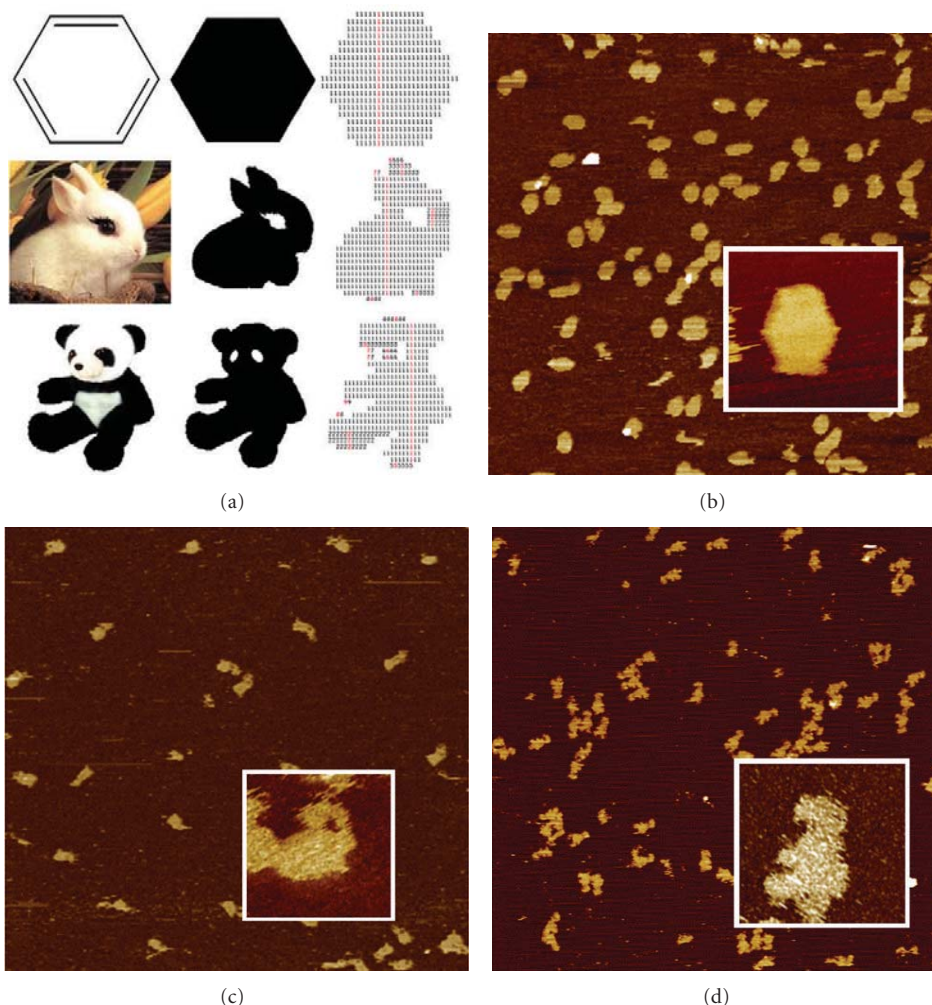


FIGURE 2: Examples for DNA nanostructure design. (a) left column: object picture; middle column: monochrome image, user uploaded; right column: digitized image, according to the user uploaded image. (b, c, d), wet-lab products observed by AFM. Uploaded image and digitized image are screenshots from our web server. In the digitized images, scaffold ssDNA forms seams on the border and along the red lines. The selected shapes for validation are a hexagon, a rabbit and a panda (a). The corresponding results are (b), (c) and (d). The pathways for the scaffold and staple DNA as well as the sequence lists for staple DNA we used for wet-lab experiments are shown in the Supplementary Materials (see Supplementary Materials available online at doi:10.1155/2012/453953).

are observed through AFM nanoscopes. We found the nanostructures were well folded according to the desired shapes, validating the power of applying our server in automatic designing of 2D DNA nanostructures. As the broad applications of 2D DNA nanostructures, such as examining single nucleotide polymorphism on DNA origami flat, attaching antibodies onto tiles and RNA hybridization assays, are continuously discovered, FOLDNA will be an efficient and powerful tool in designing either complicated or high through-put DNA nanostructures for experiments and further research.

5. Discussion

Since computer aided design of self-assembled DNA nanostructures was developed, software has provided significant convenience. Such software offers automatic design of staple

sequences according to customer scaffold structure. A manual design of a scaffold pathway is tedious and troublesome, and is not yet included in such computer applications. Thus, a smart program which works out all steps above, and can carry self-assembled DNA nanostructures into execution without using other calculation platforms will increase the accessibility and the user base of self-assembled DNA nanostructures.

Web server FOLDNA is such a program. It is the first program to provide entirely automatic design of scaffold DNA pathway according to any given continuous image. With the same customer uploaded image, a longer scaffold DNA would provide a larger structure and better details if the design is complex. Obviously, a longer scaffold needs more work in calculation. Thus, the users can customize their own nanostructures with any kind of scaffold DNA for potential uses such as probable binding, recognition,

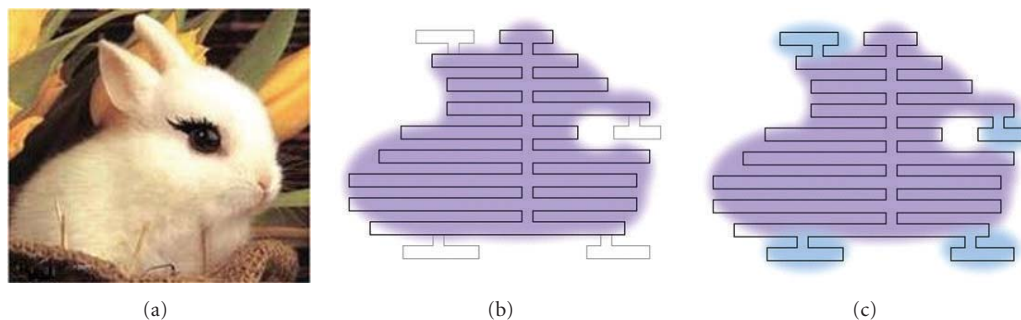


FIGURE 3: Example of scaffold prolong step by step. (a), the desired shape that need to be filled by scaffold. (b) major part along the first seam is filled up. (c) the second part along the second seam is derived from one point of the first part. Then, minor parts are filled by strands comes from its neighboring part, until the whole picture is filled.

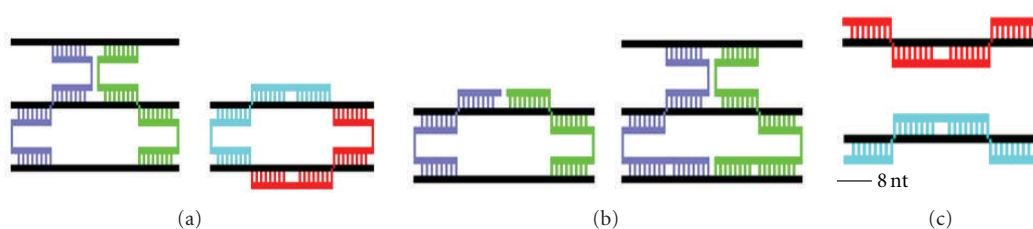


FIGURE 4: Staple DNA types. (a) general and special type staples, left: Z staple (violet) and S staple (green); right: L staple (blue) and R staple (red); (b and c), variations on the staples when located on the top and bottom edges: (b) S (violet) and Z (green) type staple variations when meeting the top of a seam (left) and the bottom of a seam (right); (c) L (red) and R (blue) type staple variations on the top edge (top) and the bottom edge (bottom).

affinity, or detection of special chemicals or macromolecules. The traditional designing method of DNA nanostructures requires you to first draw the monochrome picture onto a lattice and calculate the total area of the image by counting units. Then, the pathway that the scaffold DNA can cover is inscribed onto the lattice, and the approximate length of DNA in each line and the total number of lines in all are calculated manually. Finally the nanostructure is separated into several parts and designed part by part, ensuring the scaffold DNA to be continuous at any point. However, with the help of our FOLDNA, all steps above can be executed instantly with accuracy and quality. FOLDNA can create a planned portrayal, no matter how complicated the desired image is, or whether the image has holes or caves inside or at its edges.

6. Materials and Methods

6.1. Oligonucleotides. Single strand DNA M13mp18 was purchased from New England Biolabs, stored at 10 mM Tris-HCl (pH 7.5), 1mM EDTA. Staples DNA are ordered from GeneRay, purified by PAGE.

6.2. Methods of Forming DNA Nanostructures. In the reaction, staples are diluted to approximately 0.025 μ M. Each sample (30 μ l) contains 0.5 μ l scaffold DNA M13 mp18, 7.5 μ l TAE-Mg²⁺ buffer and 22 μ l diluted staple DNA. Self-assembled DNA is performed in PCR machine. The mixture of oligonucleotides is denatured at 95 degrees for 2 minutes,

then slowly cooling down to 20 degrees in approximately 2 hours, at the speed of 0.1 degrees every 10 seconds, for hybridization. After the assembly step is finished, the samples are stored at 4 degrees till loading for AFM imaging.

6.3. AFM Imaging. Atomic force microscope imaging was conducted in Veeco multimode nanoscope III, tapping mode in liquid phase. E scanner with NP/S tip is used for imaging. 2 μ l sample was loaded on fresh cleaved mica, and additional 20 μ l TAE-Mg²⁺ buffer were added into cantilever before place the holder into the box. The tapping amplitude setpoint was about 0.4 mV, using approximately 9.7 kHz resonance drive frequency.

6.4. Server-Side Calculation of Autoscaffold. When a monochrome image of desired shape is uploaded, it is resized to fit the length of the scaffold. The server makes the best use of the scaffold and keeps both ends of the scaffold DNA close enough to each other so that the program is compatible with either circular or linear DNA [17]. The monochrome image is then filled up by bricks as basic units which are shown as numbers in the digitized image of the output. Each brick is built up by 2 parallel lines of 8 nt and the number of the bricks in each line is even, ensuring 16 nt as the basic unit for the scaffold.

Next, in order to ensure the entire structure is flat after assembly, the server calculates the seams and pathway for the scaffold DNA according to the methods used by previous publications [2, 15]. By taking the advantage of

these methods, the seams will go across all the horizontal lines of the monochrome image, making sure that the entire image is covered by the scaffold DNA (Figure 3). The top of the longest seam is set as the default start point of the scaffold to be filled in with a default direction towards the right.

6.5. Server-Side Calculation of Autostaple. Autostaple has been already used in some software [10, 13, 15], however, with the involvement of extra short staples on the edges, manual modification of the staple DNA is necessary. However, with the help of our server, entirely complementary staples are automatically generated and filled into the bricks according to the scaffold pathway. In our program, staples are mainly divided into 2 types, with 2 subtypes in each. The general type includes S and Z subtypes, while the special type includes L and R subtypes (Figure 4).

S and Z subtypes are a general choice for complementation of the scaffold. However, this rule cannot work when a seam is located at even bricks away from the edge. The nanostructure will separate apart along the seam if this general type of staples is used. At this point, L and R subtypes are applied as to staple together the scaffold DNA at both sides of the seams.

On the top and bottom edges, the staples have a variation. On the top, the S and Z subtypes of staples have no space to extend on the top so they are 8 bases less than their general type. Meanwhile, on the bottom, they are extended 8 bases longer to complement the scaffold. For the L and R subtypes of staples, there is also a variation on the top and bottom—these staples are prolonged into a straight line.

Authors' Contribution

C. Zhou and H. Luo contributed equally to this work.

Acknowledgments

The authors thank the National Key Technology R&D Program (2012BAI01B09), the 973 Program (2010CB529600), and the National Nature Science Foundation of China (81121001) for the financial support.

References

- [1] N. C. Seeman, "Nucleic acid junctions and lattices," *Journal of Theoretical Biology*, vol. 99, no. 2, pp. 237–247, 1982.
- [2] P. W. K. Rothmund, "Folding DNA to create nanoscale shapes and patterns," *Nature*, vol. 440, no. 7082, pp. 297–302, 2006.
- [3] R. Chhabra, J. Sharma, Y. Liu, S. Rinker, and H. Yan, "DNA self-assembly for nanomedicine," *Advanced Drug Delivery Reviews*, vol. 62, no. 6, pp. 617–625, 2010.
- [4] L. Qian, Y. Wang, Z. Zhang et al., "Analogic China map constructed by DNA," *Chinese Science Bulletin*, vol. 51, no. 24, pp. 2973–2976, 2006.
- [5] Y. He, Y. Tian, A. E. Ribbe, and C. Mao, "Antibody nanoarrays with a pitch of ~20 nanometers," *Journal of the American Chemical Society*, vol. 128, no. 39, pp. 12664–12665, 2006.
- [6] Y. Ke, S. Lindsay, Y. Chang, Y. Liu, and H. Yan, "Self-assembled water-soluble nucleic acid probe tiles for label-free RNA hybridization assays," *Science*, vol. 319, no. 5860, pp. 180–183, 2008.
- [7] Z. Zhang, Y. Wang, C. Fan et al., "Asymmetric DNA origami for spatially addressable and index-free solution-phase DNA chips," *Advanced Materials*, vol. 22, no. 24, pp. 2672–2675, 2010.
- [8] Z. Zhang, D. Zeng, H. Ma et al., "A DNA-origami chip platform for label-free SNP genotyping using toehold-mediated strand displacement," *Small*, vol. 6, no. 17, pp. 1854–1858, 2010.
- [9] S. M. Douglas, H. Dietz, T. Liedl, B. Högberg, F. Graf, and W. M. Shih, "Self-assembly of DNA into nanoscale three-dimensional shapes," *Nature*, vol. 459, no. 7245, pp. 414–418, 2009.
- [10] S. M. Douglas, A. H. Marblestone, S. Teerapittayanon, A. Vazquez, G. M. Church, and W. M. Shih, "Rapid prototyping of 3D DNA-origami shapes with caDNAno," *Nucleic Acids Research*, vol. 37, no. 15, pp. 5001–5006, 2009.
- [11] "NanoEngineer-1," Nanorex Inc., Bloomfield Hills, Mich, USA, <http://www.nanorex.com>.
- [12] J. Zhu, B. Wei, Y. Yuan, and Y. Mi, "UNIQUIMER 3D, a software system for structural DNA nanotechnology design, analysis and evaluation," *Nucleic Acids Research*, vol. 37, no. 7, pp. 2164–2175, 2009.
- [13] C. S. Andersen, H. Yan, and K. V. Gothelf, "Bridging one helical turn in double-stranded DNA by templated dimerization of molecular rods," *Angewandte Chemie*, vol. 47, no. 30, pp. 5569–5572, 2008.
- [14] J. J. Birac, W. B. Sherman, J. Kopatsch, P. E. Constantinou, and N. C. Seeman, "Architecture with GIDEON, a program for design in structural DNA nanotechnology," *Journal of Molecular Graphics and Modelling*, vol. 25, no. 4, pp. 470–480, 2006.
- [15] E. S. Andersen, M. Dong, M. M. Nielsen et al., "DNA origami design of dolphin-shaped structures with flexible tails," *ACS Nano*, vol. 2, no. 6, pp. 1213–1218, 2008.
- [16] J. Li, H. Pei, B. Zhu et al., "Self-assembled multivalent DNA nanostructures for noninvasive intracellular delivery of immunostimulatory CpG oligonucleotides," *ACS Nano*, vol. 5, no. 11, pp. 8783–8789, 2011.
- [17] E. S. Andersen, M. Dong, M. M. Nielsen et al., "Self-assembly of a nanoscale DNA box with a controllable lid," *Nature*, vol. 459, no. 7243, pp. 73–76, 2009.

Research Article

Preparation and Properties of PTFE-PMMA Core-Shell Nanoparticles and Nanocomposites

Diego Antonioli,¹ Michele Laus,¹ Giampaolo Zuccheri,² Valerj Kapeliouchko,³ Maria Cristina Righetti,⁴ Luca Boarino,⁵ and Katia Sparnacci¹

¹Dipartimento di Scienze e Innovazione Tecnologica, Università del Piemonte Orientale “Amedeo Avogadro,” Interuniversity Consortium for Materials Science Technology (INSTM), UdR Alessandria, Viale T. Michel 11, 15100 Alessandria, Italy

²Dipartimento di Biochimica “G. Moruzzi,” Modena-S3, Istituto di Nanoscienze del Consiglio Nazionale delle Ricerche, Università di Bologna, Italian Interuniversity Consortium for Materials Science and Technology (INSTM), UdR Alessandria, Via Irnerio 48, 40126 Bologna, Italy

³Solvay Solexis SpA, Piazzale Donegani 5/6, Alessandria 15047 Spinetta Marengo, Italy

⁴Institute for the Chemical and Physical Processes, National Research Council, Via G. Moruzzi 1, 56124 Pisa, Italy

⁵NanoFacility Piemonte, Electromagnetism Division, Istituto Nazionale di Ricerca Metrologica, Strada delle Cacce 91, 10135 Torino, Italy

Correspondence should be addressed to Michele Laus, laus@mfu.unipmn.it

Received 4 April 2012; Accepted 16 July 2012

Academic Editor: Baoquan Sun

Copyright © 2012 Diego Antonioli et al. This is an open access article distributed under the Creative Commons Attribution License, which permits unrestricted use, distribution, and reproduction in any medium, provided the original work is properly cited.

The preparation of polytetrafluoroethylene-poly(methyl methacrylate) (PTFE-PMMA) core-shell particles was described, featuring controlled size and narrow size distribution over a wide compositional range, through a seeded emulsion polymerization starting from a PTFE seed of 26 nanometers. Over the entire MMA/PTFE range, the particle size increases as the MMA/PTFE ratio increases. A very precise control over the particle size can be exerted by properly adjusting the ratio between the monomer and the PTFE seed. Particles in the 80–240 nm range can be prepared with uniformity indexes suited to build 2D and 3D colloidal crystals. These core-shell particles were employed to prepare nanocomposites with different compositions, through an annealing procedure at a temperature higher than the glass transition temperature of the shell forming polymer. A perfect dispersion of the PTFE particles within the PMMA matrix was obtained and optically transparent nanocomposites were prepared containing a very high PTFE amount.

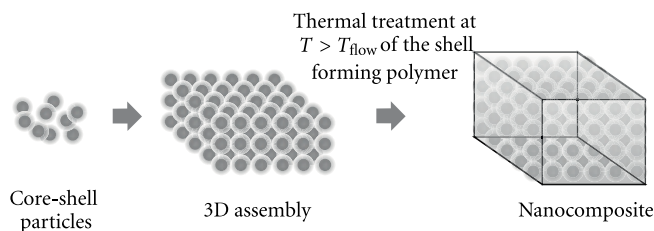
1. Introduction

Fillers are well recognized to be integral components for enhancement of polymer properties in many applications. The oldest and most conventional processing route is melt compounding which is based on a direct dispersion of the filler into the polymer during the melt leading to composites. This processing route is very well adapted for producing high-performance parts by injection molding or extrusion. In all cases, an adequate surface preparation of the filler is crucial to favor their dispersion inside the polymer.

Nanocomposites represent the evolution of the conventional composites in that the filler size is in the nanoscale

region, for example, nanoclay [1] and carbon nanotubes [2], and nanoparticles [3]. Due to the extremely high surface to volume ratio of the nanofillers, nanocomposites have pronounced properties that are not realized with traditional microscale fillers. The mechanical properties, electrical and thermal conductivity, and flammability resistance all differ in nanocomposites in comparison to conventional composites [4]. In turn, the processing aspects for this novel class of materials are definitely more critical with respect to microscale composites because of the inherently higher aggregation propensity of the nanofillers.

Although top-down approaches involving melt processing techniques are often employed because these are



SCHEME 1: Porous and compact nanocomposites from core-shell particles.

generally considered more economical, more flexible for formulation, and involve compounding and fabrication facilities commonly used in commercial practice; the ideal morphology, consisting of nanofillers individually dispersed in the polymer matrix, is frequently not achieved and varying degrees of dispersion are more common. This originates an inherent irreproducibility in the nanocomposite properties. In addition, the presence of nanofiller aggregates results particularly critical in applications in which transparency is required.

An alternative very efficient method to prepare nanocomposites featuring homogeneous nanofiller dispersion consists in the use of tailored polymer particles [5]. This bottom-up strategy involves either blends of colloidal polymer particles with a second type of particles (inorganic or polymeric) or hybrid particles consisting of a polymer phase and a second phase. A key advantage of this colloidal approach is that it offers control of structure at the nanoscale (within particles) and at the meso- and even macroscale through the formation of ordered assemblies of particles that should be considered as “building blocks” of larger structures.

In this general frame, core-shell particles are particularly suited system to produce a variety of nanostructured materials. Core-shell particles featuring a narrow size distribution can self-assemble to generate highly ordered structures, which represent promising candidates in applications such as catalysis, sensing, optics, molecular separation, single-molecule detection, and optoelectronics [6–8]. Two-dimensional structuration leads to 2D colloidal crystals, which could be employed in nanosphere lithography (NSL) [9], among others. 3D structuration leads to opals in which photonic properties can be originated from the periodic modulation in structure and composition [10]. In addition, aside from the above porous materials, compact nanocomposites can be obtained [7] by annealing a 3D assembly of core-shell particles at a temperature lower than the glass transition or melting of the core but higher than the glass transition of the shell forming polymer to assure that the flow of the shell-forming polymer fills the voids (Scheme 1).

This thermal treatment leads to the formation of a continuous polymer matrix in which the cores could be arranged in regular registry within the matrix. Since the characteristic size of the different domains is on the nanometer range, much smaller than the wavelength of light, the material should be optically transparent.

In recent studies, polytetrafluoroethylene (PTFE) latexes with particles in the submicrometer size range were successfully employed as seeds in the emulsifier-free emulsion polymerization of various monomers including styrene [11], acrylic mixtures [12], or methyl methacrylate [13] thus leading to a wide variety of core-shell nanoparticle architectures featuring a relatively narrow size distribution. Two dimensional structuration of these particles leads to 2D colloidal crystals which were employed in nanosphere lithography [14] whereas 3D structuration allowed opals to be obtained featuring interesting photonic properties [15].

Following our continuing interest in the preparation and study of PTFE-based nanocomposites from core-shell nanoparticles, in this paper we further explore this strategy extending the previous studies through the preparation of polytetrafluoroethylene-poly(methyl methacrylate) (PTFE-PMMA) core-shell particles over a wide compositional range, starting from a PTFE seed of 26 nanometers. The control of the size and size distribution of the resulting core-shell nanoparticles will be described and a variety of nanocomposites are prepared by thermally treating the corresponding core-shell nanoparticle assemblies.

2. Experimental

2.1. Materials. PTFE latex BP44 (350.4 g/L) was provided by Solvay Solexis and consists of particles with spherical shape, average diameter of 26 nm, and narrow size distribution. Their general preparation was previously reported [11]. Methyl methacrylate (MMA) (99%, Fluka) was distilled under reduced pressure in nitrogen atmosphere and stored at -18°C until use. Potassium persulfate (98%, Carlo Erba) was used without further purification.

2.2. Preparation of PTFE-PMMA Core-Shell Nanoparticles. The PTFE-PMMA core-shell colloids were synthesized in a 1 L five-neck-jacketed reactor equipped with a condenser, a mechanical stirrer, a thermometer, and inlets for nitrogen and monomer. First, the appropriate amount of PTFE latex was introduced into the reactor containing 500 mL of deionized water at room temperature with a stirring rate of 300 rpm. The mixture was purged with nitrogen for 20 min and nitrogen was flushed during the entire polymerization procedure. Next, the mixture was heated to 75°C and MMA (50.0 mL, 0.467 mol) was added. Then, after additional 15 min of equilibration time, the potassium persulfate aqueous solution (10 mL, 0.59 mmol) was added

TABLE 1: Synthesis details and yield of the various samples.

Latex	Sample	Volume of H ₂ O (mL)	Volume of MMA (mL)	Weight of PTFE (g)	Yield (%)
BP44 26 nm	PMMA	500.0	50.0	0	88.7
	BPM1	500.0	50.0	0.12	86.2
	BPM2	500.0	50.0	0.24	91.6
	BPM3	500.0	50.0	0.71	88.7
	BPM4	500.0	50.0	1.45	93.5
	BPM5	500.0	50.0	2.99	93.7
	BPM6	500.0	50.0	6.38	85.8
	BPM7	500.0	50.0	10.27	88.2
	BPM8	500.0	50.0	20.06	90.5
	BPM9	500.0	50.0	31.20	91.0
	BPM10	500.0	50.0	46.80	89.6
	BPM11	500.0	50.0	70.20	79.9
	BPM12	500.0	50.0	109.20	85.9
	BPM13	500.0	23.4	87.61	86.1
	BPM14	500.0	15.6	82.74	87.3
BPM15	500.0	11.7	98.56	85.7	

and the mixture was reacted for 24 h. The obtained latex was purified from the unreacted monomer by repeated dialyses. All the PTFE-PMMA latexes were obtained following the above general procedure by varying the initial PTFE latex amount.

Table 1 collects the details of the various preparations, including yield.

2.3. Characterization. The concentration of latex dispersion was determined gravimetrically. The particle size and size distribution of the core-shell particles were determined by scanning electron microscope (SEM), scanning force microscope (SFM), and dynamic light scattering (PCS). The microscope was an Inspect F SEM-FEG (Field Emission Gun) from FEI Company, with a beam diameter of 3 nm. The SEM micrographs were elaborated by the Scion Image processing program. From 300 to 350, individual microsphere diameters were measured for each sample. SFM analysis was performed with Tapping-Mode Scanning Force Microscopy (TM-SFM) in a NanoScope IIIa Scanning Force Microscope equipped with a Multimode head (Digital Instruments/Bruker, S. Barbara, CA, USA). TEM was performed by use of an Hitachi H 800 Microscope equipped with cold stage. For TEM observation, a certain quantity of dispersion was diluted properly by distilled water and then stained with pH 2.0 phosphotungstic acid (PTA) solution. The mixture was allowed to stand for a while, then a drop of the stained latex was placed on a carbon-formvar-coated, copper grid and dried at room temperature. Dynamic light scattering analysis was performed at 25°C, with a Malvern Zetasizer 3000 HS at a fixed scattering angle of 90°, using a 10 mV He-Ne laser and PCS software for Windows (version 1.34, Malvern, UK). Each value is the average of five measurements. Electrophoretic mobility was measured with a Malvern Zetasizer 3000 HS. Each value

is the average of five measurements. The instrument was checked using a latex with known Zeta potential. Thermogravimetric analysis (TGA) was performed with a Mettler-Toledo TGA/SDTA851e at a scanning rate of 10°C/min from room temperature up to 1100°C under nitrogen flow. Differential scanning calorimetry (DSC) was carried out using a Mettler-Toledo DSC 821 apparatus. Samples of about 5 mg were employed. The instrument was calibrated with high-purity standards (indium, naphthalene, benzoic acid, and cyclohexane) at 10°C/min. Dry nitrogen was used as purge gas. The samples for the dynamic mechanical analysis were prepared introducing the powder sample into a rectangular mould. The entire assembly was then placed between press plates with a nominal pressure of 4.9×10^7 Pa and allowed to stand at room temperature for 20 min. The temperature was then raised to 160°C and the pressure released to 4.9×10^6 Pa. After 15 min, the sample was cooled to room temperature and recovered as rectangular $30 \times 5 \times 2$ mm sheets. The modulus was measured with a dynamic mechanical analyzer Rheometric DMTA V, employing the three point bending geometry. A static to dynamic stress ratio of 120% and a scanning rate of 4°C/min were chosen. The strain was sufficiently small to be within linear viscoelastic range.

3. Results and Discussion

BP44 latex consists of spherical particles with average diameters of 26 nm and, as received, contains residual PFPE surfactant. As the presence of the residual surfactant could interfere with the emulsifier-free-seeded emulsion polymerization, the PTFE latex was thoroughly dialyzed. The conductivity of the BP44 latex was 830 μ S/cm before and 120 μ S/cm after the dialysis. The emulsifier-free seeded emulsion polymerizations were performed, as previously

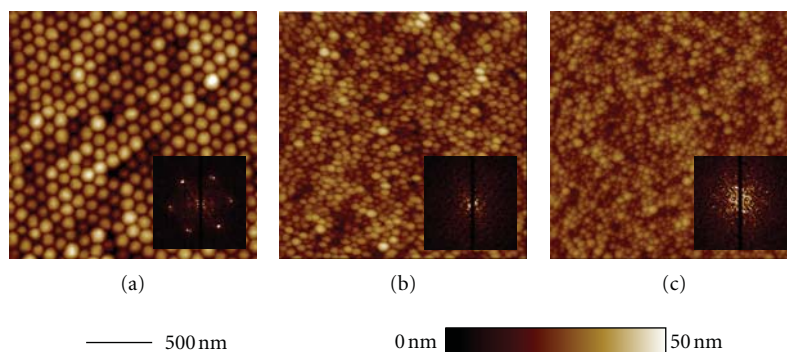


FIGURE 1: Tapping-mode AFM images of the top layer of a film obtained by slow solvent evaporation on freshly cleaved mica. (a) Image of the BPM4 specimen showing extreme regularity and very low dimension dispersion. In the inset, the 2D FFT showing distinct frequency peaks witnessing the high regularity of the hexagonal close-packed layer (FFT maxima measure an approximately 100 nm distance between particles). The direct-space measurement of the closest interparticle distances on a set of particles shows a (108 ± 8) nm distance (average \pm standard deviation); (b) same as above on the BPM6 specimen, showing a markedly lower order in the layer (the 2D FFT, in the inset, does not show any distinct maxima). Direct-space measurements of closest interparticle distances report a (46 ± 25) nm distance, also witnessing a higher dimensional dispersion on the particle dimensions and packing; (c) same as above for the BPM10 specimen. Closest interparticle distances (54 ± 25) nm with a low order multilayer (2D FFT in the inset with no distinct maxima). The size and relative heights of the micrographs are displayed according to the attached size bar and colormap.

described [11–13], by adding appropriate amounts of the PTFE latex (Table 1) and MMA into deionized water and running the reactions at 75°C for 24 hrs using potassium persulfate as the free radical source. At the end of the reaction, the latexes were purified by repeated dialyses. In all the polymerization reactions, MMA and potassium persulfate as well as the water content were kept constant, whereas variations were allowed in the amount of PTFE. Under these conditions, the initial PTFE weight percent with respect to the total weight of MMA and PTFE was varied from 0.25 to 90%. Accordingly, the sample series marked BPM n is obtained in which n is a number related to the initial PTFE weight percent. Stable latexes were obtained with nanosphere yields ranging from 85 to 93% (after the workup) and nearly quantitative MMA conversions (Table 1).

As a typical example, Figure 1 reports the tapping-mode AFM images of multilayers obtained by slow solvent evaporation on freshly cleaved mica of samples BPM4, BPM6, and BPM10, whereas Figure 2 reports representative PCS curves of core-shell samples and, for comparison purposes, of the BP44 seed latex.

No residual PTFE, deriving from BP44 latex, is present, and all the PCS curves are quite narrow. This suggests that the methyl methacrylate polymerization occurs quantitatively onto the PTFE seeds, as previously described for different systems [13]. The zeta potential of the various samples was also measured and resulted comprised between -45 and -60 mV in agreement with an electrostatic stabilization driven by the repulsions of negative charges deriving from the ionic initiator fragments. The core shell nature of the samples was confirmed by direct TEM observation. Figure 3 reports the TEM image of sample BPM10 after treatment with phosphotungstic acid at a magnification of 180,000. Although the particles appear deformed under the electronic beam, the core and shell structure can be clearly seen.

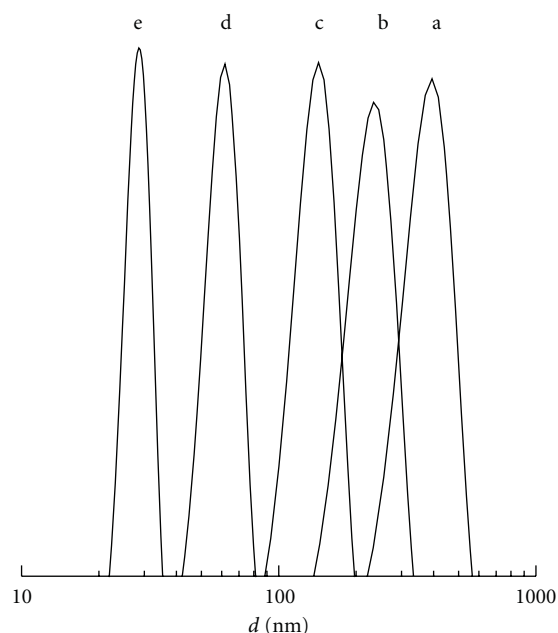


FIGURE 2: PCS spectrum of samples PMMA (a), BPM1 (b), BPM3 (c), BPM7 (d), and BP44 latex (e).

The composition of the various samples was determined by TGA and DSC data. Figure 4 reports the TGA curves of BPM n series including the BP44 latex and the TGA curve of a purely PMMA sample. The composition can be estimated from the TGA curves considering that the weight losses at 360 and 500°C correspond to PMMA and PTFE decomposition, respectively. On the other hand, in the DSC traces (Figure 5), the endothermic peak at about 325°C corresponds to PTFE melting. Consequently, the amount of PTFE in the core-shell

TABLE 2: Size and composition data of the various samples.

Sample	% PTFE estimated (W/W)	% PTFE ^(a) (DSC)	% PTFE ^(b) (TGA)	<i>d</i> estimated (nm)	<i>d</i> PCS (nm)	<i>T_g</i> DSC ^(c) (°C)
PMMA	0.0	0.0	0.0	—	391.3	121
BPM1	0.25	0.3	0.4	240	236.6	121
BPM2	0.5	0.4	0.4	191	194.4	121
BPM3	1.5	1.4	1.2	128	136.8	121
BPM4	3.0	3.1	3.4	101	112.0	121
BPM5	6.0	5.7	5.9	80	82.5	125
BPM6	12.0	12.0	15.4	63	68.5	134
BPM7	18.0	20.4	24.1	55	53.8	134
BPM8	30.0	22.8	28.8	45	48.0	131
BPM9	40.0	46.5	43.7	40	41.1	130
BPM10	50.0	53.0	48.1	37	38.4	128
BPM11	60.0	66.8	61.9	34	35.4	130
BPM12	70.0	70.3	67.2	31	31.8	Nd
BPM13	80.0	80.9	75.6	29	30.1	Nd
BPM14	85.0	84.5	86.5	29	29.4	Nd
BPM15	90.0	87.4	87.9	28	29.2	Nd

^(a) The PTFE percentage in the core-shell samples was estimated from the amount of feed PTFE and MMA assuming quantitative MMA conversion, absence of residual PTFE seeds, and no PMMA particle formation.

^(b) The amount of PTFE was estimated from the melting enthalpy of the PTFE component (endothermic peak at 325°C) considering that the melting enthalpy of the BP44 sample is 46.05 J g⁻¹ (first DSC heating curve).

^(c) First DSC heating curve at 20°/min.

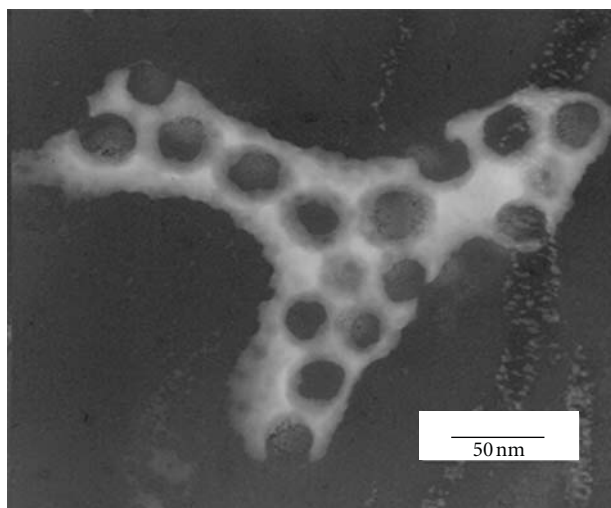


FIGURE 3: TEM micrographs of sample BPM10.

samples can be evaluated from the corresponding melting enthalpy in comparison with the melting enthalpy of the pure PTFE seed (Table 2) and, by difference, the amount of PMMA can also be determined assuming that there is no interaction between the PTFE core and the PMMA shell.

Provided that no pure PMMA or PTFE nanoparticles are present at the end of the reaction, and taking into account the yield values, the composition of the core-shell nanoparticles can be calculated from the amount of the initially added PTFE and MMA and are collected in Table 2.

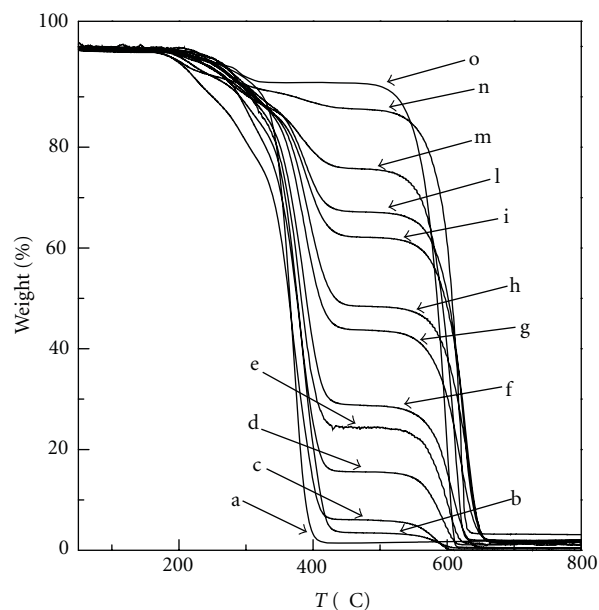


FIGURE 4: TGA curves at 10° C/min heating rate for various samples in nitrogen atmosphere: PMMA (a); BPM4 (b); BPM5 (c); BPM6 (d); BPM7 (e); BPM8 (f); BPM9 (g); BPM10 (h); BPM11 (i); BPM12 (l); BPM13 (m); BPM14 (n); BP44 (o).

The composition data estimated by TGA and DSC are in excellent agreement with those calculated (Table 2).

In case of samples with high PTFE content, it is extremely difficult to obtain good SEM images because an excessive increase in the SEM acceleration voltage degrades the

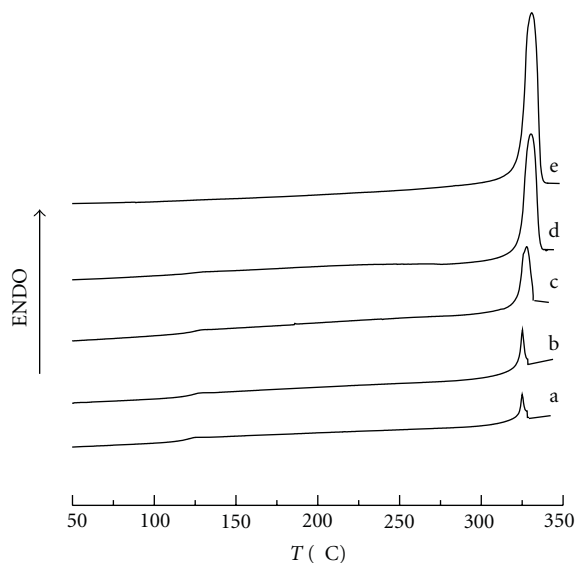


FIGURE 5: DSC second heating at $10^{\circ}\text{C}/\text{min}$ of samples: BPM4 (a), BPM5 (b), BPM7 (c), BPM11 (d), and BP44 (e).

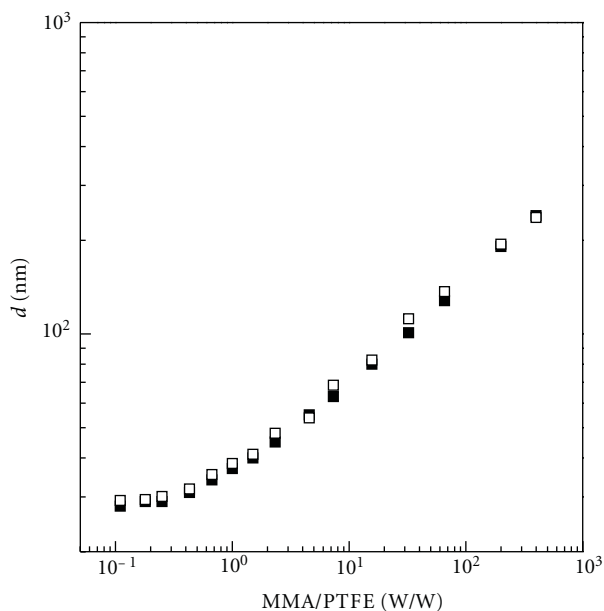


FIGURE 6: Trend of the particle diameter of the BPMn series as a function of the weight ratio between the initially added methyl methacrylate and PTFE. The full symbols refer to the calculated data, whereas the open symbols refer to the experimental results.

samples thus severely reducing the image quality. Consequently, to give a homogeneous evaluation of the size of the entire sample series, PCS data were collected (Table 2) and the relevant average diameters are reported in a double log scale in Figure 6 as a function of the weight ratio between the initial methyl methacrylate and PTFE. The full symbols in Figure 6 represent the expected final particle assuming no secondary nucleation or aggregation. Over the entire MMA/PTFE range, the particle size increases as the

MMA/PTFE ratio increases and agrees with the expected final particle size, indicating that secondary nucleation was prevented with all the monomer ending up as shell polymer. The systematic overestimation of the particle size with respect to the calculated size could derive from the inherent tendency of the PCS technique to overestimate the particle size with respect to the SEM data. To make a comparison, in case of sample BPM3 prepared with a ratio MMA/PTFE = 66, the estimated size is 128 nm whereas the PCS and the SEM data are 136 and 132 nm, respectively.

The overall picture of these data clearly indicates that a very precise control over the particle size can be exerted by properly adjusting the ratio between the monomer and the PTFE seed. The inhibition of the secondary nucleation is probably motivated by the large seed surface due to the very small size of the PTFE seeds. The wide surface area of the seed particles can capture all the unstable nuclei produced in the system even at very high MMA/PTFE ratios, thus avoiding the formation of stable secondary particles.

Figure 7 reports the SEM images of samples BPM1, BPM2, BPM4, and BPM6. The former three samples present average diameters of 236, 197, and 105 nm with uniformity ratios [16] U of 1.01, 1.01, and 1.03, respectively, whereas for sample BPM6 an increase in the size distribution can be observed, although a reliable determination of the relevant U value is not possible. The decrease in the U value as the ratio MMA/PTFE increases indicates a self-sharpening propensity for these systems, as previously observed for other systems [17]. This behavior suggests the occurrence of a competitive growth mechanism [18] of latex particles in which small latex particles grow faster in size than larger ones, thus leading to narrow size distributions. It is interesting to note that this behavior was also observed [19] for the seeded dispersion polymerization of methyl methacrylate using PMMA submicron seeds. According to the above results, and considering that U of about 1.05 is the upper limit to produce a good nanoparticle structuring [20], we can conclude that, using the above seeded polymerization technique, 2D and 3D colloidal crystals from particles in the 80–240 nm range can be prepared.

Compact nanocomposites were prepared by introducing the core-shell particles, as powder samples, into a rectangular mould. After an equilibration time at room temperature, the mould is heated to 160°C , maintained at this temperature for 15 min under pressure, and then cooled to room temperature. No structural ordering was attempted and macroscopic samples in the form of rectangular sheets of $30 \times 5 \times 2$ mm size were obtained. Figure 8 illustrates the effect of the nanoparticle size and the PTFE content on the corresponding lattices and nanocomposites appearance. Latexes containing relatively big particles appear milky, as can be seen for latex BPM4 (sample A), whereas as the particle size decreases the latexes become progressively more transparent. In contrast, the nanocomposites are transparent up to a very high PTFE content. The transparency is not totally lost also in case of sample BPM11 (sample D) that contains about 80% of PTFE.

This observation is a clear proof for an excellent dispersion of the PTFE particles within the polymer matrix.

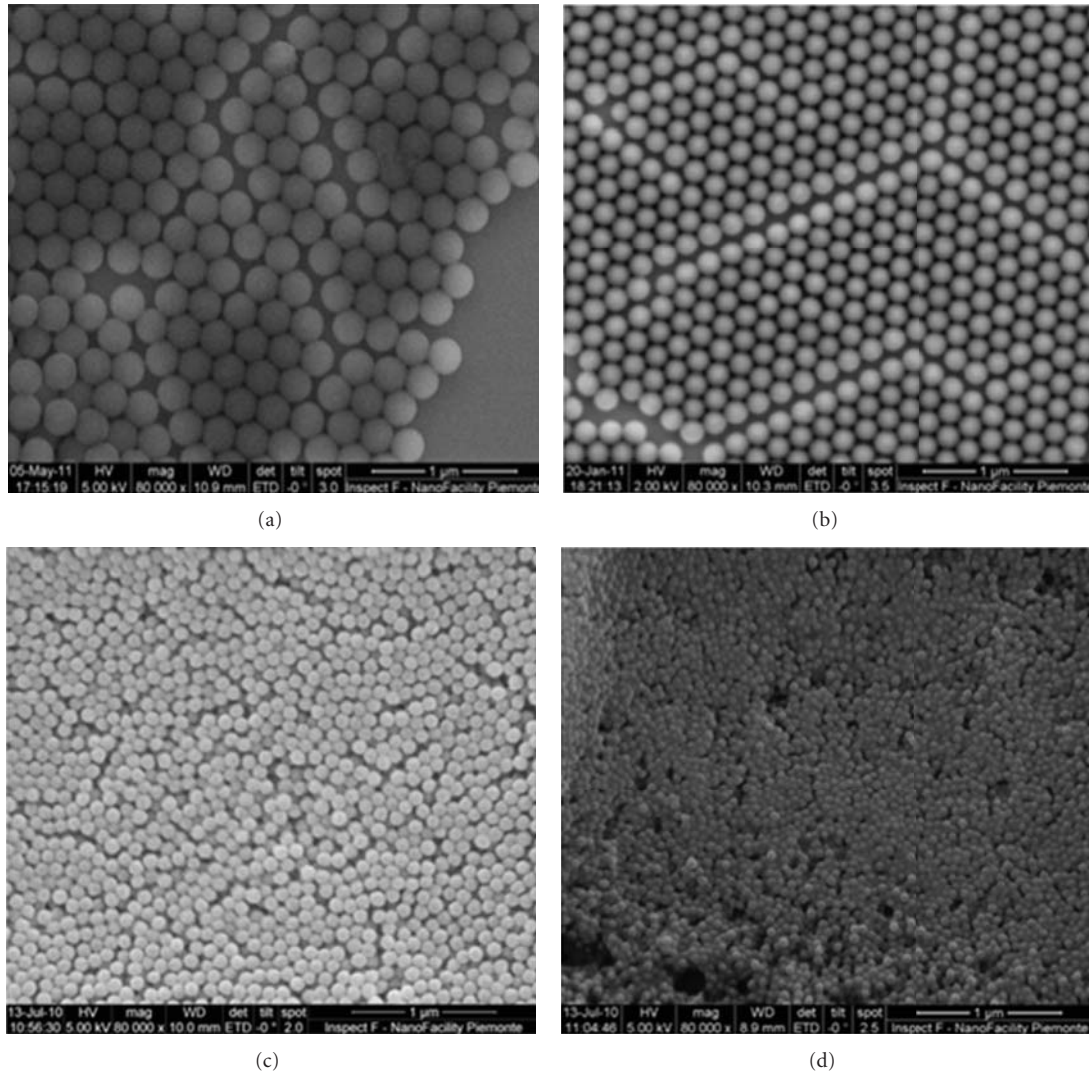


FIGURE 7: SEM micrographs of samples BPM1 (a), BPM2 (b), BPM4 (c), and BPM6 (d).

This result is also confirmed by the nanocomposite thermal behavior. In general, the melting of the PTFE occurs, with a heating rate of $10^{\circ}\text{C}/\text{min}$, at 325°C (Figure 5), whereas the minimum of the crystallization exotherm, with a cooling rate of $-10^{\circ}\text{C}/\text{min}$, is observed at 316°C (Figure 9(a)), in agreement with literature data [21]. The crystallization of the PTFE in the nanocomposites at $-20^{\circ}\text{C}/\text{min}$ is observed with minimum at 270°C (Figure 9(b–e)). This peculiar crystallization behavior, recently described and thoroughly discussed [22] for a series of PTFE-PMMA core-shell nanoparticles, can be rationalized within the frame of the fractionated crystallization mechanism [23, 24]. Due to the compartmentalization of PTFE within the core-shell nanoparticles, the number of the dispersed PTFE particles is much greater than the number of heterogeneities that usually nucleate the polymer in bulk. In these conditions, only one crystallization component at very high undercooling is observed, deriving from the homogeneous nucleation mechanism [25, 26]. In turn, the

observation of the single low-temperature crystallization exotherm can be viewed as a proof for the occurrence of a perfect dispersion of the PTFE particles in the nanocomposite.

The dynamic mechanical behavior of the nanocomposites was also studied by DMTA using the three-point bending geometry in the linear viscoelasticity region at the frequency of 1 Hz, between 40°C and the temperature at which the samples lost their dimensional stability, with a heating rate of $4^{\circ}\text{C}/\text{min}$. Figure 10 illustrates collectively the trends of the storage modulus E' and $\tan \delta$ as a function of temperature. The dynamic storage modulus E' decreases with increasing temperature with a drop at about 145°C , corresponding to the glass transition of the PMMA component.

The glass transition temperature of the PMMA component is slightly affected by the PTFE amount and only a small increase in temperature, with a parallel broadening of the relaxation process in the high-temperature side of

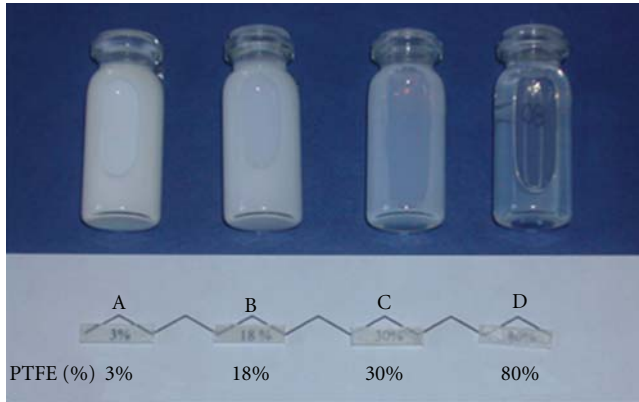


FIGURE 8: (A): BPM4 ($d = 112$ nm, 3% PTFE); (B): BPM7 ($d = 54$ nm, 18% PTFE); (C): BPM8 (48 nm, 30% PTFE); (D): BPM11 ($d = 35$ nm, 80% PTFE).

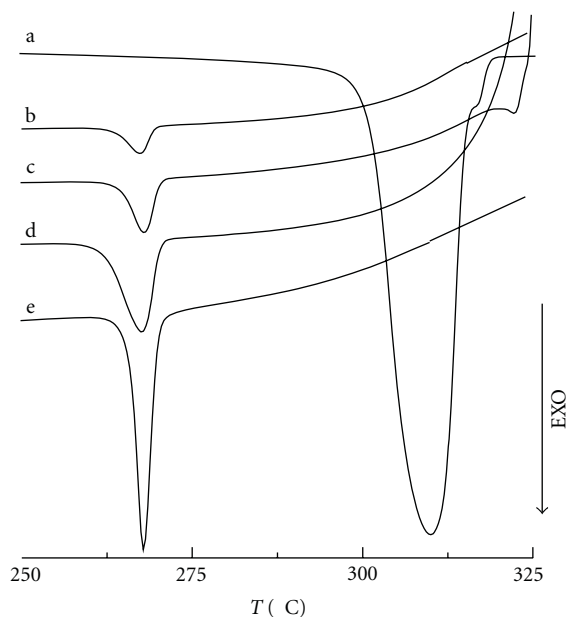


FIGURE 9: DSC cooling at $20^{\circ}\text{C}/\text{min}$ after fast heating to 330°C of samples BP44 (a), BPM4 (b), BPM5 (c), BPM6 (d), and BPM8 (e).

the transition is observed (Tables 2 and 3, Figure 10(B)). Figure 11 illustrates the trend of the storage modulus before and after the glass transition temperature. At a temperature lower than the PMMA glass transition, E' results about 2.5–3.5 GPa, irrespective of the PTFE amount. In contrast, at temperatures higher than the PMMA glass transition, the storage modulus increases linearly as the PTFE amount increases. These effects are reported in many nanostructured material systems such as PMMA/silica [27] and PS/clay nanocomposites [28] and can be explained in terms of the classical mechanical reinforcement by the relatively rigid particles and restricted mobility in the polymer matrix [29].

TABLE 3: Dynamic storage modulus E' in the glassy (50°C) and rubbery (200°C) state and glass transition temperatures from the maximum in the $\tan \delta$ peak.

Sample	E' glassy state 50°C (GPa)	E' rubbery state 200°C (MPa)	T_g ($^{\circ}\text{C}$)
PMMA	2.6	4.3	142
BPM4 (3%)	2.8	6.9	146
BPM5 (6%)	2.8	8.8	148
BPM6 (12%)	3.0	9.0	148
BPM7 (18%)	3.3	9.4	149
BPM8 (30%)	3.4	12.6	148
BPM9 (40%)	2.8	14.3	149
BPM10 (50%)	2.9	15.9	149
BPM11 (60%)	3.1	18.9	146

4. Conclusions

This paper is addressed to the preparation of PTFE-PMMA core-shell particles featuring controlled size and narrow size distribution over a wide compositional range, through an emulsifier-free seeded emulsion polymerization starting from a PTFE seed of 26 nanometers. Over the entire MMA/PTFE range, the particle size increases as the MMA/PTFE ratio increases and a very precise control over the particle size can be exerted by properly adjusting the ratio between the monomer and the PTFE seed. In addition, the particle size distribution self-sharpens as the ratio MMA/PTFE increases. Consequently, particles in the 80–240 nm range were prepared featuring uniformity indexes suited to build 2D and 3D colloidal crystals.

Compact nanocomposites can be prepared by annealing the core-shell particles at a temperature higher than the glass transition temperature of PMMA. Transparent nanocomposites are obtained up to a very high PTFE content thus indicating an excellent dispersion of the PTFE particles within the PMMA matrix which is also confirmed by the observation of fractionated crystallization effects of the PTFE particles. The dynamic mechanical behavior of various nanocomposites indicates that the glass transition of the PMMA component is slightly affected by the PTFE amount. The storage modulus, at temperatures lower than the PMMA glass transition is nearly constant in the various samples, whereas it increases linearly as the PTFE amount increases at temperatures higher than the PMMA glass transition as expected in case of a mechanical reinforcement by the relatively rigid particles and restricted mobility in the polymer matrix.

Disclosure

All the authors do not have any direct financial relation with the commercial identity mentioned in the paper that might lead to a conflict of interests.

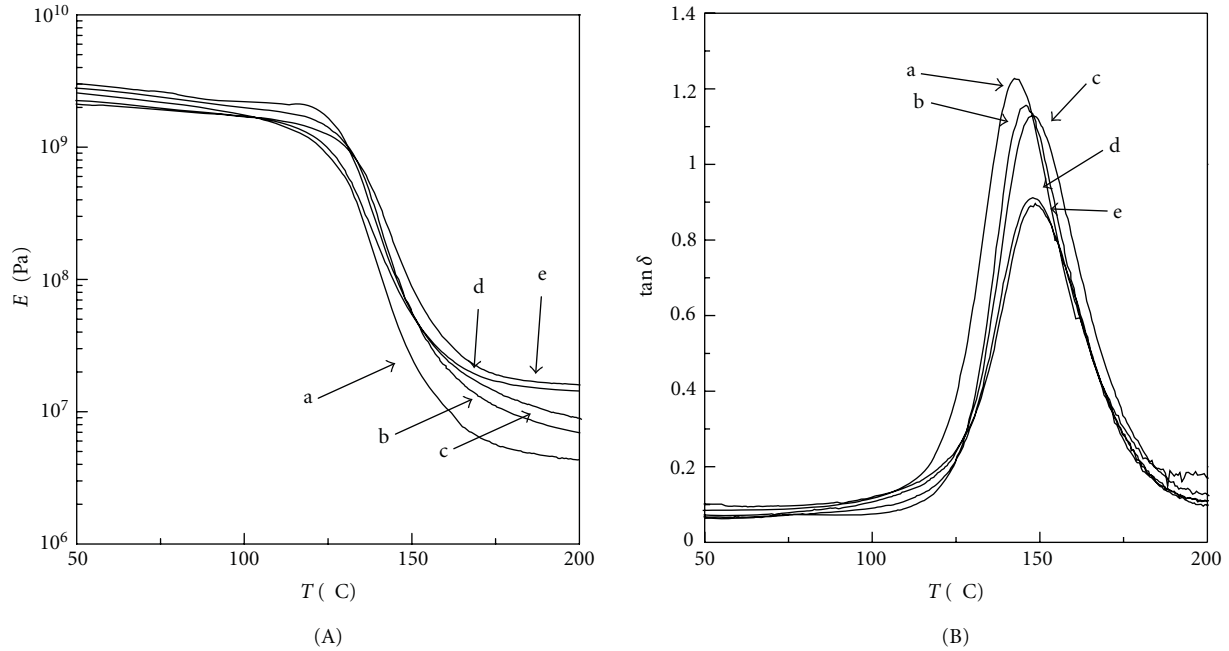


FIGURE 10: Trend of the storage modulus E' (A) and loss tangent $\tan \delta$ (B) for BPMn samples and pure PMMA sample as a function of temperature: PMMA (a), BPM4 (b), BPM6 (c), BPM9 (d), and BPM10 (e).

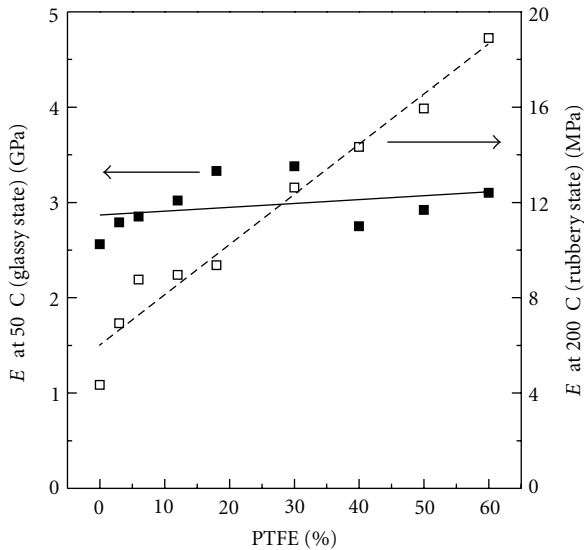


FIGURE 11: Trend of the storage modulus E' in glassy (full symbols, GPa) and rubbery (open symbols, MPa) states.

Acknowledgment

Part of this work has been performed at NanoFacility Piemonte, INRiM, a laboratory supported by Compagnia di San Paolo.

References

- [1] E. P. Giannelis, "Polymer layered silicate nanocomposites," *Advanced Materials*, vol. 8, no. 1, pp. 29–35, 1996.
- [2] P. M. Ajayan and J. M. Tour, "Materials science: nanotube composites," *Nature*, vol. 447, no. 7148, pp. 1066–1068, 2007.
- [3] B. A. Rozenberg and R. Tenne, "Polymer-assisted fabrication of nanoparticles and nanocomposites," *Progress in Polymer Science*, vol. 33, no. 1, pp. 40–112, 2008.
- [4] D. R. Paul and L. M. Robeson, "Polymer nanotechnology: nanocomposites," *Polymer*, vol. 49, no. 15, pp. 3187–3204, 2008.
- [5] T. Wang and J. L. Keddie, "Design and fabrication of colloidal polymer nanocomposites," *Advances in Colloid and Interface Science*, vol. 147–148, no. 1, pp. 319–332, 2009.
- [6] Y. Xia, B. Gates, Y. Yin, and Y. Lu, "Monodispersed colloidal spheres: old materials with new applications," *Advanced Materials*, vol. 12, no. 10, pp. 693–713, 2000.
- [7] O. Kalinina and E. Kumacheva, "Polymeric nanocomposite material with a periodic structure," *Chemistry of Materials*, vol. 13, no. 1, pp. 35–38, 2001.
- [8] U. Jeong, Y. Wang, M. Ibisate, and Y. Xia, "Some new developments in the synthesis, functionalization, and utilization of monodisperse colloidal spheres," *Advanced Functional Materials*, vol. 15, no. 12, pp. 1907–1921, 2005.
- [9] J. C. Hulthen and R. P. Van Duyne, "Nanosphere lithography: a materials general fabrication process for periodic particle array surfaces," *Journal of Vacuum Science and Technology A*, vol. 13, no. 3, pp. 1553–1558, 1995.
- [10] K. Inoue and K. Kazuo, "Photonic crystals physics, fabrication and applications," in *Ohtaka editor Springer Series in Optical Sciences*, vol. 94, Springer, Berlin, Germany, 2004.
- [11] E. Giani, K. Sparnacci, M. Laus, G. Palamone, V. Kapeliouchko, and V. Arcella, "PTFE-polystyrene core-shell nanospheres and nanocomposites," *Macromolecules*, vol. 36, no. 12, pp. 4360–4367, 2003.
- [12] K. Sparnacci, D. Antonioli, S. Deregibus et al., "PTFE-based core-soft shell nanospheres and soft matrix nanocomposites," *Macromolecules*, vol. 42, no. 10, pp. 3518–3524, 2009.

- [13] V. Kapeliouchko, G. Palamone, T. Poggio et al., "PMMA-based core-shell nanoparticles with various PTFE cores," *Journal of Polymer Science A*, vol. 47, no. 11, pp. 2928–2937, 2009.
- [14] K. Sparnacci, D. Antonioli, S. Deregibus et al., "Two-dimensional non-close-packed arrays of nanoparticles via core-shell nanospheres and reactive ion etching," *Polymers for Advanced Technologies*, vol. 23, no. 3, pp. 558–564, 2011.
- [15] D. Antonioli, S. Deregibus, G. Panzarasa et al., "PTFE-PMMA core-shell nanoparticles as building blocks for self-assembled opals: synthesis, properties and optical response," *Polymer International*, vol. 61, no. 8, pp. 1294–1301, 2012.
- [16] S. M. Heard, F. Grieser, C. G. Barraclough, and J. V. Sanders, "The characterization of ag sols by electron microscopy, optical absorption, and electrophoresis," *Journal of Colloid And Interface Science*, vol. 93, no. 2, pp. 545–555, 1983.
- [17] K. Sparnacci, D. Antonioli, S. Deregibus et al., "Preparation, properties and self-assembly behavior of PTFE-based core-shell nanospheres," *Journal of Nanomaterials*, vol. 2012, Article ID 980541, 15 pages, 2012.
- [18] C. S. Chern, *Principles and Applications of Emulsion Polymerization*, Wiley, New York, NY, USA, 2008.
- [19] S. Jiang, E. D. Sudol, V. L. Dimonie, and M. S. El-Aasser, "Seeding as a means of controlling particle size in dispersion polymerization," *Journal of Applied Polymer Science*, vol. 108, no. 6, pp. 4096–4107, 2008.
- [20] M. E. Woods, J. S. Dodge, I. M. Krieger, and P. E. Pierce, "Monodisperse lattices: emulsion polymerization with mixtures of anionic and nonionic surfactants," *Journal of Paint Technology*, vol. 40, no. 527, pp. 541–548, 1968.
- [21] X. Q. Wang, D. R. Chen, J. C. Han, and S. Y. Du, "Crystallization behavior of polytetrafluoroethylene (PTFE)," *Journal of Applied Polymer Science*, vol. 83, no. 5, pp. 990–996, 2002.
- [22] M. Laus, K. Sparnacci, D. Antonioli et al., "On the multiple crystallization behavior of PTFE in PMMA/PTFE nanocomposites from core-shell nanoparticles," *Journal of Polymer Science B*, vol. 48, no. 5, pp. 548–554, 2010.
- [23] J. A. Koutsky, A. G. Walton, and E. Baer, "Nucleation of polymer droplets," *Journal of Applied Physics*, vol. 38, no. 4, pp. 1832–1839, 1967.
- [24] R. Montenegro, M. Antonietti, Y. Mastai, and K. Landfester, "Crystallization in miniemulsion droplets," *Journal of Physical Chemistry B*, vol. 107, no. 21, pp. 5088–5094, 2003.
- [25] G. Pompe, L. Häußler, P. Pötschke et al., "Reactive polytetrafluoroethylene/polyamide compounds. I. Characterization of the compound morphology with respect to the functionality of the polytetrafluoroethylene component by microscopic and differential scanning calorimetry studies," *Journal of Applied Polymer Science*, vol. 98, no. 3, pp. 1308–1316, 2005.
- [26] L. Häußler, G. Pompe, D. Lehmann, and U. Lappan, "Fractionated crystallization in blends of functionalized poly(tetrafluoroethylene) and polyamide," *Macromolecular Symposia*, vol. 164, no. 1, pp. 411–420, 2001.
- [27] Y. H. Hu, C. Y. Chen, and C. C. Wang, "Viscoelastic properties and thermal degradation kinetics of silica/PMMA nanocomposites," *Polymer Degradation and Stability*, vol. 84, no. 3, pp. 545–553, 2004.
- [28] R. Ruggerone, C. J. G. Plummer, N. N. Herrera, E. Bourgeat-Lami, and J. A. E. Månson, "Highly filled polystyrene-laponite nanocomposites prepared by emulsion polymerization," *European Polymer Journal*, vol. 45, no. 3, pp. 621–629, 2009.
- [29] L. E. Nielsen and R. W. Landel, *Mechanical Properties of Polymers and Composites*, Marcel Dekker, New York, NY, USA, 1994.

Research Article

Ultrafine Magnetite Nanopowder: Synthesis, Characterization, and Preliminary Use as Filler of Polymethylmethacrylate Nanocomposites

Pietro Russo,¹ Domenico Acierno,² Mariano Palomba,³ Gianfranco Carotenuto,³ Roberto Rosa,⁴ Antonino Rizzuti,⁵ and Cristina Leonelli⁴

¹ Institute of Chemistry and Technology of Polymers, National Research Council of Italy, Via Campi Flegrei, 34-80072 Pozzuoli, Italy

² Departments of Materials and Production Engineering, University of Naples Federico II, Piazzale Tecchio, 80-80125 Naples, Italy

³ Institute for Composite and Biomedical Materials, National Research Council of Italy, Piazzale Tecchio, 80-80125 Naples, Italy

⁴ Department of Materials and Environmental Engineering, University of Modena and Reggio Emilia, Strada Vignolese, 905-41125 Modena, Italy

⁵ Department of Water Engineering and Chemistry, Polytechnic of Bari, Via Orabona, 4-70125 Bari, Italy

Correspondence should be addressed to Pietro Russo, pietro.russo@unina.it

Received 5 April 2012; Revised 28 June 2012; Accepted 10 July 2012

Academic Editor: Menka Jain

Copyright © 2012 Pietro Russo et al. This is an open access article distributed under the Creative Commons Attribution License, which permits unrestricted use, distribution, and reproduction in any medium, provided the original work is properly cited.

Magnetite (Fe_3O_4) nanoparticles prepared by microwave-assisted hydrothermal synthesis have been characterized in terms of morphological and structural features. Electron micrographs collected in both scanning (SEM) and transmission (TEM) modes and evaluations of X-ray powder diffraction (XRD) patterns have indicated the achievement of a monodispersed crystallite structure with particles having an average size around 15–20 nm. Structural investigations by Micro-Raman spectroscopy highlighted the obtainment of magnetite nanocrystals with a partial surface oxidation to maghemite ($\gamma\text{-Fe}_2\text{O}_3$). Preliminary attention has been also paid to the use of these magnetite nanoparticles as filler for a commercial polymethylmethacrylate resin. Hybrid formulations containing up to 3 wt% of nanoparticles were prepared by melt blending and characterized by calorimetric and thermogravimetric tests. For sake of comparison, same formulations containing commercial Fe_3O_4 nanoparticles are also reported. Calorimetric characterization indicates an increase of both glass transition temperature and thermal stability of the nanocomposite systems when loaded with the synthesized magnetite nanoparticles rather than loaded with the same amount of commercial Fe_3O_4 . This first observation represents just one aspect of the promising potentiality offered by the novel magnetic nanoparticles when mixed with PMMA.

1. Introduction

In the last decades, a considerable amount of research has been devoted to the synthesis and characterization of iron oxides nanoparticles because of their technological potentialities. In particular, nanosized oxide materials such as magnetite (Fe_3O_4), maghemite ($\gamma\text{-Fe}_2\text{O}_3$), and hematite ($\alpha\text{-Fe}_2\text{O}_3$) have found wide-ranging applications. Hematite nanoparticles, crystallizing in the rhombohedral system and showing a weak ferromagnetic behavior at room temperature [1], have been extensively used as catalyst [2, 3], pigment [4], gas sensor [5], optical devices [6], and medicine applications

[7]. Magnetite and maghemite, instead, crystallizing in the cubic crystal system and with a ferromagnetic behavior at room temperature, have been widely exploited in technological applications including information storage [8], sensors [9], refrigeration [10], and coil cores [11], as well as in contrast agent for magnetic resonance imaging [12, 13], and potential mediator for magnetic hyperthermia [14].

Among the chemical routes used so far to synthesize iron oxide based nanomaterials, it is worth to mention hydrothermal synthesis [15, 16], coprecipitation [17], sol-gel method [18], and colloidal chemistry method [19]. These methods usually involve synthesizing an iron-based

precursor gel, followed by decomposing the gel or precursor into the designed crystalline iron oxide phase at an elevated temperature. However, the uniformity of the size of the particle of these nanomaterials was rather poor [20–22].

Considering that chemical composition and morphology controls for these magnetic nanoparticles appear to be crucial for their applications, a specific interest has been dedicated to control the particle size dispersion [23–26]. Small sizes and uniform morphology are typically required for the applications of magnetic nanoparticles because of the dependence of magnetic properties on the morphologies of nanoparticles. When the size of Fe_3O_4 nanoparticles is very small, the size of single-magnetic domain is equal to that of each single particle. Fe_3O_4 nanoparticles usually exhibit superparamagnetic property [27], therefore, their fabrication is attracting a lot of interest.

Another well-established approach to control, on one side, the morphology of magnetite nanoparticles during their synthesis and, on the other hand, their dispersion in a polymer matrix is the use of suitable polymeric surfactants [28, 29]. At this regard, given the outstanding interest gained by this class of organic/inorganic materials for applications in many fields, a wide range of resins including polystyrene [30], poly(vinyl alcohol) [31], poly(pyrrole) [32], polyaniline [33, 34], and epoxy resins [35] has been already considered.

In this research, ultrafine magnetite nanoparticles were synthesized by an innovative hydrothermal microwave-assisted route and systematically characterized in terms of morphological and structural aspects. Literature references [36, 37] employ iron(III) chloride, $\text{FeCl}_3 \cdot 6\text{H}_2\text{O}$ as the metal precursor in the hydrolytic reactions, while in the present work the Fe_3O_4 precursor was $\text{FeCl}_2 \cdot 4\text{H}_2\text{O}$. This is a main difference that requires to be highlighted since most of the “soft-chemistry” synthetic strategies (both hydrolytic and nonhydrolytic) for the obtainment of magnetite nanoparticles start from iron-(III)-based precursor (see e.g., [38, 39]). Moreover, in the work by Parsons et al. [37] the product obtained at the reaction temperature of 100°C and 125°C was an iron (III) oxyhydroxide chloride, commonly known as akaganeite. An increase in the reaction temperature up to 250°C led to single hematite phase. Thus, the work by Parsons and coworkers substantially differs from ours in both the precursors used and the synthesised products.

As concerns the paper by Wang et al. [36], a further difference (apart from the use of an iron(III) precursor) with respect to our paper is represented by the use of polyethylene glycol (PEG) as surfactant. Indeed, those authors employed such a surfactant in order to obtain nanoparticles of phase pure Fe_3O_4 ; however, as they noticed (through FTIR study), the surfactant was adsorbed on the surface of nanoparticles product thus affecting the saturation magnetization.

In order to emphasize potential applications of the novel magnetic powder preliminary attention has been devoted to polymer nanocomposites based on an amorphous thermoplastic matrix. In particular, given the relevant interest gained so far by polymer systems containing magnetic particles in many different industrial areas (e.g., radio-absorbing materials, polymer welding, etc. [40, 41]), synthesized magnetite

was loaded in a polymethylmethacrylate (PMMA) by using a conventional melt-blending process.

Compounds with contents equal to 1 and 3% by weight of new magnetite were compared with analogous systems filled with commercial magnetite nanopowder in terms of thermal parameters such as glass transition and thermal stability of the matrix. At this regards, results were discussed taking the neat matrix, processed under the same conditions, as the reference material.

2. Experimental

2.1. Materials. The polymeric matrix used in this study was the polymethylmethacrylate (PMMA) Optix CA-51 (MFI 15 g/10 min) supplied by Plaskolite-Continental Acrylics.

Commercial magnetite nanopowder (named Fe_3O_4 (C) in the text and figures) was provided by Sigma Aldrich with an average particle size less than $50\ \mu\text{m}$ and a BET surface area higher than $60\ \text{m}^2/\text{g}$.

Hydrazine hydrate and NaOH (pellets) were purchased from Sigma Aldrich, while $\text{FeCl}_2 \cdot 4\text{H}_2\text{O}$ was provided by Merck. All of these precursors for the microwave-assisted hydrothermal synthesis of magnetite nanoparticles were of analytical grade and used without any purification.

2.2. Synthesis of Magnetite Nanoparticles (Fe_3O_4 (S)). The general procedure for the microwave assisted hydrothermal synthesis of Fe_3O_4 nanoparticles is as follows: 0.5150 g (2.6 mmol) of $\text{FeCl}_2 \cdot 4\text{H}_2\text{O}$ were dissolved in 13 mL of deionized water under nitrogen atmosphere, in a Teflon-lined digestion vessel. A previously prepared NaOH/hydrazine solution (0.2609 g (6.5 mmol) of NaOH in 2.174 mL (70 mmol) of $\text{N}_2\text{H}_4 \cdot \text{H}_2\text{O}$) was dropwise added to the iron (II) solution under nitrogen and vigorous magnetic stirring.

The sealed reaction vessel was hydrothermally treated using a microwave digestion system ETHOS TC (Milestone) operating at 2.45 GHz frequency, at 100°C for 120 min. with a continuous and accurate computer controlling of reaction time, temperature, pressure, and microwave power. After the reaction the product was naturally cooled to room temperature, and the obtained dark-brown powder was centrifuged (4000 rpm), washed several times with deionized water, and finally dried overnight at 80°C , under vacuum. Surface area was determined to be $81\ \text{m}^2/\text{g}$.

2.3. Preparation of PMMA/ Fe_3O_4 Nanocomposites. The inclusion of nanosized particles of magnetite in the molten PMMA was carried out in a HAAKE Minilab Rheomex microcompounder mod. CTW5 conical double-screw extruder. In this apparatus, an integrated bypass valve enables the recirculation of the melt via a back flow channel. In our case, pellets of PMMA and proper amounts of magnetite were fed to the microcompounder in a maximum time of 2 minutes, allowing a recirculation of the molten compound for 5 minutes before collecting the extruded composite systems.

A flat temperature profile of 220°C and a screw speed of 80 rpm were employed operating in corotating mode.

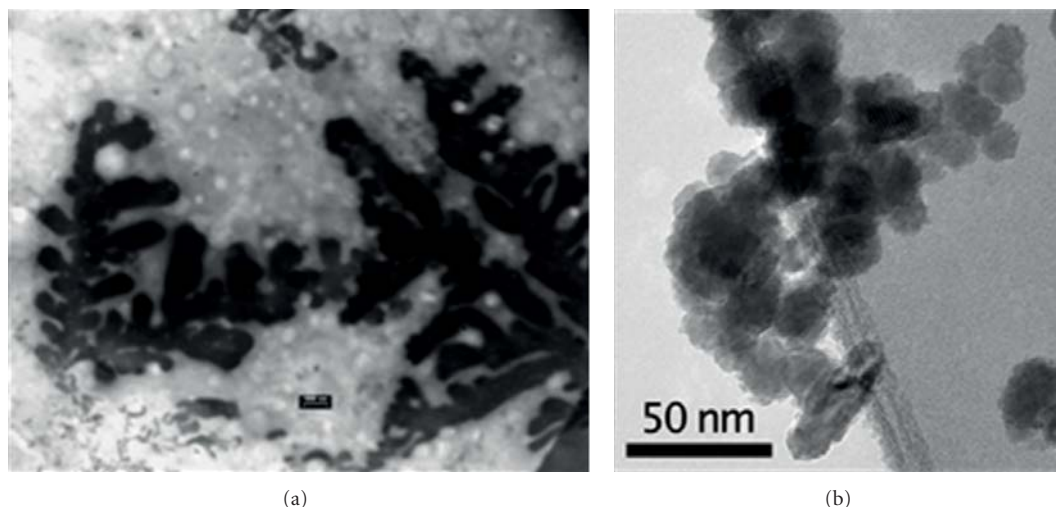


FIGURE 1: TEM micrograph showing the characteristic dendritic structure generated by the magnetite nanoparticles (left-marker: 1000 nm), and detail of the microscopic structure (right).

2.4. Characterization Techniques. Nanostructured magnetite morphology was imaged by transmission electron microscopy (TEM, Philips EM2085, 100 kV) and scanning electron microscopy (SEM, Cambridge-S360). In particular, in the preparation of specimens for the TEM investigation, the magnetite powder was dispersed in ethanol by applying ultrasounds (ultrasonic bath, Bandeline RK515CH), and a polymeric surfactant (poly (vinyl pyrrolidone), $M_w = 10,000 \text{ gmol}^{-1}$) was added in order to achieve a stable colloid. Then, a drop of this colloidal suspension was placed on a TEM copper grid coated by Formvar resin thin film and allowed to dry in air at room temperature. After drying, the copper grid was graphitized by sputtering. The crystallographic structure of magnetite was investigated by large angle X-ray powder diffraction (XRD, X'Pert PRO, PANalytical, CuK_α radiation). The structure of the magnetite powder was also investigated by Micro-Raman spectroscopy (LabRam, Horiba Jobin-Yvon, Longjumeau, France) employing a 632.81 nm wavelength laser which was used on both magnetite powders. In addition, we employed a D1 type filter in order to use 2 mW output laser power, focused onto the sample using a 10x objective lens, in order to avoid any phase transformation of the analyzed powders, as a consequence of laser-induced thermal effects. It is well known that under heat treatment magnetite easily transforms into the oxidized crystal of maghemite at around 200°C to finally complete oxidation to hematite ($\alpha\text{-Fe}_2\text{O}_3$) at around 400°C [42].

About PMMA-based nanocomposites, melt-blended products were analysed by differential scanning calorimetry using a DSC (DSC1, Mettler Toledo Instrument). Samples were run by a heating rate of 20°C/min on the temperature range from 25 to 200°C with the aim to verify any influence of magnetite nanoparticles on the glass transition temperature of nanocomposites.

Further thermogravimetric tests were carried out by using a Q5000-TA Instrument. Approximately 15 mg of each

material were submitted to a temperature ramp from 25 to 600°C at a heating rate of 10°C/min under nitrogen. The influence on magnetite nanoparticles on thermal stability and decomposition behavior of polymer matrix were investigated taking the unfilled PMMA as the reference material.

3. Result and Discussion

The as-synthesized magnetite (Fe_3O_4) was made of a very fine dark-brown powder, which exhibited a good magnetic behavior (Figure 1). As reported in a previous work [43], magnetism of the probe was measured by means of MPMSR-5S-SQUID magnetometer of Quantum-Design. In the ZFC/FC curves the Verwey transition at 120 K was observed. This transition justified the nanoparticle core constituted by stoichiometric magnetite [44]. Magnetization-temperature curves show a saturation magnetization of about 64 emu/g which therefore much lower than the bulk value of magnetite 92 emu/g, observing additional remanence and coercivity. The decrease of the saturation magnetization is, probably, due to the maghemite shell surrounding the nanoparticles.

According to the morphological investigation using transmission electron microscope (TEM), the as-prepared powder consisted of monodispersed nanoparticles with a size of ca. 15–20 nm. As visible in the TEM micrograph given in Figure 1 (left side, magnification 25000x), these particles produced very large branched or dendritic structures. Details observed at high magnification (180000x) confirmed that the sample is constituted by pseudospherical nanoparticles with a monomodal particle size distribution.

Fe_3O_4 (s) sample was characterized also by scanning electron microscopy (SEM), and according to Figure 2 the nanoparticles appear as aggregates in densely packed secondary particles. Moreover, at higher enlargements (Figure 2(a)-right) these secondary particles appear as powder grains made of closely packed spherical nanoparticles partially sintered together.

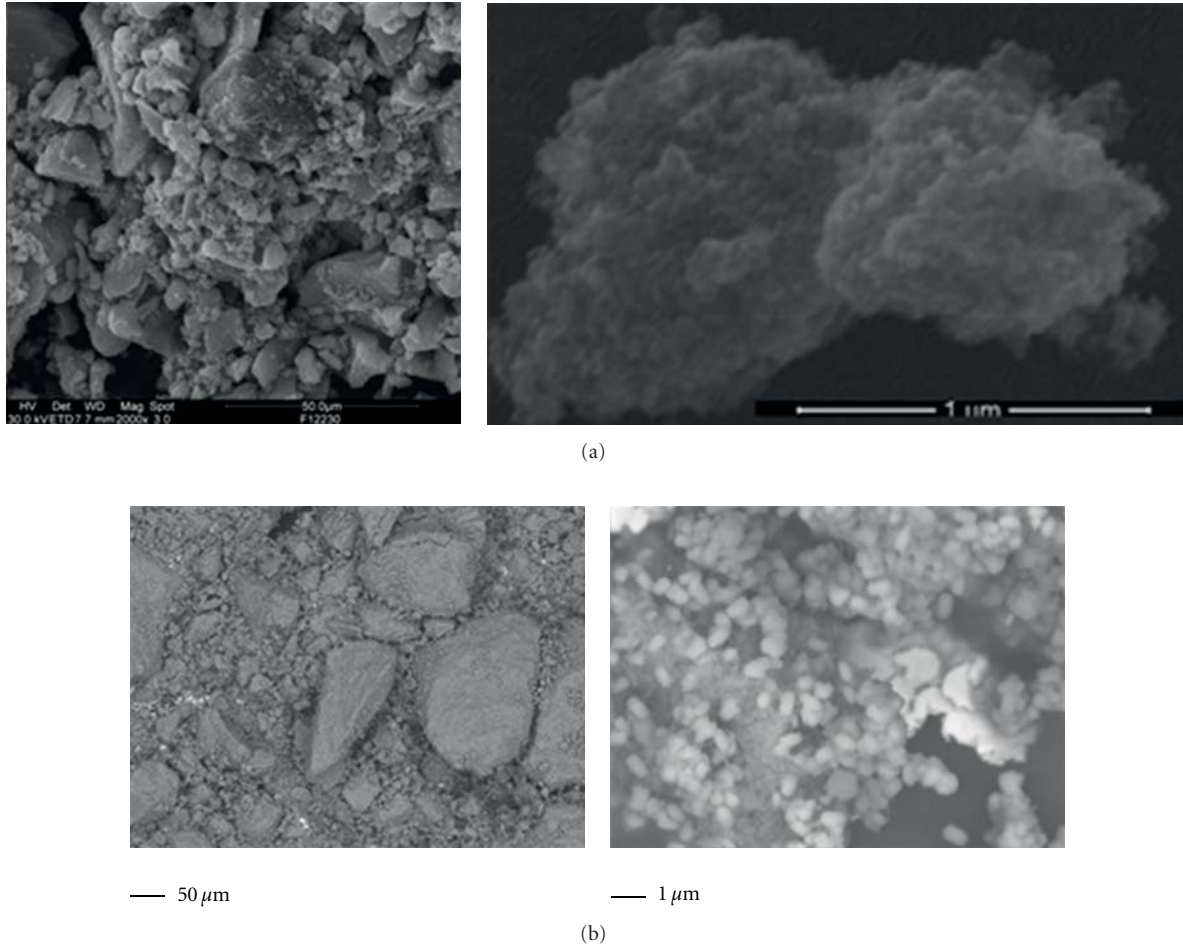


FIGURE 2: SEM micrograph of the as-synthesized powder ((a)-left), and detail of the single grain ((a)-right) and of the commercial powder at low ((b)-left) and high ((a)-right) enlargements.

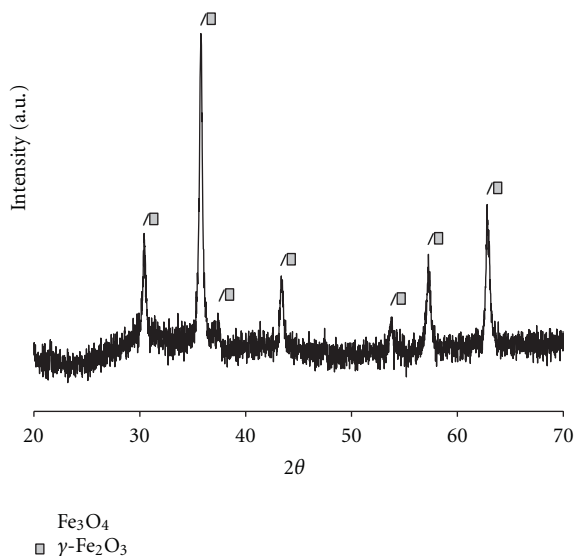


FIGURE 3: XRD pattern of the as-prepared magnetite nanoparticles.

Microstructure of commercial iron oxide powders has been also characterized by means of scanning electron microscopy. Backscattered electron (BSE) image is reported in Figure 2(b). The average grain size is in the 0.8–2.5 μm size. Differently from Fe_3O_4 hydrothermal powder the commercial one does not present an enhanced nanostructure.

As visible in Figure 3, X-ray diffractogram (XRD) of the as synthesized samples showed a diffraction pattern characteristic of magnetite (Fe_3O_4). In particular, the peaks at 2θ equal to 30.1° , 35.4° , 43.1° , 53.4° , 57.1° , and 62.6° can be indexed as (220), (311), (400), (511), and (440) lattice planes of cubic magnetite, respectively (JCPDS 19-629). The average Fe_3O_4 crystallite size was calculated by applying the Debye-Scherrer equation ($D_{\text{hkl}} = 0.9\lambda/\beta\cos\theta$, in which β stands for the half-width of the XRD diffraction line, θ is the peak position in angles, and λ is the $\text{CuK}\alpha$ radiation wavelength, that is 1.54056 \AA) to the reflection peak (311) and it resulted approximately of 10 nm. Such crystallite size approximately corresponds to the TEM (Figure 1, right) average size of particles, which indicates a monocrystalline nature of the particles.

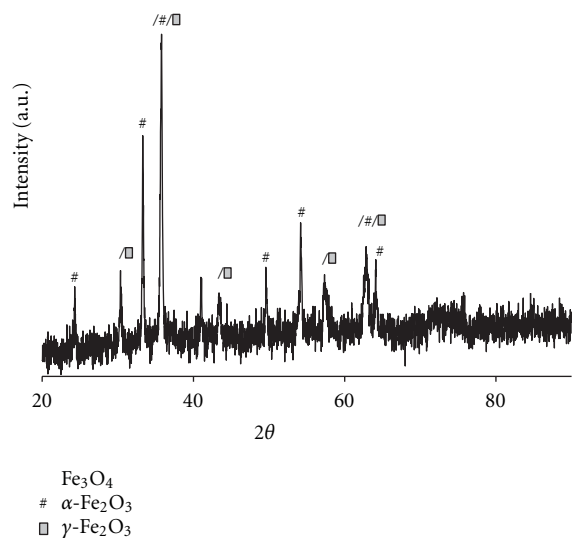


FIGURE 4: XRD pattern of the commercial magnetite nanostructured particles.

The presence of hematite, beside to the major magnetite phase, has been confirmed by X-ray diffraction analysis on the commercial iron oxide nanopowders (Figure 4).

To evaluate the purity of crystalline phases in the two magnetite powders, a specific characterization procedure was set up.

The XRD patterns of magnetite (Fe_3O_4) and maghemite ($\gamma\text{-Fe}_2\text{O}_3$) differ only for the presence of a few diffraction peaks with intensity lower than 5%. Thus, the absence of these low-intensity peaks, from the X-ray diffractogram of Figure 4, can not be considered a proof of the obtention of pure magnetite phase during the microwave assisted hydrothermal synthesis [40]. An alternative technique has been envisaged in Raman spectroscopy that is considered to be a powerful tool to distinguish the different structural phases of iron oxides [43].

Raman spectra of both commercial and synthetic iron oxide nanopowders are reported in Figure 5 (please notice that the y -axis is not the same for both spectra).

The presence of nanostructured crystalline powders in the sample of hydrothermally prepared magnetite is clearly visible from the broadness of the peaks in Figure 5(a). Magnetite phase is easily discernible by its main band centred at around 667 cm^{-1} . Thus, magnetite can be assumed to be present in both commercial and synthetic iron oxide nanopowders. In the Raman spectrum of as-prepared magnetite nanoparticles, typical maghemite band (720 cm^{-1} [44, 45]) is clearly evident, thus confirming the obtention of magnetite nanocrystals with the surface partially oxidised to maghemite. Accordingly to [46] maghemite phase should show an additional band at 511 cm^{-1} , which could be either the one centred at 460 cm^{-1} or could be identified as the minor peak at its right.

On the other hand, commercial iron oxide nanoparticles consist of a complex mixture of magnetite, maghemite, and hematite phases. The latter can be easily individualised by the

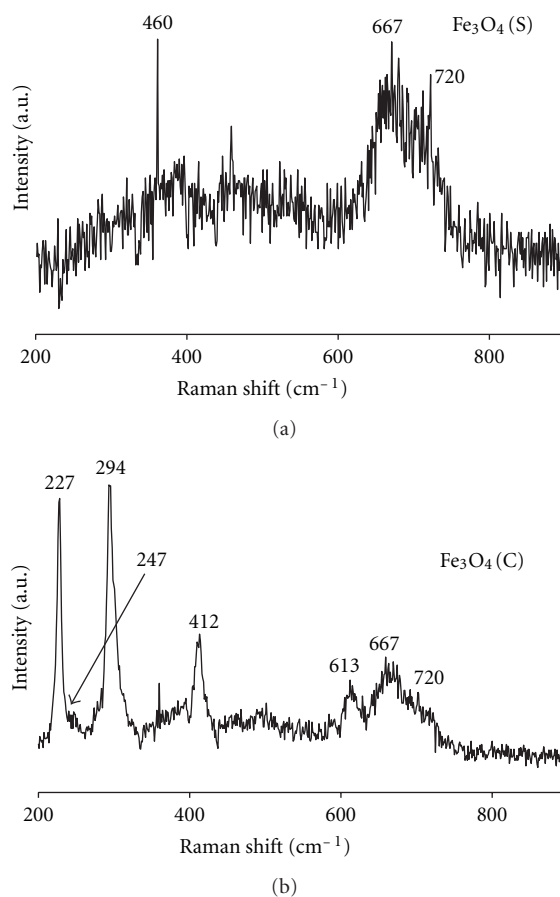


FIGURE 5: Raman spectra of as-prepared magnetite nanoparticles (a) and the commercial magnetite nanostructured particles (b).

bands situated at 227 , 247 , 294 , 412 , and 613 cm^{-1} , according to literature [44, 45]. The presence of hematite phase has been also confirmed by X-ray diffraction analysis on the commercial iron oxide nanopowders (Figure 4).

Regarding thermal properties of melt-blended nanocomposite systems based on polymethylmethacrylate, PMMA, in Figure 6, the comparison of thermograms collected by calorimetric tests is depicted. In particular, a clear shift of the inflection point usually associated with the glass-rubber transition is observed for all hybrid formulations.

The analysis showed an increase of the glass transition temperature T_g , evaluated as the temperature at the inflection point of the thermograms. This parameter appeared to increase with the filler content especially in presence of synthesized magnetite nanoparticles (denoted as S sample), with respect to commercial powders (denoted as C samples).

This behavior is usually ascribed to restrictions of the polymer chains mobility by the inclusion of rigid nanoparticles. Moreover, islands of nanoparticles may adsorb portion of adjacent chains, especially if longer than the average size of macromolecules constituting the matrix and, thus, having the highest relaxation times, enhancing this effect.

Appreciating the evaluations shown in Figure 5 in the light of the range of experimental error evaluated on at

TABLE 1: Thermal parameters of PMMA-based materials (H_{\max} : DTG peak height; FWMH: full width at medium height of DTG peak).

Material	$T_{-5\%}$ ($^{\circ}\text{C}$)	T_{peak} DTG ($^{\circ}\text{C}$)	H_{\max}	FWMH ($^{\circ}\text{C}$)
Neat extruded PMMA	355.2 ± 0.5	379.1 ± 0.7	45	42
PMMA/1 wt% Fe_3O_4 (C)	357.8 ± 1.2	397.4 ± 0.9	38	46
PMMA/3 wt% Fe_3O_4 (C)	358.8 ± 0.7	393.8 ± 0.6	41	45
PMMA/1 wt% Fe_3O_4 (S)	358.1 ± 0.8	395.1 ± 0.3	38	47
PMMA/3 wt% Fe_3O_4 (S)	359.4 ± 0.7	395.5 ± 0.4	38	48

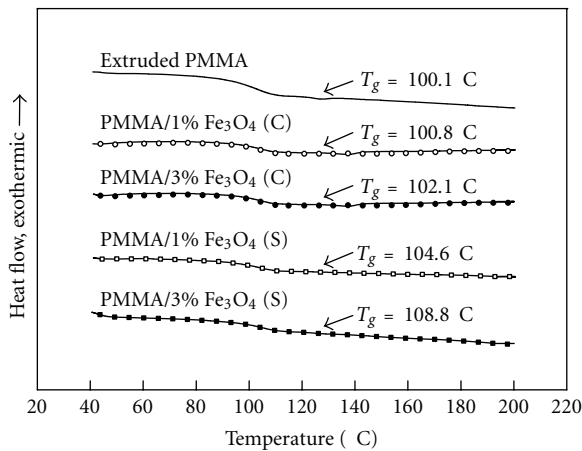


FIGURE 6: Comparison of DSC curves of the nanocomposites based on PMMA taking the neat matrix as reference material.

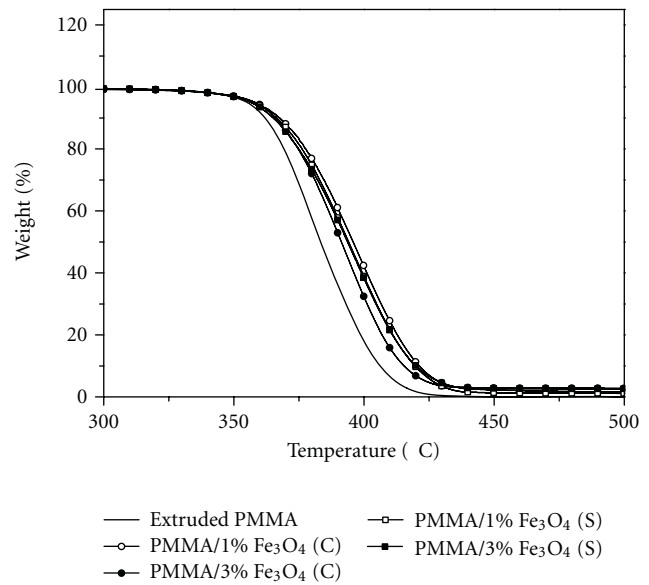
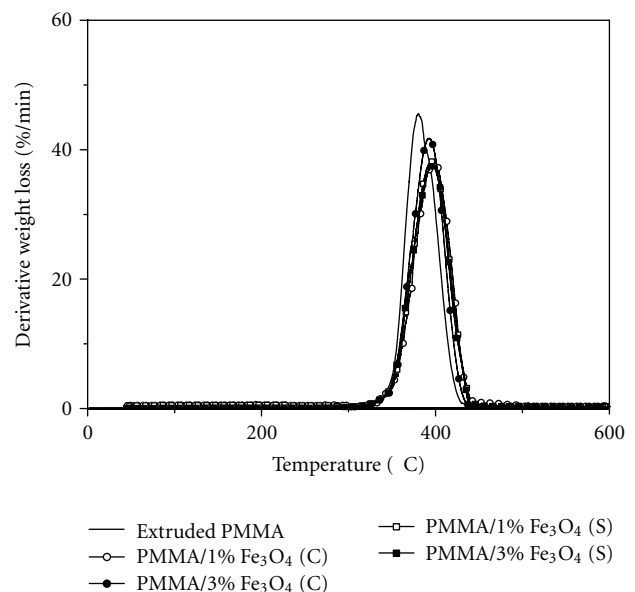
least 5 tests for each material and approximately equal to 2%, it can be stated that the commercial magnetite does not significantly alter the glass transition temperature of the matrix, at least on the interval compositions examined so far. On the contrary, the T_g is changed from 100.1°C for the neat matrix to 104.6 and 108.8°C for nanocomposites containing 1 and 3 wt%, respectively, of microwave hydrothermally synthesized magnetite. On the basis of the above considerations, these benefits can be explained by assuming the establishment of specific chemical-physical interactions at the filler-matrix interface such as to improve the thermal performance of the amorphous matrix.

Finally, Figures 7 and 8 report thermogravimetric (TG) mass loss curves and their first derivative, respectively, for all PMMA nanocomposites.

In more details, looking to the data, averaged on at least 3 tests for each material and summarized in Table 1, the following considerations may be drawn.

Assuming the temperature at which a 5% of weight loss is achieved ($T_{-5\%}$) as the thermal stability of the material, a slight increase of this parameter can be observed for all nanocomposite systems with respect to the neat matrix. This effect can be ascribed to the restrictions of the polymer chains mobility already invoked to explain the increase of the glass transition temperature as well as to the absorption of polymer on the oxide surface by methoxycarbonyl groups ($-\text{C}(\text{O})\text{OCH}_3$) [47].

Moreover, in all cases, the residue at 600°C is comparable with the amount of magnetite nanoparticles, initially included in the PMMA.

FIGURE 7: TG mass loss curves of all investigated materials under N_2 . (Heating rate $10^{\circ}/\text{min}$).FIGURE 8: Derivative TG curves of all investigated materials under N_2 . (Heating rate $10^{\circ}/\text{min}$).

The comparison of derivative signals in Figure 8, instead, has allowed to assess any effect related to the presence of magnetite nanoparticles on the thermal behaviour of investigated materials. Starting from the evidence showing the existence of a single decomposition signal for both unfilled matrix and nanocomposite systems, additions of magnetite always induced a shift of the maximum decomposition signal (T_{peak} DTG) to higher temperature with respect to the reference neat matrix (see Table 1). In addition, the hybrid formulations showed a reduction in the height of the decomposition signal.

This behavior appeared to be influenced by the type of magnetite used. In particular, for samples containing 1% by weight of nanoparticles a reduction in the height of the signal equal to about 15% compared to the reference material was shown regardless of the type of included magnetite: as shown in Table 1, the height of the decomposition signal goes from 45 to 38°C. But further increase of the content of filler implied an inversion of the trend for systems containing commercial magnetite (Fe_3O_4 (C)), with a reduction in the lowering of the signal compared to the reference value equal to approximately 9% (from the reference value 45 to 41°C). Instead, no further effects were observed in presence of synthesized filler (Fe_3O_4 (S)).

Finally, a slight widening of the decomposition signal was observed for all hybrid formulations with respect to unfilled PMMA and evaluated in terms of full width at medium height (FWMH) (see Table 1).

These phenomena, probably related to the influence of filler on involved combustion processes, are still under investigation.

4. Conclusions

The microwave hydrothermally prepared nanoparticles of magnetite are compared to the commercial ones in terms of effects on the thermal properties of PMMA nanocomposites. The smaller particles size of the synthesized nanoparticles with respect to the commercial ones and the absence of agglomeration allows a better dispersion in the polymeric matrix via extrusion process.

The effects of nanoparticles dispersion in the PMMA have been measured in terms of glass transition temperature and thermal stability of melt-blended systems compared with the unfilled matrix.

The experimental results showed an increase of both of these parameters especially in the case of new nanoparticles. This effect, attributed to specific filler-matrix interactions, probably more efficient for the greater uniformity of size distribution of synthesized magnetites with respect to the commercial ones, highlights their interesting potentialities of use.

Finally, being aware that a magnetic characterization of the nanocomposite systems is as important as the morphological and thermal ones, authors are also expecting better magnetic properties in the Fe_3O_4 -synthetic-PMMA samples.

Acknowledgments

Authors are particularly grateful to Prof. Pietro Baraldi, Department of Chemistry, University of Modena and Reggio

Emilia, for useful discussion on Raman spectra and to Kilian Pollok, Bayerisches Geoinstitut, Universität Bayreuth, Germany, for providing one of the TEM images.

References

- [1] Z. Jing and S. Wu, "Synthesis and characterization of monodisperse hematite nanoparticles modified by surfactants via hydrothermal approach," *Materials Letters*, vol. 58, no. 27-28, pp. 3637-3640, 2004.
- [2] Z. Zhong, J. Lin, S. P. Teh, J. Teo, and F. M. Dautzenberg, "A rapid and efficient method to deposit gold particles on catalyst supports and its application for CO oxidation at low temperatures," *Advanced Functional Materials*, vol. 17, no. 8, pp. 1402-1408, 2007.
- [3] A. P. Kozlova, S. Sugiyama, A. I. Kozlov, K. Asakura, and Y. Iwasawa, "Iron-oxide supported gold catalysts derived from gold-phosphine complex $\text{Au}(\text{PPh}_3)(\text{NO}_3)$: state and structure of the support," *Journal of Catalysis*, vol. 176, no. 2, pp. 426-438, 1998.
- [4] D. Hradil, T. Grygar, J. Hradilová, and P. Bezdička, "Clay and iron oxide pigments in the history of painting," *Applied Clay Science*, vol. 22, no. 5, pp. 223-236, 2003.
- [5] X. Q. Liu, S. W. Tao, and Y. S. Shen, "Preparation and characterization of nanocrystalline $\alpha\text{-Fe}_2\text{O}_3$ by a sol-gel process," *Sensors and Actuators B*, vol. 40, no. 2-3, pp. 161-165, 1997.
- [6] M. J. Espin, A. V. Delgado, and J. D. G. Durán, "Optical properties of dilute hematite/silicone oil suspensions under low electric fields," *Journal of Colloid and Interface Science*, vol. 287, no. 1, pp. 351-359, 2005.
- [7] S. Laurent, D. Forge, M. Port et al., "Magnetic iron oxide nanoparticles: synthesis, stabilization, vectorization, physicochemical characterizations and biological applications," *Chemical Reviews*, vol. 108, no. 6, pp. 2064-2110, 2008.
- [8] A. H. Lu, E. L. Salabas, and F. Schüth, "Magnetic nanoparticles: synthesis, protection, functionalization, and application," *Angewandte Chemie*, vol. 46, no. 8, pp. 1222-1244, 2007.
- [9] J. Zhang, S. Rana, R. S. Srivastava, and R. D. K. Misra, "On the chemical synthesis and drug delivery response of folate receptor-activated, polyethylene glycol-functionalized magnetite nanoparticles," *Acta Biomaterialia*, vol. 4, no. 1, pp. 40-48, 2008.
- [10] C. Flesch, C. Delaite, P. Dumas, E. Bourgeat-Lami, and E. Duguet, "Grafting of poly(ϵ -caprolactone) onto maghemite nanoparticles," *Journal of Polymer Science A*, vol. 42, no. 23, pp. 6011-6020, 2004.
- [11] J. Sun, S. Zhou, P. Hou et al., "Synthesis and characterization of biocompatible Fe_3O_4 nanoparticles," *Journal of Biomedical Materials Research A*, vol. 80, no. 2, pp. 333-341, 2007.
- [12] C.-M. Lee, H.-J. Jeong, E.-M. Kim et al., "Synthesis and characterization of iron oxide nanoparticles decorated with carboxymethyl curdlan," *Macromolecular Research*, vol. 17, no. 2, pp. 133-136, 2009.
- [13] S. Wada, K. Tazawa, I. Furuta, and H. Nagae, "Antitumor effect of new local hyperthermia using dextran magnetite complex in hamster tongue carcinoma," *Oral Diseases*, vol. 9, no. 4, pp. 218-223, 2003.
- [14] V. Sreeja and P. A. Joy, "Microwave-hydrothermal synthesis of $\gamma\text{-Fe}_2\text{O}_3$ nanoparticles and their magnetic properties," *Materials Research Bulletin*, vol. 42, no. 8, pp. 1570-1576, 2007.
- [15] T. J. Daou, G. Pourroy, S. Bégin-Colin et al., "Hydrothermal synthesis of monodisperse magnetite nanoparticles," *Chemistry of Materials*, vol. 18, no. 18, pp. 4399-4404, 2006.

- [16] K. Simeonidis, S. Mourdikoudis, M. Moulla et al., "Controlled synthesis and phase characterization of Fe-based nanoparticles obtained by thermal decomposition," *Journal of Magnetism and Magnetic Materials*, vol. 316, no. 2, pp. e1–e4, 2007.
- [17] I. Nedkov, T. Merodiiska, L. Slavov, R. E. Vandenberghe, Y. Kusano, and J. Takada, "Surface oxidation, size and shape of nano-sized magnetite obtained by co-precipitation," *Journal of Magnetism and Magnetic Materials*, vol. 300, no. 2, pp. 358–367, 2006.
- [18] J. Hu, G. Chen, and I. M. C. Lo, "Removal and recovery of Cr(VI) from wastewater by maghemite nanoparticles," *Water Research*, vol. 39, no. 18, pp. 4528–4536, 2005.
- [19] P. D. Cozzoli, E. Snoeck, M. A. Garcia et al., "Colloidal synthesis and characterization of tetrapod-shaped magnetic nanocrystals," *Nano Letters*, vol. 6, no. 9, pp. 1966–1972, 2006.
- [20] P. Berger, N. B. Adelman, K. J. Beckman, D. J. Campbell, A. B. Ellis, and G. C. Lisensky, "Preparation and properties of an aqueous ferrofluid," *Journal of Chemical Education*, vol. 76, no. 7, pp. 943–948, 1999.
- [21] S. C. Gu, T. Shiratori, and M. Konno, "Synthesis of monodisperse, magnetic latex particles with polystyrene core," *Colloid and Polymer Science*, vol. 281, no. 11, pp. 1076–1081, 2003.
- [22] T. Belin, N. Guigue-Millot, T. Caillot, D. Aymes, and J. C. Niepce, "Influence of grain size, oxygen stoichiometry, and synthesis conditions on the γ -Fe₂O₃ vacancies ordering and lattice parameters," *Journal of Solid State Chemistry*, vol. 163, no. 2, pp. 459–465, 2002.
- [23] S. Sun and H. Zeng, "Size-controlled synthesis of magnetite nanoparticles," *Journal of the American Chemical Society*, vol. 124, no. 28, pp. 8204–8205, 2002.
- [24] I. Nyiro-Kosa, D. C. Nagy, and M. Pósfai, "Size and shape control of precipitated magnetite nanoparticles," *European Journal of Mineralogy*, vol. 21, no. 2, pp. 293–302, 2009.
- [25] N. Mizutani, T. Iwasaki, S. Watano, T. Yanagida, and T. Kawai, "Size control of magnetite nanoparticles in hydrothermal synthesis by coexistence of lactate and sulfate ions," *Current Applied Physics*, vol. 10, no. 3, pp. 801–806, 2010.
- [26] D. Shi, J. P. Cheng, F. Liu, and X. B. Zhang, "Controlling the size and size distribution of magnetite nanoparticles on carbon nanotubes," *Journal of Alloys and Compounds*, vol. 502, no. 2, pp. 365–370, 2010.
- [27] X. T. Wen, J. X. Yang, B. He, and Z. Gu, "Preparation of monodisperse magnetite nanoparticles under mild conditions," *Current Applied Physics*, vol. 8, no. 5, pp. 535–541, 2008.
- [28] X. Wang, C. Zhang, X. Wang, and H. Gu, "The study on magnetite particles coated with bilayer surfactants," *Applied Surface Science*, vol. 253, no. 18, pp. 7516–7521, 2007.
- [29] P. Guardia, B. Battle-Brugal, A. G. Roca et al., "Surfactant effects in magnetite nanoparticles of controlled size," *Journal of Magnetism and Magnetic Materials*, vol. 316, no. 2, pp. e756–e759, 2007.
- [30] L. Jiang, W. Sun, and J. Kim, "Preparation and characterization of ω -functionalized polystyrene-magnetite nanocomposites," *Materials Chemistry and Physics*, vol. 101, no. 2-3, pp. 291–296, 2007.
- [31] A. K. Bajpai and R. Gupta, "Synthesis and characterization of magnetite (Fe₃O₄) polyvinyl alcohol-based Nanocomposites and study of superparamagnetism," *Polymer Composites*, vol. 31, no. 2, pp. 245–255, 2010.
- [32] S.-J. Yen, E.-C. Chen, R.-K. Chiang, and T.-M. Wu, "Preparation and characterization of polypyrrole/magnetite nanocomposites synthesized by in situ chemical oxidative polymerization," *Journal of Polymer Science B*, vol. 46, no. 13, pp. 1291–1300, 2008.
- [33] J. H. Kim, F. F. Fang, H. J. Choi, and Y. Seo, "Magnetic composites of conducting polyaniline/nano-sized magnetite and their magnetorheology," *Materials Letters*, vol. 62, no. 17-18, pp. 2897–2899, 2008.
- [34] H. Gu, Y. Huang, X. Zhang et al., "Magnetoresistive polyaniline-magnetite nanocomposites with negative dielectric properties," *Polymer*, vol. 53, no. 3, pp. 801–809, 2012.
- [35] L. A. Ramajo, A. A. Cristóbal, P. M. Botta, J. M. Porto López, M. M. Reboredo, and M. S. Castro, "Dielectric and magnetic response of Fe₃O₄/epoxy composites," *Composites A*, vol. 40, no. 4, pp. 388–393, 2009.
- [36] W. W. Wang, Y. J. Zhu, and M. L. Ruan, "Microwave-assisted synthesis and magnetic property of magnetite and hematite nanoparticles," *Journal of Nanoparticle Research*, vol. 9, no. 3, pp. 419–426, 2007.
- [37] J. G. Parsons, C. Luna, C. E. Botez, J. Elizalde, and J. L. Gardea-Torresdey, "Microwave-assisted synthesis of iron(III) oxyhydroxides/oxides characterized using transmission electron microscopy, X-ray diffraction, and X-ray absorption spectroscopy," *Journal of Physics and Chemistry of Solids*, vol. 70, no. 3-4, pp. 555–560, 2009.
- [38] X. Yang, W. Jiang, L. Liu et al., "One-step hydrothermal synthesis of highly water-soluble secondary structural Fe₃O₄ nanoparticles," *Journal of Magnetism and Magnetic Materials*, vol. 324, no. 14, pp. 2249–2257, 2012.
- [39] M. Niederberger and G. Garnweitner, "Organic reaction pathways in the nonaqueous synthesis of metal oxide nanoparticles," *Chemistry*, vol. 12, no. 28, pp. 7282–7302, 2006.
- [40] A. V. Mitin, V. A. Tarasov, V. N. Doronin, and R. A. Nazipov, "Magnetic nanostructured polymer composites," *Physics of the Solid State*, vol. 53, no. 12, pp. 2336–2339, 2011.
- [41] L. E. Nita, A. P. Chiriac, I. Neamtu, and C. Vasile, "Magnetic composites obtainment based on styrene polymers," *Journal of Applied Polymer Science*, vol. 100, no. 5, pp. 4133–4141, 2006.
- [42] N. Pinna, S. Grancharov, P. Beato, P. Bonville, M. Antonietti, and M. Niederberger, "Magnetite nanocrystals: nonaqueous synthesis, characterization, and solubility," *Chemistry of Materials*, vol. 17, no. 11, pp. 3044–3049, 2005.
- [43] B. Nigrovski, A. Rizzuti, C. Leonelli, B. Ondruschka, and P. Scholz, "Preparation of magnetite nanoparticles via microwave-assisted hydrothermal process," in *Proceedings of the WG 003/04 COST D32 Action, Chemistry under High-Energy Microenvironments, Final Meeting, Krakow, Poland, September 2009*.
- [44] R. Aragón, J. P. Shepherd, J. W. Koenitzer, D. J. Buttrey, R. J. Rasmussen, and J. M. Honig, "Influence of nonstoichiometry on the Verwey transition in Fe₃(1- δ)O₄," *Journal of Applied Physics*, vol. 57, no. 8, pp. 3221–3222, 1985.
- [45] O. N. Shebanova and P. Lazor, "Raman study of magnetite (Fe₃O₄): laser-induced thermal effects and oxidation," *Journal of Raman Spectroscopy*, vol. 34, no. 11, pp. 845–852, 2003.
- [46] A. M. Jubb and H. C. Allen, "Vibrational spectroscopic characterization of hematite, maghemite, and magnetite thin films produced by vapor deposition," *ACS Applied Materials and Interfaces*, vol. 2, no. 10, pp. 2804–2812, 2010.
- [47] A. Laachachi, M. Cochez, M. Ferriol, J. M. Lopez-Cuesta, and E. Leroy, "Influence of TiO₂ and Fe₂O₃ fillers on the thermal properties of poly(methyl methacrylate) (PMMA)," *Materials Letters*, vol. 59, no. 1, pp. 36–39, 2005.

Research Article

Self-Organization of K^+ -Crown Ether Derivatives into Double-Columnar Arrays Controlled by Supramolecular Isomers of Hydrogen-Bonded Anionic Biimidazolate Ni Complexes

Makoto Tadokoro,¹ Kyosuke Isoda,¹ Yasuko Tanaka,¹ Yuko Kaneko,¹
Syoko Yamamoto,¹ Tomoaki Sugaya,¹ and Kazuhiro Nakasuji²

¹ Department of Chemistry, Faculty of Science, Tokyo University of Science, Kagurazaka 1-3, Shinjuku-ku, Tokyo 162-8601, Japan

² Fukui University of Technology, Gakuen 3-6-1, Fukui 910-8505, Japan

Correspondence should be addressed to Makoto Tadokoro, tadokoro@rs.kagu.tus.ac.jp

Received 27 March 2012; Accepted 18 May 2012

Academic Editor: Hongmei Luo

Copyright © 2012 Makoto Tadokoro et al. This is an open access article distributed under the Creative Commons Attribution License, which permits unrestricted use, distribution, and reproduction in any medium, provided the original work is properly cited.

Anionic tris (biimidazolate) nickelate (II) ($[Ni(Hbim)_3]^-$), which is a hydrogen-bonding (H-bonding) molecular building block, undergoes self-organization into honeycomb-sheet superstructures connected by complementary intermolecular H-bonds. The crystal obtained from the stacking of these sheets is assembled into channel frameworks, approximately 2 nm wide, that clathrate two cationic K^+ -crown ether derivatives organised into one-dimensional (1D) double-columnar arrays. In this study, we have shown that all five cationic guest-included crystals form nanochannel structures that clathrate the 1-D double-columnar arrays of one of the four types of K^+ -crown ether derivatives, one of which induces a polymorph. This is accomplished by adaptably fitting two types of anionic $[Ni(Hbim)_3]^-$ host arrays. One is a $\Delta\Lambda-\Delta\Lambda-\Delta\Lambda \cdots$ network with H-bonded linkages alternating between the two different optical isomers of the Δ and Λ types with flexible H-bonded $[Ni(Hbim)_3]^-$. The other is a $\Delta\Delta\Delta-\Lambda\Lambda\Lambda \cdots$ network of a racemate with 1-D H-bonded arrays of the same optical isomer for each type. Thus, $[Ni(Hbim)_3]^-$ can assemble large cations such as K^+ crown-ether derivatives into double-columnar arrays by highly recognizing flexible H-bonding arrangements with two host networks of $\Delta\Lambda-\Delta\Lambda-\Delta\Lambda \cdots$ and $\Delta\Delta\Delta-\Lambda\Lambda\Lambda \cdots$.

1. Introduction

Self-assembled supramolecular architectures are currently of considerable interest owing to their intriguing network topologies and their potential applications in microelectronics, nonlinear optics, porous materials, and other technologies [1–10]. A tenet of crystal engineering, which belongs to supramolecular chemistry as well, is to control multidimensional network topologies in crystals constructed from molecular building blocks that are connected by means of mutual interactions of H-bonds and metal-coordination bonds [11–26]. For example, three-dimensional (3-D) molecular networks such as complicated (10,3)-*a* and (10,3)-*b* nets in crystals can also be produced in the field of crystal engineering by a rational design of artificial molecular building blocks [27–43].

In a previous report, we showed that 2,2'-biimidazolate monoanions ($Hbim^-$) was convenient for fabricating, via one-pot self-organization, controlled crystal structures that are not only coordinated to a transition metal ion but also connected to each other through intermolecular H-bonds of the complementary dual N-H \cdots N type [44–50]. The self-organizing superstructures formed from the H-bonded networks of the transition metal complexes with $Hbim^-$ can be controlled in multidimensional networks by the molecular structures of the building blocks [51] or the existing counter ions [27, 52]. Thus, in the case of neutral building blocks, the superstructures form multidimensional networks such as 0-D H-bonded molecular dimers, 1-D linear and zigzag chains, 2-D honeycomb sheets, and 3-D helicates. These structures are constructed from the self-organisation of simple molecular building blocks, such as

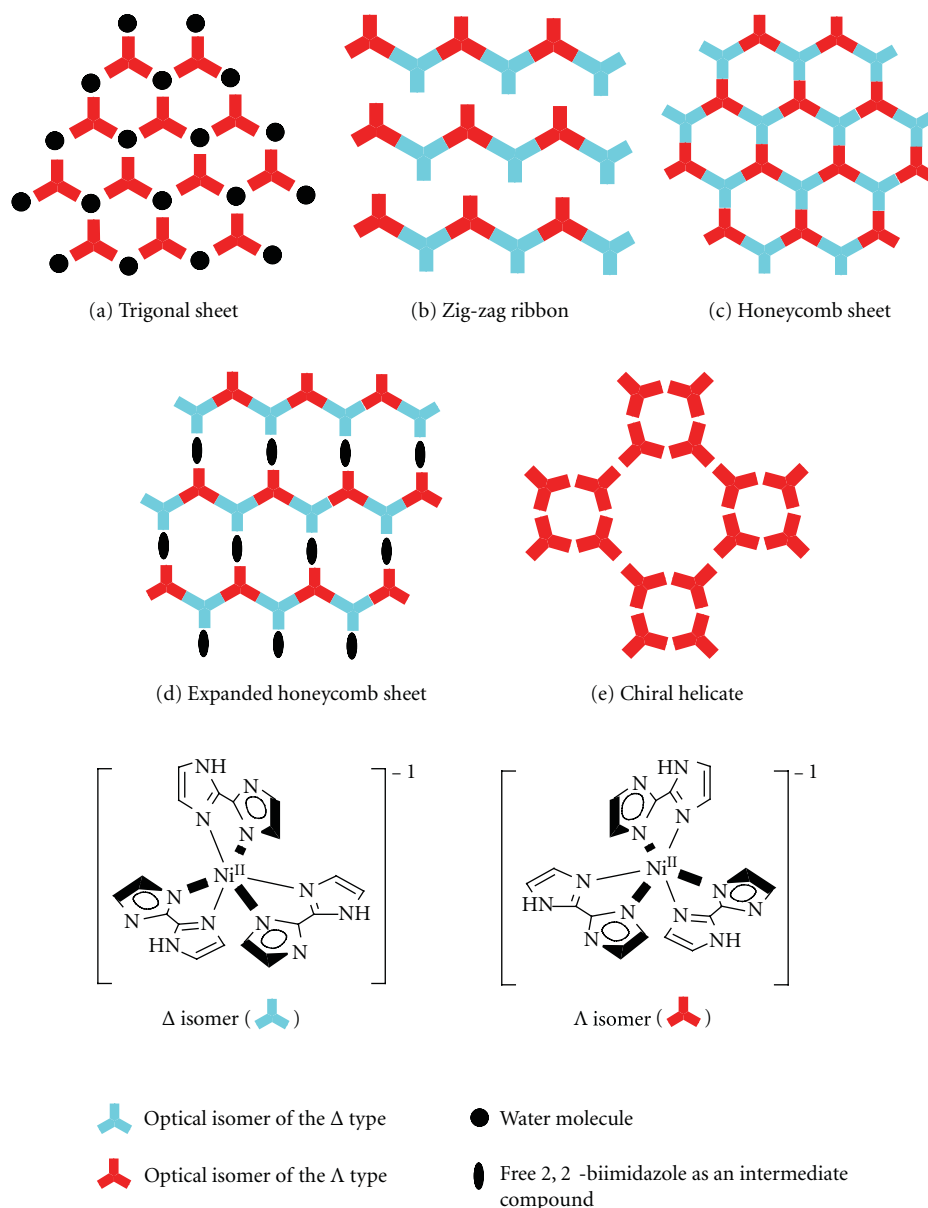


FIGURE 1: Schematic representations of five superstructure networks formed from hydrogen-bonding $[\text{Ni}(\text{Hbim})_3]^-$ depending on the kind of counter cations.

metal complexes with mono coordination of Hbim^- , dual coordination of *trans*- and *cis*-configurations, and ternary coordination of *racemic* and *optical-resolution* compounds of Δ - and Λ -configurations, respectively. On the other hand, building blocks with ternary coordination of Hbim^- such as a $[\text{Ni}(\text{Hbim})_3]^-$ produce multidimensional host anionic superstructures with H-bonded networks based on Δ - and Λ -optical isomers that depend on a variety of counter-cations. Some relatively large cations such as $[\text{K-DCH}(18\text{-crown-6})]^+$ (DCH(18-crown-6) dicyclohexyl 18-crown-6), $[\text{K}(\text{Cryptand})]^+$, and $[\text{PPh}_4]^+$ (tetraphenyl phosphonium) lead to a honeycomb sheet network (Figure 1(c)) formed from alternating linkages between Δ - and Λ -optical isomers of $[\text{Ni}(\text{Hbim})_3]^-$. The sheet stacking of these isomers in

crystal is arranged in parallel with the cavities to form 1-D channel formations approximately 2 nm in width and filled with a double-columnar array of the cations. Other small alkyl ammonium cations such as NMe_4^+ , N^nPr_4^+ , and NEt_4^+ , as well as a mixture of N^nPr_4^+ and Cs^+ , induce $[\text{Ni}(\text{Hbim})_3]^-$ to self-organise into other superstructures in crystal, such as a 0-D water molecule-mediated trigonal sheet (Figure 1(a)), a 1-D zigzag ribbon (Figure 1(b)) with an alternating arrangement of Δ - and Λ -isomers, an expanded honeycomb sheet inserted with the neutral H_2bim (Figure 1(d)), and a (10,3)-*a* net with double helicates (Figure 1(e)). However, we have also found $[\text{Ni}(\text{Hbim})_3]^-$ to form cation-stuffed channel structures stacked, for example, with honeycomb sheets (Figure 1(c)) by the use of the

relatively small cations of a planar [PEPY]⁺ (4-phenylethyl pyridinium) and a flexible [TMEA]⁺ (trimethyl ethynyl ammonium) [53]. Thus, the channel spaces can be filled with ionic pairs with a ClO₄⁻ anion and two cations such as [(PEPY)₂·ClO₄]⁺ and [(TMEA)₂·ClO₄]⁺, respectively. Since they are not completely filled with, only two cations to be smaller volume than the pore sizes of the hexagonal channel formed from six [Ni(Hbim)₃]⁻. Here, we have demonstrated that three new crystals 2–4, with a crystal structure similar to those of {[Ni(Hbim)₃][K-DCH(18-crown-6)]}_n (crystal 1) and {[Ni(Hbim)₃][K-(Cryptand)]}_n (crystal 5), are also self-organised into a guest-included channel formation constructed from the stacking of honeycomb sheets. The stackings for crystals 1–5 are controlled by the K⁺ crown-ether derivatives of potassium monocyclohexyl-18-crown-6 complex ([K-MCH(18crown6)]⁺), potassium monobenzo-18-crown-6 complex ([K-MBZ(18crown6)]⁺), potassium cryptand complex ([K-cryptand]⁺), and [K-DCH(18-crown-6)]⁺, respectively. Thus, anionic [Ni(Hbim)₃]⁻ not only aggregates into cation-stuffed channel formations with K⁺-crown ether complexes approximately 20 Å in diameter; their cationic arrays are also controlled in double-columnar structures by adaptably fitting flexible H-bonding networks formed from either of two different host sequences with the repeating units of ΔΛ–ΔΛ–ΔΛ... or ΔΔΔ–ΛΛΛ... (Figures 2(a) and 2(b)).

2. Results and Discussion

2.1. Syntheses. The self-organization of crystals 1–5 was performed under the same conditions as those of the one-pot procedures in MeOH with Ni²⁺ ions, H₂bim, potassium *n*-butoxide, and the relevant crown ether derivative to obtain five types of blue or violet crystal, respectively. In preparation with cryptand, two polymorphs of the violet and blue crystals 4 and 5 were grown from the same batch solution of MeOH. All crystal structures of crystals 1–5 were identified by X-ray crystallographic analysis. Each was confirmed to consist of a cation-stuffed channel framework that included one of the four types of K⁺-crown ether complexes. On the other hand, preparations based on [K-(18-crown-6)]⁺ with a nonsubstituted simple crown ether and [K-DBZ(18-crown-6)]⁺ (potassium dibenzo-18-crown-6 complex) with a large steric hindrance of phenyl groups have no known crystal structure at present. This suggests that each one of the two cationic complexes cannot be accommodated in the hexagonal cavity as a unit of the channel framework in a crystal.

2.2. Crystal Structures. Figure 3 shows the structures of each hexagonal cavity as repeating units of stuffed channel frameworks that clathrate two K⁺-crown ether complexes for each of the crystals 1–5. Each of the hexagonal cavities is constructed from alternating linkages through H-bonds between the Δ and Λ optical isomers of six [Ni(Hbim)₃]⁻ molecules and contains two K⁺-crown ether complexes within it owing to the charge balance. As shown in Figure 3(a), it is interesting that only the *cis-syn-cis* structural isomer of [K-DCH(18crown6)]⁺ is included in a hexagonal cavity, despite

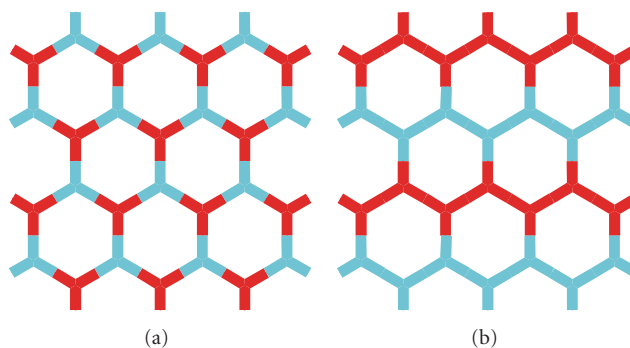


FIGURE 2: Schematic representations of two supramolecular isomers of (a) ΔΛ–ΔΛ–ΔΛ... and (b) ΔΔΔ–ΛΛΛ... sequences formed from [Ni(Hbim)₃]⁻.

the use of a commercial preparation with a mixture of structural isomers of the crown ethers including the *cis-anti-cis*, *cis-syn-trans*, *cis-anti-trans*, *trans-anti-trans*, and *trans-syn-trans* forms. The two K⁺-crown ether complexes are held to face each other in a saddle-shaped formation within the hexagonal cavity (distance between two K⁺ ions in the crown ethers: 7.698(3) Å). The hydrophilic ether oxygens are aligned toward the outer wall of the cavity, whereas the two hydrophobic cyclohexyl groups are oriented toward the centre. Furthermore, stacking along the *c*-axis with two K⁺-crown complexes leads to the formation of a small channel space, which includes the solvent molecules (methanol and water). As a result, the channel consists of both a small inner channel due to the stacking of two K⁺-crown complexes and a large outer channel due to the hexagonal cavities (Figure 4(a)). Figures 3(b) and 3(c) show that each of the hexagonal cavities includes double stacking arrays along the *c*-axis for [K-MCH(18crown6)]⁺ and [K-MBZ(18crown6)]⁺, respectively. The hydrophilic ether oxygens, with their two K⁺-crown ether complexes, are positioned toward the outer wall of the cavity, and hydrophobic cyclohexyl and phenyl groups are each positioned around the centre of the hexagonal cavity. Therefore, their two complexes are aligned as stacked double-columnar structures in the channels, respectively, (Figures 4(b) and 4(c)). The two polymorphous crystals 4 and 5 induced by [K-cryptand]⁺ also contain the stacked double-columnar structures, as shown in Figures 3(d) and 3(e). In the stacking channels of both 4 and 5, residual spaces (excluding the double columns) are occupied by a number of methanol molecules. One reason why [K-cryptand]⁺ forms two polymorphs may be that it has a spherical structure. The results of these structural analyses have demonstrated that the vicinity of the outer wall of the channel is hydrophilic (Figures 4(d) and 4(e)). The honeycomb sheets in crystal 5 form at the deviated slide stack (Each honeycomb sheet stacks diagonally for the *ac* plane.) along the *c*-axis, as shown in Figure 6. The most important characteristic of [Ni(Hbim)₃]⁻ networks is that four K⁺-crown ether complexes are clathrated into the stacking channels, and crystallised as single crystals 1–5 by adaptably fitting flexible H-bonding distortions with the networks and sequential change between the ΔΛ–ΔΛ–ΔΛ and ΔΔΔ–ΛΛΛ

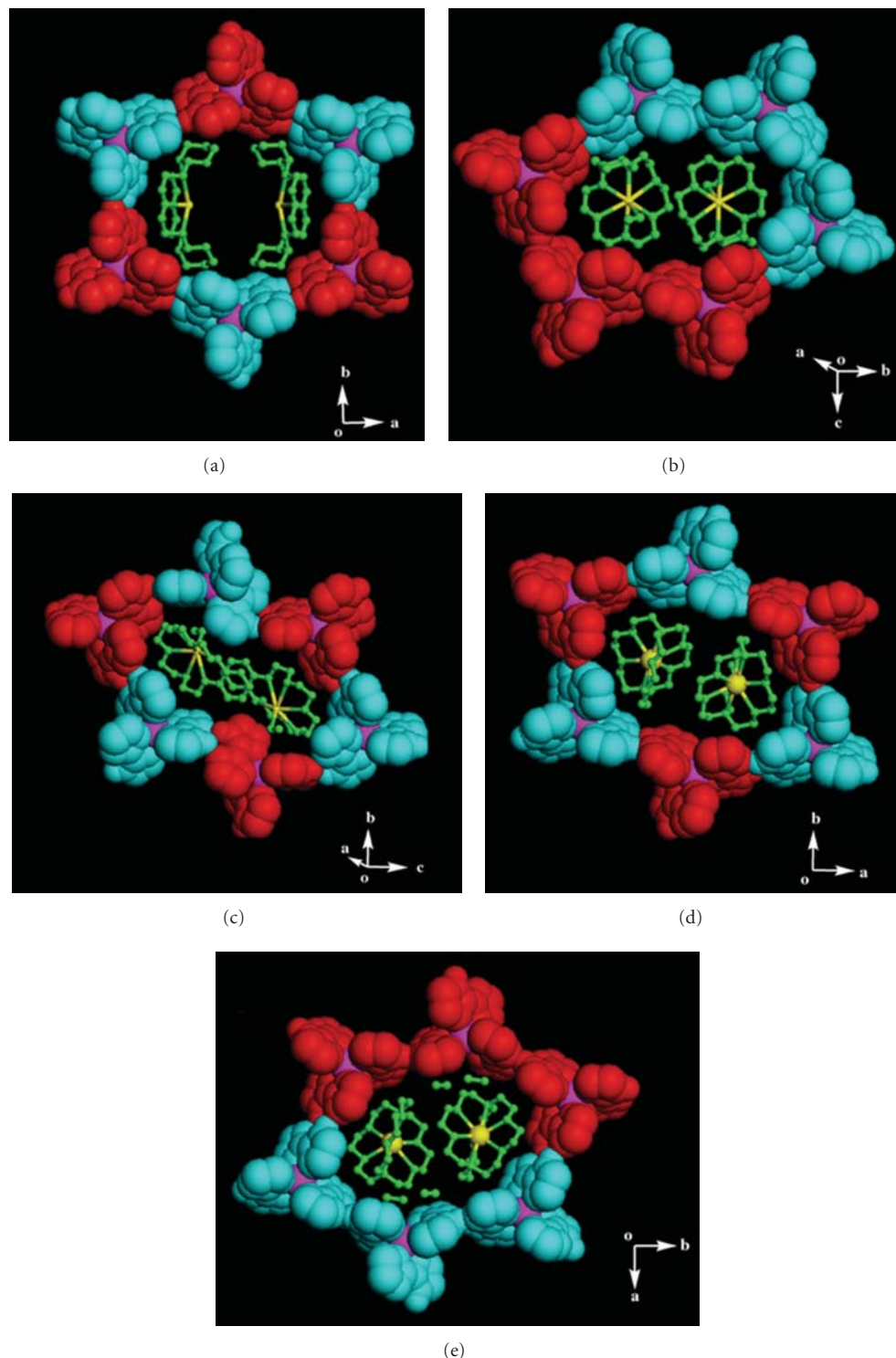


FIGURE 3: Structural view of each hexagonal cavity for crystals 1–5. (a) The structure of the hexagonal cavity of 1 is constructed from nondistorted hydrogen bond connections of six $[\text{Ni}(\text{Hbim})_3]^-$ molecules with alternating $\Delta\Lambda-\Delta\Lambda-\Delta\Lambda$ sequences of the Δ (red sphere) and Λ (blue sphere) optical isomers and includes two $[\text{K-DCH}(18\text{-crown-6})]^+$. The frameworks of K^+ -crown ether derivatives and MeOH molecules are represented by the green ball-and-stick lines. The potassium and nickel (II) ions are drawn with yellow and magenta spheres, respectively. ((b) and (e)) The hexagonal cavities of 2 and 5, which are represented by H-bonded connections of the $\Delta\Delta\Delta-\Lambda\Lambda\Lambda$ sequence with the distorted connection of the same optical isomers, include two $[\text{K-MCH}(18\text{-crown-6})]^+$ and two $[\text{K-cryptand}]^+$ molecules, respectively. (c) The hexagonal cavity of 3 that includes $[\text{K-MZB}(18\text{-crown-6})]^+$ is constructed from a sequence similar to that of 1 ($\Delta\Lambda-\Delta\Lambda-\Delta\Lambda$), although the hydrogen bonding connections are distorted. (d) The hexagonal cavity of 4 that includes $[\text{K-cryptand}]^+$, which is also a polymorph of 5, is constructed from the $\Delta\Lambda-\Delta\Lambda-\Delta\Lambda$ sequence.

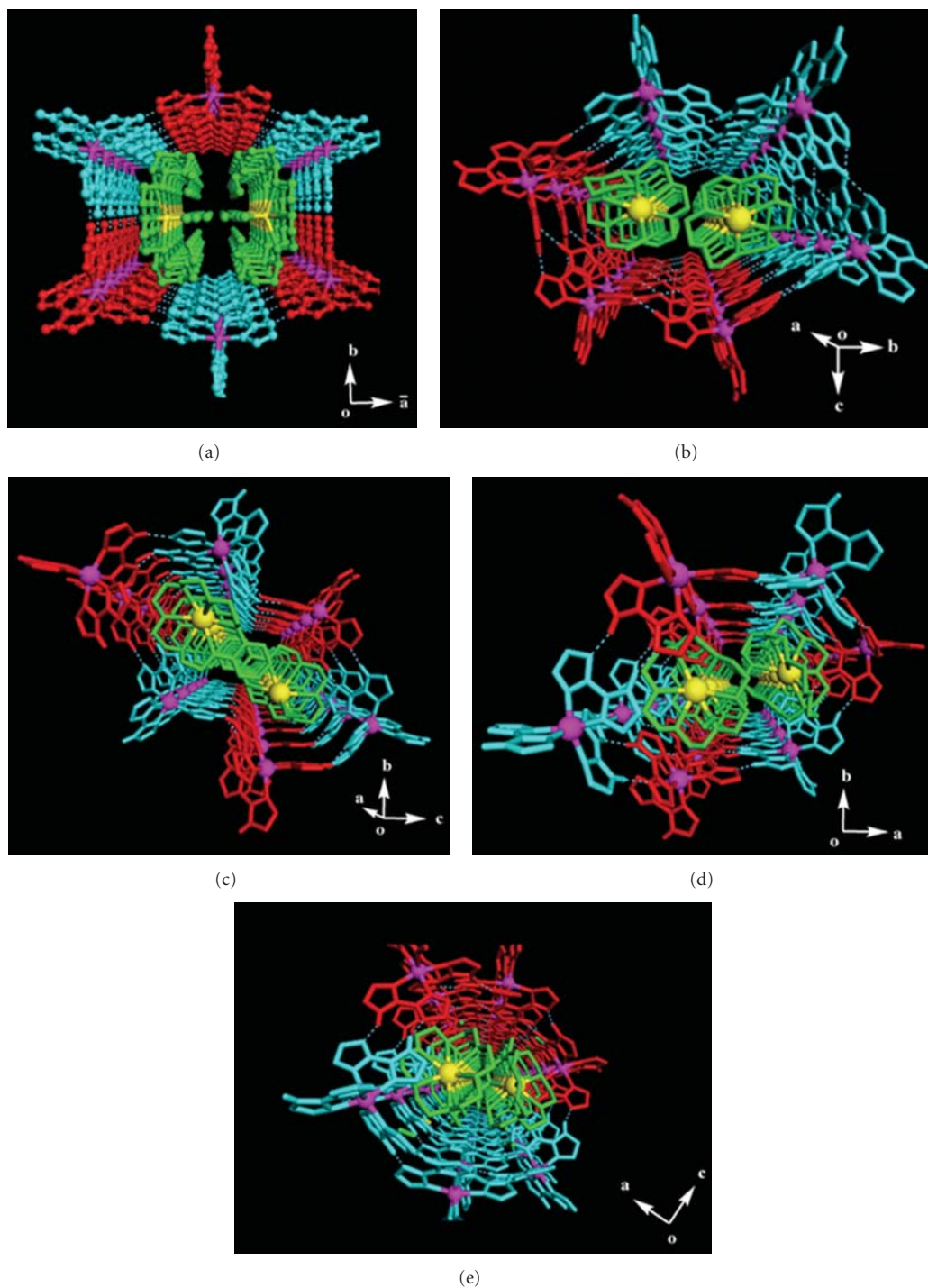


FIGURE 4: Perspective views of the channel structures through each hexagonal cavity for crystals 1–5. Each hexagonal cavity is stacked to form the channel structures. The channel structures of all crystals are constructed from segregated stacking, that is, from different stacking columns of each of the Δ and Λ optical isomers of $[\text{Ni}(\text{Hbim})_3]^-$ along the channel axis. The Δ and Λ isomers of $[\text{Ni}(\text{Hbim})_3]^-$ are represented by the red and blue lines, respectively. The crown ether frameworks and MeOH molecules are shown in green. The potassium and nickel (II) ions are drawn as yellow and magenta spheres, respectively.

formations. Figure 5 shows the sequence structures of the $[\text{Ni}(\text{Hbim})_3]^-$ networks in each of the connected hexagonal cavities in crystals 1–5. As shown in Figures 5(a) and 5(e), two hexagonal cavities in crystals 1 and 5 are constructed

by hexagonal alignments almost without distortion, built up by the $\Delta\Lambda-\Delta\Lambda-\Delta\Lambda$ sequence of $[\text{Ni}(\text{Hbim})_3]^-$. In contrast, the hexagonal cavity of crystal 2 is constructed from the heavily distorted arrangements of $\Delta\Lambda-\Delta\Lambda-\Delta\Lambda$ in order

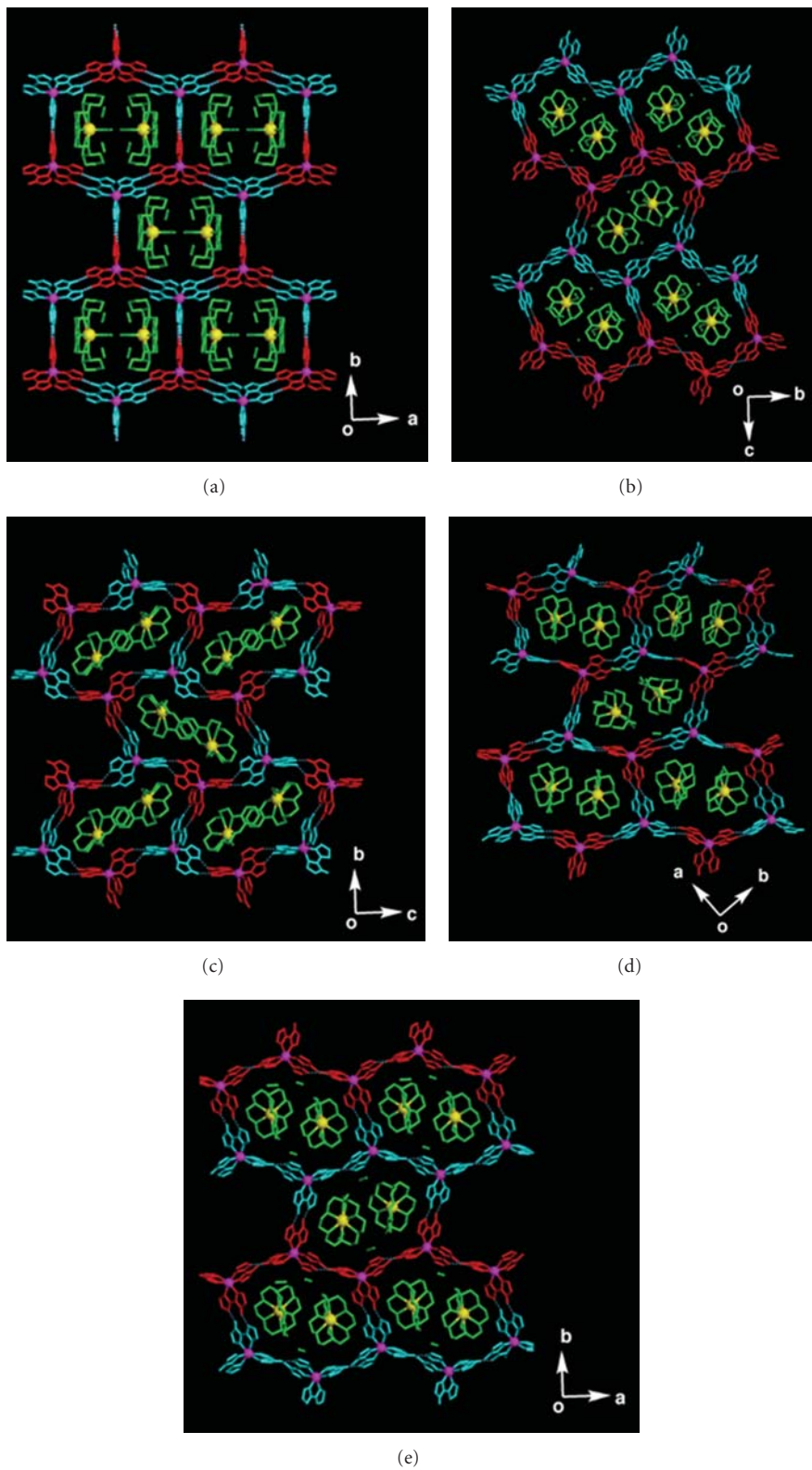


FIGURE 5: Views of honeycomb-sheet structures for crystals 1–5 are represented. Three sheet structures of crystals 1, 3, and 4 ((a), (c), and (d)) are constructed from alternating H-bonded connections with the $\Delta\Lambda\text{-}\Delta\Lambda\text{-}\Delta\Lambda$ sequence. In contrast, crystals 2 and 5 ((b) and (e)) are constructed from hydrogen-bonding connections with the $\Delta\Delta\Delta\text{-}\Lambda\Lambda\Lambda$ sequence between the two infinite $\Delta\Delta\Delta\cdots$ and $\Lambda\Lambda\Lambda\cdots$ zigzag chains. The Δ and Λ isomers of $[\text{Ni}(\text{Hbim})_3]^-$ are represented by red and blue lines, respectively. The crown ether frameworks and MeOH molecules are shown in green. The potassium and nickel (II) ions are drawn as yellow and magenta spheres, respectively.

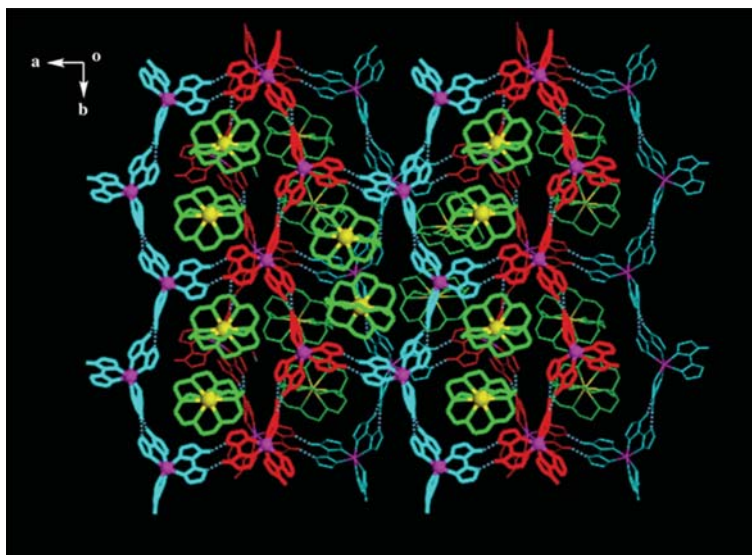


FIGURE 6

to adaptably fit $[\text{K-MCH}(18\text{crown}6)]^+$, as shown in Figure 5(b). On the other hand, both hexagonal cavities of crystals 3 and 4 are constructed from arrangements with the $\Delta\Delta\Delta-\Lambda\Lambda\Lambda$ sequences, which differ from the alternating $\Delta\Lambda-\Delta\Lambda-\Delta\Lambda$ sequences (Figures 5(c) and 5(d)). However, the arrangement of the hexagonal cavity in crystal 3 is heavily distorted to adaptably fit $[\text{K-MBZ}(18\text{crown}6)]^+$.

In this study, we identified five structures of crystals 1–5 induced by four K^+ -crown ether complexes. All of the crystals have stuffed channel frameworks with 1-D channels formed from $[\text{Ni}(\text{Hbim})_3]^-$. Each of the channels also includes a double-columnar array of the K^+ -crown ether complexes. The result indicates that $[\text{Ni}(\text{Hbim})_3]^-$ as a host molecule self-organizes into a stuffed channel framework, with widths of approximately two nanometres, induced by larger K^+ -crown ether complexes, similar to the urea crystal with guest-induced channel structures [54].

3. Conclusions

It is difficult to determine the positions and structures of guest molecules such as urea [54], zeolite [55], and MOF [56, 57], included in a nanoporous framework. This is because the resultant structures have a very robust porous framework made of an inorganic polymer such as aluminosilicate, owing to the heavy disordering of the included guest molecules. However, in a cation-clathrated porous framework formed from $[\text{Ni}(\text{Hbim})_3]^-$, as we have shown here, a crystal structure is obtained under conditions in which guest molecules have already been included in the nanochannels by one-pot synthesis. This is different from typical porous crystals such as zeolite, which do not have guest molecules. Thus, it is necessary not only to isolate the crystal of unstable nanoporous frameworks in advance, but also to fix the included guest cations by adaptable fitting of self-organised porous host frameworks formed from $[\text{Ni}(\text{Hbim})_3]^-$. The crystal structure of the included guest

molecules is clearly determined because adaptably fitting into the host H-bonding network prevents disordering of the guest molecules. In this study, we have compared five crystal structures induced by relatively large K^+ -crown ether derivatives. In contrast to host molecules that usually capture certain guest molecules in the well-known field of molecular recognition, the host arrays of $[\text{Ni}(\text{Hbim})_3]^-$ suggest a new host-guest chemistry because the self-organised supramolecular isomer, which is different from H-bonded superstructures, recognises certain guest molecules in the crystal. Here, K^+ -crown ether derivatives have been one-dimensionally arranged in the channel, the K^+ ion conductivity is not observed in the crystal. In the future, we hope that Li^+ ion-conductivity will be produced from an anionic nanochannel crystal that includes Li^+ -crown ether derivatives. Such a controlled crystal structure by induced fitting to $[\text{Ni}(\text{Hbim})_3]^-$ must be found as new structural-chemical investigation on the guest molecules included into a porous crystal.

4. Experimental Sections

4.1. Synthesis of $[\text{Ni}(\text{Hbim})_3][\text{K-DCH}(18\text{-crown-}6)] \cdot \text{MeOH} \cdot \text{H}_2\text{O}$ (1). A suspension of H_2bim (0.13 g, 1.0 mmol), $\text{DCH}(18\text{crown}6)$ (0.12 g, 0.31 mmol), and KO^tBu (0.30 g, 2.6 mmol) was added to methanol (30 cm^3) and heated under reflux until the ligand dissolved. $\text{Ni}(\text{ClO})_4 \cdot 6\text{H}_2\text{O}$ (0.11 g, 0.31 mmol) in methanol (20 cm^3) was added dropwise to the resulting solution, and the mixture was heated under reflux for 15 min. The insoluble components were removed by filtration, and the filtrate was allowed to stand at room temperature. Blue prisms were obtained from the filtrate after several days. Elemental analysis: Calcd for $[\text{Ni}(\text{Hbim})_3][\text{K-DCH}(18\text{crown}6)] \cdot 1.5\text{H}_2\text{O}$ ($\text{C}_{38}\text{H}_{52}\text{N}_{12}\text{O}_{6.5}\text{NiK}$): C, 50.90%; H, 6.07%; N, 18.74%; Found: C, 50.85%; H, 5.86%; N, 18.77% (dried in vacuo for 6 h at

100°C). IR (KBr) 2937 cm⁻¹ (ν (CH)), ~2500 cm⁻¹ (br, ν (NH)), 1895 cm⁻¹ (br, 2 γ (NH)).

4.2. Synthesis of $\{[Ni(Hbim)_3][K-MCH(18-crown-6)]\cdot MeOH\cdot H_2O\}_n$ (2). This crystal was obtained by a method similar to that employed for 1; however, MCH(18crown6) (0.10 g, 0.31 mmol) was used instead of DCH(18crown6). Elemental analysis: Calcd for $[Ni(Hbim)_3][K-MCH(18-crown-6)]\cdot 3.5H_2O$ (C₃₄H₅₂O_{9.5}N₁₂NiK): C, 46.48%; H, 5.97%; N, 19.13%; Found: C, 46.48%; H, 5.50%; N, 18.87% (dried in vacuo for 6 h at 100°C). IR (KBr) 2938 cm⁻¹ (ν (CH)), ~2500 cm⁻¹ (br, ν (NH)), 1896 cm⁻¹ (br, 2 γ (NH)).

4.3. Synthesis of $\{[Ni(Hbim)_3][K-MBZ(18-crown-6)]\cdot MeOH\}_n$ (3). This crystal was obtained by a method similar to that employed for 1; however, MBZ(18crown6) (0.10 g, 0.31 mmol) was used instead of DCH(18crown6). Elemental analysis: Calcd for $[Ni(Hbim)_3][K-MBZ(18crown6)]\cdot H_2O$ (C₃₄H₄₁O₇N₁₂NiK): C, 49.35%; H, 4.99%; N, 20.31%; Found: C, 49.57%; H, 5.13%; N, 20.23% (dried in vacuo for 6 h at 100°C). IR (KBr) 2941 cm⁻¹ (ν (CH)), ~2500 cm⁻¹ (br, ν (NH)), 1899 cm⁻¹ (br, 2 γ (NH)).

4.4. Syntheses of $\{[Ni(Hbim)_3][K-cryptand]\cdot 2MeOH\}_n$ (4) and $\{[Ni(Hbim)_3][K-cryptand]\cdot MeOH\}_n$ (5). This crystal was obtained by a method similar to that employed for 1; however, cryptand (0.12 g, 0.31 mmol) was used instead of DCH(18crown6). Elemental analysis: Calcd for $[Ni(Hbim)_3][K-cryptand]\cdot H_2O$ (C₃₆H₅₃O₇N₁₄NiK): C, 48.49%; H, 5.99%; N, 21.99%. Found: C, 47.99%; H, 5.98%; N, 21.64% (dried in vacuo for 6 h at 100°C and analysed the mixture of 4 and 5). IR (KBr) 2940 cm⁻¹ (ν (CH)), ~2500 cm⁻¹ (br, ν (NH)), 1898 cm⁻¹ (br, 2 γ (NH)).

Crystal Data for 1. C₄₁H₆₇O₁₁N₁₂NiK, FW = 1001.85, *Monoclinic*, space group C2/m (number 12) with $a = 19.077(3)$ Å, $b = 29.074(3)$ Å, $c = 9.769(3)$ Å, $\beta = 110.39(2)^\circ$, $V = 5078(1)$ Å³, $Z = 4$, $D_{\text{calcd}} = 1.310$ g/cm³, $F(000) = 2128.00$. 314 parameters, $R_1 = 0.070$, $wR_2 = 0.152$, and GOF = 1.054 for all 1419 data ($I > 3\sigma(I)$); $\mu(\text{CuK}\alpha) = 18.38$ cm⁻¹; 3797 reflections collected; the values of the minimum and maximum residual electron densities are 0.36 and -0.28 eÅ³, respectively.

Crystal Data for 2. C₃₄H₅₁O₈N₁₂NiK, FW = 853.65, *Monoclinic*, space group P2₁/n (number 14) with $a = 8.780(1)$ Å, $b = 17.039(3)$ Å, $c = 28.327(2)$ Å, $\beta = 91.50(1)^\circ$, $V = 4236.3(9)$ Å³, $Z = 4$, $D_{\text{calcd}} = 1.338$ g/cm³, $F(000) = 1800.00$. 559 parameters, $R_1 = 0.075$, $wR_2 = 0.174$, and GOF = 1.117 for 3854 data ($I > 3\sigma(I)$); $\mu(\text{CuK}\alpha) = 20.57$ cm⁻¹; 6582 reflections collected; the values of the minimum and maximum residual electron densities are 0.48 and -0.86 eÅ³, respectively.

Crystal Data for 3. C₃₅H₄₃O₇N₁₂NiK, FW = 841.60, *Monoclinic*, space group C2₁/n (number 14) with $a = 9.294(2)$ Å, $b = 25.183(5)$ Å, $c = 17.099(2)$ Å, $\beta = 95.64(1)^\circ$, $V = 3982(1)$ Å³, $Z = 4$, $D_{\text{calcd}} = 1.403$ g/cm³, $F(000) = 1760.00$.

544 parameters, $R_1 = 0.066$, $wR_2 = 0.179$, and GOF = 1.829 for all 3448 data ($I > 3\sigma(I)$); $\mu(\text{CuK}\alpha) = 21.65$ cm⁻¹; 4243 reflections collected; the values of the minimum and maximum residual electron densities are 0.22 and -0.22 eÅ³, respectively.

Crystal Data for 4. C₇₄H₁₁₀O₁₄N₂₈Ni₂K₂, FW = 1811.46, *Monoclinic*, space group P-1 (number 2) with $a = 13.962(1)$ Å, $b = 25.636(3)$ Å, $c = 12.937(1)$ Å, $\alpha = 100.034(8)^\circ$, $\beta = 93.221(8)^\circ$, $\gamma = 101.778(7)^\circ$, $V = 4443.4(8)$ Å³, $Z = 2$, $D_{\text{calcd}} = 1.354$ g/cm³, $F(000) = 3824.00$. 1165 parameters, $R_1 = 0.094$, $wR_2 = 0.213$, and GOF = 1.511 for all 5963 data ($I > 3\sigma(I)$); $\mu(\text{CuK}\alpha) = 19.89$ cm⁻¹; 12427 reflections collected; the values of the minimum and maximum residual electron densities are 0.99 and -1.14 eÅ³, respectively.

Crystal Data for 5. C₃₈H₅₉O₈N₁₄NiK, FW = 937.77, *Monoclinic*, space group C2/c (number 15) with $a = 18.966(2)$ Å, $b = 19.058(2)$ Å, $c = 25.469(2)$ Å, $\beta = 103.201(8)^\circ$, $V = 8962(1)$ Å³, $Z = 4$, $D_{\text{calcd}} = 1.390$ g/cm³, $F(000) = 3968.00$. 587 parameters, $R_1 = 0.074$, $R_w = 0.164$, and GOF = 1.189 for all 3530 data ($I > 3\sigma(I)$); $\mu(\text{CuK}\alpha) = 20.08$ cm⁻¹; 6033 reflections collected; the values of the minimum and maximum residual electron densities are 1.03 and -0.59 eÅ³, respectively.

The data collection for crystals 1–5 was performed by a Rigaku AFC7R—the 4-circle single-crystal X-ray diffractometer based on Lorenz-polarization corrections and graphite monochromatic Cu-K α ($\lambda = 1.54178$ Å)—for all crystals. Their structures were then solved by using direct method techniques with the SIR92 [58] and full-matrix least-squares (DIRDIF99) refinement [59]. The hydrogen atom positions were fixed. Further details of the data collection and structure solution of crystals 1–5 are provided as crystal data in Supplementary Material available online at doi:10.1155/2012/216050. Crystallographic data (excluding structure factors) for the structures reported in this paper have been deposited at the Cambridge Crystallographic Data Center as supplementary publication numbers CCDC-829900 (1), CCDC-829901 (2), CCDC-829897 (3), CCDC-829899 (4), and CCDC-829898(5). Copies of the data can be obtained free of charge on application to the Director, CCDC, 12 Union Road, Cambridge CB21EZ (fax: Int. Code (+44)1223/336-033; e-mail: deposit@chemcryst.cam.ac.uk).

Acknowledgments

This work was supported by a Grant-in-Aid for Scientific Research (nos. 22108531 and 22013016) on Priority Areas from the Ministry of Education, Science, and Culture, Japan. The authors thank the Analytical Center in Osaka City University for providing the 4-circle single-crystal X-ray diffractometer and the elemental analysis equipment.

References

- [1] J.-M. Lehn, "Supramolecular chemistry—scope and perspectives molecules, supermolecules, and molecular devices

- (Nobel Lecture),” *Angewandte Chemie*, vol. 27, no. 1, pp. 89–112, 1988.
- [2] J.-M. Lehn, *Supramolecular Chemistry-Concepts and Perspectives*, Wiley-VCH, Weinheim, Germany, 1995.
- [3] S. R. Batten and R. Robson, “Interpenetrating nets: ordered, periodic entanglement,” *Angewandte Chemie*, vol. 37, no. 11, pp. 1460–1494, 1998.
- [4] M. Yoshizawa, M. Nagao, K. Umemoto et al., “Side chain-directed assembly of triangular molecular panels into a tetrahedron vs. open cone,” *Chemical Communications*, no. 15, pp. 1808–1809, 2003.
- [5] J. Zubietta, P. J. Hagrman, and D. Hagrman, “Organic–inorganic hybrid materials: from “Simple” coordination polymers to organodiamine-templated molybdenum oxides,” *Angewandte Chemie*, vol. 38, no. 18, pp. 2638–2684, 1999.
- [6] C. B. Aakeröy, A. M. Beatty, and K. R. Lorimer, “Assembly of 2-D inorganic/organic lamellar structures through a combination of copper(I) coordination polymers and self-complementary hydrogen bonds,” *Journal of the Chemical Society, Dalton Transactions*, no. 21, pp. 3869–3872, 2000.
- [7] A. L. Gillon, G. R. Lewis, A. G. Orpen et al., “Organic–inorganic hybrid solids: control of perhalometallate solid state structures,” *Journal of the Chemical Society, Dalton Transactions*, no. 21, pp. 3897–3905, 2000.
- [8] D. B. Mitzi, “Templating and structural engineering in organic–inorganic perovskites,” *Journal of the Chemical Society, Dalton Transactions*, no. 1, pp. 1–12, 2001.
- [9] J.-C. Bünzli and C. Piguet, “Lanthanide-containing molecular and supramolecular polymeric functional assemblies,” *Chemical Reviews*, vol. 102, no. 6, pp. 1897–1928, 2002.
- [10] L. Carlucci, G. Ciani, and D. M. Proserpio, “Polycatenation, polythreading and polyknotting in coordination network chemistry,” *Coordination Chemistry Reviews*, vol. 246, no. 1–2, pp. 247–289, 2003.
- [11] S. Subramanian and M. J. Zaworotko, “Exploitation of the hydrogen bond: recent developments in the context of crystal engineering,” *Coordination Chemistry Reviews*, vol. 137, pp. 357–401, 1994.
- [12] G. R. Desiraju, “Supramolecular synthons in crystal engineering—a new organic synthesis,” *Angewandte Chemie*, vol. 34, no. 21, pp. 2311–2327, 1995.
- [13] A. D. Burrows, C.-W. Chan, M. M. Chowdhry, J. E. McGrady, and D. M. P. Mingos, “Multidimensional crystal engineering of bifunctional metal complexes containing complementary triple hydrogen bonds,” *Chemical Society Reviews*, vol. 24, no. 5, pp. 329–339, 1995.
- [14] I. Dance, “Supramolecular inorganic chemistry,” in *The Crystal as Supramolecular Entity*, G. R. Desiraju, Ed., vol. 5, pp. 145–248, John Wiley & Sons, 1996.
- [15] N. Ohata, H. Masuda, and O. Yamauchi, “Programmed self-assembly of copper(II)-L- and -D-arginine complexes with aromatic dicarboxylates to form chiral double-helical structures,” *Angewandte Chemie*, vol. 35, no. 5, pp. 531–532, 1996.
- [16] A. D. Burrows, D. M. P. Mingos, A. J. P. White, and D. J. Williams, “Crystal engineering of metal complexes based on charge-augmented double hydrogen-bond interactions between thiosemicarbazides and carboxylates,” *Chemical Communication*, no. 1, pp. 97–100, 1996.
- [17] C. B. Aakeröy and A. M. Beatty, “Supramolecular assembly of low-dimensional silver(I) architectures via amide–amide hydrogen bonds,” *Chemical Communications*, no. 10, pp. 1067–1068, 1998.
- [18] C. B. Aakeröy, A. M. Beatty, and D. S. Leinen, “The oxime functionality: a versatile tool for supramolecular assembly of metal-containing hydrogen-bonded architectures,” *Journal of the American Chemical Society*, vol. 120, no. 29, pp. 7383–7384, 1998.
- [19] C. B. Aakeröy, A. M. Beatty, and B. A. Helfrich, “Two-fold interpenetration of 3-D nets assembled via three-co-ordinate silver(I) ions and amide–amide hydrogen bonds,” *Journal of the Chemical Society, Dalton Transactions*, no. 12, pp. 1943–1946, 1998.
- [20] D. Braga, L. Maini, and F. Grepioni, “Crystal engineering of organometallic compounds through cooperative strong and weak hydrogen bonds: a simple route to mixed-metal systems,” *Angewandte Chemie*, vol. 37, no. 16, pp. 2240–2242, 1998.
- [21] J. C. Mareque Rivas and L. Brammer, “Hydrogen bonding in substituted-ammonium salts of the tetracarboxylcobaltate (–I) anion: some insights into potential roles for transition metals in organometallic crystal engineering,” *Coordination Chemistry Reviews*, vol. 183, no. 1, pp. 43–80, 1999.
- [22] M. T. Allen, A. D. Burrows, and M. F. Mahon, “Hydrogen bond directed crystal engineering of nickel complexes: the effect of ligand methyl substituents on supramolecular structure,” *Journal of the Chemical Society, Dalton Transactions*, no. 2, pp. 215–222, 1999.
- [23] D. Braga and F. Grepioni, “Complementary hydrogen bonds and ionic interactions give access to the engineering of organometallic crystals,” *Journal of the Chemical Society, Dalton Transactions*, no. 1, pp. 1–8, 1999.
- [24] L. Brammer, J. C. Mareque Rivas, R. Atencio, S. Fang, and F. C. Pigge, “Combining hydrogen bonds with coordination chemistry or organometallic π -arene chemistry: strategies for inorganic crystal engineering,” *Journal of the Chemical Society, Dalton Transactions*, no. 21, pp. 3855–3867, 2000.
- [25] M. M. Bishop, L. F. Lindoy, B. W. Skelton, and A. H. White, “Modification of supramolecular motifs: some effects of incorporation of metal complexes into supramolecular arrays,” *Journal of the Chemical Society, Dalton Transactions*, no. 3, pp. 377–382, 2002.
- [26] L. Brammer, “Metals and hydrogen bonds,” *Journal of the Chemical Society, Dalton Transactions*, no. 16, pp. 3145–3157, 2003.
- [27] M. Tadokoro, T. Shiomi, K. Isobe, and K. Nakasuji, “Cesium(I)-mediated 3-D superstructures by one-pot self-organization of hydrogen-bonded nickel complexes,” *Inorganic Chemistry*, vol. 40, no. 22, pp. 5476–5478, 2001.
- [28] L. Öhrström and K. Larsson, “What kinds of three-dimensional nets are possible with tris-chelated metal complexes as building blocks?” *Journal of the Chemical Society, Dalton Transactions*, no. 3, pp. 347–353, 2004.
- [29] C. S. Abrahams, R. L. Collin, and W. N. Lipscomb, “The crystal structure of hydrogen peroxide,” *Acta Crystallographica*, vol. 4, pp. 15–20, 1951.
- [30] F. Robinson and M. J. Zaworotko, “Triple interpenetration in [Ag(4,4′-bipyridine)][NO₃], a cationic polymer with a three-dimensional motif generated by self-assembly of “T-shaped” building blocks,” *Journal of the Chemical Society, Chemical Communications*, no. 23, pp. 2413–2414, 1995.
- [31] O. M. Yaghi and H. L. Li, “T-shaped molecular building units in the porous structure of Ag(4,4′-bpy)·NO₃,” *Journal of the American Chemical Society*, vol. 118, no. 1, pp. 295–296, 1996.
- [32] O. M. Yaghi, C. E. Davis, G. M. Li, and H. L. Li, “Selective guest binding by tailored channels in a 3-D porous zinc(II)–benzenetricarboxylate network,” *Journal of the American Chemical Society*, vol. 119, no. 12, pp. 2861–2868, 1997.

- [33] K. Biradha and M. Fujita, "A springlike 3D-coordination network that shrinks or swells in a crystal-to-crystal manner upon guest removal or readsorption," *Angewandte Chemie*, vol. 41, no. 18, pp. 3392–3395, 2002.
- [34] M. Fujita, Y. J. Kwon, S. Washizu, and K. Ogura, "Preparation, clathration ability, and catalysis of a two-dimensional square network material composed of cadmium(II) and 4,4'-bipyridine," *Journal of the American Chemical Society*, vol. 116, no. 3, pp. 1151–1152, 1994.
- [35] L. Carlucci, G. Cianni, D. M. Proserpio, and A. Sironi, "Polymeric helical motifs from the self-assembly of silver salts and pyridazine," *Inorganic Chemistry*, vol. 37, no. 22, pp. 5941–5943, 1998.
- [36] R. Atencio, K. Biradha, T. L. Hennigar et al., "Flexible bilayer architectures in the coordination polymers $[M^{II}(\text{NO}_3)_2(1,2\text{-BIS}(4\text{-pyridyl})\text{ethane})_{1.5}]_n$ ($M^{II} = \text{Co}, \text{Ni}$)," *Crystal Engineering*, vol. 1, no. 3–4, pp. 203–212, 1998.
- [37] S. S.-Y. Chui, S. M.-F. Lo, J. P. H. Charmant, A. G. Orpen, and I. D. Williams, "A chemically functionalizable nanoporous material $[\text{Cu}_3(\text{TMA})_2(\text{H}_2\text{O})_3]_n$," *Science*, vol. 283, no. 5405, pp. 1148–1150, 1999.
- [38] O. R. Evans, R.-G. Xiong, Z. Wang, G. K. Wong, and W. Liu, "Crystal engineering of acentric diamondoid metal-organic coordination networks," *Angewandte Chemie*, vol. 38, no. 4, pp. 536–538, 1999.
- [39] A. J. Blake, N. R. Champness, P. Hubberstey, W.-S. Li, M. A. Withersby, and M. Schröder, "Inorganic crystal engineering using self-assembly of tailored building-blocks," *Coordination Chemistry Reviews*, vol. 183, no. 1, pp. 117–138, 1999.
- [40] A. J. Blake, N. R. Champness, P. A. Cooke, and J. E. B. Nicolson, "Synthesis of a chiral adamantoid network—the role of solvent in the construction of new coordination networks with silver(I)," *Chemical Communications*, no. 8, pp. 665–666, 2000.
- [41] S. R. Batten, B. F. Hoskins, and R. Robson, "Interdigitation, interpenetration and intercalation in layered cuprous tricyanomethanide derivatives," *Chemistry*, vol. 6, no. 1, pp. 156–161, 2000.
- [42] S. Kitagawa, R. Kitaura, and S. Noro, "Functional porous coordination polymers," *Angewandte Chemie*, vol. 43, no. 18, pp. 2334–2375, 2004.
- [43] K. Takaoka, M. Kawano, M. Tominaga, and M. Fujita, "In situ observation of a reversible single-crystal-to-single-crystal apical-ligand-exchange reaction in a hydrogen-bonded 2D coordination network," *Angewandte Chemie*, vol. 44, no. 14, pp. 2151–2154, 2005.
- [44] M. Tadokoro, J. Toyoda, K. Isobe et al., "Dimeric hydrogen-bonded transition metal complex containing bidentate monodeprotonated 2,2'-biimidazolate ligand," *Chemistry Letters*, vol. 24, no. 8, pp. 613–614, 1995.
- [45] M. Tadokoro and K. Nakasujii, "Hydrogen bonded 2,2'-biimidazolate transition metal complexes as a tool of crystal engineering," *Coordination Chemistry Reviews*, vol. 198, no. 1, pp. 205–218, 2000.
- [46] L. Öhrström, K. Larsson, S. Borg, and S. T. Norberg, "Crucial influence of solvent and chirality—the formation of helices and three-dimensional nets by hydrogen-bonded biimidazolate complexes," *Chemistry*, vol. 7, no. 22, pp. 4805–4810, 2001.
- [47] R. Atencio, M. Chacon, T. Gonzalez, A. Brice, G. Agrifoglio, and A. Sierraalta, "Robust hydrogen-bonded self-assemblies from biimidazole complexes. Synthesis and structural characterization of $[\text{M}(\text{biimidazole})_2(\text{OH}_2)_2]^{2+}$ ($M = \text{Co}^{2+}, \text{Ni}^{2+}$) complexes and carboxylate modules," *Dalton Transactions*, no. 4, pp. 505–513, 2004.
- [48] B. H. Ye, B. B. Ding, Y. Q. Weng, and X. M. Chen, "Multidimensional networks constructed with isomeric benzenedicarboxylates and 2,2'-biimidazole based on mono-, bi-, and trinuclear units," *Crystal Growth & Design*, vol. 5, no. 2, pp. 801–806, 2005.
- [49] R. L. Sang and L. Xu, "Counteranion-induced formation of *cis* and *trans* singly and doubly H₂biim-bridged Di-, Hexa-, and polymeric Ag–H₂biim complexes," *European Journal of Inorganic Chemistry*, vol. 2006, no. 6, pp. 1260–1267, 2006.
- [50] L. Ion, D. Morales, J. Pérez et al., "Ruthenium biimidazole complexes as anion receptors," *Chemical Communications*, no. 1, pp. 91–93, 2006.
- [51] M. Tadokoro, H. Kanno, T. Kitajima et al., "Self-organizing super-structures formed from hydrogen-bonded biimidazolate metal complexes," *Proceedings of the National Academy of Sciences of the United States of America*, vol. 99, no. 8, pp. 4950–4955, 2002.
- [52] M. Tadokoro, K. Isobe, H. Uekusa et al., "Cation-dependent formation of superstructures by one-pot self-organization of hydrogen-bonded nickel complexes," *Angewandte Chemie*, vol. 38, no. 1–2, pp. 95–98, 1999.
- [53] M. Tadokoro, T. Shiomi, M. Kaneyama, and Y. Miyazato, "Controlled super-structures of hydrogen bonding Ni^{II} complexes organizing one-dimensional double cationic arrays," *Journal of Nanoscience and Nanotechnology*, vol. 9, no. 1, pp. 301–306, 2009.
- [54] M. D. Hollingsworth and K. D. M. Harris, "Urea, thiourea, and selenourea," in *Comprehensive Supramolecular Chemistry*, J. L. Atwood, J. E. D. Davies, D. D. MacNicol, F. Vögtle, and J.-M. Lehn, Eds., vol. 6, pp. 177–238, Pergamon Press, 1996.
- [55] H. Gies and B. Marler, "Crystalline microporous silicas as host-guest systems," in *Comprehensive Supramolecular Chemistry*, J. L. Atwood, J. E. D. Davies, D. D. MacNicol, F. Vögtle, and J.-M. Lehn, Eds., vol. 6 of *Solid-State Supramolecular Chemistry: Crystal Engineering*, pp. 851–883, Pergamon Press, 1996.
- [56] M. E. Davis, "Ordered porous materials for emerging applications," *Nature*, vol. 417, pp. 813–821, 2002.
- [57] N. W. Ockwig, O. Delgado-Friedrichs, M. O'Keeffe, and O. M. Yaghi, "Reticular chemistry: occurrence and taxonomy of nets and grammar for the design of frameworks," *Accounts of Chemical Research*, vol. 38, no. 3, pp. 176–182, 2005.
- [58] A. Altomare, G. Casciarano, C. Giacovazzo et al., "SIR92—a program for automatic solution of crystal structures by direct methods," *Journal of Applied Crystallography*, vol. 27, no. 1, pp. 435–441, 1994.
- [59] P. T. Beurskens, G. Admiraal, G. Beurskens et al., "The DIRDIF-99 program system".

Research Article

Wear-Resistant Ultrahigh-Molecular-Weight Polyethylene-Based Nano- and Microcomposites for Implants

S. V. Panin,^{1,2} L. A. Kornienko,¹ N. Sonjaitham,² M. V. Tchaikina,³
V. P. Sergeev,¹ L. R. Ivanova,¹ and S. V. Shilko⁴

¹Institute of Strength Physics and Materials Science SB RAS, Laboratory of Composite Polymeric Materials, pr. Akademicheskii, 2/4, Tomsk 634021, Russia

²National Research Tomsk Polytechnic University, Institute of Physics of High Technologies, Lenin Avenue, 30, Tomsk 634050, Russia

³Institute of Solid State Chemistry and Mechanochemistry SB RAS, Laboratory of Intercalation and Mechanochemical Reactions, Kutateladze 18, Novosibirsk 630128, Russia

⁴V.A. Belyi Metal-Polymer Research Institute NASB, Department of Mechanics of Adaptive Materials and Biomechanics, 32A Kirov Street, 246050 Gomel, Belarus

Correspondence should be addressed to S. V. Panin, paninsergey@yahoo.co.uk

Received 10 April 2012; Accepted 18 May 2012

Academic Editor: Guifu Zou

Copyright © 2012 S. V. Panin et al. This is an open access article distributed under the Creative Commons Attribution License, which permits unrestricted use, distribution, and reproduction in any medium, provided the original work is properly cited.

The influence of modification by hydroxyapatite (HA) nano- and microparticles on tribotechnical properties of ultrahigh-molecular-weight polyethylene (UHMWPE) was investigated to develop polymer implants for endoprosthesis. It was shown that modification of UHMWPE by hydroxyapatite nanoparticles within range of 0.1–0.5 wt.% results in increase of wear resistance at dry sliding by 3 times. On the other hand adding of 20 wt.% of micron size HA gives rise to the same effect. The effect of increasing wear resistance is not substantially changed at surface treatment of the nano- and microcomposites by N⁺ ion beams as compared with nonirradiated blends. Preliminary joint mechanical activation of UHMWPE powder and fillers results in more uniform distribution of nanofillers in the matrix and, as a result, formation of more ordered structure. Structure within bulk material and surface layers was studied by means of optical profilometry, scanning electron microscopy, infrared spectroscopy, and differential scanning calorimetry. It is shown that adding of hydroxyapatite nanoparticles and high-energy surface treatment of the composite by N⁺ ion implantation improve tribotechnical properties of UHMWPE due to formation of chemical bonds in the composite (crosslinking) and ordering of permolecular structure.

1. Introduction

Since having relatively high strength characteristics, low friction factor, high wear and chemical resistance in corrosive media ultrahigh-molecular-weight polyethylene (UHMWPE) is used for the manufacturing of implants (artificial joints, face surgery, etc.). The reason for its wide use as a material for implants is related to its similarity to biotissues on chemical nature and physical-mechanical properties [1–4]. UHMWPE-based nanocomposites with biocompatible fillers are currently not well-studied objects in the modern medical materials science [5–9]. The variety of biocompatible filler is extremely limited. In [10] which is to date the most comprehensive handbook on manufacturing and operation of UHMWPE in medical practice, the

focus is done on the improvement tribotechnical properties of this polymer by means of ion implantation that is generally combined with the procedure of sterilization. However, reinforcement of polymeric materials for medical applications is mostly limited by using HA particles. In doing so the optimum weight fraction is still a matter of systematic investigations. Hydroxyapatite (HA or calcium hydroxyl phosphate) (C₁₀(PO₄)₆(OH)₂) belongs to the class of biologically active materials with properties of high surface activity, high biocompatibility which are similar to the bone matrix structure providing reliable fixation of implants.

From the point of view of HA use as a prospective filler for bioimplants it should be noted that presence of micron-size HA particles during interaction of the filled polymer with articular fluid will be accompanied by their gradual

TABLE 1: Mechanical properties of nano- and microcomposites based on UHMWPE.

Content of HA filler, wt.%	Density, g/sm ³	Strength, MPa	Elongation, %
0	0.936	33.5	380.4
Nano (20–30 nm)			
0.1	0.935	29.6	430.6
0.5	0.937	32.4	481.9
1	0.939	31.4	492.3
2	0.944	32.6	461.3
Micro (7–8 μ m)			
5	0.954	26.9	398.5
10	0.986	31.7	473.8
20	1.071	25.8	433.7
40	1.095	14.2	231.1

resorption and formation of micron-size pore skeleton which is adversely affecting the strength and wear resistance. Adding of the nanosize hydroxyapatite particles will provide formation of porous nanoskeleton that should not reduce the strength properties and will be accompanied by the accumulation of synovial liquid within the pores. The liquid will be partly allocated at the interface of plastic cup and metal (CoNiCr) head hip prostheses, to reduce the intensity of polymer wear by several times [1, 2].

Certain prospects at obtaining materials for manufacturing implants with high mechanical and tribotechnical properties might be found in the area of combined use of biocompatible fillers and high energy electron beam treatment of composites. However, studies of UHMWPE-based composites to be performed at combined use of various methods for treatment of polymer composites for medical applications at present are hardly to be found in the literature.

In this work physical-mechanical and tribotechnical characteristics of UHMWPE-based composites with biocompatible nano- and microfillers based on hydroxyapatite were studied. Comparative analysis of wear resistance of nano- and microcomposites as well as influence of high-energy treatment (ion implantation) of the above-mentioned composites on their wear resistance was carried out.

2. Experimental

In the paper the powder of UHMWPE (GUR-2122 by Ticona) with molecular weight of 4.0 million and its composites with various weight fraction of HA ($C_{10}(PO_4)_6(OH)_2$) nano- and microparticles were used. The size of nanoparticles obtained by mechanosynthesis made 20–30 nm while microparticles obtained by grinding animal bones made 7–8 μ m. Specimens of polymer composites were obtained by hot pressing at specific pressure of 10 MPa, temperature of 190°C and cooling rate of 3–4°C/min. Industrial type planetary ball mill MR/0.5 * 4 [11] was employed for powder mechanical activation as well as mixing of UHMWPE polymeric binder and fillers.

Ion implantation by N^+ ions was carried out using “DIANA-2” setup (fluence of 0.5, 1 and 2 * 10^{17} ion/cm²)

at accelerating voltage of 60 kV, with ion beam current amplitude of 490 mA and pulse frequency 50 Hz. Wear resistance of test materials under dry sliding was determined by “block-on-ring” scheme at load of 160 N and revolution rate 100 rpm in accordance with ASTM G99 and DIN 50324 with the use of SMT-1 machine. Size of specimens made 7 * 7 * 10 mm³. Diameter of the roller made 62 mm.

Wear track surfaces were investigated with the use of optical profilometer Zygo New View 6200. Wear track area was estimated with the help of “Rhino Ceros 3.0” software by manual allocation of wear track contour and subsequent automated calculation. Measurements of degree of crystallinity were performed by the help of SDT Analyzer Q600. Infrared spectra were registered by FTIR spectrometer NIKOLET 5700. Structure investigations were performed using scanning electron microscope LEO EVO 50 at acceleration voltage of 20 kV on surface of fractured specimens failing just after extracting them from liquid nitrogen.

3. Results and Discussion

The data to summarize results of measuring mechanical properties of UHMWPE-based composites with micro- and nanofillers are presented in Table 1. The data show that ultimate strength is decreased when polymer is filled by either nano- or microfillers, but it does not depend on volume fraction of the fillers. In doing so, elongation at tension is increased as filler weight fraction is enlarged while this also weakly depends on nanofillers weight fraction. It can be seen that 0.5 wt.% of HA to be added into nanocomposite is enough to reach the optimum (maximum) values of strength and ductility. Mechanical properties of the composites are decreased sharply when the HA (micro) weight fraction exceeds 20 wt.%.

In terms of tribotechnical characteristics the influence of variation weight fraction of the hydroxyapatite filler possesses different trend. Curves of kinetic wear for all tested composites are presented in Figure 1, while wear intensity (I , mm²/min) diagram of the composites under study to be measured at steady-state wearing stage is depicted in Figure 2. One can see that wear resistance of UHMWPE with the volume fraction of nanoparticles of 0.1–0.5 wt.%

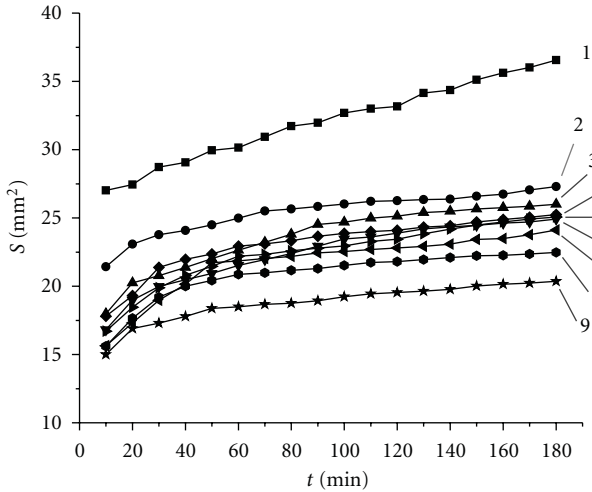


FIGURE 1: Kinetic wear curves of UHMWPE-based specimens: (1) pure UHMWPE; nanocomposites: UHMWPE +0.1 (2), +0.5 (3), +1 (4), +2 (5) wt.% HA and microcomposites UHMWPE: +5 (6), +10 (7), +20 (8), +40 (9) wt.% HA.

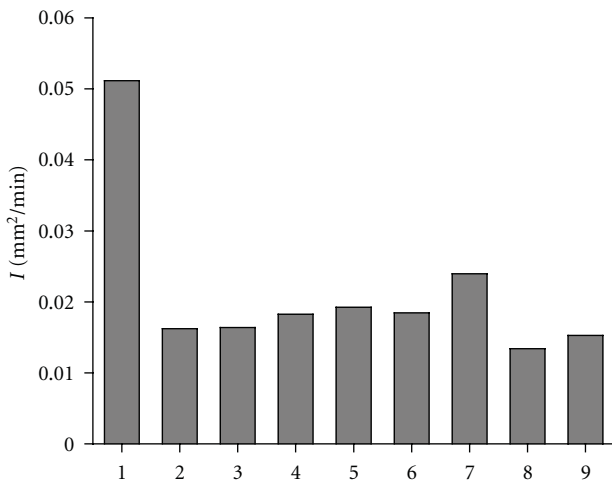


FIGURE 2: Wear intensity (I) of specimens: pure UHMWPE (1), nanocomposites UHMWPE +0.1 (2), 0.5 (3), 1 (4), 2 (5) wt.% HA and microcomposites UHMWPE +5 (6), 10 (7), 20 (8), 40 (9) wt.% HA at the steady-state wearing stage.

is increased by 3.5 times. Wear resistance of the specimens is decreased (columns 4, 5) when the weight fraction of nanoparticles is increased up to 1-2 wt.%. In doing so, wear resistance of nanocomposites with HA volume fraction of 0.1–0.5 wt.% is approximately equal to one of composites with 20 wt.% of HA micron size filler (columns 2, 8).

Dependence of wear track surface roughness (R_a , μm) as a function of the filler (nano- and micro-) weight fraction in the composites is the same (Figure 3). Therefore, further analysis on the influence of high energy treatment (N^+ ion implantation) was carried out for the nanocomposites UHMWPE +0.5 wt.% HA and microcomposites UHMWPE +20 wt.% HA.

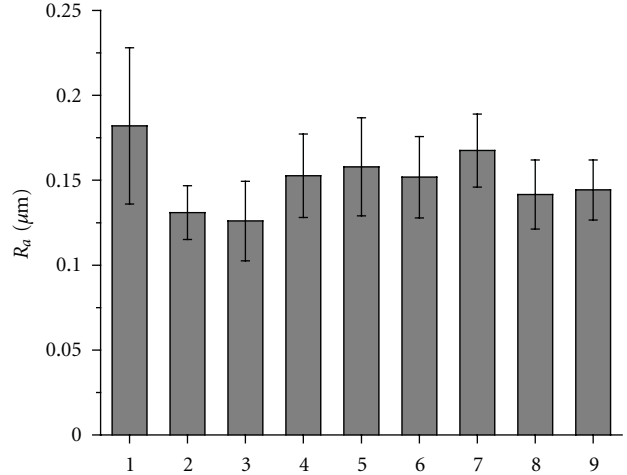


FIGURE 3: Dependence of surface roughness of wear track (R_a) in pure UHMWPE (1), nanocomposites UHMWPE +0.1 (2), 0.5 (3), 1 (4), 2(5) wt.% HA and microcomposites UHMWPE +5 (6), 10 (7), 20 (8), 40 (9) wt.% HA at the steady-state wearing stage.

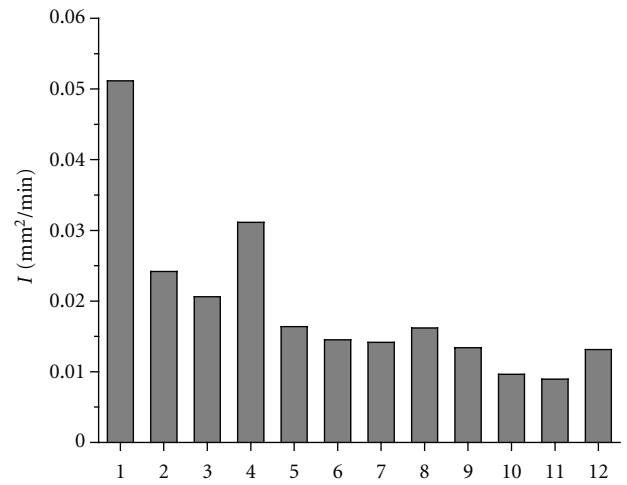


FIGURE 4: Wear intensity (I) of UHMWPE specimens: pure (1) and N^+ ion implanted with doses of 0.5 (2), 1 (3), $2 \cdot 10^{17}$ (4); nanocomposites UHMWPE +0.5 wt.% HA in the initial state (5) and implanted one with doses 0.5 (6), 1 (7), $2 \cdot 10^{17}$ N^+ (8); microcomposites UHMWPE +20 wt.% HA without surface treatment (9) and implanted ones with doses of 0.5 (10), 1 (11), $2 \cdot 10^{17}$ N^+ (12) at the steady-state wearing stage.

Analysis of wear intensity of composites implanted by N^+ ions has shown that, firstly, the optimum fluence made $1 \cdot 10^{17}$ ion/cm² both for the nonfilled polymer (Figure 4, columns 1–4) and for the composites (Figure 4, columns 5–8, and 9–12). Secondly, for the unfilled UHMWPE specimens wear resistance at ion implantation is increased by three times, whereas for composites (nano and micro) only by 10–30 %. Thirdly, wear resistance of implanted microcomposites (UHMPE +20 wt.% HA) is slightly higher than that in nanocomposites (columns 7 and 11). Roughness of wear track surface of the implanted UHMPE specimens and composites on its basis is presented in Figure 5.

TABLE 2: Crystallinity (χ , %) in UHMWPE-based composites.

UHMWPE	0.5 wt.% HA (nano)	20 wt.% HA (micro)
56.6	41.1	41.4
60.2	48.9	46.8

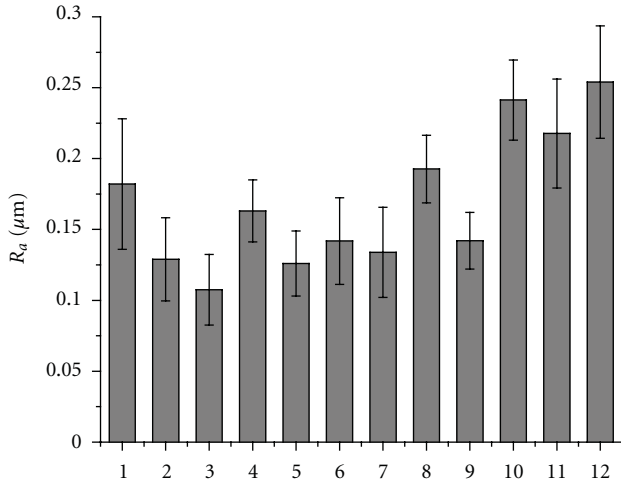


FIGURE 5: Dependence of surface roughness of wear track (R_a) of specimens under tests: pure UHMWPE (1), N^+ implanted UHMWPE with doses: 0.5 (2), 1 (3), $2 \cdot 10^{17}$ (4); nanocomposites: UHMWPE +0.5 wt.% HA without surface treatment (5) and implanted with doses 0.5 (6), 1 (7), $2 \cdot 10^{17}$ N^+ (8); microcomposites: UHMWPE +20 wt.% HA without ion implantation (9) and implanted with doses 0.5 (10), 1 (11), $2 \cdot 10^{17}$ N^+ (12) at the steady-state wearing stage.

Comparative analysis of permolecular structure to result from filling polymer by various sizes hydroxyapatite particles and subsequent high energy N^+ ion beam treatment of different doses was made to clarify the mechanism of improving wear resistance of UHMWPE-based nano- and microcomposites. The results of measurement of crystallinity degree of pure UHMWPE and composites on its basis (raw 2) and implanted ones with fluence of $1-10^{17}$ ion/cm² (raw 3), obtained by the method of differential scanning calorimetry (DSC), are presented in Table 2.

As becomes clear from Table 2, the filling of the polymer by HA nano- and microparticles results in decrease of composite crystallinity. The latter in the surface layer (raw 3) is increased due to the N^+ ions surface treatment of the UHMWPE specimens and the composites. Permolecular structure of the pure UHMWPE is spherulitic one (Figure 6(a)). Filling of polymer by HA nanoparticles does not alter the nature of the permolecular structure (Figure 6(b)). At the same time microfillers suppress the formation of spherulitic permolecular structure (Figures 6(c) and 6(d)).

The ion treatment of UHMWPE specimen surface and its composites causes structure change in the surface layer (Figure 7). The depth of the modified surface layer with lamellar permolecular structure in the nanocomposite UHMWPE +0.5 wt.% HA is less than that in the implanted UHMWPE and makes 500–800 μm . In our view, nanofiller shields the

rearrangement of macromolecules under the high-energy effect. As a result the permolecular structure in deeper layers becomes amorphous (jelly-like) (Figures 7(a) and 7(b)). Structurally modified layer in the microcomposites UHMWPE +20 wt.% is extremely thin, and crystallinity (structural order) also slightly increases (Table 2).

IR-spectra of bulk material and surface layers of the polymer specimens were studied before and after the implantation for more detailed analysis of structural changes to take place in the UHMWPE specimens and (nano- and micro-) composites on its basis. IR-spectra for pure UHMWPE and its composites UHMWPE +0.5 wt.% HA (nano) and UHMWPE +20 wt.% HA (micro) are given in Figure 8 for the sake of comparison. One can see that the intensities of carbonyl group peaks 1700, 1620, 1040, and 1240 cm^{-1} relevant to C=O, C=C and C–O–C, C–C–O bonds [4] are increased in the spectrum of filled specimens. In doing so, nanofiller tends to be more active (Figure 8, curve 2). In the regions 2250, 3200, 3300, 3500 cm^{-1} there occur bonds of the C=N, N–H, O–H type which are missing in the spectra of the nanocomposite (Figure 8, curve 3). Surface treatment of the nanocomposites by N^+ ions does not change the general pattern of the spectrum (Figure 9). The intensity of the above-mentioned bonds in the surface layer of the specimen treated by ion beam becomes lower. The same pattern is observed in the surface layer of microcomposites treated by ion beam. In doing so, the crystallinity in the surface layer of implanted nano- and microcomposites increases in comparison with one in untreated specimens (Table 2), which is related to increased wear resistance of UHMWPE and UHMWPE-based composites due to the implantation of N^+ ions (Figure 4). It should be noted that the treatment of the pure UHMWPE by ion beam is more efficient than implantation of UHMWPE-based composites. Nano- and micro-HAs hinder macromolecules rearrangement in a surface layer caused by high energy effect. Therefore, as a result of the ion implantation, the depth of the modified surface layer is highest in pure UHMWPE. As for the nanocomposites it is decreased, while for the microcomposites it has minimum thickness.

The comparative analysis of two methods of high-energy treatment of UHMWPE surface and nanocomposites based on its basis (ion implantation and electron beam treatment) has been performed. Influence of electron beam on wear resistance of UHMWPE and nanocomposites on its basis has been previously described in [4]. Analysis of tribotechnical characteristics and structural changes in a bulk material and surface layers after high-energy treatments showed that wear resistance of UHMWPE after electron beam treatment at steady-state stage of wear is equivalent the wear resistance of ion-implanted UHMWPE with the dose of $1 \cdot 10^{17}$ ion/cm² (N^+). This is due to an identity of permolecular (lamellar) structure being formed in the surface layer of polymer under the high-energy effect.

As was shown by analysis made in this paper as well as in [4] the permolecular structure formed is similar to one in UHMWPE after mechanical activation [11]. As a result, wear resistance of UHMWPE after electron-beam

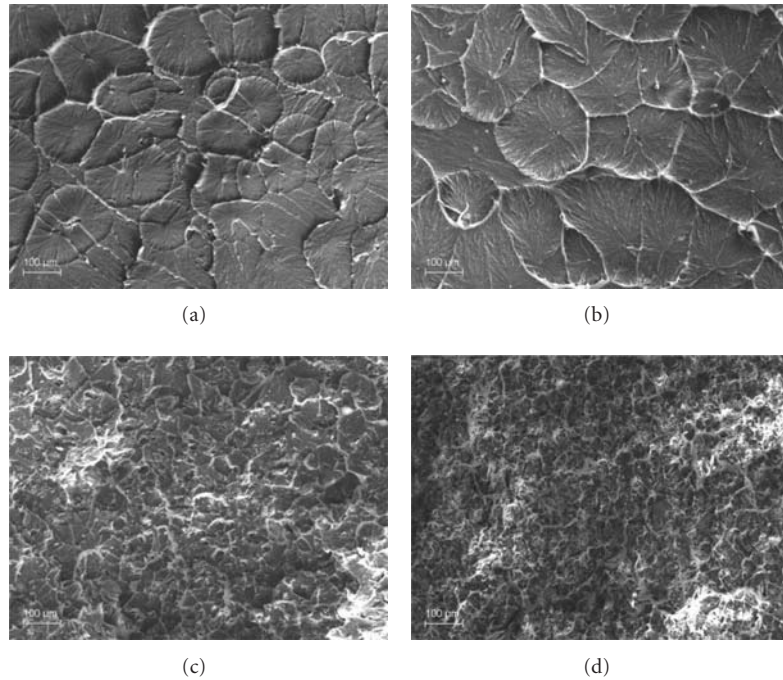


FIGURE 6: Perimolecular structure of the pure UHMWPE (a), nanocomposite UHMWPE +0.5 wt.% HA (b) and microcomposites: UHMWPE +10 wt.% HA (c), UHMWPE +20 wt.% HA (d).

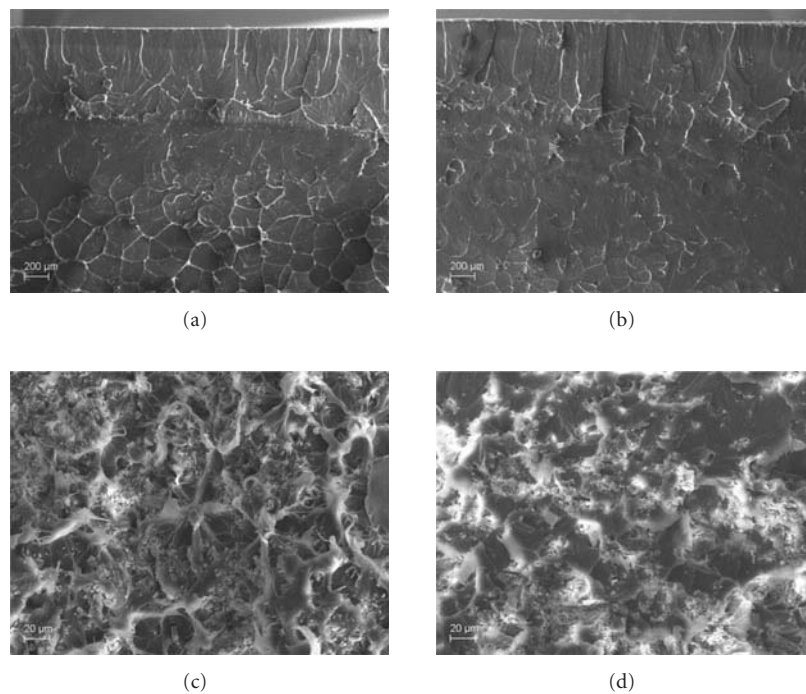


FIGURE 7: Perimolecular structure of the implanted UHMWPE (a), nanocomposite UHMWPE +0.5 wt.% HA (b) and microcomposites: UHMWPE +10 wt.% HA (c), UHMWPE +20 wt.% HA (d). Dose: $N^+ 1 \cdot 10^{17}$.

treatment and ion implantation at steady-state wearing stage is similar to one of the polymer after mechanical activation. So, the electron-beam surface treatment of UHMWPE and mechanical activation can be used as equivalent ways to increase wear resistance of polymer.

In contrast with our previous data the characteristic feature of HA as a filler for UHMWPE is its chemical and surface activity that gives rise to chemical bonding with the polymer [12]. HA microfiller demonstrates these properties to a less extent (Figure 8). Therefore, the effectiveness of

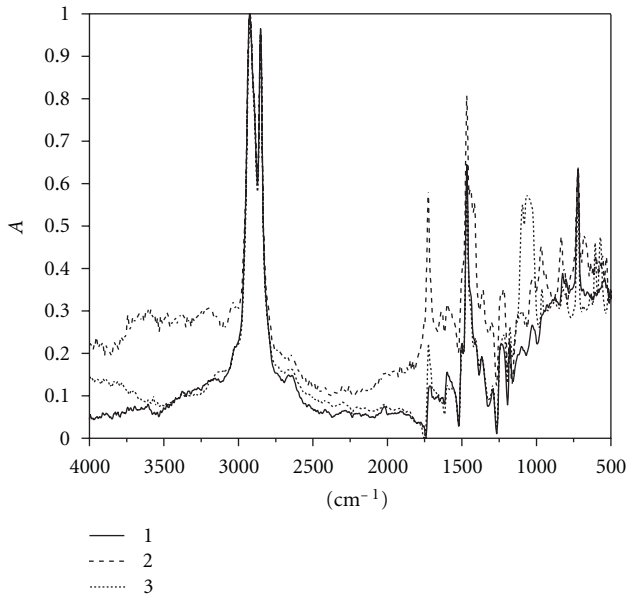


FIGURE 8: IR spectra of pure UHMWPE (1), UHMWPE-based nanocomposite (with 0.5 wt.% HA) (2) and UHMWPE-based microcomposite (with 20 wt.% HA) (3).

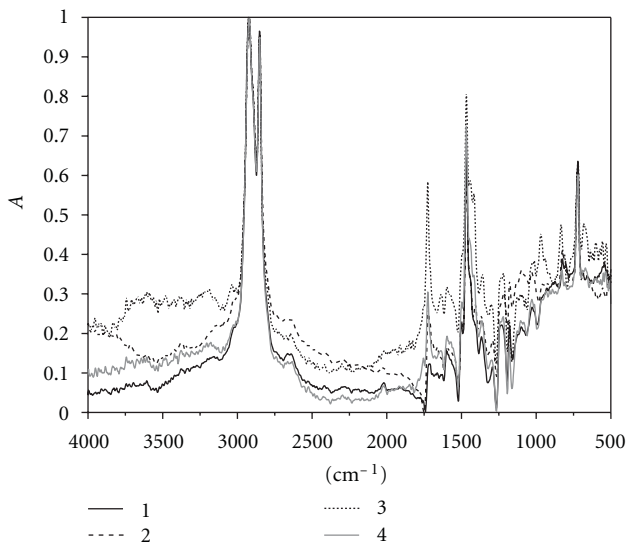


FIGURE 9: IR spectra of pure UHMWPE (1), implanted UHMWPE (2), UHMWPE-based nanocomposite (with 0.5 wt. % HA) (3), UHMWPE-based microcomposite (with 20 wt. % HA) (4). Dose: $N^+ 1 \cdot 10^{17}$.

the electron-beam surface treatment of the UHMWPE-based composites (with nano- and micro-HA) to increase wear resistance is low being compared with one of the pure UHMWPE [13, 14]. Hardening due to formation of chemical bonds (crosslinking) is realized by adding HA nanofillers. Electron-beam surface treatment of the UHMWPE-based composites gives only to slight additional crosslinking of molecules providing complimentary sterilization of specimens (items for medical use).

On the other hand, HA nanofillers “oscillating” in a destructured surface layer of composite and synovial fluid of a joint eventually create a porous nanoframework filled by synovial fluid [1]. Composite with a weight fraction of 20 wt.% HA microfiller are capable of similar wear resistance, but it will bring to the gradual resorption and formation of micron-sized pores framework which will adversely affect the strength and wear resistance. Since HA fillers partially shield rearrangement of a structure, crosslinking of macromolecules (their ordered packing) which is the main mechanism for improving its wear resistance [15], the high-energy surface treatment of nanocomposites can be used in combination with nanofilling as well as a method of sterilization.

4. Conclusion

- (i) Nanofilling of UHMWPE by 0.1–0.5 wt.% HA increases its wear resistance in 3.5 times compared to the pure polymer. Adding of 20 wt.% HA micron size particles provides the similar wear resistance.
- (ii) High-energy treatment by N^+ ion beam brings structural rearrangement and crosslinking of macromolecules in the polymer surface layers resulting in increase of its wear resistance. HA fillers “shield” structural rearrangement in the surface layers and only slightly increase the wear resistance of composites.
- (iii) Wear resistance of ion-implanted UHMWPE and composites on its basis is comparable with the one after the electron-beam treatment that caused the identity of permolecular structure modification of surface layers under the high-energy effect.
- (iv) The high-energy treatment of UHMWPE-based composites can be used in combination with filling by HA nanoparticles of as a method of sterilization of products for medical applications (orthopaedic implants).

References

- [1] L. S. Pinchuk, M. Y. Chernyakova, and V. À. Goldade, “Tribology of joints and the problems of modern orthopedics,” *Journal of Friction and Wear*, vol. 29, no. 3, pp. 224–233, 2008.
- [2] L. S. Pinchuk, “Modern trends in evolution of joint endoprostheses,” in *Proceedings of the 14th International Colloquium Tribology*, vol. 3 of *Tribology and Lubrication Engineering*, pp. 1735–1739, Technische Akademie Esslingen, Ostfildern, Germany, January 2004.
- [3] S. V. Panin, L. À. Kornienko, Ò. Poowadin, V. P. Sergeev, L. R. Ivanova, and S. V. Shilko, “Friction and Wear of the ion-implanted ultra-high molecular weight polyethylene for implants,” *Trenie i Smazka v Machinakh i Mekhanizmaxh*, no. 10, pp. 3–12, 2010 (Russian).
- [4] O. N. Tretinnikov and Y. Ikada, “Surface characterization of ion-implanted polyethylene,” *Journal of Polymer Science, Part B*, vol. 36, no. 4, pp. 715–725, 1998.

- [5] S. V. Panin, L. À. Kornienko, Ò. Poowadin et al., "Friction and wear of the ultra-high molecular weight polyethylene modified by electron-beam high-energy treatment," *Trenie i Smazka v Machinakh i Mekhanizmakh*, no. 12, pp. 26–31, 2011 (Russian).
- [6] N. K. Myshkin, M. I. Petrokovets, and A. V. Kovalev, "Tribology of polymers: adhesion, friction, wear, and mass-transfer," *Tribology International*, vol. 38, no. 11-12, pp. 910–921, 2005.
- [7] S. M. Lee, S. W. Choi, Y. C. Nho, and H. H. Song, "Modification of microstructures and physical properties of ultra high molecular weight polyethylene by electron beam irradiation," *Journal of Polymer Science, Part B*, vol. 43, no. 21, pp. 3019–3029, 2005.
- [8] A. M. Avilov, V. A. Deryga, and G. F. Popov, "Composite materials formation for orthopaedic implants," *Problems of Atomic Science and Technology*, no. 1, pp. 181–183, 2004.
- [9] J. Zhou and F. Yan, "Improvement of the tribological behavior of ultra-high-molecular-weight polyethylene by incorporation of poly (phenyl p-hydroxyzoate)," *Journal of Applied Polymer Science*, vol. 96, no. 6, pp. 2336–2343, 2005.
- [10] S. M. Kurtz, *The UHMWPE Handbook: Ultra-High Molecular Weight Polyethylene in Total Joint Replacement*, Academic Press, 2004.
- [11] V. E. Panin, S. V. Panin, L. A. Kornienko, S. Vannasri, L. R. Ivanova, and S. V. Shil'ko, "Effect of mechanical activation of ultra-high-molecular-weight polyethylene on its mechanical and triboengineering properties," *Journal of Friction and Wear*, vol. 31, no. 2, pp. 121–127, 2010.
- [12] S. V. Panin, L. A. Kornienko, S. Vannasri et al., "Comparison of the efficiency of modification of SHMPE by nanofibers (C, Al₂O₃) and nanoparticles (Cu, SiO₂) when obtaining antifriction composites," *Journal of Friction and Wear*, vol. 31, no. 6, pp. 460–468, 2010.
- [13] A. Toth, I. Bertoti, E. Szilagy et al., "Surface characterization of ultrahigh molecular weight polyethylene after nitrogen ion implantation," *Surface and Interface Analysis*, vol. 30, pp. 434–438, 2000.
- [14] S. R. Sinha and B. J. Briscoe, *Polymer Tribology*, Imperial college Press, London, UK, 2009.
- [15] J. R. Cooper, D. Dowson, and J. Fisher, "Macroscopic and microscopic wear mechanisms in ultra-high molecular weight polyethylene," *Wear*, vol. 162–164, pp. 378–384, 1993.

Review Article

Nanotechnological Strategies for Biofabrication of Human Organs

**Rodrigo A. Rezende,¹ Fábio de Souza Azevedo,¹
Frederico David Pereira,¹ Vladimir Kasyanov,² Xuejun Wen,³
Jorge Vicente Lopes de Silva,¹ and Vladimir Mironov¹**

¹ *Division of 3D Technologies, Renato Archer Center for Information Technology, 13069-901 Campinas, SP, Brazil*

² *Institute of Anatomy and Anthropology Riga Stradins University, Riga 1007, Latvia*

³ *Department of Bioengineering, Clemson University, Clemson, SC 29425, USA*

Correspondence should be addressed to Rodrigo A. Rezende, rodrigo.rezende@cti.gov.br

Received 6 April 2012; Accepted 4 June 2012

Academic Editor: Guifu Zou

Copyright © 2012 Rodrigo A. Rezende et al. This is an open access article distributed under the Creative Commons Attribution License, which permits unrestricted use, distribution, and reproduction in any medium, provided the original work is properly cited.

Nanotechnology is a rapidly emerging technology dealing with so-called nanomaterials which at least in one dimension have size smaller than 100 nm. One of the most potentially promising applications of nanotechnology is in the area of tissue engineering, including biofabrication of 3D human tissues and organs. This paper focused on demonstrating how nanomaterials with nanolevel size can contribute to development of 3D human tissues and organs which have macrolevel organization. Specific nanomaterials such as nanofibers and nanoparticles are discussed in the context of their application for biofabricating 3D human tissues and organs. Several examples of novel tissue and organ biofabrication technologies based on using novel nanomaterials are presented and their recent limitations are analyzed. A robotic device for fabrication of compliant composite electrospun vascular graft is described. The concept of self-assembling magnetic tissue spheroids as an intermediate structure between nano- and macrolevel organization and building blocks for biofabrication of complex 3D human tissues and organs is introduced. The design of in vivo robotic bioprinter based on this concept and magnetic levitation of tissue spheroids labeled with magnetic nanoparticles is presented. The challenges and future prospects of applying nanomaterials and nanotechnological strategies in organ biofabrication are outlined.

1. Introduction

Biofabrication may be defined as an application principle of engineering and information sciences for automated robotic bioassembly of living 3D human tissue and organs [1–3]. In a more narrow sense, biofabrication is basically a biomedical application of rapid prototyping technology or computer-aided additive fabrication. Although biofabrication is closely related to the more established field of tissue engineering and could even be considered as an integral part of this broader field, biofabrication focuses on and emphasizes using robotic automated engineering approaches in tissue bioassembly. In this context, the recent situation in tissue engineering and biofabrication could be compared to the situation of the

microelectronic industry before and after the introduction of automated robotic technologies for fabricating microchips and microprocessors. The transformation of the labor intensive and still predominantly manual field of tissue engineering into a robotic automated industry needs innovative and creative approaches. The history of technology development teaches us that one of the important principles that contribute to the emergence of a new technology is the creative application of knowledge from other disciplines outside the narrow domain of an existing technology. It is also a well-established fact that robotization and automation help to transform emerging promising technologies into economically feasible industries.

Nanotechnology is one of the most promising technologies of the XXI century. During last decade we witnessed the exponentially growing applications of nanotechnology in the area of tissue engineering [4–12]. Tissue engineering meetings and conferences now regularly include nanotechnology sessions. The number of nanotechnology-related papers in tissue engineering journals and tissue-engineering-related papers in nanotechnology journal has also dramatically increased especially during last decade. Finally, recent reviews on nanotechnology applications in tissue engineering are another confirmation of this trend [13–22]. However, it is not immediately obvious how nanomaterials with nanolevel organization could be used for biofabricating 3D tissue and organs which have macrolevel of organization. In other words, application of nanotechnology does not reduce existing size of human organs. However, the review of already existing and emerging approaches can provide interesting insights on probably the most important and nontrivial question on the interface of nanotechnology and tissue engineering: how employment of nanomaterials can enable biofabrication of human organs on macrolevel?

Thus, this paper is focused on demonstrating how recent advances in application of nanomaterials in tissue engineering can enable robotic and automated biofabrication of 3D human tissues and organs. The most impressive examples of emerging robotic tissue and organ biofabrication devices and related technologies will be presented. Finally, challenges and future prospects of application of nanomaterials in tissue engineering and nanotechnological strategies in organ biofabrication will be outlined.

2. Nanofibers

Over the last two decades, electrospinning has emerged as a relatively simple and scalable nanotechnological method for the generation of nanostructured scaffolds that closely mimic the dimensions of collagen fibrils of ECM. The general aspects of this technology have been reviewed extensively elsewhere [15, 23–25]. We will focus our attention here on the accomplishments and challenges in the utilization of electrospinning technology in the field of vascular tissue engineering.

A broad spectrum of synthetic polymers has been successfully employed in electrospinning. Moreover, electrospinning of natural proteins, such as collagen and elastin, either alone or in combinations, as well as in blends with synthetic polymers, has been reported [23, 26–29]. However, it is naive to believe that imitating the relative compositions of structural proteins, such as collagen and elastin, in natural vascular walls would lead to the development of vascular scaffolds with natural-like biomechanical properties. Indeed, the reported stability of vascular scaffolds created by electrospinning of only natural proteins is still far from desirable levels [27].

It has been demonstrated that electrospinning allows the control of the diameter of the spun fibers and produces nanofibers and scaffolds that imitate the nanostructure of natural ECMs, as confirmed by a more efficient vascular

cell attachment and spreading [27–31]. Although dense nanofiber meshworks provide excellent conditions for cell attachment and the spreading of endothelial cells on the luminal surface of the scaffold [30], they also preclude effective cell migration into the scaffold and thus impede smooth muscle cell migration and the sequential formation of muscular layers inside the vascular tissue engineered constructs.

Electrospinning allows the fabrication of a large variety of nanofibers and nanostructured scaffolds with special characteristics and functionalities (Figure 1). The obtained nanofibers vary in size, shape, and composition: they can be solid, composite, hollow, porous, decorated, helical, and branched. This diversity of possible electrospun nanofibers offers interesting opportunities for the enhancement of vascular-scaffold functionality. For example, the hollow nanofibers and nanoshells created by a coaxial extruder, as well as composite-coated or decorated nanofibers, could provide additional functionalities, including the capacity to release oxygen and to present growth factors and RGD peptides [32]. However, the full potential of electrospinning for the engineering of the full array of nanofibers with different functionalities remains to be explored.

Significant progress has already been made in controlling fiber orientation [33], which is an important step toward the rational design of biomimetic vascular scaffolds. However, in our opinion, controlling only the orientation of the nanofiber will probably not be sufficient. The recapitulation of the entire matrix architecture and the nonlinear biomechanical behavior of the natural vascular wall are equally crucial.

The most exciting breakthrough in electrospinning is the successful one-step rapid fabrication of a vascular scaffold with integrated living cells [34]. In these studies, previously reported methods for the encapsulation of living cells were combined with the electrospinning of nanofibers into one procedure. Further optimization of this electrospinning strategy might offer the greatest potential for rapid biofabrication of vascular-tissue constructs and might eventually eliminate the need for time-consuming and expensive bioreactor-based cell seeding and scaffold cellularization. Despite this impressive progress in vascular tissue engineering with the help of innovative electrospinning technologies, rapid cell integration into scaffolds and their optimal mechanical properties remain the main challenges.

Due to mimicking geometrical size and organization of natural extracellular matrix fibers, the electrospun matrices are ideal substrates for growing and implantation of cell monolayers and can even compete with popular cell sheet technology developed by Teruo Okano group in Japan [35]. Their main advantage is strong potential for functionalization and turning them into drug eluting matrices and scaffold. However, in case of 3D tissue engineering despite the existence of numerous publications and patents on using electrospinning in tissue engineering, we have paradoxical situation. Electrospun matrices are not permissive for cell invasion and seeding and their gross material properties are inferior. Scaffold which is not permissive for effective cell seeding and which has poor material properties is not

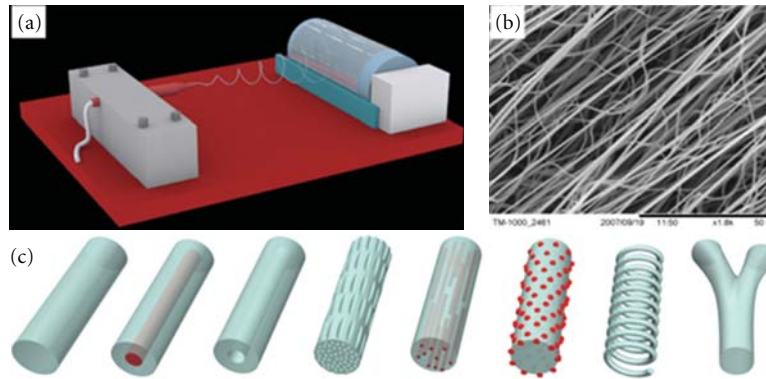


FIGURE 1: Nanofibers: electrospinning nanotechnology. (a) Scheme demonstrating principle of electrospinning technology and electrospinning apparatus; (b) Electrospun tissue engineered scaffold (scanning electron microscopy), (c) Scheme demonstrating different diverse classes of nanofibers that can be obtained by electrospinning. Shown are, from left to right, solid, core-shell, hollow, porous, composite, decorated, spiral, and branched nanofibers [3].

highly desirable scaffold in tissue engineering. These two still unsolved problems are main impediments on the way of successful clinical application of electrospun matrices from nanofibers.

In recent excellent review the first problem was very carefully addressed. It looks like it is possible to create large pore scaffold permissive for cell seeding using additional electrospinning sacrificial polymers or cryoelectrospinning [36].

We have recently developed an elegant solution for the second problem-creating electrospun scaffold with superior natural-like gross material properties using hybrid composite approach. In order to accomplish this, a special fabrication apparatus has been developed which includes a X-Y-Z robot with two nozzles allowing using two different polymers and a rotational collecting cylinder with periodically changeable diameter enabling formation of wavy nanofibers (Figure 2).

Development of an “out-of-shelf” compliant composite electrospun vascular graft will be important development in the application of nanofibers in vascular tissue engineering.

Combination of compliant composite electrospun scaffold with the use of coaxial electrospinning will allow creating also drug eluting vascular graft which in case of clinical success could be considered a very important development in the application of electrospinning in tissue engineering. Finally, another interesting breakthrough development is the combination of electrospinning with rapid prototyping, and developing hybrid composite technology, which allows to dramatic increasing of the bioprinted scaffold properties [37]. Thus, using nanofibers fabricated by the electrospinning method offers realistic opportunities to enhance tissue engineering.

3. Nanoparticles

There are at least several rapidly emerging nanotechnological strategies for using nanoparticles in tissue engineering [13–15, 38–40]. They are mostly based on employing magnetic nanoparticles. The emerging platform technology was

named as magnetic-forces-driven tissue engineering [41]. It is important to indicate that living cells can endocytize magnetic nanoparticles without strong toxic effect (Figure 3).

Moreover, at least one type of superparamagnetic iron oxide nanoparticles known as “Feridex” has been already approved for clinical use as a MRI contrast enhancing agent. First strategy is magnetic-forces-enhanced cell seeding of tissue-engineered scaffold. In certain extent this approach is similar to enhancing cell seeding using centrifugal forces. The principal difference is that driven force is not centrifugal forces but magnetic field forces that translocate cells labeled with magnetic nanoparticles. It has been demonstrated that using this technology dramatically accelerates and improves both speed and quality of cell seeding in porous tissue engineered biodegradable scaffolds [42–44]. One of the most interesting areas of application of magnetic-force-driven cell seeding is vascular tissue engineering. Several groups around the world independently developed rapid magnetic-force-based cell seeding technologies for vascular graft and scaffold [39, 40] summarized and illustrated on Figure 4.

The second strategy is based on using magnetic forces and so-called “nanoshuttle” for biofabrication and bioassembly of tissue spheroids [45]. However, in the reported approach the size of fabricated tissue spheroids is variable. In this context, the reported technology is still inferior as compared to other tissue spheroids biofabrication, but elegant simplicity of this method is attractive and it could be optimized. It is interesting that authors suggested to use their “nanoshuttle” method for magnetic-forces-based biofabrication histological structure of complex geometry [45]. Tissue spheroids fabricated from living cells labeled by magnetic nanoparticles have been used for patterning and assembly of 3D patterns by several groups [46, 47]. The way how magnetic force can be used for layer-by-layer fabrication of a 3D structure has been recently demonstrated by George Whiteside group from Harvard University [48]. Another group from the same University used hydrogel labeled with nanoparticles for successful assembly of a 3D living structure [49]. However, the most advanced published record in using

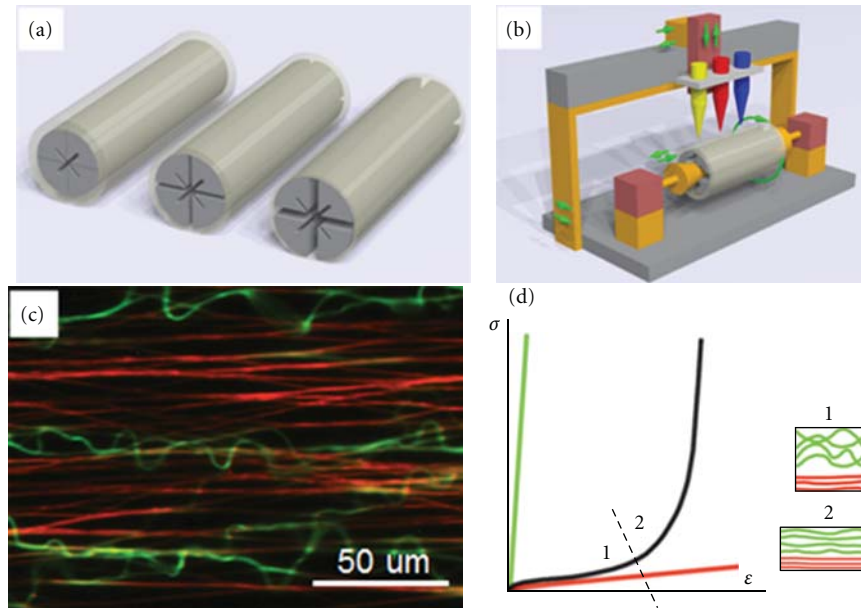


FIGURE 2: Robotic fabricator of compliant composite electrospun vascular graft. (a) Computer-aided design of rotational collecting cylinder with periodically changing external diameter; (b) Computer-aided design of robotic fabricator of compliant composite electrospun vascular graft (c) Confocal microscopy of compliant vascular graft fabricated from wavy (green) and nonwavy nanofibers (red); (d) Scheme explaining biomimetic mechanical behavior of compliant composite electrospun vascular graft.

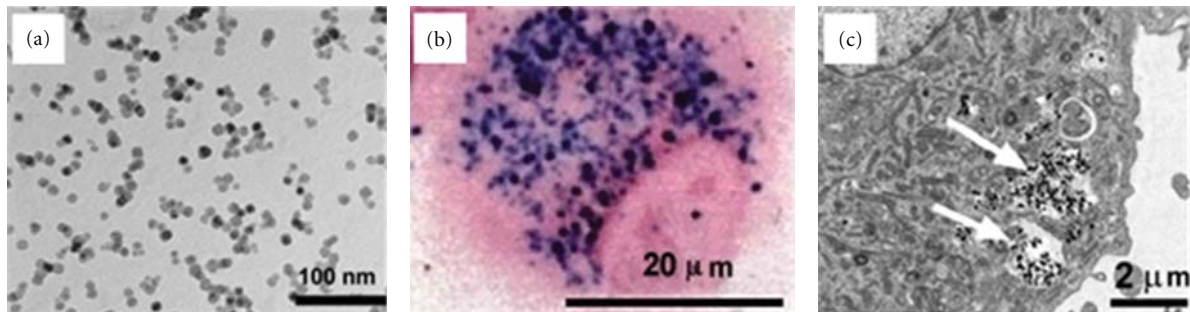


FIGURE 3: Nanoparticles. Labeling of cells with nanoparticles for magnetic-driven tissue engineering [3]: (a) Transmission electron micrograph of a typical population of metallic nanoparticles; (b) Light micrograph of human mesenchymal cells derived from bone marrow, which are capable of vascular lineage differentiation. The cells have been labeled with superparamagnetic iron oxide nanoparticles. Staining with Prussian Blue indicates the presence of nanoparticles inside of cells. (c) Transmission electron micrograph of human endothelial cells that were labeled with nanoparticles. White arrows indicate clusters of nanoparticles that had been endocytosed inside the cell.

nanoparticles for biofabrication of diverse human tissues belongs to members of Japanese group [41] who are pioneers of magnetic-force-driven tissue engineering. These authors, using magnetic forces driven tissue engineering, were able to fabricate functional epithelial, myocardial, skeletal muscle, skin, liver tissue and many other tissues. Finally, there is an emerging third approach which represents probably the most interesting strategy of using nanoparticles in tissue engineering. We are talking about certain attempts of using nanoparticles in bioprinting process [50]. Up to now, these attempts are still limited to incorporating nanoparticles in bioprintable hydrogels [50]. However, as it was proposed in our previous review publication using magnetic force and specially fabricated magnetic tissue spheroids could eventually lead to the development of a bioprinter based on

principles of magnetic levitation [15]. Another interesting approach is a fabrication janus-like tissue spheroids [51], which enables self-directed self-assembly of tissue spheroids in linear, circular, and branched structures (Figure 5).

4. Nanotechnology and Organ Printing

Organ printing is a biomedical variant of rapid prototyping technology or computer-aided robotic layer-by-layer additive biofabrication of 3D human tissues and organs using self-assembling tissue spheroids as building blocks [52–54]. The fundamental basic principle of organ bioprinting technology is the phenomenon of tissue fusion of closely placed tissue spheroids. The tissue fusion process is driven by physical forces such as surface tension and implies

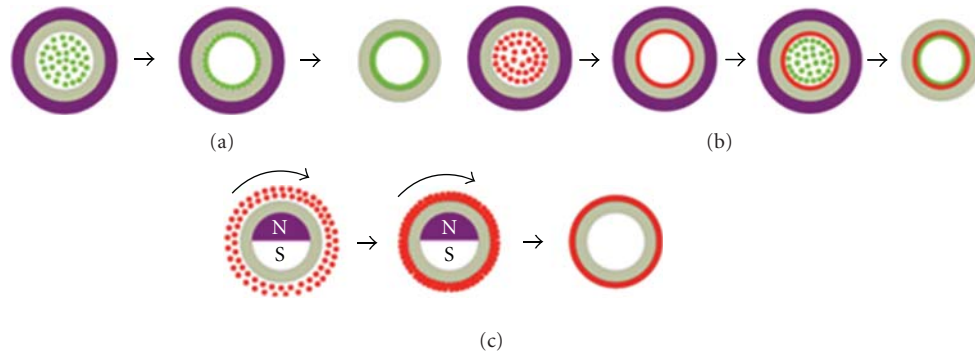


FIGURE 4: Magnetic-forces-driven vascular tissue engineering. The schematic illustrations shown above present three possible variations of magnetic-driven vascular tissue engineering, depending on the cells used and the placement of the vascular scaffold. In the first arrangement (a), the magnet (purple) is placed outside of the vascular scaffold and cells labeled with magnetic nanoparticles (green) are placed into the lumen. The magnet force causes the endothelial cells to adhere to and spread on the luminal surface of the vascular scaffold with the subsequent formation of a continuous endothelial monolayer. The second variation (b) is similar to the previous in that the magnet (purple) is placed outside of the scaffold (grey), but smooth muscle (red) and endothelial cells (green), both labeled with magnetic nanoparticles, are sequentially placed into the lumen for rapid adhesion and cellularization. In the third variation (c), the magnet (purple) is placed inside the vascular scaffold (grey) and smooth muscle cells labeled with magnetic nanoparticles (red) are placed outside of the scaffold. Rotation of the magnet enables the cell attachment with the subsequent formation of a concentric layer of smooth muscle cells on the external surface of the vascular scaffold. Endothelialization of the internal luminal surface can then be achieved as described in first variation.

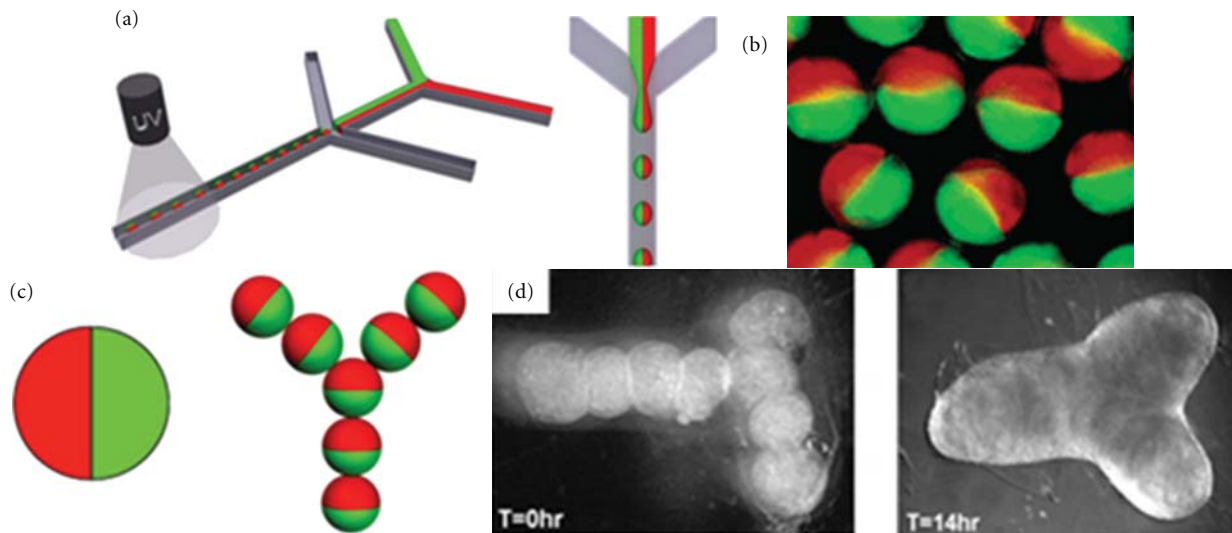


FIGURE 5: Fabrication of janus-like self-assembling tissue spheroids with magnetic nanoparticles. (a) Scheme demonstrating biofabrication of janus-like tissue spheroids using microfluidics [51]; (b) Janus-like spheroids fabricated by microfluidics devices [51]; (c) Scheme demonstrating magnetic-forces-driven self-directed self-assembly of closely placed janus-like magnetic tissue spheroids; (d) Branched structure formed as a result of fusion of closely placed tissue spheroids [52].

viscoelastic-plastic physical nature of tissue spheroids. However, when tissue spheroids under influence of inductive signal differentiate into so-called “osteospheres” or “chondrospheres,” then their material properties also change and their capacities for rapid tissue fusion are dramatically reduced. In order to escape this problem we have designed and developed interlockable miniscaffold or “lockyballs” which can interlock using specially designed “hook” and “lops” mechanism similar to famous Velcro and thus provide desirable material properties for 3D tissue constructs. Lockyballs also can contain encaged tissue spheroids which will still

have capacities for tissue fusion. The opposite is the situation when tissue spheroids are fusing too fast even before the actual bioprinting process. In order to prevent this situation, encapsulation in thin layer of sacrificial hydrogel is desirable. Thus, bioprinter can be loaded with three variant of tissue spheroids: (i) free tissue spheroids; (ii) tissue spheroids encapsulated in hydrogel; and (iii) tissue spheroids encaged into lockyballs or miniscaffold (Figure 6).

Now, if one wants to employ the magnetic levitation principle in the design of a robotic bioprinter for harvesting, translocating and delivery of tissue spheroids then

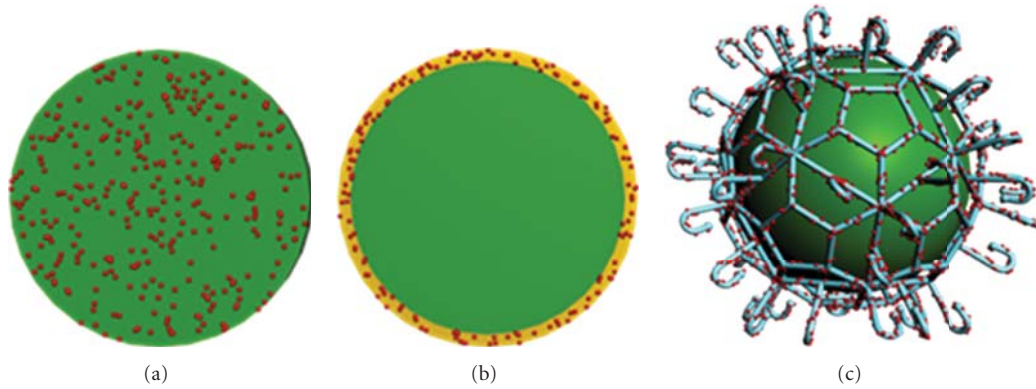


FIGURE 6: Enabling technologies for magnetic levitation of tissue spheroids. Three possible variants of modifications of tissue spheroids making them suitable for magnetic levitation: (a) biofabrication of tissue spheroid from cells labelled with magnetic nanoparticles; (b) encapsulation of tissue spheroid into hydrogel containing magnetic nanoparticles; (c) engaging tissue spheroid in magnetic microscaffolds.

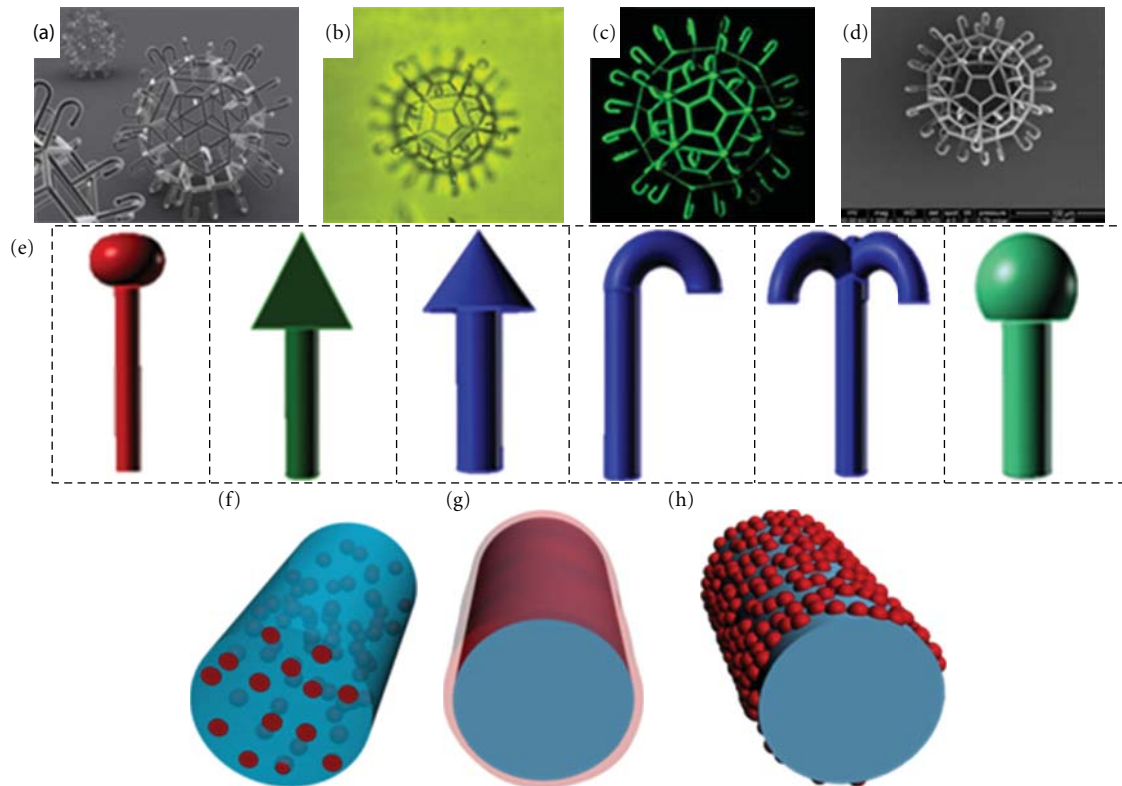


FIGURE 7: “Lockyballs” or interlockable microscaffolds for engaging living tissue spheroids. (a) Computer-aided design of lockyball; (b) Light microscopy of lockyball; (c) Confocal microscopy of lockyball; (d) Scanning electron microscopy of lockyball; (e) Different design variants of lockyball “hooks” which can be used as interlocking mechanism; (f) Section of lockyballs demonstrating magnetic nanoparticles inside; (g) Lockyball with magnetic nanosurface; (h) Section of lockyball demonstrating functionalization with nanoparticles on external surface.

nanotechnology can offer at least three basic approaches: (i) magnetic tissue spheroids could be biofabricated from cells labeled with magnetic nanoparticles; (ii) magnetic tissue spheroids can be fabricated from tissue spheroids encapsulated in hydrogel loaded with magnetic nanoparticles; and, finally, (iii) magnetic tissue spheroids can be fabricated by providing magnetic properties to miniscaffold or lockyballs engaging these tissue spheroids (Figure 7).

At least three different approaches may be adopted to obtain magnetic lockyballs. First, by placing magnetic nanoparticles inside a photosensitive polymer before two photon polymerization steps; second, by coating the lockyballs surface with a magnetic nanosurface; or third, by coating it with immobilized magnetic nanoparticles. All three approaches at least can make lockyballs and tissue spheroids engaged inside them suitable for magnetic levitation (Figure 8).

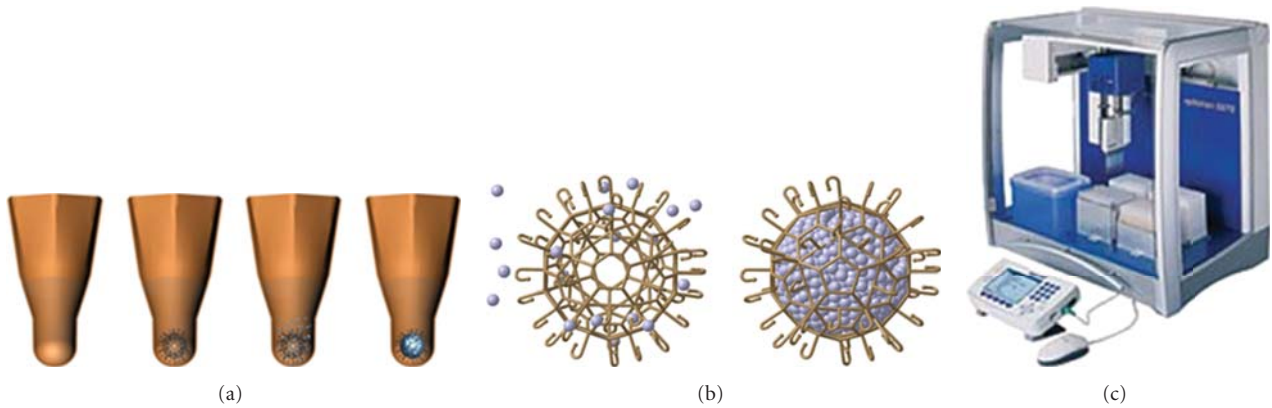


FIGURE 8: Robotic tissue spheroids biofabricator. (a) Scheme demonstrating sequential steps of encasing tissue spheroids in micro scaffold (lockyballs) in molded agarose hydrogel; (b) Scheme demonstrating cell seeding and tissue spheroid formation in lockyballs; (c) Robotic dispenser (Eppendorf, Germany).

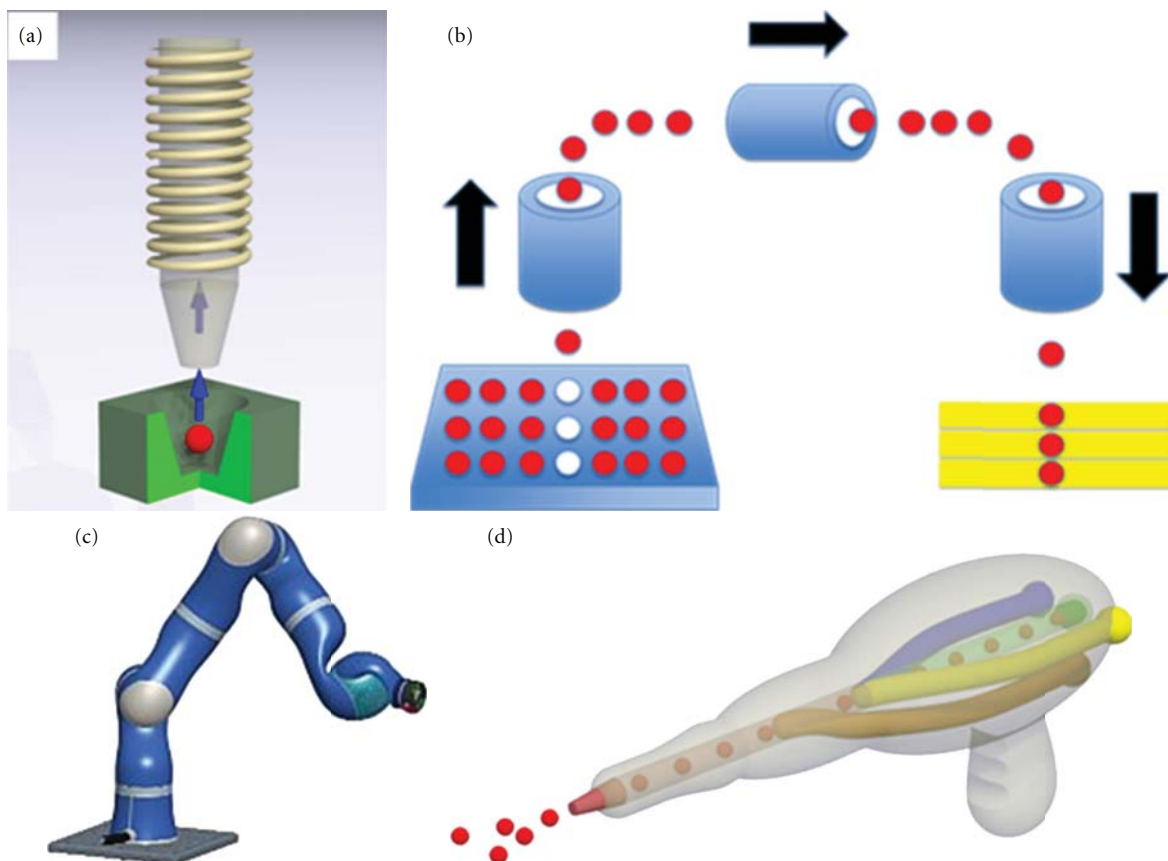


FIGURE 9: Design elements of a clinical robotic bioprinter. (a) Tissue spheroids harvester based on magnetic levitation of tissue spheroids; (b) Principal scheme of clinical robotic bioprinter demonstrating how tissue spheroids can be harvested from multiwells, translocated and dispensed in living tissue using magnetic levitation; (c) Elegant robotic hand developed by group of robotics and mechanotronics at German Aerospace Institute (http://www.dlr.de/rm/en/desktopdefault.aspx/tabid-3803/6175_read-8961/) which can be employed as an essential component in robotic clinical bioprinter for automated nozzle positioning; (d) Computer-aided design of nozzle of clinical robotic bioprinter containing several channels: two channels for fibrinogen and thrombin, one channel for tissue spheroids and additional channel for pressurized air for enabling fibrin hydrogel spraying.

The conceptual design of an *in vivo* robotic bioprinter based on the principle of magnetic levitation is presented on Figure 9. Magnetic forces driven *in vivo* bioprinter must have a magnetic harvesting device (magnetic solenoid) controlled by an X-Y-Z robot, a magnetic translocating device, and a magnetic dispensing nozzle controlled manually or by a robotic hand (Figure 9). The nozzle will include two channels for fibrinogen and thrombin, one or more channels for dispensing tissue spheroids (or different type of tissue spheroids) and one or more channels providing pressurized air which will enable spraying fibrin hydrogel. The potential areas of clinical application of such *in vivo* robotic bioprinter based on magnetic levitation are bioprinting of skin, cartilage and bone. The nanotechnological strategies described above could also be employed for designing more sophisticated bioprinters for bioprinting more complex 3D human tissues and organs such as kidney.

5. Conclusion and Future Perspectives

The research on the interface and integration of nanotechnology and tissue engineering is not just a highly desirable dream or science fiction anymore, but rather a well-established reality or already ongoing and rapidly expanding globally funded project. Nanotechnology found in tissue engineering field one of its most attractive, promising and also socially sounded applications. From another side, tissue engineers, by embracing nanotechnology, dramatically increased their research arsenal, broadening their “toolkit,” and were able to develop several novel impressive bioengineering platform technologies by applying nanomaterials. Thus, it is safe to predict that mutually beneficial collaboration of nanotechnologists and tissue engineers will only continue to grow. Moreover, with time the difference between these two professions will become increasingly semantic.

However, researches on the interface between nanotechnology and tissue engineering are still facing some serious challenges.

The first and most obvious challenge is toxicology of nanomaterials [55]. Although there are several solid researches which established principal safety of certain nanomaterials, the growing public concern about potential toxicity of nanomaterials must be systematically addressed. Thus, biocompatibility of nanomaterials for tissue engineering must be an integral part of the design principles as early as on the stage of project ideation.

The second challenge is functionalization of nanomaterials. Recent advance in designing drug eluting nanofibers using coaxial electrospinning is an excellent example of desirable progress in this direction. Functionalization of nanoparticles and carbon nanotubes is also under way.

The third challenge is design, synthesis, and fabrication of novel nanomaterials with biomimetic properties. This trend is already obvious in the fabrication of nanofibers using electrospinning technology. A similar approach is highly desirable for other forms of nanomaterials employed in tissue engineering. Development of composite nanomaterials is one of the most promising approaches in this direction.

The fourth challenge is standardization of nanomaterials. The standardization on certain stage of development of any emerging technology is a necessary step on the way to industrial product certification. Standardization is especially important in a biomedical application which needs regulatory agencies approval of new products. Finally, certain degree of standardization will enable comparing research results.

The fifth and last (we believe the most important) challenge is a seamless integration of nanomaterials into macrolevel biofabrication technologies. The introduction of nanomaterials will not reduce existing human organs size. Although we already have demonstrated some impressive examples of such integration, it is only the beginning and even more exciting new technology platforms will emerge on the interface between nanotechnology and biofabrication.

In the long term, perspective functional biomimetic nanomaterials can enable regenerative medicine (healing from inside) and thus reduce need for tissue engineering *ex vivo*. Drug eluting electrospun vascular graft is one possible example of this trend. Magnetic-forces-driven minimally-invasive technologies for targeted delivery of bone tissue constructing nanomaterials and stem cells *in vivo* in myocardial infarct area are other interesting examples. Finally, the *in vivo* robotic bioprinter described in this review could transform and reinvent surgical robotics.

Authors' Contribution

J. V. L. Silva and V. Mironov, both senior authors, made equal contribution to this paper.

Acknowledgments

Authors thank Dr. Jan Torgersen, Dr. Aleks Ovsianikov, and Dr. Jürgen Stampfl from the Vienna University of Technology, Vienna, Austria. This work was sponsored by São Paulo Research Foundation (FAPESP), the Brazilian Institute of Biofabrication (INCT-BIOFABRIS), and the National Council for Scientific and Technological Development (CNPq).

References

- [1] V. Mironov, T. Trusk, V. Kasyanov, S. Little, R. Swaja, and R. Markwald, “Biofabrication: a 21st century manufacturing paradigm,” *Biofabrication*, vol. 1, no. 2, Article ID 022001, 2009.
- [2] F. Guillemot, V. Mironov, and M. Nakamura, “Bioprinting is coming of age: report from the International Conference on Bioprinting and Biofabrication in Bordeaux (3B'09),” *Biofabrication*, vol. 2, no. 1, Article ID 010201, 2010.
- [3] V. Mironov, V. Kasyanov, and R. R. Markwald, “Organ printing: from bioprinter to organ biofabrication line,” *Current Opinion in Biotechnology*, vol. 22, no. 5, pp. 667–673, 2011.
- [4] D. Khang, J. Carpenter, Y. W. Chun, R. Pareta, and T. J. Webster, “Nanotechnology for regenerative medicine,” *Biomedical Microdevices*, vol. 12, no. 4, pp. 575–587, 2010.

- [5] M. C. Rpecp, "Nanotechnology: convergence with modern biology and medicine," *Current Opinion in Biotechnology*, vol. 14, no. 3, pp. 337–346, 2003.
- [6] Š. Kubinová and E. Syková, "Nanotechnologies in regenerative medicine," *Minimally Invasive Therapy and Allied Technologies*, vol. 19, no. 3, pp. 144–156, 2010.
- [7] S. Verma, A. J. Domb, and N. Kumar, "Nanomaterials for regenerative medicine," *Nanomedicine*, vol. 6, no. 1, pp. 157–181, 2011.
- [8] E. Engel, A. Michiardi, M. Navarro, D. Lacroix, and J. A. Planell, "Nanotechnology in regenerative medicine: the materials side," *Trends in Biotechnology*, vol. 26, no. 1, pp. 39–47, 2008.
- [9] H. F. Tibbals, *Medical Nanotechnology and Nanomedicine*, Perspectives in Nanotechnology, CRC Press, 2010.
- [10] M. Navarro and J. A. Planell, *Nanotechnology in Regenerative Medicine: Methods and Protocols*, Methods in Molecular Biology, Humana Press, 2012.
- [11] C. T. Laurencin and L. S. Nair, *Nanotechnology and Tissue Engineering: The Scaffold*, CRC Press, 2008.
- [12] K. Papat, *Nanotechnology in Tissue Engineering and Regenerative Medicine*, CRC Press, 2010.
- [13] T. Dvir, B. P. Timko, D. S. Kohane, and R. Langer, "Nanotechnological strategies for engineering complex tissues," *Nature Nanotechnology*, vol. 6, no. 1, pp. 13–22, 2011.
- [14] H. Park, C. Cannizzaro, G. Vunjak-Novakovic, R. Langer, C. A. Vacanti, and O. C. Farokhzad, "Nanofabrication and micro-fabrication of functional materials for tissue engineering," *Tissue Engineering*, vol. 13, no. 8, pp. 1867–1877, 2007.
- [15] V. Mironov, V. Kasyanov, and R. R. Markwald, "Nanotechnology in vascular tissue engineering: from nanoscaffolding towards rapid vessel biofabrication," *Trends in Biotechnology*, vol. 26, no. 6, pp. 338–344, 2008.
- [16] B. Zhang, Y. Xiao, A. Hsieh, N. Thavandiran, and M. Radisic, "Micro- and nanotechnology in cardiovascular tissue engineering," *Nanotechnology*, vol. 22, no. 49, Article ID 494003, 2011.
- [17] M. Perán, M. A. García, E. López-Ruiz et al., "Functionalized nanostructures with application in regenerative medicine," *International Journal of Molecular Sciences*, vol. 13, no. 3, pp. 3847–3886, 2012.
- [18] B. S. Harrison and A. Atala, "Carbon nanotube applications for tissue engineering," *Biomaterials*, vol. 28, no. 2, pp. 344–353, 2007.
- [19] S. D. McCullen, S. Ramaswamy, L. I. Clarke, and R. E. Gorga, "Nanofibrous composites for tissue engineering applications," *Nanomedicine and Nanobiotechnology*, vol. 1, no. 4, pp. 369–390, 2009.
- [20] V. Lionetti, M. Cecchini, and C. Ventura, "Nanomechanics to drive stem cells in injured tissues: insights from current research and future perspectives," *Stem Cells and Development*, vol. 20, no. 4, pp. 561–568, 2011.
- [21] C. M. Kelleher and J. P. Vacanti, "Engineering extracellular matrix through nanotechnology," *Journal of the Royal Society Interface*, vol. 7, supplement 6, pp. S717–S729, 2010.
- [22] J. Thomas Webster, *Nanotechnology For the Regeneration of Hard and Soft Tissues*, World Scientific Publishing Company, 2007.
- [23] C. P. Barnes, S. A. Sell, E. D. Boland, D. G. Simpson, and G. L. Bowlin, "Nanofiber technology: designing the next generation of tissue engineering scaffolds," *Advanced Drug Delivery Reviews*, vol. 59, no. 14, pp. 1413–1433, 2007.
- [24] R. Murugan, Z. M. Huang, F. Yang, and S. Ramakrishna, "Nanofibrous scaffold engineering using electrospinning," *Journal of Nanoscience and Nanotechnology*, vol. 7, no. 12, pp. 4595–4603, 2007.
- [25] R. Murugan and S. Ramakrishna, "Nano-featured scaffolds for tissue engineering: a review of spinning methodologies," *Tissue Engineering*, vol. 12, no. 3, pp. 435–447, 2006.
- [26] E. D. Boland, J. A. Matthews, K. J. Pawlowski, D. G. Simpson, G. E. Wnek, and G. L. Bowlin, "Electrospinning collagen and elastin: preliminary vascular tissue engineering," *Frontiers in Bioscience*, vol. 9, pp. 1422–1432, 2004.
- [27] J. L. Sang, J. J. Yoo, G. J. Lim, A. Atala, and J. Stitzel, "In vitro evaluation of electrospun nanofiber scaffolds for vascular graft application," *Journal of Biomedical Materials Research*, vol. 83, no. 4, pp. 999–1008, 2007.
- [28] M. Li, M. J. Mondrinos, M. R. Gandhi, F. K. Ko, A. S. Weiss, and P. I. Leikes, "Electrospun protein fibers as matrices for tissue engineering," *Biomaterials*, vol. 26, no. 30, pp. 5999–6008, 2005.
- [29] J. Stitzel, J. Liu, S. J. Lee et al., "Controlled fabrication of a biological vascular substitute," *Biomaterials*, vol. 27, no. 7, pp. 1088–1094, 2006.
- [30] B. Bondar, S. Fuchs, A. Motta, C. Migliaresi, and C. J. Kirkpatrick, "Functionality of endothelial cells on silk fibroin nets: comparative study of micro- and nanometric fibre size," *Biomaterials*, vol. 29, no. 5, pp. 561–572, 2008.
- [31] W. He, T. Yong, W. E. Teo, Z. Ma, and S. Ramakrishna, "Fabrication and endothelialization of collagen-blended biodegradable polymer nanofibers: potential vascular graft for blood vessel tissue engineering," *Tissue Engineering*, vol. 11, no. 9-10, pp. 1574–1588, 2005.
- [32] Y. Z. Zhang, X. Wang, Y. Feng, J. Li, C. T. Lim, and S. Ramakrishna, "Coaxial electrospinning of (fluorescein isothiocyanate-conjugated bovine serum albumin)-encapsulated poly(ϵ -caprolactone) nanofibers for sustained release," *Biomacromolecules*, vol. 7, no. 4, pp. 1049–1057, 2006.
- [33] R. Murugan and S. Ramakrishna, "Design strategies of tissue engineering scaffolds with controlled fiber orientation," *Tissue Engineering*, vol. 13, no. 8, pp. 1845–1866, 2007.
- [34] J. J. Stankus, J. Guan, K. Fujimoto, and W. R. Wagner, "Microintegrating smooth muscle cells into a biodegradable, elastomeric fiber matrix," *Biomaterials*, vol. 27, no. 5, pp. 735–744, 2006.
- [35] I. E. Hannachi, M. Yamato, and T. Okano, "Cell sheet technology and cell patterning for biofabrication," *Biofabrication*, vol. 1, no. 2, Article ID 022002, 2009.
- [36] S. Zhong, Y. Zhang, and C. T. Lim, "Fabrication of large pores in electrospun nanofibrous scaffolds for cellular infiltration: a review," *Tissue Engineering Part B*, vol. 18, no. 2, pp. 77–87, 2012.
- [37] W. Schuurman, V. Khristov, M. W. Pot, P. R. van Weeren, W. J. Dhert, and J. Malda, "Bioprinting of hybrid tissue constructs with tailorable mechanical properties," *Biofabrication*, vol. 3, no. 2, Article ID 021001, 2011.
- [38] J. Dobson, "Remote control of cellular behaviour with magnetic nanoparticles," *Nature Nanotechnology*, vol. 3, no. 3, pp. 139–143, 2008.
- [39] K. Shimizu, A. Ito, M. Arinobe et al., "Effective cell-seeding technique using magnetite nanoparticles and magnetic force onto decellularized blood vessels for vascular tissue engineering," *Journal of Bioscience and Bioengineering*, vol. 103, no. 5, pp. 472–478, 2007.
- [40] A. Ito, K. Ino, M. Hayashida et al., "Novel methodology for fabrication of tissue-engineered tubular constructs using magnetite nanoparticles and magnetic force," *Tissue Engineering*, vol. 11, no. 9-10, pp. 1553–1561, 2005.

- [41] A. Ito and M. Kamihira, "Tissue engineering using magnetite nanoparticles," *Progress in Molecular Biology and Translational Science*, vol. 104, pp. 355–395, 2011.
- [42] P. Thevenot, S. Sohaebuddin, N. Poudyal, J. Ping Liu, and L. Tang, "Magnetic nanoparticles to enhance cell seeding and distribution in tissue engineering scaffolds," in *Proceedings of the 8th IEEE Conference on Nanotechnology (IEEE-NANO '08)*, pp. 646–649, August 2008.
- [43] T. Sasaki, N. Iwasaki, K. Kohno et al., "Magnetic nanoparticles for improving cell invasion in tissue engineering," *Journal of Biomedical Materials Research*, vol. 86, no. 4, pp. 969–978, 2008.
- [44] K. Shimizu, A. Ito, and H. Honda, "Mag-seeding of rat bone marrow stromal cells into porous hydroxyapatite scaffolds for bone tissue engineering," *Journal of Bioscience and Bioengineering*, vol. 104, no. 3, pp. 171–177, 2007.
- [45] G. R. Souza, J. R. Molina, R. M. Raphael et al., "Three-dimensional tissue culture based on magnetic cell levitation," *Nature Nanotechnology*, vol. 5, no. 4, pp. 291–296, 2010.
- [46] R. Z. Lin, W. C. Chu, C. C. Chiang, C. H. Lai, and H. Y. Chang, "Magnetic reconstruction of three-dimensional tissues from multicellular spheroids," *Tissue Engineering Part C*, vol. 14, no. 3, pp. 197–205, 2008.
- [47] V. H. B. Ho, K. H. Müller, A. Barcza, R. Chen, and N. K. H. Slater, "Generation and manipulation of magnetic multicellular spheroids," *Biomaterials*, vol. 31, no. 11, pp. 3095–3102, 2010.
- [48] K. A. Mirica, F. Ilievski, A. K. Ellerbee, S. S. Shevkoplyas, and G. M. Whitesides, "Using magnetic levitation for three dimensional self-assembly," *Advanced Materials*, vol. 23, no. 36, pp. 4134–4140, 2011.
- [49] F. Xu, C. A. Wu, V. Rengarajan et al., "Three-dimensional magnetic assembly of microscale hydrogels," *Advanced Materials*, vol. 23, no. 37, pp. 4254–4260, 2011.
- [50] K. Buyukhatipoglu, R. Chang, W. Sun, and A. M. Clyne, "Bioprinted nanoparticles for tissue engineering applications," *Tissue Engineering Part C*, vol. 16, no. 4, pp. 631–642, 2010.
- [51] R. F. Shepherd, J. C. Conrad, S. K. Rhodes et al., "Microfluidic assembly of homogeneous and janus colloid-filled hydrogel granules," *Langmuir*, vol. 22, no. 21, pp. 8618–8622, 2006.
- [52] V. Mironov, R. P. Visconti, V. Kasyanov, G. Forgacs, C. J. Drake, and R. R. Markwald, "Organ printing: tissue spheroids as building blocks," *Biomaterials*, vol. 30, no. 12, pp. 2164–2174, 2009.
- [53] V. Mironov, V. Kasyanov, C. Drake, and R. R. Markwald, "Organ printing: promises and challenges," *Regenerative Medicine*, vol. 3, no. 1, pp. 93–103, 2008.
- [54] V. Mironov, T. Boland, T. Trusk, G. Forgacs, and R. R. Markwald, "Organ printing: computer-aided jet-based 3D tissue engineering," *Trends in Biotechnology*, vol. 21, no. 4, pp. 157–161, 2003.
- [55] C. S. Yah, G. S. Simate, and S. E. Iyuke, "Review: nanoparticles toxicity and their routes of exposures," *Pakistan Journal of Pharmaceutical Sciences*, vol. 25, no. 2, pp. 477–491, 2012.

Research Article

The Optimum Dispersion of Carbon Nanotubes for Epoxy Nanocomposites: Evolution of the Particle Size Distribution by Ultrasonic Treatment

Tomas Roll Frømyr,^{1,2} Finn Knut Hansen,^{1,2} and Torbjørn Olsen¹

¹Norwegian Defence Research Establishment, P.O. Box 25, 2027 Kjeller, Norway

²Department of Chemistry, University of Oslo, P.O. Box 1033, Blindern, 0315 Oslo, Norway

Correspondence should be addressed to Finn Knut Hansen, f.k.hansen@kjemi.uio.no

Received 9 March 2012; Accepted 23 April 2012

Academic Editor: Huisheng Peng

Copyright © 2012 Tomas Roll Frømyr et al. This is an open access article distributed under the Creative Commons Attribution License, which permits unrestricted use, distribution, and reproduction in any medium, provided the original work is properly cited.

The ultrasonic dispersion of multiwalled carbon nanotube (MWCNT) suspensions was assessed by studying the differential sedimentation of the particles in an acid anhydride often employed as a curing agent for epoxy resins. The particle size distributions were characterized by the means of a disc centrifuge, and the effect of dispersion time, power density, and total energy input, for both bath and circulation probe ultrasonic dispersing equipment was investigated. The mass of freely suspended MWCNTs relative to agglomerated MWCNTs was estimated as a measure of the quality of the dispersions, and the results showed that this ratio followed a power law scaling with the energy dissipated in the sonication treatment. If the sonication power level was too high, sonochemical degradation of the curing agent could occur. The mean agglomerate MWCNT size distribution was estimated, and the fragmentation of the agglomerates was modeled by means of fragmentation theory. Indications of both rupture and erosion fragmentation processes for the MWCNT agglomerates were observed.

1. Introduction

Carbon nanotubes (CNTs) have been studied extensively since the landmark paper by Iijima in 1991 [1]. The exceptional mechanical, thermal, and electrical properties combined with the high aspect ratio and large surface area have made CNTs a promising material for a wide range of applications. However, there are major challenges to overcome in order to utilize these properties. There are several different production methods for CNTs, such as laser ablation, electrolysis, electric arc discharge, sonochemistry, chemical vapour deposition, and catalyst arrays [2]. These methods produce different CNTs with different chemical structure, length, diameter, defects, and varying types and degrees of contamination [3]. This will affect physical properties, such as differences in nanotube curvature, reactivity, failure mechanisms, mechanical properties, and surface interactions.

Although the mechanical properties of carbon nanotubes are superior to, for example, continuous and short

carbon fibres, problems with dispersion, load transfer, and alignment in a polymer matrix have, so far, not led to CNT composites being a competitive alternative to these more traditional materials. Carbon-fibre-reinforced polymers (CFRPs) are more suitable for use in structural composites. The primary role of a polymer matrix is to hold the fibres in place and transfer load, but there are modes of deformation where an increase in the mechanical properties of the polymer matrix is of importance. In this context, CNTs have been considered as a reinforcing material with a random orientation similar to conventional short fibre reinforced composites [4–6]. However, to achieve any form of reinforcement effect, processing challenges such as poor wettability, heavy aggregation, and viscosity build up in dispersions of even low concentrations must be overcome [7]. In order to obtain improvement of the composites mechanical properties, the interfacial shear strength between the CNTs and polymer matrix should be maximized to transfer the load to the reinforcing particles [8]. Studies have shown

that the load transfer between individual nanotubes is low [9], probably because of slippage between them, and that larger agglomerates have poor mechanical properties [10]. To achieve good dispersions, with a minimal amount of agglomerates, is therefore of vital importance to minimize these effects and to optimize the CNT-matrix interface for improved load transfer.

Several different dispersion methods have been suggested for carbon nanotubes. In high viscosity systems, such as epoxy resins, calendaring, milling, grinding, high speed shear mixing, high-pressure homogenization, and sonication have been used [11, 12]. Sonication, which is the most commonly reported method, is a process where a transducer is used to irradiate a liquid with a high pressure sound field with the result of growth of cavities which implode with a violent and localised release of energy. In a bath-type sonicator the sound field is close to uniform, and the treatment of the suspension is equally homogenous. Unfortunately, the sound pressure in a bath sonicator is low compared to a horn, that is, tip sonicator. Tip sonicators can generate large sound pressures by connecting the transducer to a resonating metal rod. A high-intensity sound field is generated at the end of the rod, inducing mixing by turbulent fluxes and acoustic streaming in suspensions [13]. Furthermore, ultrasonic cavitation can also produce high-energy inter-particle collisions and particle surface damage caused by implosion shock waves and micro jets [14].

These effects lead to the fragmentation of agglomerates in the suspension [15], and are quite effective at treating smaller volumes of low viscosity liquids. However, because of the localization of the high-energy sound field around the tip of the sonicator, stirring is normally needed for larger volumes to ensure a homogenous treatment of the entire sample. Dispersion in higher-viscosity liquids, such as polymers or prepolymers, is a more complex problem, in that the viscosity will also affect the cavitation of the liquid [13, 16]. One way to overcome this problem is to dilute the suspension with a liquid of lower viscosity; another way is to predisperse the particles in another liquid before mixing with the high-viscosity liquid [2, 17]. A typical problem with this approach is how to completely remove the excess solvent and how to avoid reagglomeration of CNTs during this removal. In composite materials production, a low molecular weight inert liquid is undesirable, because solvent residues may act as a softener in the matrix. Another processing route is, at least for low to medium viscosity systems, to use a flow cell and direct the flow of the suspension through the high-intensity sound field at the sonicator tip. Flow cells are available as standard equipment for most high power lab sonicators.

Dispersion, purification, and functionalization of carbon nanotubes have been investigated extensively. Characterization of the final dispersion is important, because the procedures developed for one type of CNT may be inappropriate for another. Common characterization techniques have been difficult to carry out on CNT suspensions, and the results are often ambiguous. Electrozone, light scattering, and different types of microscopy/image analysis methods are the main techniques for particle sizing in this size range, but they all have significant drawbacks. The electrozone method works

well for insulating particles, but conducting nanotube poses problems. In addition, the interpretation of the signal for nonspherical particles is also a challenge. Flow particle image analysis (FPIA) has gained significant popularity in recent years because of the advances in electronics and computing power. However, single CNTs cannot be resolved by this method. Electron microscopy with image analysis works well in the whole size range, but samples must be deposited on a suitable surface and dried. This sample preparation may change the state of dispersion in the sample. The method is also very laborious, and statistically reliable data are difficult to obtain for very wide size distributions.

Static and/or dynamic light scattering (DLS) methods translate angular- and/or time-resolved light scattering to particle size distributions (PSD) with very good results for more or less monodispersed spherical particles. For CNTs, light-scattering theory for high-aspect ratio particles must be used to get reliable results [18, 19]. In addition, there are serious challenges with LS techniques when the particle distribution is wide, as is often the case with suspensions of heavy-agglomerated carbon nanotubes. Schaefer and Justice [20] used scattering techniques such as small-angle X-ray scattering (SAXS) and small-angle neutron scattering (SANS) along with ultra-small-angle X-ray scattering (USAXS) and ultra-small-angle neutron scattering (USANS) and correlated this to conventional light scattering. Advances in USANS in recent years have increased the signal-to-noise ratio significantly and made USANS particularly interesting. Still, both small-angle X-ray and neutron scattering demand specialized facilities and are hardly routine techniques. The inherent problem of scattering techniques is that spatial averaging leads to a loss of information. In broad and multimodal systems, the difference between real PSDs and data from scattering experiments can be significant. By using supporting optical and electron imaging techniques, model assumptions about the real PSD can be made. With these assumptions, the angular scattering intensities can be fitted to extract useful information about the sample mass distribution. Two problems arise: (1) sample preparation for imaging may drastically change the distribution, making the model assumptions needed for the scattering experiments erroneous, and (2) the sensitivity to changes in the PSD is low for broad and multimodal distributions, because the scattering efficiency changes significantly with size. Schaefer and Justice have partly, and cleverly, addressed problem number 2 by using data from different scattering techniques to study dispersions of carbon nanotubes. However, only average particle size ranges are discussed, because scattering techniques lack the resolution needed to construct a continuous PSD for dispersions of CNTs. Only coarse estimates of the degree of dispersion are possible, and the size and shape evolution of the submicron CNT agglomerate size distribution is not possible. Kim et al. [21] have shown that DLS can be used in conjunction with differential scanning calorimetry to assess the quality of dispersion in CNT-epoxy composites.

Different sedimentation techniques are known to be well suited for addressing the problem of wide size distributions. Ultracentrifugation with subsequent measurement of UV/vis transmittance of the suspension has been used to assess the

quality of dispersion [22], but time-resolved measurements of the light transmittance are necessary to obtain information of particle size distributions. Such information is available with an analytical centrifuge, where the transmittance measurements can be done in real time, while the sample is spinning [23]. Pegel et al. and others [12, 24–26] have shown that this technique can be applied to CNT suspensions. A more direct determination of the particle size distribution of CNT suspensions is *differential sedimentation particle size analysis* (DCP). This is a classical sizing technique which can be used to determine high-resolution size distribution data [27], and the most common instrument for this purpose is the analytic disk centrifuge (DCF). In this instrument, the particles settle in a liquid in a centrifugal field within a hollow disk. A small sample is deposited on the liquid surface, and the sedimentation time using a detector at the outer rim of the disc is recorded. Because larger particles have a shorter sedimentation time than smaller particles, the inherent size fractionation makes this method well suitable for wide distributions of particles with varying geometry. Recently, this technique has received attention for the analysis of CNT dispersions. The group of Nadler et al. [28] have shown the suitability of DCP in analysing dispersions of CNTs, and they have used the technique to compare the effectiveness of a bath sonicator with a three-roll mill. Typical particle size distributions show a bimodal shape with a mass fraction of free unentangled nanotubes and another mass fraction of entangled agglomerated CNTs [29]. In the work of Nadler et al., the separation of nanotubes from agglomerates was seen as an exfoliation process, and the mass percentage of exfoliated nanotubes was defined as the *degree of exfoliation* and determined directly from PSD data.

In this investigation we have studied the effects of sonication on the dispersion of multiwalled carbon nanotubes (MWCNTs) in an epoxy hardener. The advantage of this scheme is that the dispersion can be added directly to an epoxy resin, and cast without any solvent removal, to prepare nanoenforced epoxy composites. In order to stabilise the dispersions, a polymer stabiliser is added and care has been taken to treat the samples with reproducible homogenous sonication. The dispersions have been characterized using DCF and scanning electron microscopy (SEM).

2. Experimental

2.1. Materials. Multiwalled carbon nanotubes made by Arkema, Graphistrength C100, were obtained from Sigma-Aldrich. These nanotubes are made by catalytic chemical vapour deposition (CVD). According to the supplier, the carbon content is above 90% (w/w) and metallic impurities were below 10% (w/w). The outer diameter was 10–15 nm, and the inner diameter was 2–6 nm. The length range was 0.1–10 μm , and the wall thickness was reported to be 5–15 graphene layers. SEM images revealed that the supplied material consisted of agglomerated, highly entangled nanotubes, which is normal for CNTs produced by CVD. Moreover, the nanotubes had large curvatures, probably because of defects or a low degree of graphitization.

2.2. Dispersion. MWCNTs were dispersed in methyl tetrahydrophthalic anhydride (MTHPA, Aradur 917, Huntsman). MTHPA is a versatile epoxy curing agent that gives a long pot life and good mechanical properties with a suitable epoxy resin. It is a liquid with a relatively low viscosity at room temperature (50–100 mPas at 25°C), allowing for solvent free sonication with CNTs. Amine-based curing agents were also considered, as several of them exhibit low viscosity and do not react with water. Unfortunately, the mixing ratio between epoxy resin and amines is normally quite high, whereas MTHPA is typically mixed with epoxy resins in ratios close to 1:1. A lower-weight fraction of CNTs in the MTHPA curing agent is needed to reach a certain loading level in the cured epoxy, compared with amine-curing agents. Disperbyk 2150 (D 2150, Byk additives) was used as dispersing agent for the CNTs in MTHPA. D 2150 is a “solution of a block-copolymer with basic pigment affinic groups” according to the manufacturer. Supposedly, it is well suited for carbon particles in organic liquids, and has been used successfully for CNTs [28, 30, 31].

2.3. Ultrasonication. First, 3% (w/w) of D 2150 was dissolved in MTHPA, then 1% (w/w) of CNTs was added. Sonication was performed in either a bath ultrasonicator (Bandelin Sonorex Digital 10P, 352 kHz, 480 W) or a horn type ultrasonicator (Branson Digital Sonifier S-450D, 25 kHz, 400 W) with a flow cell attachment with a cooling jacket. A peristaltic pump (Watson Marlow 503U) with silicon tubing (8 mm outer diameter, 4.8 mm inner diameter, Watson Marlow) was used to generate the flow through the cell.

With the horn sonicator, both the effect of time and intensity of the sonication could be investigated. The energy delivered by the horn sonicator was controlled by changing the amplitude at the tip of the resonating horn. The sonicator control unit varies the power delivered to keep the oscillation of the horn tip at constant amplitude. Suspensions were run in a closed loop at different horn tip amplitudes, given as a percentage of the maximum tip amplitude of 145 μm . It was possible to operate the transducer at amplitudes up to 70% of the maximum value. The cooling jacket was water-cooled and held at 20°C. The temperature of the dispersion rose during sonication, but the maximum recorded temperature inside the flow cell was always below 50°C.

The bath sonicator, on the other hand, was run at maximum power in all experiments, since the intensity is low even at the 100% amplitude setting. The water level was kept at the recommended fill level, and the suspensions were completely immersed in the bath. The temperature equilibrated at approximately 50°C during bath sonication.

2.4. Characterization. The dispersions were characterised in a disc centrifuge (DCF) (DC24000, CPS instruments Inc.). The disc centrifuge operates by the principles of differential sedimentation, and a solution with a density gradient is needed for stable operation. A 5–15% (v/v) gradient of Halocarbon 1.8 (Solvadis) in methyl isobutyl ketone (MIBK) (>99% Merck) was created with a linear density gradient former (Beckmann) before each measurement.

The density gradient showed excellent baseline stability over several hours. The MTHPA dispersions were diluted 1:20 in MIBK, that is, 0.05% (w/w) CNT, and sonicated one minute in the bath sonicator immediately before analysis. 0.1 mL of the sample was injected and the DCF was run at 24000 rpm.

The disc centrifuge uses a detector with a 405 nm light source, and calculates the particle concentration from the transmittance of the light source. From (1), the turbidity (τ) is a function of the number of particles (N) in the light path, the particle's geometric cross-section (A), and the light extinction efficiency (Q_{ext})

$$\tau = NAQ_{\text{ext}}. \quad (1)$$

Both light absorption and elastic scattering are functions of both the particle diameter and its complex refractive index [32] and are accounted for in the term Q_{ext} . Given the refractive index, the instrument calculates Q_{ext} as a function of the particle size, assuming spherical particles. It then calculates the fractional mass distribution as a function of the particle size from the detector signal. Integrating the fractional mass, W_D , for a given size range gives the total particle mass within that range. The apparent Stokes equivalent spherical diameter, D_{ST} , of the particles is calculated from the sedimentation time. It is the equivalent diameter of a hard sphere with the same density, having the same sedimentation time as the measured particles. The resulting particle size distribution is a plot of W_D as a function of D_{ST} .

Drops of the diluted dispersions were also deposited on silicon wafers and dried. Electron micrographs of the surfaces were taken at low acceleration voltages in a field emission scanning electron microscope (Hitachi SU-6600).

2.5. Thermogravimetric Analysis. To check for possible chemical reactions between the nanotubes and the other components in the dispersion or for excessive damage of the CNTs [33, 34], thermogravimetric analysis (TGA) was run on a TGA2950 Hi-Res instrument (TA instruments). A lowered oxidation onset temperature would indicate degradation of the nanotubes [35]. Prior to the analysis solvent was removed from the suspension by the following cleaning procedure: 1 g of suspension was diluted with 35 mL MIBK, then it was run for 1 min in the ultrasonic bath, and finally centrifuged, for 2 h at 30000 rpm (WX Ultra 80, Sorvall). The precipitate was dried in a vacuum oven at 60°C overnight before it was diluted once more, centrifuged, and dried, all under the same conditions. Approximately 5 mg of sample was deposited in a platinum cup and heated at 5°C/min in dynamic rate Hi-Res mode [36], where the heating rate is slowed down during significant changes in mass. The resolution is enhanced compared to constant heating at the same rate. Compressed air (AGA) at 100 mL/min was used as purge gas. The components of the suspension were analysed separately as a reference. No sample preparation was done prior to the TGA with these samples.

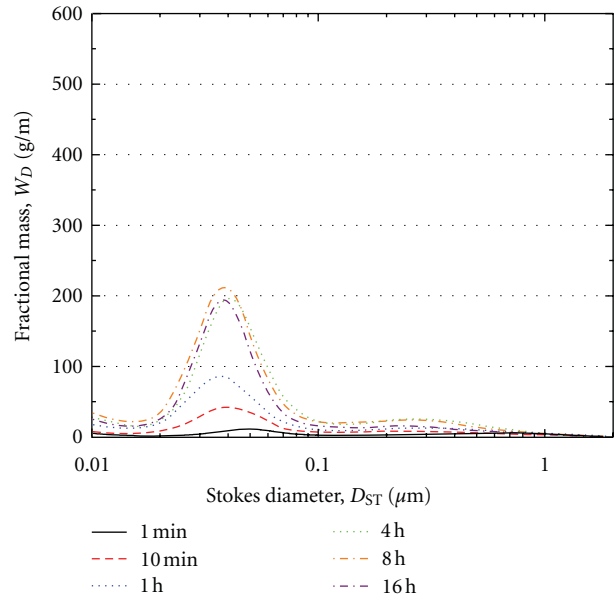


FIGURE 1: Particle size distributions of Arkema CNTs with increasing sonication time in an ultrasonic bath.

3. Results and Discussion

Broad bimodal particle size distributions were observed for all dispersions of CNTs. The distinct peaks in the distributions between 20 nm and 100 nm, shown in Figure 1, are attributed to the free, fully dispersed, that is, exfoliated, carbon nanotubes. The mass fractions above 100 nm are attributed to agglomerates of CNTs. This is in agreement with the previous observations of Nadler et al. [28].

There are indications of a mass fraction below 20 nm in the PSDs for the Arkema CNTs. Care must, however, be taken when interpreting data in this size range, as this signal may be an artefact due to drift in the baseline. To calculate the amount of particles in the suspension, the turbidity is divided by the light extinction efficiency, Q_{ext} , which approaches zero with decreasing particle size for small particles in the Rayleigh regime. A small drift in the turbidity baseline can occur, even though the baseline showed excellent stability throughout the experiments. The instrument calculates an initial linear baseline drift and compensates for this, but any change in the drift during an experiment remains uncorrected. Degradation of the density gradient in the spin fluid and temperature fluctuations within the instrument are the main causes for the instrument drift. For long sedimentation times, the drift can be nonlinear and significant. Hence, the instrument measures a small positive or negative signal and correlates this to a particle size, given the sedimentation time. To calculate the fractional mass, the signal is divided by Q_{ext} , (see (1)), which approaches zero at long times. In the case of fractions below 20 nm, the extinction efficiency is close to zero [32]. Consequently, a nonlinear drift in the baseline gives a significant change in the calculated mass fraction for very small particles and is amplified significantly in the PSDs for particles in this size range. Therefore, the slight increase

of mass between 10 nm and 20 nm cannot conclusively be attributed to a fraction of small nanoparticles (Figures 1, 2, 3, 4, and 5). This is supported by SEM micrographs of the suspensions, which did not reveal a mass fraction of very small particles.

It is expected that the transmittance of CNT suspensions decreases with sonication time, as the number of particles in the liquid increases. This has been used as a measure of the quality of the dispersion [30, 37]. We see the same trend in the PSDs from the ultrasonic bath (Figure 1). The transmittance decreased, as the number density of particles, due to fragmentation of agglomerates, increased with sonication time. However, not only the particle density, but also the total mass in the size range from 10 nm–2 μm increased with sonication time. Agglomerates larger than 2 μm cannot be detected at this running condition in the DCF. Particles larger than 2 μm will break up into smaller ones and the concentration of these larger particles is not insignificant at shorter sonication times.

The flow-through horn sonicator can be used to investigate the effects of higher-energy sonication. At the lowest setting of 10%, the sonication was mild and had a low-power output of 10–15 W. The results, see Figure 2, are comparable to the ultrasonic bath, although it seems that even at this low energy output, the dispersion is better, when comparing corresponding treatment times. Increasing the amplitude setting to 20%, as shown in Figure 3, led only to a small increase in the quality of the dispersions. This is somewhat surprising, because larger amplitudes mean larger displacements of liquid, steeper pressure changes, and therefore a higher volume of cavitation [38]. If cavitation is the main process in the exfoliation of the CNTs, increasing the amplitude should have a more pronounced, positive effect on the dispersability.

Increasing the amplitude to 40% and higher, on the other hand, led to significant changes in particle size distributions, as shown in Figure 4 (40%) and Figure 5 (70%). At 40% tip amplitude, the dispersion was significantly better at comparable sonication times. However, PSDs of experiments at large amplitudes and longer times showed deviation from the previously observed bimodal behaviour. In the experiments at 70%, the amount of free CNTs in the PSDs appeared to decrease with increasing sonication time and the bimodal shape was lost at longer times. At increasing times the mode of the emerging monomodal distribution was also shifted to larger particles compared to the free, exfoliated nanotubes. Sonochemical reactions of some of the constituents, associative effects, nanotube damage, or reagglomeration are some of the possible explanations for this behaviour. Thermogravimetric analysis and SEM imaging were performed to check for possible explanations. These results are discussed in Section 3.2.

3.1. Time Dependence. As discussed above, the total mass increases markedly with sonication time during low-intensity sonication, both for the bath sonicator and the tip sonicator at low amplitude. By integrating the PSDs, two particle mass parameters were determined. These are W_{CNT} , which

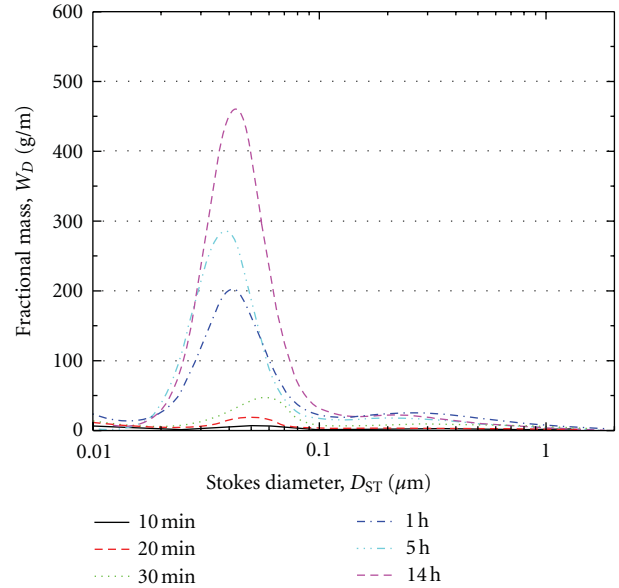


FIGURE 2: Particle size distributions of Arkema CNTs with increasing sonication time using a horn sonicator with flow cell at 10% amplitude.

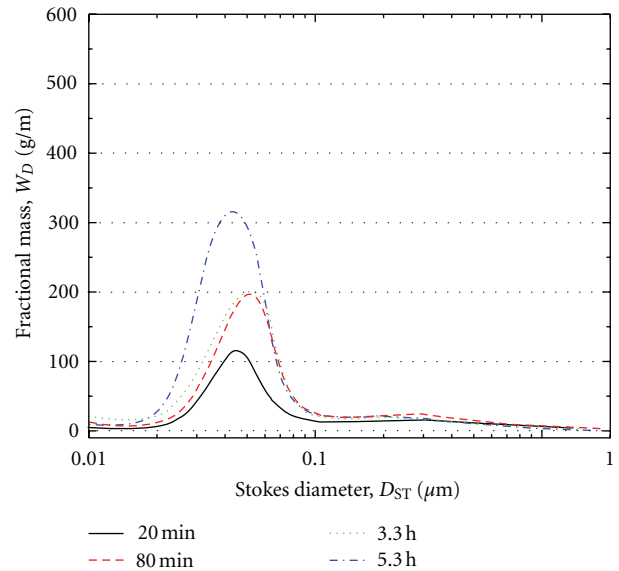


FIGURE 3: Particle size distributions of Arkema CNTs with increasing sonication time using a horn sonicator with flow cell at 20% amplitude.

is the particle mass in the dispersion ranging from 20 nm to 100 nm and W_{OBS} , the total mass in the size range from 20 nm to 2 μm . In general, W_{OBS} should increase and approach a constant value, determined by the CNT concentration in the suspension, if the sonication is effectively dispersing particles larger than 2 μm . Moreover, the ratio $W_{\text{CNT}}/W_{\text{OBS}}$ gives the mass fraction of exfoliated CNTs in the same manner as the cumulative weight distribution used by Nadler et al. [28] and is denoted as the *degree of exfoliation*.

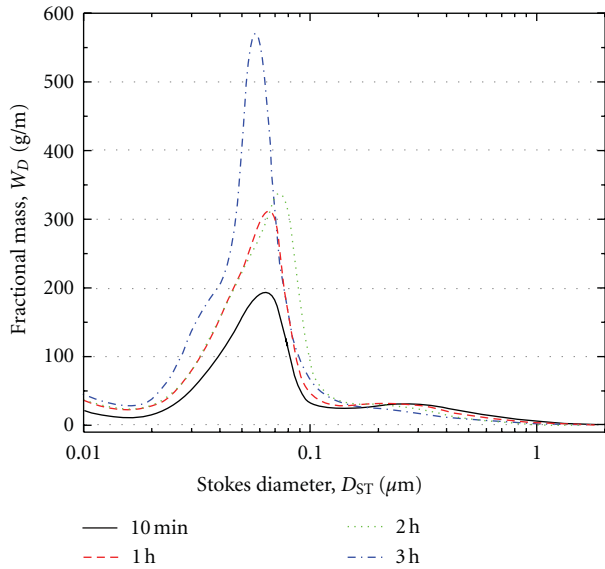


FIGURE 4: Particle size distributions of Arkema CNTs with increasing sonication time using a horn sonicator with flow cell at 40% amplitude.

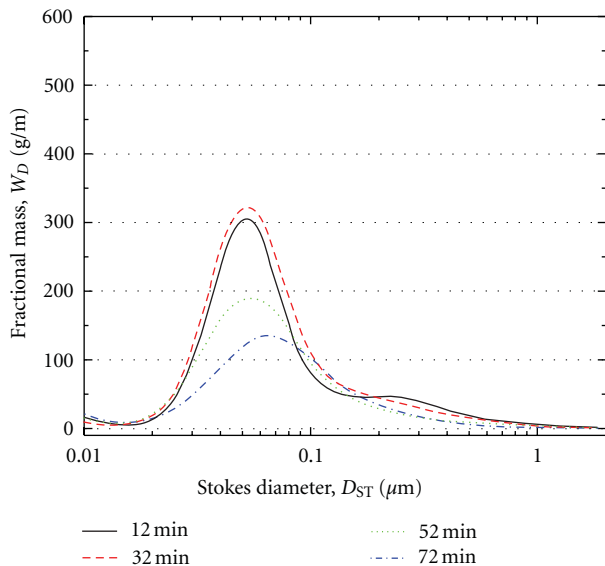


FIGURE 5: Particle size distributions of Arkema CNTs with increasing sonication time using a horn sonicator with flow cell at 70% amplitude.

The amount of exfoliated CNTs increases slowly with time in the bath sonicator and a plateau is reached after a few hours, see Figure 6. The horn sonicator is more efficient than the bath, but equilibrium is not reached within the time frame of the experiments. At short and intermediate times, that is, the first hour, the mass of freely dispersed carbon nanotubes is comparable for the bath sonicator and the horn sonicator at the lowest setting of 10%. At longer times, the tip sonicator has the ability to produce better dispersions, even at the lowest power input. The same increase of W_{CNT} against

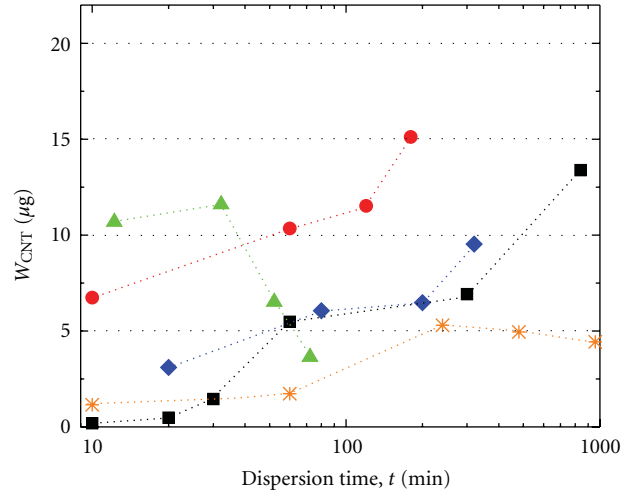


FIGURE 6: Mass of CNTs in the suspension, W_{CNT} , as a function of sonication time and horn amplitude: 10% (■), 20% (◆), 40% (●), 70% (▲), and bath sonicator (*).

time, apparently a log-linear relationship, was observed for the 20% and 40% case. Increasing the amplitude up to 40% had a clear effect on the rate of dispersion, as comparable amounts of CNTs were exfoliated in a tenth of the time compared to the 10% case. In the PSDs at 70%, see Figure 5, there is an evident broadening in the particle size distribution of the mass fraction of CNTs with increasing sonication time. At 72 minutes, the PSD is close to monomodal, ranging from 20 nm to 1 μm . Discussion of the particle mass, W_{CNT} , in the same way as in the other experiments is not relevant in this case, because the distribution is much broader than the mass fraction from 20–100 nm used to calculate W_{CNT} . A distinction between exfoliated and agglomerated CNTs is not possible in the PSDs. The dataset at 70% is included in Figure 6 to Figure 8 for comparison, but is omitted in later figures.

Not only the mass of exfoliated CNTs, but also the total observed mass (Figure 7), increased with sonication time. The increase is clearly dependent on the sonication intensity. For the bath sonicator and the horn sonicator at the 10% setting, the increase is significant up to a dispersion time of around 400 minutes. For the 40% amplitude the maximum observed mass was higher and nearly constant after only 10 minutes. An even higher mass was reached at 70% (after 20 minutes), but decreased markedly at longer times. This indicates that there are large strongly bound agglomerates that need high-intensity sonication to be broken, and that the breakup of these large agglomerates is a quick process at high-intensities. This is similar to observations using high-pressure homogenization, where the first pass through the homogenizer is the most significant in breaking the agglomerates [25]. However, at such high-sonication intensities, undesired side effects or CNT breakage may occur during the sonication treatment (see below) [18].

The log-linear increase of $W_{\text{CNT}}/W_{\text{OBS}}$ with dispersion time is seen for all of the experiments, except at 70% (Figure 8). The mass of exfoliated CNTs, W_{CNT} , increases even

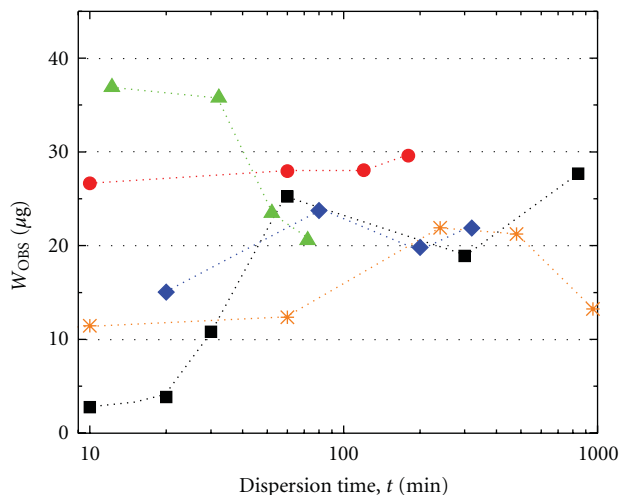


FIGURE 7: Total detected mass between 20 nm and 2 μm , W_{OBS} , as a function of sonication time and horn amplitude: 10% (■), 20% (◆), 40% (●), 70% (▲), and bath sonicator (*).

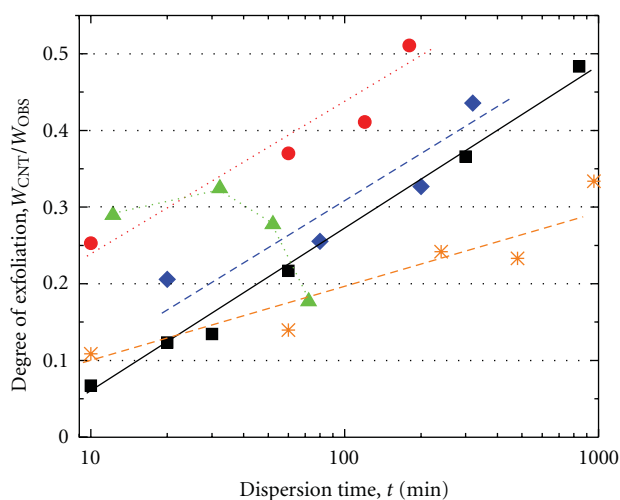


FIGURE 8: Mass fraction of CNTs relative to the total observed mass in suspensions, $W_{\text{CNT}}/W_{\text{OBS}}$, as a function of sonication time and horn amplitude: 10% (■), 20% (◆), 40% (●), 70% (▲), and bath sonicator (*). The straight lines are guides to the eye.

when W_{OBS} is constant, as seen in the measurements at 40%. Therefore, there must be an exfoliation of CNTs from these smaller agglomerates over time. The intensity of the sound field is high enough to break up these agglomerates, even at 10% amplitude, but the rate of the dispersion is low unless the sonication intensity is high. The degree of exfoliation was approximately 50%, so there is clearly room for improvement in the dispersion procedure. Further optimisation of the dispersion process by changing the flow cell geometry and temperature, or using diluents, should probably be possible.

3.2. High-Power Sonication. Dispersions at 70% tip amplitude did not give the typical bimodal PSDs at sonication

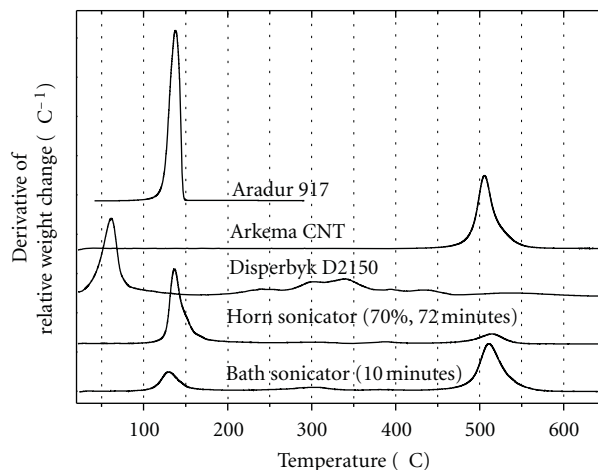


FIGURE 9: Thermogravimetric analysis of two suspensions and reference samples. The curves have been shifted on the Y-axis for better clarity. The reference samples were measured as received. The polymer stabilizer (D2150) was dissolved in a solvent by the supplier, and the large mass loss at 70°C is due to evaporation of this solvent.

times of 32 minutes and above, as can be seen in Figure 5. We believe that at this high energy input, other processes in addition to pure cluster break-up are taking place, and we have given this phenomenon some consideration, as described below: all of the constituents in the dispersion were examined with TGA, as shown in Figure 9. A sample that is sonicated for 72 minutes at 70% was compared to the same type of dispersion treated for only 10 minutes in the bath sonicator. The sample preparation (by centrifugation) showed significant differences between these samples. The sample from the bath sonicator revealed a dry powder as is normal for nanotubes, however, in the 70% case, the nanotubes were embedded in a viscous phase after the purification procedure. This paste was poorly dissolved in MIBK, compared to dispersions at lower intensities, which are easily dissolved in MIBK. The TGA measurements did not reveal any significant shift in the decomposition temperatures of the CNTs, but the purified sample from the 70% case did contain a significantly larger amount of MTHPA, compared with the purified sample from the bath sonicator. Scanning electron micrographs revealed that the CNTs were indeed embedded in a viscous medium. The TGA experiments showed that MTHPA decomposes below 150°C, and heating the sample prepared for the SEM to 200°C for 48 h, removed the viscous phase, as seen in Figure 10. The sample was heated above the decomposition temperature of MTHPA, but below that of D2150, and therefore, MTHPA is most likely the primary substance of the viscous phase.

It may be thought that at very high energy input, the CNTs themselves may be damaged, and therefore, the CNTs were checked for sonication damage (Figure 11). Severe damage was not evident in the SEM images, even at long sonication times at high-power. We therefore believe that the broad monomodal PSDs seen in Figure 5 are probably related to a sonically or thermally induced reaction of the anhydride in the dispersion. Since MIBK was a poor solvent for the

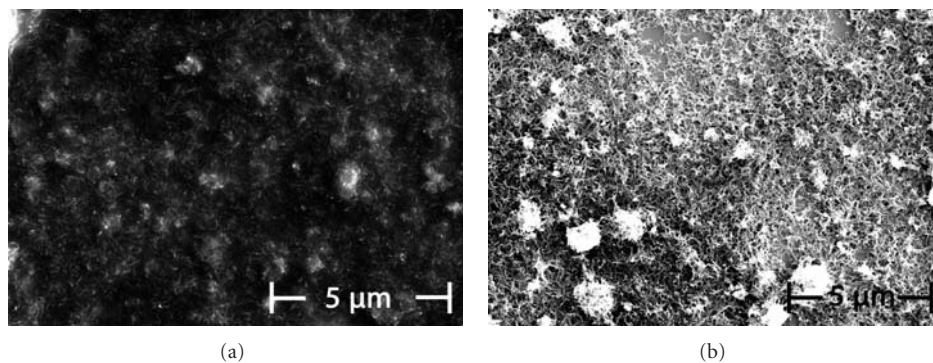


FIGURE 10: Scanning electron micrographs of the MWCNTs after TGA sample preparation. MWCNTs dispersed at 70% for 72 min (a) and the same specimen heated to 200°C for 48 h (b).

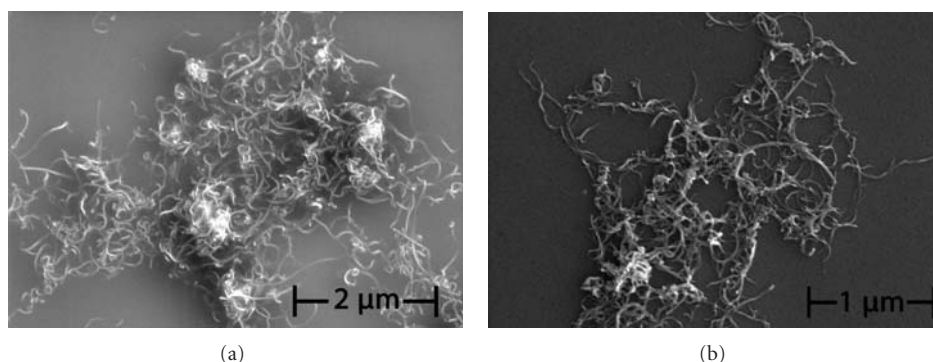


FIGURE 11: Scanning electron micrographs of the MWCNTs after TGA sample preparation. MWCNTs dispersed 10 min in a bath sonicator (a) and at 70% for 72 min (b).

mentioned viscous phase, the dilution step before injection in the DCF was probably not very effective, and is a likely reason for the observed PSDs at 70% tip amplitude. This means that the acid anhydride is not stable in sonication at 70%, and that the abnormalities in the PSDs could be caused by this viscous phase entangling the nanotubes. Apart from these considerations; we have not seen it as timely to investigate these side effects further in this work.

3.3. Specific Energy Input. The sonicator control electronics reports the energy consumption of the transducer while keeping constant amplitude of the resonating horn. This can be used to estimate the specific energy input to the suspension. In Figure 12, the power consumption is plotted as a function of the amplitude. The relationship between the power consumption and tip amplitude is linear in the amplitude range from 10% to 40%. The conditions were less reproducible at 70% and more energy was needed, comparably, to keep constant amplitude. The small confined space of the flow cell may give excessive damping of the horn resonance at large amplitudes. Larger amplitudes than 70% were not possible with the attached flow cell, because the instrument could not establish a resonance in the horn. The flow cell was constructed with the inlet straight beneath the horn tip and the suspension was pumped through a ceramic orifice fixed a short distance from the tip (0.8 mm).

The high-intensity sound field was mainly focused at this small volume of approximately 0.5 mL. At 10% amplitude, the power throughput is around 15 W, which gave a very intense sonication of 30 W/mL. In comparison, the bath sonicator had a total power of around 270 W dissipated into a volume of 2 L. This equals a much less intense sonication treatment of 0.14 W/mL. The resulting specific energy input of the bath is 0.5 kJ/mL per hour. Even though the specific power at the horn tip is high, the suspension resides in the sonicator's acoustic field only for a fraction of the treatment time. The suspension is circulated through the flow cell, and the total volume was 100 mL in all of the experiments. The specific energy input in the flow cell at 10% was therefore also 0.5 kJ/mL per hour.

The power consumption changed very little over time in these experiments, which led to a linear relationship between energy input and sonication time. Consequently, the same trends in W_{CNT} and W_{OBS} can be seen when plotted as a function of total energy input, E_{US} , as shown in Figure 13. Bath sonicator experiments are plotted in the same figure as a reference. To compare the data from the two sonicators, the estimated specific energy dissipation, 0.5 kJ/mL per hour, of the bath sonicator was used to calculate an energy input in the sample.

Up to 40% amplitude, a higher-intensity sonication is more effective at exfoliating CNTs at comparable energy

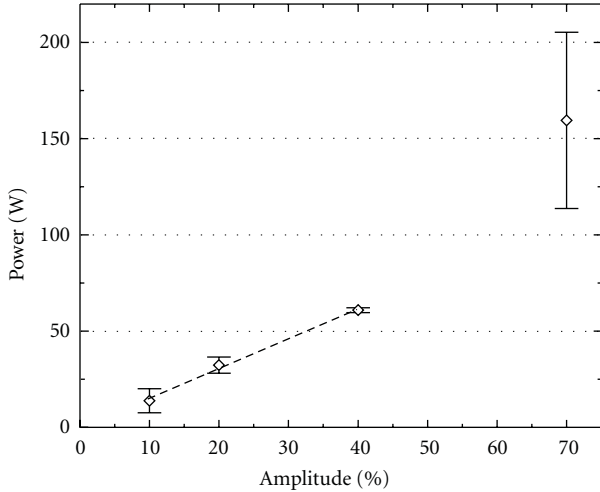


FIGURE 12: Horn transducer power consumption as a function of tip amplitude.

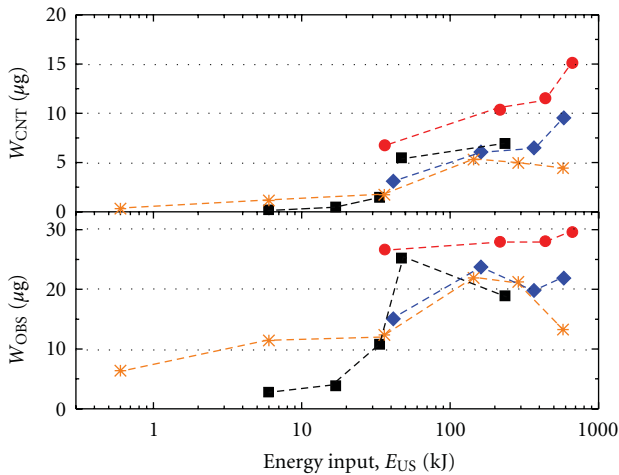


FIGURE 13: Mass of CNTs in the suspension, W_{CNT} , (upper graph) and the total detected mass between 20 nm and 2 μm , W_{OBS} , (lower graph) at increasing energy input, E_{US} at different horn amplitudes: 10% (■), 20% (◆), 40% (●), and bath sonicator (*).

inputs. The same is true for breaking large particles/agglomerates into smaller ones below 2 μm . Most noteworthy is that the relative mass of CNTs showed a power law dependency with the energy input, as shown in Figure 14. A nonlinear curve fit showed the scaling to be $W_{\text{CNT}}/W_{\text{OBS}} \sim E_{\text{US}}^{0.33}$.

Nadler et al. [28] investigated bath sonication of Baytubes C150P MWCNTs in water. If we assume their sonicator bath was filled to the recommended volume, the specific energy input should be 0.7 times the one used in this work. From [28], the relative exfoliation of Baytubes C150P in an aqueous suspension scales well with $\sim E_{\text{US}}^{0.4}$ up to at least 50% exfoliation. However, the Baytubes CNTs in aqueous suspension reached a much higher degree of exfoliation than the Arkema CNTs in MTHPA reported in this paper, at least within the experimental time frame. Naturally, the power law dependency breaks down as the CNTs approach 100%

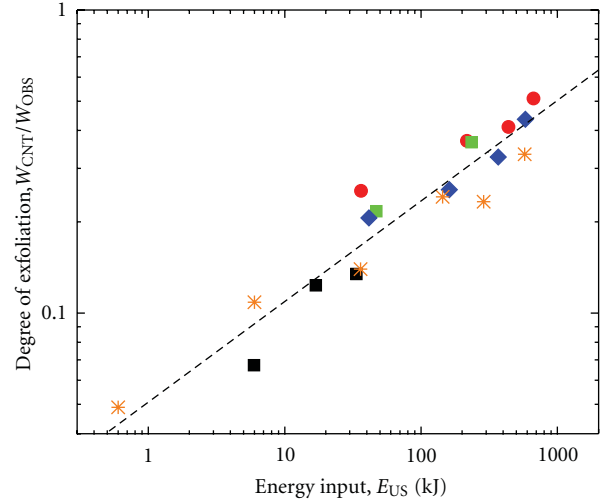


FIGURE 14: Mass fraction of CNTs relative to the total observed mass fraction in suspensions, $W_{\text{CNT}}/W_{\text{OBS}}$, at increasing energy input and different horn amplitudes: 10% (■), 20% (◆), 40% (●), and bath sonicator (*). Dashed line, $y = 0.05x^{0.33}$, shows a nonlinear curve fit of the data.

exfoliation. It cannot be concluded that there is a true power law dependency from these data alone [39].

Hennrich et al. [40] used atomic force microscopy (AFM) to show that the length (L) of single-walled nanotubes decreased with $L \sim t^{0.5}$ (constant power) (where t is time). Lucas et al. [18] found, with dynamic light scattering, similar results for multiwall nanotubes. In their case, a slower decrease of $L \sim E_{\text{US}}^{0.2}$ was observed. An optimum dispersion of carbon nanotubes is achieved when the amount of agglomerates is minimised, while the aspect ratio of the CNTs is retained. The above mentioned works indicates that there is a trade-off between the level of dispersion and sonically induced damage, when conventional sonication is used. Sonication schemes should be adjusted according to the intended usage of the dispersions. For good electrical conductivity, a high aspect ratio is probably more important than small amounts of agglomerate residues. As mechanical reinforcements, these agglomerates could be critical, ultimately weakening the composite. Significant reinforcement has been demonstrated at particle loading levels below 1% (w/w) [41]. At higher loadings, the strength tends to go down, possibly because of an increased number of agglomerates.

3.4. Mechanisms of Separation. Fragmentation theory describes the processes of breaking particles into smaller constituents. A thorough treatment of dispersion mechanisms in the context of fragmentation theory has been given by, for example, Cheng and Redner [42]. They make a clear distinction between agglomerates and aggregates. Agglomerates consist of a number of aggregates and can break up during a typical dispersion process. Aggregates, for example, primary particles or small crystals, are the smallest possible particles produced in the dispersion process. Further fragmentation of these particles does not occur during the dispersion process.

In our case, the primary particle would be the exfoliated nanotube, but as noted earlier, further fragmentation of CNTs, that is, nanotube breakage, can happen in a typical dispersion scheme [2, 18, 19, 22, 43].

In a continuous fragmentation process, the particle concentration, $c(x, t)$, of particles with mass x at time t can be expressed by

$$\frac{\partial c(x, t)}{\partial t} = -a(x)c(x, t) + \int_x^\infty c(y, t)a(y)f(x | y)dy. \quad (2)$$

Here, $a(x)$ is the fragmentation rate of particles of mass x , and $f(x | y)$ is a relative fragmentation rate, given by the conditional probability of a breakup event where a particle of mass x is produced from a larger particle of mass y [42, 44, 45]. Depending on the dispersion process, different fracture phenomena may occur, and three characteristic regimes can be defined as (1) *rupture* (or cleavage), (2) *erosion* (or abrasion), and (3) *shattering* (or destructive breaking). Ottino et al. [45] introduced a dimensionless parameter characterising the fragmentation process similar to the well-established capillary number (Ca) which is useful in the discussion of the above-mentioned fracture regimes. This *fragmentation number* (Fa), is the ratio between the viscous shear stress and the strength of the agglomerated particles

$$Fa = \frac{\mu\dot{\gamma}}{T}, \quad (3)$$

where μ is the viscosity, and $\dot{\gamma}$ is the shear rate. Furthermore, T quantifies the cohesive strength, analogous to the surface tension for a droplet. In shear flow dispersion, Fa increases with the energy input. At sufficient energy inputs, then $Fa > Fa_{\text{critical}}$, and the liquid shear stress exceeds the cohesive strength of the agglomerates. This results in a rupture of the original particle into two or more particles of similar size. At $Fa < Fa_{\text{critical}}$, fragmentation can still occur. Erosion is then the main mechanism of dispersion, where small (primary) particles detach from the surface of the mother particle. Erosion can be a significant effect when the agglomerates consist of discrete primary particles, such as carbon nanotubes, and the resulting particle size distribution is bimodal [28]. Erosion and cleavage are extremes on a continuous scale of fracture. The distinction between these processes is given (arbitrarily) in different ways in the literature. Rwei et al. [46] defines erosion as rupture with child particles of less than 10% of the volume of the mother particle, while Ottino et al. [45] use the term more loosely about fragmentation when $Fa > Fa_{\text{critical}}$. It should be stressed that erosion can be significant even when rupture is the dominating process [47]. Erosion is, in nature, a surface effect, and rupture of larger particles will create fresh surfaces which subsequently can undergo erosion. Recently, Kasaliwal et al. [48, 49] have studied the effects of erosion and rupture processes for CNT suspensions in polycarbonate (PC). By the use of a microcompounder, the shear rate could be varied to separate the two effects.

As stated earlier, $a(x)$ in (2) is the rate of fragmentation. In a homogenous fragmentation process, $a(x) \sim x^\lambda$, where λ is the *homogeneity index* [44]. In the most common case,

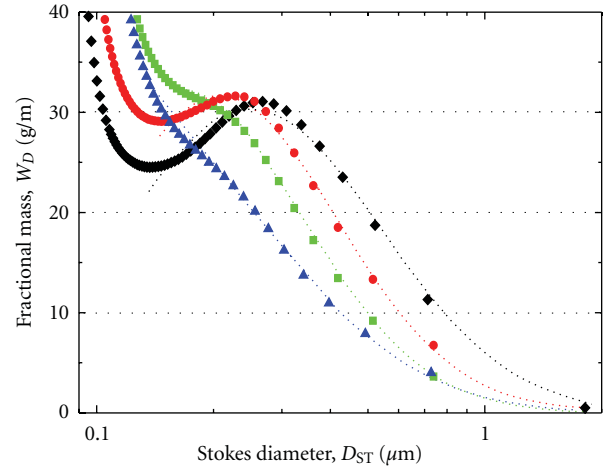


FIGURE 15: Particle size distributions of CNTs (symbols) at different sonication times at 40% tip amplitude: 10 min (◆), 1 h (●), 2 h (■), and 3 h (▲). The dotted lines show the corresponding fitted log-normal distributions.

λ is positive, and the rate of fragmentation due to rupture will decrease with particle size (mass). At the same time, the number of particles, and also the surface area, increases with rupture. In total, erosion should become more prominent, relative to rupture, as dispersion time increases, and consequently the size of the particles decreases. If λ is negative, shattering occurs. In this case, the rate of fragmentation will increase with decreasing particle size, and mass “vanishes” from the observed PSD as the agglomerates shatter into infinitesimally small particles. Equation (2) has been analyzed for different fragmentation phenomena, but mainly for rupture.

If “mother particles” break into random-sized particles through a stochastically determined process (Markov process), the final distribution will be log-normal in the limit of small particles, as first shown in the theory of Kolmogorov [50]. For the MWCNTs in this study, the initial agglomerate size is 10–1000 μm [26]. After prolonged sonication, the agglomerates in the size range from 0.1–2 μm exhibited a particle size distribution approaching a log-normal shape, as seen in Figure 15, indicating a rupture mechanism even though the bimodal shape of the PSDs clearly suggests an erosion-like behaviour of the MWCNTs. The agglomerate size distribution indicates that both erosion-like and rupture-like breakup events occur.

Further sonication did not change the general log-normal shape of the distribution, even though the average agglomerate size decreased. This self-similarity is predicted by the Kolmogorov model. Hansen et al. [44] argue that the average agglomerate size, s , scales with time as

$$s(t) \sim t^{-1/\lambda}, \quad (4)$$

where λ is the previously mentioned homogeneity index. Equation (4) holds for rupture-like breakup events with positive values of λ [51]. The parameter s is estimated as the mean value from the fitted log-normal distributions, as seen in Figure 15. At long sonication treatments, a power law

TABLE 1: Exponents of fitted data to (4) as shown in Figure 16.

Experiment	$-1/\lambda$	λ
10%	-0.24	4.13
20%	-0.24	4.17
40%	-0.27	3.72
Bath	-0.24	4.09

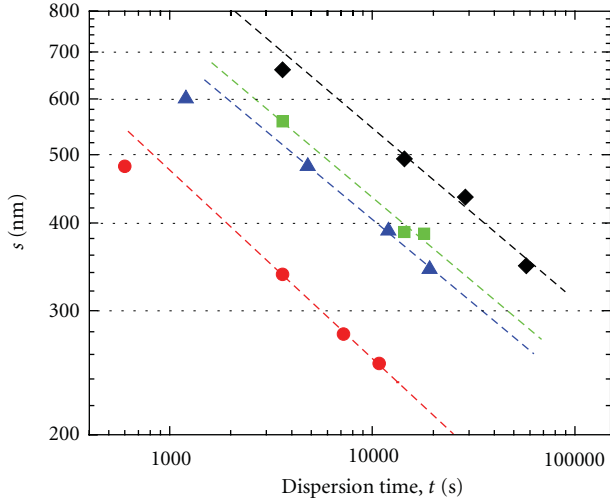


FIGURE 16: Mean agglomerate size data from fitted log-normal functions as a function of sonication time, t , at different tip amplitudes: 10% (■), 20% (▲), 40% (●), and bath sonicator (◆). For each tip amplitude, the three longest times were used to fit (4).

dependence, as given in (4), was observed (see Figure 16 and Table 1). The time dependence of the mean agglomerate size is very similar for the lowest tip amplitudes and for the bath. The fitted parameter, λ , is ranging from 4.09 to 4.17. Consequently, the rate of fragmentation is similar in these experiments. At 40% amplitude, a slightly lower value of 3.72 is found. A lower value of λ indicates that the fragmentation rate is less dependent on the particle size. It could be that the higher share rate increases the probability of rupture of much smaller agglomerates than at the lower amplitudes. At sufficiently high share rates, the probability of rupture is constant for particles of any size, because all particles will break, irrespective of size. Consequently, the homogeneity index will be zero in this case. A lower value of λ is therefore expected when the acoustic power of the sonicator increases.

Power law behaviour has also been described without the use of fragmentation theory. Bittmann et al. [52] correlated the size of dispersed TiO₂ nanoparticles to the power input of a tip sonicator,

$$s(t) \sim P_v^{-b_1} \cdot t_v^{-b_2} \approx (P_v \cdot t_v)^{-b}, \quad (5)$$

where P_v is the power input in the cavitation zone, and t_v is the mean residence time in the same zone. In the current setup, this cavitation zone is between the ceramic orifice and

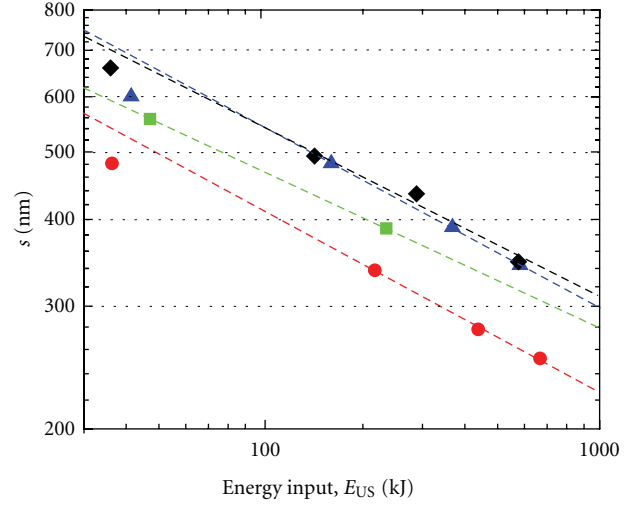


FIGURE 17: Mean agglomerate size data from fitted log-normal functions as a function of sonication energy input, E_{US} , at different tip amplitudes: 10% (■), 20% (▲), 40% (●), and bath sonicator (◆). For each tip amplitude, the same datasets as in Figure 16 were used to fit (6).

the sonicator tip inside the flow cell. If the right hand side of (5) holds, we can rewrite it as

$$s(t) \sim E_{US}^{-b}, \quad (6)$$

where E_{US} is the energy input from the tip sonicator, given the energy input scales with the cavitation activity inside the flow-cell cavitation zone. The same data set as seen in Figure 16 was fitted against the energy input, E_{US} . The data is well described by the volume based model in (6), as seen in Figure 17.

The data shows approximately the same scaling relationship with the average agglomerate diameter as a function of sonicator energy input. However, the dispersion of the agglomerates is both faster at 40%, than in the experiments with less intense sonication (see Figure 16), and the process is also much more energy efficient (Figure 17). This suggests that the initial breakup of the large agglomerates is dependent on the sonication power, but that the further dispersion process is more dependent on the total energy input.

A model, where the particle erosion is proportional to the particle surface and applied shear was proposed by Kao and Mason [53] and later developed and investigated by others [44, 46, 54]. Instead of a power law dependency, an exponential decay with time is expected, as seen in Equation (7):

$$s(t) \sim s_0 e^{(-K\dot{\gamma}t)} + c, \quad (7)$$

where s is the average agglomerate size and s_0 the initial size of the agglomerates. $\dot{\gamma}$ is the applied shear rate, c is an integration constant, and K is a constant dependent on factors such as the type of flow, agglomerate strength, and the liquid shear stress [46]. This exponential relationship is similar to the model used by Kasaliwal et al. [49]. They showed that the size of agglomerates in the range from 1–10 μm decreased

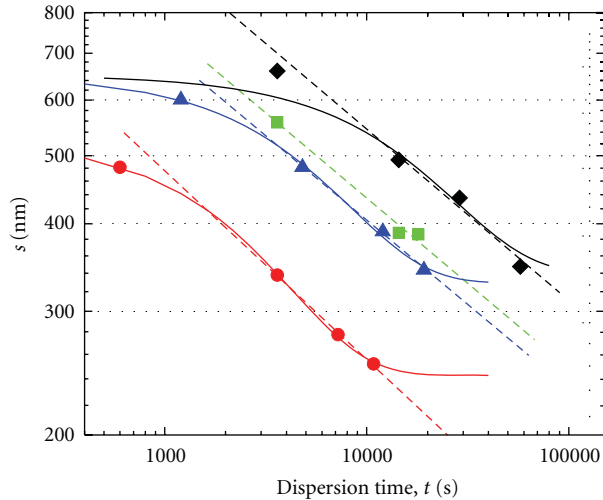


FIGURE 18: Agglomerate size data at 20% and 40% amplitude were fitted using (4) (dotted lines), and (7) (solid lines). Marquardt non-linear curve fit did not give converging results for the other two datasets. Equation (7) was plotted with estimated parameters as a guide for data from the bath sonicator. Amplitudes 10% (■), 20% (▲), 40% (●), bath sonicator (◆).

exponentially over time and attributed this to an erosional dispersion of CNT agglomerates.

Average agglomerate size data from our experiments was fitted to (7), and the results are given in Figure 18.

Convergent results were obtained from experiments at 20% and 40% tip amplitude. At short sonication times, the agglomerate size distribution did not correspond well to a log-normal distribution. Consequently, the estimated average size, s , was not well estimated at short times at low-energy input. Still, (7) could be plotted for the bath sonicator series, with estimated parameters. As seen in Figure 18, both a power law dependency and an exponential decay fit these data sets reasonably well. As previously mentioned, both erosion and rupture are likely to occur in this kind of experiment, but conclusive information about the dominating process of fragmentation could not be drawn from these datasets. From a physical point of view, erosion is a likely process for CVD type MWCNTs. Agglomerates are highly entangled, and the cohesive strength of the primary particles are very large compared to the particle-particle interaction. An erosion-type dispersion will probably lead to less damage to the tubes than a dispersion process where rupture is the dominating fragmentation event.

4. Summary

Ultrasonic dispersion of carbon nanotubes was investigated. 1% (w/w) of MWCNT in a commercially available curing agent was dispersed using both a bath sonicator and a horn sonicator with a flow cell attachment at different horn tip amplitudes. Subsequently, suspensions of CNTs were characterized using a disc centrifuge. The horn sonicator was shown to be superior to the low-power bath sonicator, achieving much better dispersions within reasonable sonication times.

Particle size distributions showed a broad bimodal distribution of CNTs in the suspension. The lower-sized mode is attributed to freely suspended nanotubes, and the broader mode at larger particle sizes to agglomerate CNTs. Increasing the dispersion time or acoustic intensity of the sonication had a positive effect on the quality of the dispersion, by increasing the mass fraction of the free, un-entangled nanotubes. However, at 70% tip amplitude, unwanted side effects were detected. SEM and TGA investigations indicated that a sonochemically induced reaction with the anhydride occurred. Therefore, optimal horn tip amplitude of approximately 40% was found as a compromise between rate of dispersion and minimizing side reactions in the suspension.

The relative mass fraction of unentangled CNTs compared to the total mass of CNTs observed in the PSD was estimated and denoted as the degree of exfoliation in accordance with earlier works. This mass fraction increased with sonication time with a log-linear behaviour. Increasing the tip amplitude (energy input) gave a higher degree of exfoliation, but approximately the same log-linear increase with time was observed for all of the horn sonicator experiments. The relative mass of CNTs increased much slower in the bath sonicator, reaching only 30% exfoliation after 16 h.

The energy input from the sonicators was correlated to the degree of exfoliation, and the data showed a strong power law dependency condensing onto the same master curve. The degree of exfoliation increased with the energy input with an exponent of 0.33 in all of the dispersion experiments. We conclude that the quality of the dispersion was controlled by the total energy input, and that a sufficiently intense acoustic sound field is needed to efficiently produce dispersions of good quality.

The size distribution of agglomerates showed a strong log-normal shape at longer sonication times, indicating that the larger agglomerates broke into smaller ones in a rupture process. However, the mean agglomerate size, s , was estimated and fitted to three different models. A power law behaviour both with the energy input and sonication time, showed that s scaled well with both time and energy input. Furthermore, a model for erosional particle fragmentation, with an exponential decrease in agglomerate size, fitted the data reasonably as well.

The disc centrifuge can be used to reliably study the evolution of the dispersion process during sonication. Both the amount of unentangled CNTs and parts of the agglomerate size range can be estimated with this technique. A detailed analysis of the size distribution is of vital importance to understand these processes and to be able to evaluate the optimum conditions for the dispersion of CNTs in liquids.

Acknowledgments

The authors would like to acknowledge Mette Grorud for assistance with the sonication experiments, Tomas Lunde Jensen (FFI) for help with the TGA measurements, and Dr. Tom Thorvaldsen, Dr. Bernt Brønmo Johnsen (FFI), and Dr. Marc Steinmetz (CPS instruments) for valuable discussions. The authors of this contribution do not have any direct

financial relation with any commercial identities mentioned in the paper that might lead to a conflict of interest for any of the authors.

References

- [1] S. Iijima, "Helical microtubules of graphitic carbon," *Nature*, vol. 354, no. 6348, pp. 56–58, 1991.
- [2] J. Hilding, E. A. Grulke, Z. G. Zhang, and F. Lockwood, "Dispersion of carbon nanotubes in liquids," *Journal of Dispersion Science and Technology*, vol. 24, no. 1, pp. 1–41, 2003.
- [3] P. X. Hou, C. Liu, and H. M. Cheng, "Purification of carbon nanotubes," *Carbon*, vol. 46, no. 15, pp. 2003–2025, 2008.
- [4] D. L. Shi, X. Q. Feng, Y. Y. Huang, K. C. Hwang, and H. Gao, "The effect of nanotube waviness and agglomeration on the elastic property of carbon nanotube-reinforced composites," *Journal of Engineering Materials and Technology, Transactions of the ASME*, vol. 126, no. 3, pp. 250–257, 2004.
- [5] A. Godara, L. Mezzo, F. Luizi et al., "Influence of carbon nanotube reinforcement on the processing and the mechanical behaviour of carbon fiber/epoxy composites," *Carbon*, vol. 47, no. 12, pp. 2914–2923, 2009.
- [6] E. J. Garcia, B. L. Wardle, and A. John Hart, "Joining prepreg composite interfaces with aligned carbon nanotubes," *Composites A*, vol. 39, no. 6, pp. 1065–1070, 2008.
- [7] J.-H. Du, J. Bai, and H.-M. Cheng, "The present status and key problems of carbon nanotube based polymer composites," *Express Polymer Letters*, vol. 1, no. 5, pp. 253–273, 2007.
- [8] R. K. Duncan, X. G. Chen, J. B. Bult, L. C. Brinson, and L. S. Schadler, "Measurement of the critical aspect ratio and interfacial shear strength in MWNT/polymer composites," *Composites Science and Technology*, vol. 70, no. 4, pp. 599–605, 2010.
- [9] A. H. Barber, S. R. Cohen, S. Kenig, and H. D. Wagner, "Interfacial fracture energy measurements for multi-walled carbon nanotubes pulled from a polymer matrix," *Composites Science and Technology*, vol. 64, no. 15, pp. 2283–2289, 2004.
- [10] A. Martone, C. Formicola, M. Giordano, and M. Zarrelli, "Reinforcement efficiency of multi-walled carbon nanotube/epoxy nanocomposite," *Composites Science and Technology*, vol. 70, no. 7, pp. 1154–1160, 2010.
- [11] P. C. Ma, N. A. Siddiqui, G. Marom, and J. K. Kim, "Dispersion and functionalization of carbon nanotubes for polymer-based nanocomposites: a review," *Composites A*, vol. 41, no. 10, pp. 1345–1367, 2010.
- [12] S. Azoubel and S. Magdassi, "The formation of carbon nanotube dispersions by high pressure homogenization and their rapid characterization by analytical centrifuge," *Carbon*, vol. 48, no. 12, pp. 3346–3352, 2010.
- [13] O. Behrend, K. Ax, and H. Schubert, "Influence of continuous phase viscosity on emulsification by ultrasound," *Ultrasonics Sonochemistry*, vol. 7, no. 2, pp. 77–85, 2000.
- [14] K. S. Suslick and G. J. Price, "Applications of ultrasound to materials chemistry," *Annual Review of Materials Science*, vol. 29, pp. 295–326, 1999.
- [15] J. Dooher, R. Lippman, T. Morrone, H. Pohle, and D. Wright, "Ultrasonic disintegration of particles," pp. 11–16, 1978.
- [16] T. J. Mason and P. L. Lorimer, *Applied Sonochemistry: Uses of Power Ultrasound in Chemistry and Processing*, Wiley-VCH, Weinheim, Germany, 2002.
- [17] C. McClory, S. J. Chin, and T. McNally, "Polymer/carbon nanotube composites," *Australian Journal of Chemistry*, vol. 62, no. 8, pp. 762–785, 2009.
- [18] A. Lucas, C. Zakri, M. Maugey, M. Pasquali, P. Van Der Schoot, and P. Poulin, "Kinetics of nanotube and microfiber scission under sonication," *Journal of Physical Chemistry C*, vol. 113, no. 48, pp. 20599–20605, 2009.
- [19] S. Badaire, P. Poulin, M. Maugey, and C. Zakri, "In situ measurements of nanotube dimensions in suspensions by depolarized dynamic light scattering," *Langmuir*, vol. 20, no. 24, pp. 10367–10370, 2004.
- [20] D. W. Schaefer and R. S. Justice, "How nano are nanocomposites?" *Macromolecules*, vol. 40, no. 24, pp. 8501–8517, 2007.
- [21] S. H. Kim, W. I. Lee, and J. M. Park, "Assessment of dispersion in carbon nanotube reinforced composites using differential scanning calorimetry," *Carbon*, vol. 47, no. 11, pp. 2699–2703, 2009.
- [22] T. Liu, S. Luo, Z. Xiao, C. Zhang, and B. Wang, "Preparative ultracentrifuge method for characterization of carbon nanotube dispersions," *Journal of Physical Chemistry C*, vol. 112, no. 49, pp. 19193–19202, 2008.
- [23] G. Ralston, "Introduction to analytical ultracentrifugation," 1992, <https://www.beckmancoulter.com/>.
- [24] B. Krause, G. Petzold, S. Pegel, and P. Pötschke, "Correlation of carbon nanotube dispersability in aqueous surfactant solutions and polymers," *Carbon*, vol. 47, no. 3, pp. 602–612, 2009.
- [25] S. Pegel, P. Pötschke, G. Petzold, I. Alig, S. M. Dudkin, and D. Lellinger, "Dispersion, agglomeration, and network formation of multiwalled carbon nanotubes in polycarbonate melts," *Polymer*, vol. 49, no. 4, pp. 974–984, 2008.
- [26] B. Krause, M. Mende, P. Pötschke, and G. Petzold, "Dispersability and particle size distribution of CNTs in an aqueous surfactant dispersion as a function of ultrasonic treatment time," *Carbon*, vol. 48, no. 10, pp. 2746–2754, 2010.
- [27] F. K. Hansen, "Particle size measurements with a disc centrifuge," in *Particle Size Distribution II*, T. Provder, Ed., pp. 169–183, ACS Symposium Series, Washington, DC, USA, 1991.
- [28] M. Nadler, T. Mahrholz, U. Riedel, C. Schilde, and A. Kwade, "Preparation of colloidal carbon nanotube dispersions and their characterisation using a disc centrifuge," *Carbon*, vol. 46, no. 11, pp. 1384–1392, 2008.
- [29] J. Mejia, F. Tichelaar, C. Saout et al., "Effects of the dispersion methods in Pluronic F108 on the size and the surface composition of MWCNTs and their implications in toxicology assessment," *Journal of Nanoparticle Research*, vol. 13, no. 2, pp. 655–667, 2011.
- [30] L. Zhao and L. Gao, "Stability of multi-walled carbon nanotubes dispersion with copolymer in ethanol," *Colloids and Surfaces A*, vol. 224, no. 1–3, pp. 127–134, 2003.
- [31] Q. Li, M. Zaiser, and V. Koutsos, "Carbon nanotube/epoxy resin composites using a block copolymer as a dispersing agent," *Physica Status Solidi (A) Applied Research*, vol. 201, no. 13, pp. R89–R91, 2004.
- [32] M. Kerker, *The Scattering of Light*, Academic Press, New York, NY, USA, 1969.
- [33] A. Koshio, M. Yudasaka, M. Zhang, and S. Iijima, "A Simple Way to Chemically React Single-Wall Carbon Nanotubes with Organic Materials Using Ultrasonication," *Nano Letters*, vol. 1, no. 7, pp. 361–363, 2001.
- [34] A. Koshio, M. Yudasaka, and S. Iijima, "Thermal degradation of ragged single-wall carbon nanotubes produced by polymer-assisted ultrasonication," *Chemical Physics Letters*, vol. 341, no. 5–6, pp. 461–466, 2001.

- [35] K. L. Lu, R. M. Lago, Y. K. Chen, M. L. H. Green, P. J. F. Harris, and S. C. Tsang, "Mechanical damage of carbon nanotubes by ultrasound," *Carbon*, vol. 34, no. 6, pp. 814–816, 1996.
- [36] P. S. Gill, S. R. Sauerbrunn, and B. S. Crowe, "High resolution thermogravimetry," *Journal of Thermal Analysis*, vol. 38, no. 3, pp. 255–266, 1992.
- [37] N. Grossiord, O. Regev, J. Loos, J. Meuldijk, and C. E. Koning, "Time-dependent study of the exfoliation process of carbon nanotubes in aqueous dispersions by using UV-visible spectroscopy," *Analytical Chemistry*, vol. 77, no. 16, pp. 5135–5139, 2005.
- [38] T. Hielscher, "Ultrasonic production of nano-size dispersions and emulsions," *European Nano Systems*, pp. 138–143, 2005.
- [39] A. Clauset, C. R. Shalizi, and M. E. J. Newman, "Power-law distributions in empirical data," *SIAM Review*, vol. 51, no. 4, pp. 661–703, 2009.
- [40] F. Hennrich, R. Krupke, K. Arnold et al., "The mechanism of cavitation-induced scission of single-walled carbon nanotubes," *Journal of Physical Chemistry B*, vol. 111, no. 8, pp. 1932–1937, 2007.
- [41] S. G. Prolongo, M. R. Gude, and A. Urena, "Improving the flexural and thermomechanical properties of amino-functionalized carbon nanotube/epoxy composites by using a pre-curing treatment," *Composites Science and Technology*, vol. 71, pp. 765–771, 2011.
- [42] Z. Cheng and S. Redner, "Kinetics of fragmentation," *Journal of Physics A*, vol. 23, no. 7, pp. 1233–1258, 1990.
- [43] K. Yang, M. Gu, Y. Guo, X. Pan, and G. Mu, "Effects of carbon nanotube functionalization on the mechanical and thermal properties of epoxy composites," *Carbon*, vol. 47, no. 7, pp. 1723–1737, 2009.
- [44] S. Hansen, D. V. Khakhar, and J. M. Ottino, "Dispersion of solids in nonhomogeneous viscous flows," *Chemical Engineering Science*, vol. 53, no. 10, pp. 1803–1817, 1998.
- [45] J. M. Ottino, P. DeRoussel, S. Hansen, and D. V. Khakhar, "Mixing and dispersion of viscous liquids and powdered solids," in *Advances in Chemical Engineering*, J. Wei, Ed., vol. 25, pp. 105–204, Academic Press, New York, NY, USA, 1999.
- [46] S. P. Rwei, I. Manas-Zloczower, and D. L. Feke, "Characterization of agglomerate dispersion by erosion in simple shear flows," *Polymer Engineering & Science*, vol. 31, no. 8, pp. 558–562, 1991.
- [47] S. P. Rwei, I. Manas-Zloczower, and D. L. Feke, "Analysis of dispersion of carbon black in polymeric melts and its effect on compound properties," *Polymer Engineering & Science*, vol. 32, no. 2, pp. 130–135, 1992.
- [48] G. Kasaliwal, A. Gödel, and P. Pötschke, "Influence of processing conditions in small-scale melt mixing and compression molding on the resistivity and morphology of polycarbonate-MWNT composites," *Journal of Applied Polymer Science*, vol. 112, no. 6, pp. 3494–3509, 2009.
- [49] G. R. Kasaliwal, S. Pegel, A. Gödel, P. Pötschke Petra, and G. Heinrich, "Analysis of agglomerate dispersion mechanisms of multiwalled carbon nanotubes during melt mixing in polycarbonate," *Polymer*, vol. 51, no. 12, pp. 2708–2720, 2010.
- [50] A. N. Kolmogorov, "The logarithmically normal law of distribution of dimensions of particles when broken into small parts," *Doklady Akademii Nauk*, vol. 31, pp. 99–101, 1941.
- [51] A. F. Filippov, "On the distribution of the sizes of particles which undergo splitting," *Theory of Probability and its Applications*, vol. 6, pp. 275–294, 1961.
- [52] B. Bittmann, F. Hauptert, and A. K. Schlarb, "Ultrasonic dispersion of inorganic nanoparticles in epoxy resin," *Ultrasonics Sonochemistry*, vol. 16, no. 5, pp. 622–628, 2009.
- [53] S. V. Kao and S. G. Mason, "Dispersion of particles by shear," *Nature*, vol. 253, no. 5493, pp. 619–621, 1975.
- [54] R. L. Powell and S. G. Mason, "Dispersion by laminar flow," *AIChE Journal*, vol. 28, no. 2, pp. 286–923, 1982.

Research Article

Exfoliated Graphite Reinforced PMMA Composite: A Study on Nanoindentation and Scratch Behavior

Himel Chakraborty,¹ Arijit Sinha,¹ Nillohit Mukherjee,² and Partha Protim Chattopadhyay³

¹ School of Materials Science and Engineering, Bengal Engineering and Science University, Shibpur, Howrah 711103, India

² Centre of Excellence for Green Energy and Sensor Systems, Bengal Engineering and Science University, Shibpur, Howrah 711103, India

³ Department of Metallurgy and Materials Engineering, Bengal Engineering and Science University, Shibpur, Howrah 711103, India

Correspondence should be addressed to Nillohit Mukherjee, nilsci@yahoo.co.uk

Received 5 April 2012; Accepted 10 May 2012

Academic Editor: Huisheng Peng

Copyright © 2012 Himel Chakraborty et al. This is an open access article distributed under the Creative Commons Attribution License, which permits unrestricted use, distribution, and reproduction in any medium, provided the original work is properly cited.

The present work aims to compare the scratch hardness (H_s) with the indentation hardness (H_{IT}) obtained from nanoindentation measurements of exfoliated graphite/poly (methyl methacrylate) (EG/PMMA) composites. EG/PMMA composites with thickness $50\ \mu\text{m}$ each were produced by in situ melt mixing method. Scratch hardness was measured from the scratch width formed at low applied load during the course of the scratch measurements. The measured scratch hardness values were compared with the indentation hardness. There is a good correlation between the scratch hardness and the indentation hardness at low indentation depths, with a linear relationship between hardness and the reinforcement content of exfoliated graphite.

1. Introduction

Nanoindentation has been established as a reliable tool for measuring mechanical properties of polymer composite at the submicron scale [1–6]. An extensive study of nanoindentation on poly (methyl methacrylate) (PMMA) composites has been reported by Jee and Lee [6, 7]. In nanoindentation, the depth of penetration together with the known geometry of the indenter provide an indirect measure of the projected area of contact at maximum load, and thus hardness is obtained by dividing the maximum applied load by the projected area of contact. In the depth sensing instrumented indentation technique, hardness and elastic modulus can be determined by the Oliver and Pharr model [8–12]. The scratch test is a simple and widely used method for investigating polymer composite surface [13]. In the scratch test an indenter is lowered on to the sample at increasing loads as the indenter tip is moved across the surface of the sample. Scratch hardness can also be measured from the scratch track made by the scratch tester. Scratch hardness has been defined as the load per unit load-bearing area during scratching, taking into account the formation of ridges and

a prow. Since it is quite difficult to measure the load-bearing area during the course of scratch experiments, it is calculated from the width of the scratch obtained after the completion of the test [14, 15]. An advantage of scratch hardness relative to indentation hardness measurements is the possibility of studying the variation of hardness along the length of the scratch. The hardness of different constitute phases can be determined by making one single scratch. The absolute values at specific positions can be calculated by measuring the groove width and by applying the appropriate hardness formula.

2. Material and Methods

Commercially available natural graphite flakes ($200\text{--}300\ \mu\text{m}$) were chemically treated by sintering with NaOH followed by 10% HNO_3 treatment. Expandable graphite samples from chemically treated graphite (99.8%) with nitric acid as an intercalate was prepared as described in [16] and was subjected to a thermal shock at 900°C in order to obtain exfoliated graphite (EG). The PMMA pellets were added to the Thermo Haake (Rheomix) and allowed to melt at

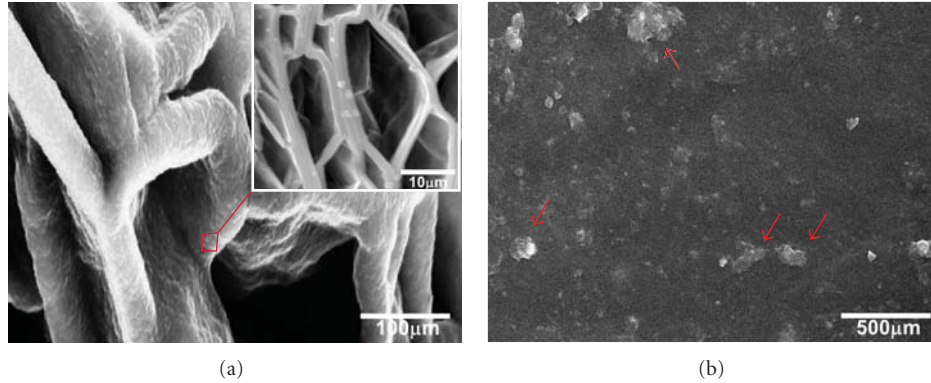


FIGURE 1: SEM micrographs of (a) exfoliated graphite, (b) 1 wt.% exfoliated graphite reinforced PMMA matrix.

220°C. EG with 0.25, 0.5, and 1 wt% were then added to the molten PMMA, and dispersion was carried out using high-speed shear mixing with two counter rotating stainless steel sigma shaped rotors at 20 rpm. A control sample of neat (i.e., unfilled) PMMA was also subjected to the melt mixing procedure [17] to bring uniformity in the sample preparation technique.

Nanoindentation testing on unreinforced PMMA and EG/PMMA composites samples was carried out using a CSM NHTX S/N: 55-0019 nanohardness tester with a triangular pyramidal diamond indenter (Berkovich, B-I 93, tip radius = 0.2 μm (inset of Figure 2(A))) under a constant load of 10 mN. The Berkovich diamond indenter with total included angle of 142.3° was used for all the measurements, and the load and displacement resolutions of the instrument were 1 μN and 0.03 nm, respectively. The nanohardness tester was calibrated by using glass and fused silica samples for a range of operating conditions. The instrumented hardness (H_{IT}) and instrumented elastic modulus (E_{IT}) were estimated from the initial gradient of the unloading curves using the Oliver and Pharr [8] model. Five measurements were made at each load on the unreinforced and reinforced PMMA composites.

Scratch testing was carried out on all samples using CSM NST: 50-133 nanoscratch tester with a diamond sphero-conical indenter (Ref: SB-A63, $R = 2 \mu\text{m}$) inside a cantilever (serial number: HL: 126, stiffness: 6.6717 mN/ μm , $F_n D_Z$ coefficient at 100 μm : 11.67 $\mu\text{m}/\text{V}$) over a scratch distance of 1.0 mm with a scratch speed of 2 mm/minutes. The load was increased from 0 to 10 mN at a specified loading rate. A loading rate of 100 mN/mm was used for the scratch tests. Load can be measured at any place from the loading rate and the length of the scratch track. For indenter tip of circular cross-sectional area (cones, spheres, and parabolas) the equation for scratch hardness is defined as follows [16, 17]:

$$H_s = \frac{8F_N}{\pi b^2}, \quad (1)$$

where F_N is the applied normal load and b is the scratch track width. All scratches were carried out five times in the same direction. Images of the scratches were obtained

using Hitachi S3400N scanning electron microscope (SEM) to measure the width of the scratch tracks.

3. Results and Discussion

3.1. SEM Images. Figure 1(a) shows the network-like structure of the exfoliated graphite particles. Large expansions can be seen in the graphite flakes due to the intercalation between the graphite sheets. The higher magnifications image as inset of Figure 1(a) clearly reveals the sheets from the exfoliated graphite with average sheet width of 2 μm . The void between the sheets was observed mainly due to a greater volume expansion of the exfoliated graphite intercalated compound (GIC).

Figure 1(b) shows the SEM image of the exfoliated graphite reinforced PMMA composite. The exfoliated graphite particulates look like regularly dispersed in PMMA matrix (depicts with arrow marks in Figure 1(b)). However, a tendency towards agglomeration due to increase in exfoliated graphite content in PMMA matrix was also observed.

3.2. Nanoindentation Measurements. In order to investigate the indentation behaviour, unreinforced PMMA and exfoliated graphite reinforced PMMA composites were subjected to the nanoindentation measurement. Figure 2 shows the load-penetration depth curves obtained from unreinforced PMMA and after reinforcing with 0.25, 0.5 and 1 wt% of EG in PMMA matrix at a maximum load of 10 mN. The load-penetration depth behaviour is typical of that for soft materials with a very little signature of an elastic recovery indicating a permanent deformation of the surface beneath the indenter.

The unreinforced PMMA is soft in comparison with the 0.25 wt% EG/PMMA composite, which has a hardness at around 0.45–0.46 GPa. There was an increase in the measured hardness with the increase in reinforcement content. It is also seen that the elastic recovery (area enclosed between the unloading portion of the load-penetration depth profiles and the depth at maximum load) is maximum in the case of 0.5 wt.% EG/PMMA composite, which indicates an increase in the hardness values as compared to the unreinforced PMMA as clearly revealed from the magnified view

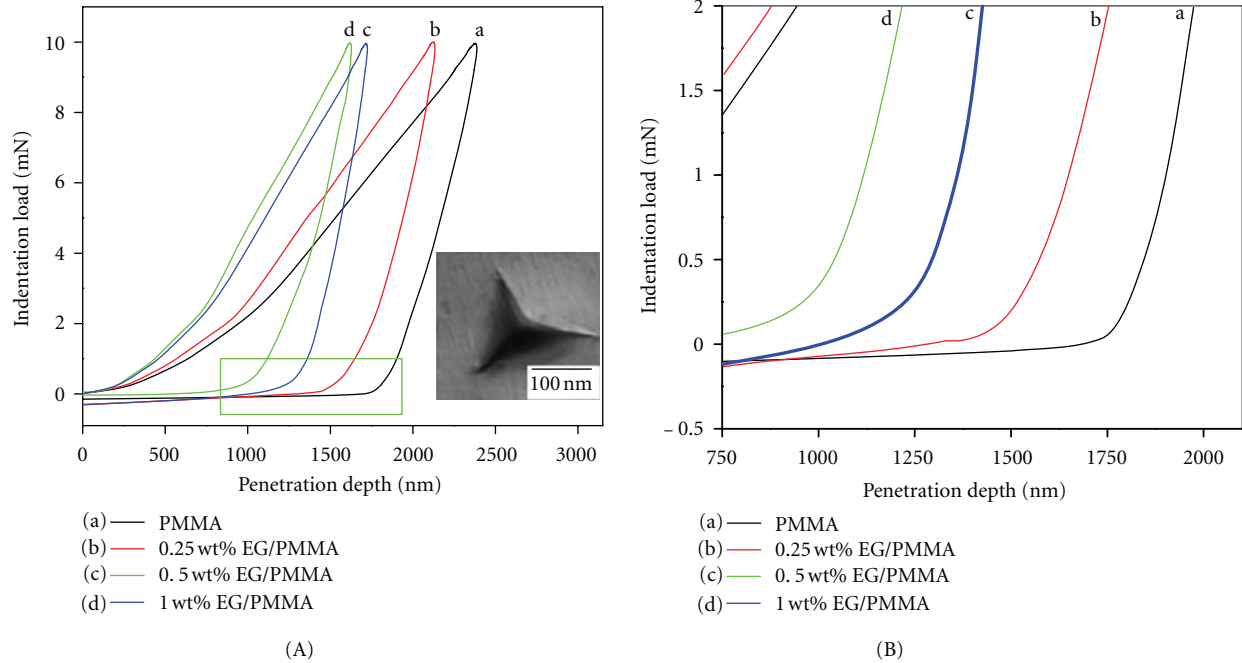


FIGURE 2: (A) Load-penetration depth curves for unreinforced PMMA and EG reinforced PMMA composites at 10 mN load and (B) enlarge view of the elastic recovery of the unreinforced PMMA and EG reinforced PMMA composites.

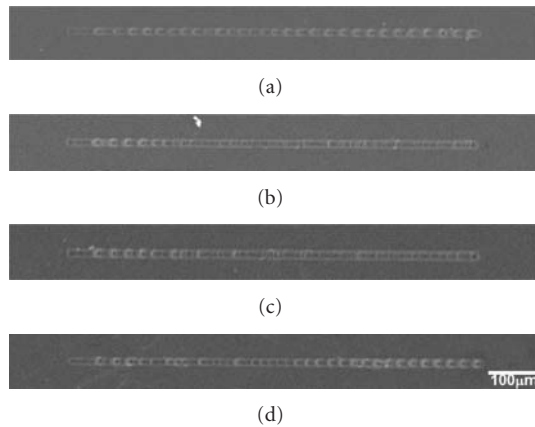


FIGURE 3: SEM micrographs of scratch deformed surface of (a) unreinforced PMMA, (b) 0.25 wt% EG/PMMA, (c) 0.5 wt% EG/PMMA, and (d) 1 wt% EG/PMMA composites.

(Figure 2(B)) of the bottom portion of unloading load-penetration depth curves. This is attributed mainly due to the effect of higher EG reinforcement on the measured hardness. For the 1 wt.% EG/PMMA composite, the elastic recovery is less as compared to the 0.5 wt.% EG/PMMA composite, which results in lesser hardness values of the same. This might be due to the agglomeration of the reinforced EG (Figure 1(b)) with increase in the content of the reinforcements.

In the scratch test with continues fixed load, initially, the load and depth of penetration were significantly low along the scratch track. The load can be measured at any position along the track and also at any value of loading rate. Figures 3(a)–3(d) compares the SEM images of a scratch track in unreinforced PMMA and after incorporating the

different amount of EG in the PMMA matrix. From the SEM images it is possible to obtain valuable information such as the scratch track width and depth of the edge ridges. Scratch track width is measured at a load of 10 mN, and from Figures 4(a)–4(d) the scratch depths are found to be 9.6, 8.15, 7.89, and 6.73 nm for unreinforced PMMA and 0.25, 0.5, and 1 wt% EG/PMMA composites, respectively. The scratch hardness is found using (1) using the applied normal load and the scratch width at that load. In Figures 4(a)–4(d) the relation between coefficient of friction (COF) and the scratch depth are shown. It can be observed that the COF reduced with reducing the depth of penetration. On the other hand, with an increase in the amount of EG, both the depth of penetration and COF values were found to decrease more than that of the unreinforced PMMA.

In Figure 5, the calculated scratch hardness (H_S) was compared with the nanoindentation hardness (H_{IT}) and the nanoindentation modulus (E_{IT}). It was clearly observed that for the unreinforced PMMA and EG/PMMA composites, with the increase in EG content, the trend of scratch and indentation hardness follows the same pattern. But the calculated scratch hardness is found to be higher than the depth sensing instrumented hardness. A good correlation between the scratch hardness and the nanoindentation hardness was found. Both the hardness values increase with an increase in the amount of EG. The indentation modulus is also found to be improved for the EG/PMMA composites more than that of unreinforced PMMA.

4. Conclusion

EG/PMMA composites with various amount of reinforcement have been prepared by in situ melt mixing method.

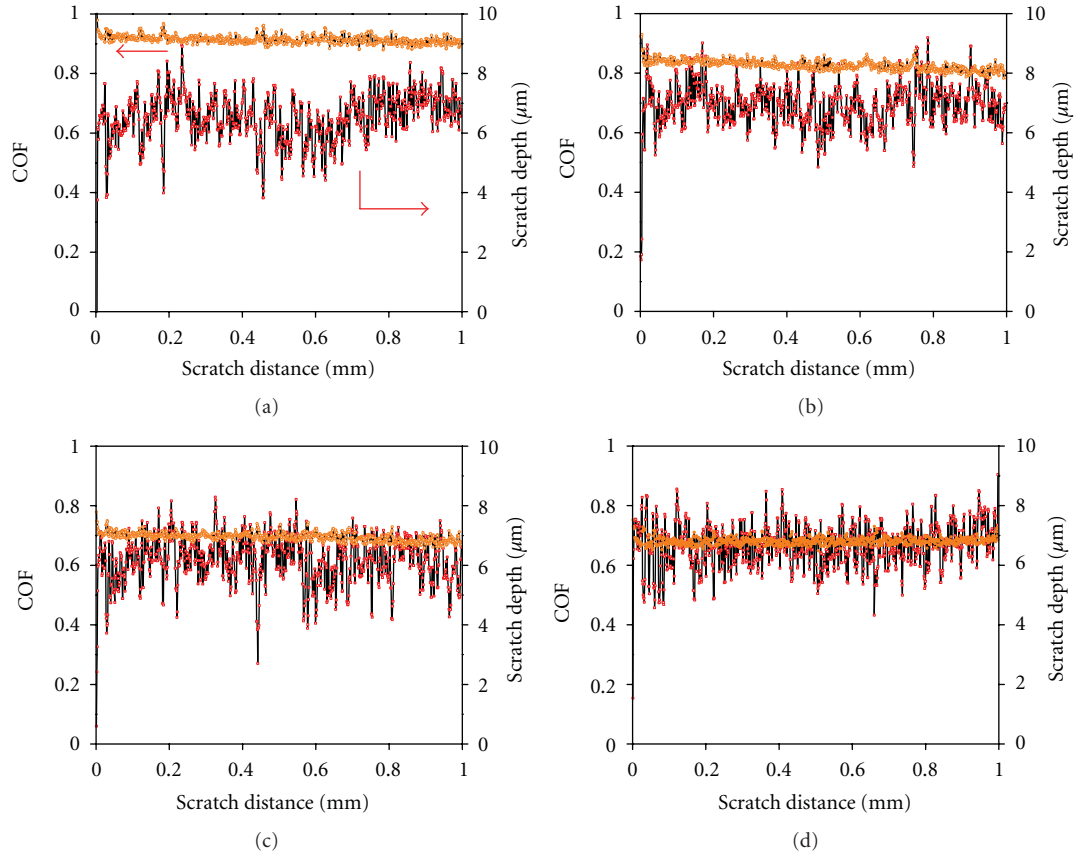


FIGURE 4: Variation of coefficient of friction (COF) and scratch depth with scratch distance for (a) unreinforced PMMA, (b) 0.25 wt.% EG/PMMA, (c) 0.5 wt.% EG/PMMA, and (d) 1 wt.% EG/PMMA composites.

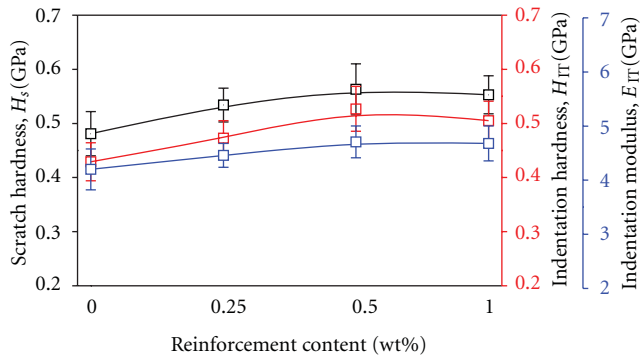


FIGURE 5: Comparison between the scratch hardness (H_s), indentation hardness (H_{IT}) and indentation modulus (E_{IT}), for unreinforced PMMA and EG/PMMA nanocomposites.

The hardness and elastic modulus by the nanoindentation technique of the unreinforced PMMA and EG/PMMA composites were measured. Scratch hardness was determined by single pass scratch test using scratch widths. The measured scratch hardness values were compared with conventional nanoindentation hardness and most interestingly it was observed that at lower indentation depth there is a good correlation between the scratch hardness and the nanoindentation hardness.

Acknowledgments

One of the authors (Himel Chakraborty) is indebted to the Human Resources Development Group, Council for Scientific and Industrial Research (HRDG-CSIR) India, for financial support through Senior Research Fellowship (Award no. 003(0061)2009-EMR-I).

References

- [1] G. Gonçalves, P. A. A. P. Marques, A. B. Timmons et al., "Graphene oxide modified with PMMA via ATRP as a reinforcement filler," *Journal of Materials Chemistry*, vol. 20, no. 44, pp. 9927–9934, 2010.
- [2] D. Stojanovic, A. Orlovic, S. Markovic, V. Radmilovic, P. S. Uskokovic, and R. Aleksic, "Nanosilica/PMMA composites obtained by the modification of silica nanoparticles in a supercritical carbon dioxide-ethanol mixture," *Journal of Materials Science*, vol. 44, no. 23, pp. 6223–6232, 2009.
- [3] M. K. Singh, T. Shokuhfar, J. J. A. Gracio et al., "Hydroxyapatite modified with carbon-nanotube-reinforced poly (methyl methacrylate): a nanocomposite material for biomedical applications," *Advanced Functional Materials*, vol. 18, no. 5, pp. 694–700, 2008.
- [4] M. Tehrani, M. Safdari, and M. S. Al-Haik, "Nanocharacterization of creep behavior of multiwall carbon nanotubes/epoxy nanocomposite," *International Journal of Plasticity*, vol. 27, no. 6, pp. 887–901, 2011.

- [5] F. Mammeri, J. Teyssandier, C. Connan, E. L. Bourhis, and M. M. Chehimi, "Mechanical properties of carbon nanotube-PMMA based hybrid coatings: the importance of surface chemistry," *RSC Advances*, vol. 2, no. 6, pp. 2462–2468, 2012.
- [6] A. Y. Jee and M. Lee, "Mechanical properties of polycarbonate and poly (methyl methacrylate) films reinforced with surface-functionalized nanodiamonds," *Journal of Nanoscience and Nanotechnology*, vol. 11, no. 1, pp. 533–536, 2011.
- [7] A. Y. Jee and M. Lee, "Comparative analysis on the nanoindentation of polymers using atomic force microscopy," *Polymer Testing*, vol. 29, no. 1, pp. 95–99, 2010.
- [8] W. C. Oliver and G. M. Pharr, "Improved technique for determining hardness and elastic modulus using load and displacement sensing indentation experiments," *Journal of Materials Research*, vol. 7, no. 6, pp. 1564–1580, 1992.
- [9] W. C. Oliver and G. M. Pharr, "Measurement of hardness and elastic modulus by instrumented indentation: advances in understanding and refinements to methodology," *Journal of Materials Research*, vol. 19, no. 1, pp. 3–20, 2004.
- [10] A. C. Fischer-Cripps, "Critical review of analysis and interpretation of nanoindentation test data," *Surface and Coatings Technology*, vol. 200, no. 14–15, pp. 4153–4165, 2006.
- [11] D. Tranchida and S. Piccarolo, "On the use of the nanoindentation unloading curve to measure the young's modulus of polymers on a nanometer scale," *Macromolecular Rapid Communications*, vol. 26, no. 22, pp. 1800–1804, 2005.
- [12] U. D. Cakmak, T. Schöberl, and Z. Major, "Nanoindentation of polymers," *Meccanica*, vol. 47, no. 3, pp. 707–718, 2012.
- [13] Y. Hu, S. Zhou, and L. Wu, "Surface mechanical properties of transparent poly (methyl methacrylate)/zirconia nanocomposites prepared by in situ bulk polymerization," *Polymer*, vol. 50, no. 15, pp. 3609–3616, 2009.
- [14] M. Sangermano and M. Messori, "Scratch resistance enhancement of polymer coatings," *Macromolecular Materials and Engineering*, vol. 295, no. 7, pp. 603–612, 2010.
- [15] A. Dasari, Z. Z. Yu, and Y. W. Mai, "Fundamental aspects and recent progress on wear/scratch damage in polymer nanocomposites," *Materials Science and Engineering*, vol. 63, no. 2, pp. 31–80, 2009.
- [16] B. J. Briscoe, P. D. Evans, S. K. Biswas, and S. K. Sinha, "The hardnesses of poly (methylmethacrylate)," *Tribology International*, vol. 29, no. 2, pp. 93–104, 1996.
- [17] S. K. Sinha, T. Song, X. Wan, and Y. Tong, "Scratch and normal hardness characteristics of polyamide 6/nano-clay composite," *Wear*, vol. 266, no. 7–8, pp. 814–821, 2009.

Research Article

Preparation of Mesoporous Silica-Supported Palladium Catalysts for Biofuel Upgrade

Ling Fei, Harvind Kumar Reddy, Joshua Hill, Qianglu Lin, Bin Yuan, Yun Xu, Peter Dailey, Shuguang Deng, and Hongmei Luo

Department of Chemical Engineering, New Mexico State University, Las Cruces, NM 88003, USA

Correspondence should be addressed to Hongmei Luo, hluo@nmsu.edu

Received 15 February 2012; Accepted 29 March 2012

Academic Editor: Guifu Zou

Copyright © 2012 Ling Fei et al. This is an open access article distributed under the Creative Commons Attribution License, which permits unrestricted use, distribution, and reproduction in any medium, provided the original work is properly cited.

We report the preparation of two hydrocracking catalysts Pd/CoMoO₄/silica and Pd/CNTs/CoMoO₄/silica (CNTs, carbon nanotubes). The structure, morphologies, composition, and thermal stability of catalysts were studied by X-ray diffraction (XRD), scanning electron microscopy (SEM), Raman spectroscopy, transmission electron microscopy (TEM), energy-dispersive X-ray (EDX), and thermogravimetric analysis (TGA). The catalyst activity was measured in a Parr reactor with camelina fatty acid methyl esters (FAMEs) as the feed. The analysis shows that the palladium nanoparticles have been incorporated onto mesoporous silica in Pd/CoMoO₄/silica or on the CNTs surface in Pd/CNTs/CoMoO₄/silica catalysts. The different combinations of metals and supports have selective control cracking on heavy hydrocarbons.

1. Introduction

Large expansion of the human population has caused a sharp increase in energy consumption resulting in a rapid decrease in the earth's fossil reserves [1–6]. The combustion of fossil fuels releases a large amount of CO₂ and has caused serious climate changes and other global problems [6]. Biodiesel (fatty acid methyl esters, FAMEs), derived from renewable sources like biomass and animal fats, has been considered as clean, renewable, sustainable alternatives to fossil fuels and has received increasing attention as transportation fuel. A problem with transesterification products is that they are mainly composed of ester, which shows limited compatibility with petroleum-derived fuel because of high oxygen content, lower thermal stability, and poor cold flow properties [6, 7]. Posttreatment processes like hydrocracking or pyrolysis with hydrotreating must then be applied to eliminate oxygen and shorten carbon chains. These processes change the transesterified product to resemble conventional fuel derived from fossil sources [5]. This paper focuses on the preparation of catalysts for the hydrocracking process, which is one of the key processes to convert heavy feedstocks to high-quality fuels like gasoline and middle distillate [8–15].

The role and importance of catalysts in the hydrocracking processes has been intensely studied [14–27]. Generally, the hydrocracking catalysts composed of noble metals or transition metals paired with a mesoporous support have dual functions in the reaction process. These are (a) cracking C–C bonds from high-molecular weight hydrocarbons and (b) hydrogenating the unsaturated hydrocarbons formed in the cracking steps and/or were already present in the feedstock [17, 18]. The most conventional catalysts are NiW, NiMo, and CoMo bimetallic paired on a number of supports, including zeolite, silica-alumina, and alumina [19–22]. Recently, Pd-based catalysts have also been widely used due to their high activity on hydrocracking sulfur-free heavy hydrocarbons [24–27]. Besides the catalyst compositions, it was also found that the selectivity of a catalyst highly depends on the support materials and dispersion of metals in the supports [16, 26]. Due to specific interaction between metals and supports, different supports can result in distinctive results.

Carbon nanotubes (CNTs), one of the most important materials since it was discovered, have been widely applied to composite materials, lithium ion batteries, supercapacitors, microelectronics, probe microscopy, and miscellaneous

energy storage [28, 29]. Its high accessible surface area and chemical stability also make it a promising candidate for use as a catalyst support. Metal-decorated CNTs applied in the field of catalysis have shown interesting catalytic properties and outstanding performance. For example, Pd-CNT has been proved to be very efficient in catalyzing Suzuki-Miyaura couplings [30, 31]. Inspired by previous reports, we are interested in designing Pd/CoMoO₄/silica and Pd/CNTs/CoMoO₄/silica catalyst systems for hydrocracking. On the one hand, Pd and CoMoO₄ are catalysts for hydrocracking; on the other, the CoMo bimetallic supported on silica has been reported as good catalyst for growing CNTs [32, 33] and has also proven to be effective on hydrodesulfurization, which helps lower the chance of sulfur poisoning the Pd catalyst [34, 35].

Herein, we report the synthesis of two catalysts: Pd directly loaded on a silica support and Pd loaded on CNTs. The performance of the catalytic production of jet fuel range carbon-chained molecules (C8–C16) from camelina fatty acid methyl esters (FAMES) shows that the two catalysts have good selectivity in a hydrocracking test.

2. Experimental Procedures

2.1. CoMoO₄ Catalyst Prepared by Polymer-Assisted Solution Method. 0.291 g Co (NO₃)₂ · 6H₂O and 0.353 g (NH₄)₆Mo₇O₂₄ · 4H₂O were dissolved together. 0.808 g ethylenediaminetetraacetic acid (EDTA) and 1.62 g polyethyleneimine (PEI, 50 wt%, from Sigma-Aldrich, average $M_n \sim 60,000$, $M_w \sim 750,000$) were dissolved in about 35 mL H₂O. The previous two solutions were mixed under magnetic stirring for 10 min. The solution was heated at 600 °C in air for 1 hour with a ramping rate of 1 °C/min.

2.2. CoMoO₄ Catalyst Incorporated into Mesoporous Silica (CoMoO₄/Silica). 0.06 g CoMoO₄ catalyst was dispersed in deionized water to form a suspension, into which 1 g silica (70–230 mesh, 60 Å) was added. The suspension was aged at room temperature overnight and then heated at 600 °C in air for 1 hour with a ramp rate of 1 °C/min (6 wt% CoMoO₄ loading).

2.3. Pd/CoMoO₄/Silica Catalyst by the Reduction of Pd. 0.108 g Pd(NO₃)₂ · 2H₂O, 0.294 g sodium citrate, and 0.198 g sodium ascorbate were each dissolved in water in 3 separate tubes. Deionized water was added to 1.56 g CoMoO₄/silica, in which Pd(NO₃)₂ solution was then added under magnetic stirring. Then sodium citrate solution was added to the mixture. After another 10 min, sodium ascorbate was added. The final product was obtained after stirring the mixture solution for 30 min and then drying at 90 °C overnight (5 wt% Pd loading).

2.4. Pd/CNTs/CoMoO₄/Silica Catalyst. All steps remained the same in the preparation of Pd/CoMoO₄/silica, except that CNTs were grown before the reduction of Pd. CNTs were grown by chemical vapor deposition (CVD): the CoMoO₄/silica was reduced in H₂ flow at 500 °C for 0.5 hours. The flow was then changed to He for 0.5 hours. Next,

the CoMoO₄/silica was exposed to a flow of pure C₂H₂ for 1 hour. Finally, the furnace was cooled to room temperature.

2.5. Characterization. The phase and structure of the catalysts were characterized by X-ray diffraction (XRD) using Cu radiation on a powder Scintag XRD operating at 45 kV and 36 mA. The morphology, microstructure, and composition were investigated by H-7650 transmission electron microscopy (TEM) and S-3400 N II scanning electron microscope equipped with energy-dispersive X-ray (EDX). Raman spectroscopy was performed using 632.8 nm (1.96 eV) laser excitation. Thermogravimetric analysis (TGA) was performed by Pyris 1 TGA. The Brunauer-Emmett-Teller (BET) specific surface area of the samples was determined by an ASAP 2010 using the standard N₂ adsorption and desorption isotherm measurements at 77 K.

The hydrocracking of camelina biodiesel reaction was carried out in a PARR 4593 stainless steel bench top reactor accompanied by a 4843 controller unit (Parr Instrument Company). Feedstock camelina fatty acid methyl esters (FAMES) were fed to the reactor along with 10 wt% of catalyst. The reactor was purged with nitrogen twice to remove oxygen present in the reactor. The temperature was then raised up to 300 °C in 25 min, and the reaction was carried out for 2 hours. Hydrogen was supplied to the reactor semicontinuously at 450 psi pressure during entire course of reaction, as it also acted as a carrier gas for removing CO₂ and H₂O formed during the reaction. After completion of the reaction, the reactor was cooled down to room temperature and the product sample was collected. The crude processed fuel was then analyzed with gas chromatography-mass spectrometry (GC-MS) system composed of an Agilent 5975 C MSD and an Agilent 7890 A GC equipped with a capillary column (DB-23, 60 m × 250 mm × 0.15 mm nominal).

3. Results and Discussion

A recent report on bimetallic catalysts pointed out that chemically bonded bimetallic catalysts have a synergistic effect in reactions and that catalysts with more than two metal substances were mostly prepared by physical mixture method [23]. The method used here to prepare CoMoO₄ is polymer-assisted chemical solution method [36, 37]. In the solution, soluble polymers bind to the metal ions to prevent premature precipitation. The calcination removing of polymers leads to high surface area sponge-like oxides. CoMoO₄ was then incorporated into silica gel by incipient wetness impregnation. Subsequently, Pd/CoMoO₄/silica was obtained by the addition of Pd(NO₃)₂ precursor and a reducing agent in CoMoO₄/silica [38]. The second catalyst, Pd/CoMoO₄/CNTs/silica, was prepared in the same procedure, except that CNTs were grown before the Pd-reducing step.

Figure 1(a) shows the XRD pattern of CoMoO₄. All the peaks can be indexed to CoMoO₄ (JCPDS, number 21-0868). By applying Scherrer's equation in (1) on three main peaks, the average grain size calculated is around 29 nm:

$$D = \frac{0.89\lambda}{\beta \cos \theta}, \quad (1)$$

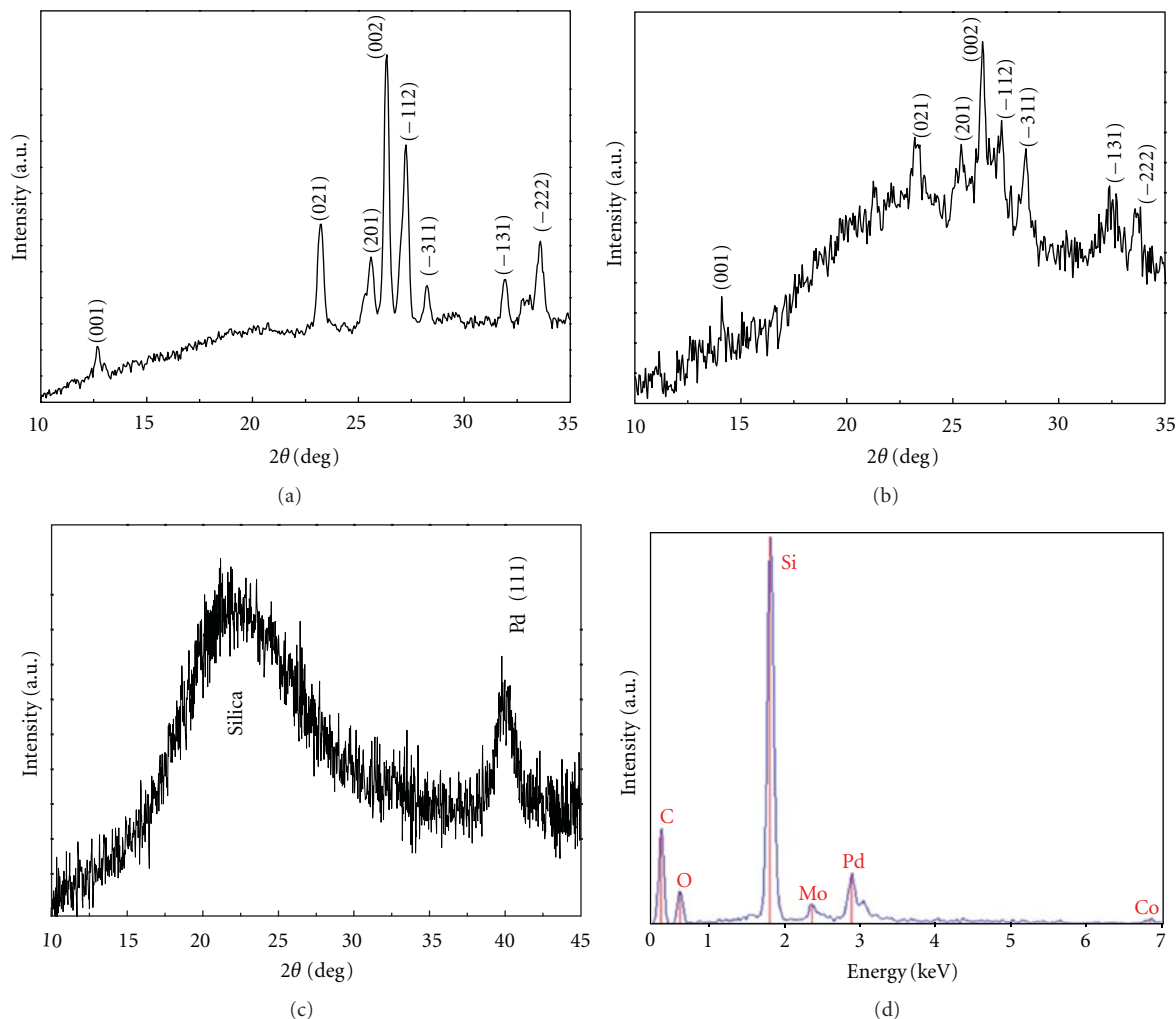


FIGURE 1: XRD patterns of CoMoO_4 (a), $\text{CoMoO}_4/\text{silica}$ (b), $\text{Pd}/\text{CoMoO}_4/\text{silica}$ (c), and EDX of $\text{Pd}/\text{CoMoO}_4/\text{silica}$ catalysts (d).

where D is the average grain size, factor 0.89 is characteristic of spherical objects, λ is the X-ray wavelength, β is the full-width at half-maximum of the diffraction peaks, and θ is the diffraction peak angle, respectively.

Figure 1(b) shows 6 wt% CoMoO_4 incorporated into amorphous mesoporous silica. Only several main peaks of CoMoO_4 remain as compared with Figure 1(a) due to its small ratio in silica. In Figure 1(c), 5 wt% palladium is reduced and incorporated into the $\text{CoMoO}_4/\text{silica}$. The observed Pd (111) peak indicates that $\text{Pd}(\text{NO}_3)_2$ was successfully reduced at room temperature. Since the intensities of palladium and silica background are stronger than CoMoO_4 peaks, it is hard to identify CoMoO_4 peaks here. In Figure 1(d), the EDX analysis confirms the presence of Co and Mo in the catalysts with the C peak from the carbon grid. The XRD and EDX analyses show that the $\text{Pd}/\text{CoMoO}_4/\text{silica}$ catalysts have been synthesized successfully step by step.

For the $\text{Pd}/\text{CoMoO}_4/\text{CNTs}/\text{silica}$ catalyst, which can be seen in Figure 2(a), the SEM image shows that the catalyst surface is well covered by CNTs, which is consistent with a sharp decrease in BET surface area of the catalyst after

CNT growth. The BET surface area of $\text{Pd}/\text{CoMoO}_4/\text{silica}$ is $243 \text{ m}^2/\text{g}$, while $\text{Pd}/\text{CNTs}/\text{CoMoO}_4/\text{silica}$ is only $8 \text{ m}^2/\text{g}$. Compared with mesoporous silica with a surface area of $500 \text{ m}^2/\text{g}$, the lower surface area of $\text{Pd}/\text{CoMoO}_4/\text{silica}$ is attributed to the impregnation of CoMoO_4 and Pd; the extremely lower surface area of $\text{Pd}/\text{CNTs}/\text{CoMoO}_4/\text{silica}$ is due to the coverage of CNTs. In the Raman spectrum shown in Figure 2(b), D band ($\sim 1330 \text{ cm}^{-1}$) and G band ($\sim 1595 \text{ cm}^{-1}$) indicate the presence of carbon material. High D band indicates that lots of defects existed in the CNTs, which corresponded to TEM images (Figure 3(c)) which show that the surface of CNT is in fact not smooth. From TEM images in Figure 3, we can also see that the CNTs are multiwalled with a diameter as large as 150 nm. The rough surface of CNTs is amorphous and good for palladium embedding. As can be confirmed in Figures 3(d), 3(e), and 3(f) palladium particles are almost evenly embedded onto the surface of CNTs. Therefore, even though the BET surface of the $\text{Pd}/\text{CoMoO}_4/\text{CNTs}/\text{silica}$ is low, the catalytic reaction surface is actually quite large, taking place on the surface of CNTs and guaranteeing the catalytic effectiveness.

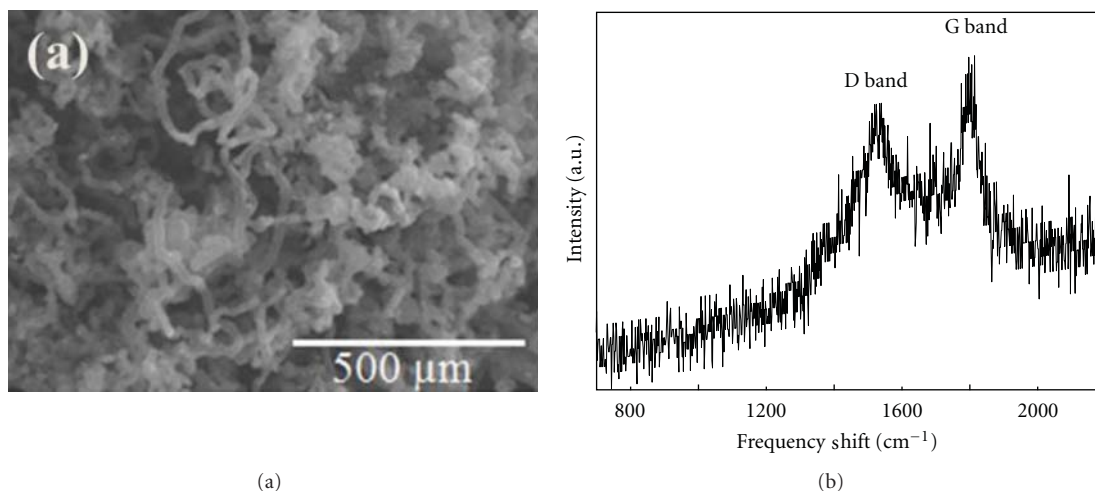


FIGURE 2: SEM image (a) and Raman spectrum (b) of Pd/CNTs/CoMoO₄/silica catalysts.

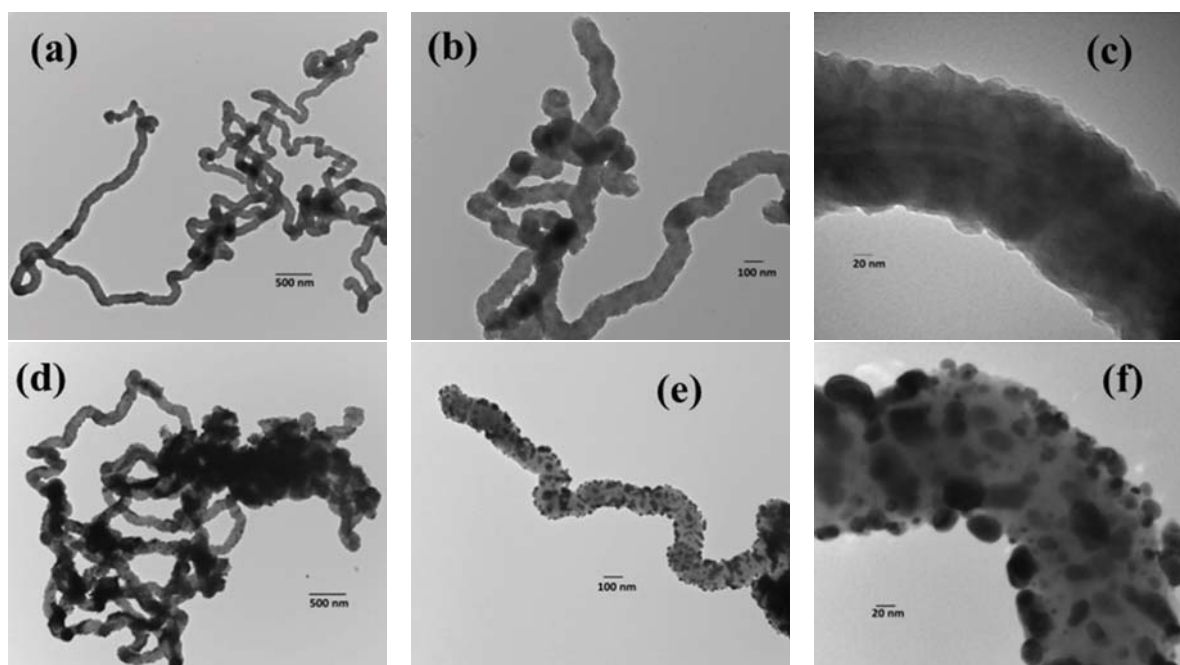


FIGURE 3: TEM images of CNTs/CoMoO₄/silica (a, b, and c) and Pd/CNTs/CoMoO₄/silica catalysts (d, e, and f).

As displayed in Figure 4, the TGA curve reveals that the CNTs begin to decompose at around 500°C, which means that the catalyst is stable at the reaction temperature of 300°C. This shows good thermal stability of the catalysts. There is about 45 wt% CNTs in the catalyst. The high percentage of CNTs offers large surface area for catalysts anchoring, leading to high and uniform catalysts dispersion, thus improving catalyst selectivity [26].

The GC-MS analytical results of the upgraded fuel samples are shown in Figure 5. Without catalysts, the target C8–C16 carbon-chained molecules percentage is far lower than 5%, except when looking at C15. In comparison, the two

catalysts have obviously increased the target group of hydrocarbons with a different product range. Pd/CoMoO₄/silica catalysts are inclusively effective on C8, C14, and C16, while Pd/CNTs/CoMoO₄/silica shows a broad range of impact from C10–C16 with C15 as the most favorable product. Due to the short reaction time, few unsaturated hydrocarbons are observed (C14:1, C15:1, C16:1). We speculate that the selectivity shown in the two catalysts is originated from the different dispersion of metals in the two supports. For Pd/CoMoO₄/silica, both Pd and CoMoO₄ are loaded in mesopores of silica, where they are in close contact and can actively react with feedstock. For Pd/CNTs/CoMoO₄/silica,

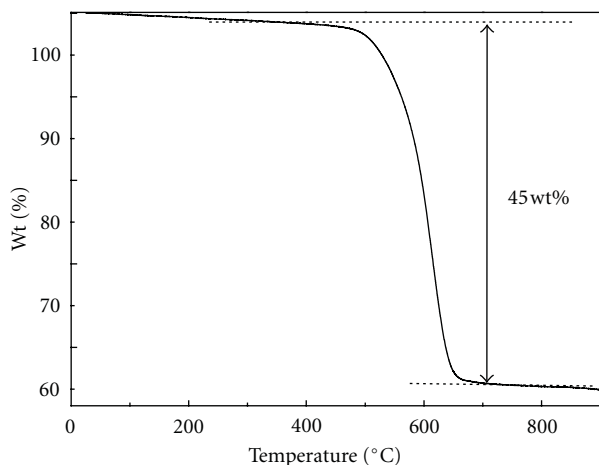


FIGURE 4: TGA curve of Pd/CNTs/CoMoO₄/silica catalysts.

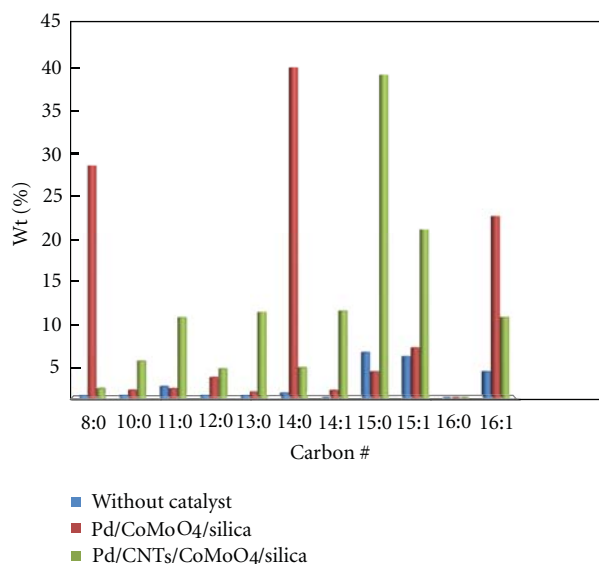


FIGURE 5: Hydrocracking performance of Pd/CoMoO₄/silica and Pd/CNTs/CoMoO₄/silica: C₈–C₁₆ fraction before and after hydrocracking. C_{*n*:0} indicates saturated hydrocarbons, and C_{*n*:1} for the unsaturated ones.

Pd is loaded on the surface of the CNTs while CoMoO₄ is loaded in the mesopores of silica. In this case, Pd and CoMoO₄ are separated by the second support—CNTs—and have a small chance to cooperate with each other. This separation is indicated by the extremely small BET surface area of Pd/CNTs/CoMoO₄/silica.

For Pd/CoMoO₄/silica, the catalyst support is mesoporous silica. When CoMoO₄ is loaded on silica, it may locate either on the surface of silica or in the pores of silica. The CoMoO₄ coverage of pores in silica results in the decrease of BET surface area. As CNTs grow on CoMoO₄ catalysts, CNTs further block the pores of silica. Therefore, it results in sharp decrease of BET surface area. Under this situation, the role

of mesoporous silica is not significant for the hydrocracking reaction. However, it is still crucial for the structure and morphology of the catalysts. Because its mesopores offer space for CoMoO₄, thus CoMoO₄ can evenly load on the support and CNTs can grow on CoMoO₄. If without silica, the CoMoO₄ may aggregate together. Therefore, the selectivity of the Pd/CoMoO₄/silica may be attributed to the synergic effect of Pd and CoMoO₄, as Pd/CNTs/CoMoO₄/silica only has Pd as the active ingredient. Also, the reaction sites may have influence on the selectivity as well: one with reaction sites in mesopores of silica and the other with reaction sites on CNTs' surface.

4. Conclusions

Two nanocomposite catalysts, Pd/CoMoO₄/silica and Pd/CNTs/CoMoO₄/silica, were prepared and their catalytic performance was tested in the hydrocracking of camelina FAMES. The catalyst supports played important roles in the catalytic process. Different support resulted in different selectivity of specific target groups due to synergism between metals and different reaction sites where the catalysts were loaded. Overall, the two catalysts both show high conversion and selectivity in a hydrocracking catalytic reaction. They are very promising and look to make a large impact in the application of biofuel upgrade.

Acknowledgment

The authors acknowledge the funding support from the Department of Defense, Air Force Research Laboratory, through contract FA8650-11-C-2127. They do not have a conflict of interest and do not have direct financial relation with the commercial identity mentioned in the paper.

References

- [1] A. Srivastava and R. Prasad, "Triglycerides-based diesel fuels," *Renewable & Sustainable Energy Reviews*, vol. 4, no. 2, pp. 111–133, 2000.
- [2] M. Snäre, I. Kubičková, P. Mäki-Arvela, K. Eränen, and D. Y. Murzin, "Heterogeneous catalytic deoxygenation of stearic acid for production of biodiesel," *Industrial and Engineering Chemistry Research*, vol. 45, no. 16, pp. 5708–5715, 2006.
- [3] G. Knothe, "Biodiesel and renewable diesel: a comparison," *Progress in Energy and Combustion Science*, vol. 36, no. 3, pp. 364–373, 2010.
- [4] G. W. Huber, S. Iborra, and A. Corma, "Synthesis of transportation fuels from biomass: chemistry, catalysts, and engineering," *Chemical Reviews*, vol. 106, no. 9, pp. 4044–4098, 2006.
- [5] G. W. Huber and A. Corma, "Synergies between bio- and oil refineries for the production of fuels from biomass," *Angewandte Chemie - International Edition*, vol. 46, no. 38, pp. 7184–7201, 2007.
- [6] E. W. Ping, R. Wallace, J. Pierson, T. F. Fuller, and C. W. Jones, "Highly dispersed palladium nanoparticles on ultra-porous silica mesocellular foam for the catalytic decarboxylation of stearic acid," *Microporous and Mesoporous Materials*, vol. 132, no. 1-2, pp. 174–180, 2010.

- [7] D. Kubička, P. Šimáček, and N. Žilková, "Transformation of vegetable oils into hydrocarbons over mesoporous-alumina-supported CoMo catalysts," *Topics in Catalysis*, vol. 52, no. 1-2, pp. 161–168, 2009.
- [8] P. Dufresne, P. H. Bigeard, and A. Billon, "New developments in hydrocracking: low pressure high-conversion hydrocracking," *Catalysis Today*, vol. 1, no. 4, pp. 367–384, 1987.
- [9] N. Ohshio, T. Enomoto, K. Honna et al., "Development of zeolite-based catalyst for resid hydrocracking," *Fuel*, vol. 83, no. 14-15, pp. 1895–1898, 2004.
- [10] J. W. Ward, "Hydrocracking processes and catalysts," *Fuel Processing Technology*, vol. 35, no. 1-2, pp. 55–85, 1993.
- [11] J. W. Scott and J. R. Kittrell, "Trends in the development of the modern hydrocracking process," *Industrial & Engineering Chemistry*, vol. 61, no. 7, pp. 18–22, 1969.
- [12] S. Zhang, D. Liu, W. Deng, and G. Que, "A review of slurry-phase hydrocracking heavy oil technology," *Energy and Fuels*, vol. 21, no. 6, pp. 3057–3062, 2007.
- [13] L. Pellegrini, S. Bonomi, S. Gamba, V. Calemma, and D. Molinari, "The 'all components hydrocracking model'," *Chemical Engineering Science*, vol. 62, no. 18–20, pp. 5013–5020, 2007.
- [14] B. Qiu, X. Yi, L. Lin, W. Fang, and H. Wan, "Influence of the incorporation of cobalt on non-sulfided Ni-H₃PW₁₂O₄₀/SiO₂ hydrocracking catalysts," *Catalysis Communications*, vol. 10, no. 9, pp. 1296–1299, 2009.
- [15] A. M. Alsobaai, R. Zakaria, and B. H. Hameed, "Hydrocracking of petroleum gas oil over NiW/MCM-48-USY composite catalyst," *Fuel Processing Technology*, vol. 88, no. 9, pp. 921–928, 2007.
- [16] E. Benazzi, L. Leite, N. Marchal-George, H. Toulhoat, and P. Raybaud, "New insights into parameters controlling the selectivity in hydrocracking reactions," *Journal of Catalysis*, vol. 217, no. 2, pp. 376–387, 2003.
- [17] M. A. Ali, T. Tatsumi, and T. Masuda, "Development of heavy oil hydrocracking catalysts using amorphous silica-alumina and zeolites as catalyst supports," *Applied Catalysis A*, vol. 233, no. 1-2, pp. 77–90, 2002.
- [18] A. M. Stumbo, P. Grange, and B. Delmon, "Spillover hydrogen effect on amorphous hydrocracking catalysts," *Catalysis Letters*, vol. 31, no. 2-3, pp. 173–182, 1995.
- [19] A. M. Alsobaai, R. Zakaria, and B. H. Hameed, "Gas oil hydrocracking on NiW/USY catalyst: effect of tungsten and nickel loading," *Chemical Engineering Journal*, vol. 132, no. 1–3, pp. 77–83, 2007.
- [20] Y. Rezgui and M. Guemini, "Effect of acidity and metal content on the activity and product selectivity for n-decane hydroisomerization and hydrocracking over nickel-tungsten supported on silica-alumina catalysts," *Applied Catalysis A*, vol. 282, no. 1-2, pp. 45–53, 2005.
- [21] I. Morawski and J. Mosio-Mosiewski, "Effects of parameters in Ni-Mo catalysed hydrocracking of vacuum residue on composition and quality of obtained products," *Fuel Processing Technology*, vol. 87, no. 7, pp. 659–669, 2006.
- [22] W. S. Choi, K. H. Lee, K. Choi, and B. H. Ha, "Hydrocracking of vacuum gas oil on CoMo/alumina (or silica-alumina) containing zeolite," *Studies in Surface Science and Catalysis*, vol. 127, pp. 243–250, 1999.
- [23] S. G. Jeon, J. Na, C. H. Ko, K. B. Yi, N. S. Rho, and S. B. Park, "Preparation and application of an oil-soluble CoMo bimetallic catalyst for the hydrocracking of oil sands bitumen," *Energy & Fuels*, vol. 25, no. 10, pp. 4256–4260, 2011.
- [24] J. Lee, S. Hwang, J. G. Seo, U. G. Hong, J. C. Jung, and I. K. Song, "Pd catalyst supported on SiO₂-Al₂O₃ xerogel for hydrocracking of paraffin wax to middle distillate," *Journal of Industrial and Engineering Chemistry*, vol. 17, no. 2, pp. 310–315, 2011.
- [25] K. M. Cho, S. Park, J. G. Seo et al., "Production of middle distillate in a dual-bed reactor from synthesis gas through wax cracking: effect of acid property of Pd-loaded solid acid catalysts on the wax conversion and middle distillate selectivity," *Applied Catalysis B*, vol. 83, no. 3-4, pp. 195–201, 2008.
- [26] I. Nam, K. M. Cho, J. G. Seo, S. Hwang, K. W. Jun, and I. K. Song, "Production of middle distillate from synthesis gas in a dual-bed reactor through hydrocracking of wax over mesoporous Pd-Al₂O₃ composite catalyst," *Catalysis Letters*, vol. 130, no. 1-2, pp. 192–197, 2009.
- [27] K. M. Cho, S. Park, J. G. Seo et al., "Effect of calcination temperature of alumina supports on the wax hydrocracking performance of Pd-loaded mesoporous alumina xerogel catalysts for the production of middle distillate," *Chemical Engineering Journal*, vol. 146, no. 2, pp. 307–314, 2009.
- [28] P. M. Ajayan and O. Z. Zhou, "Applications of carbon nanotubes," in *Carbon Nanotubes Synthesis, Structure, Properties and Applications*, M. S. Dresselhaus, G. Dresselhaus, and Ph. Avouris, Eds., Springer, Berlin, Germany, 2001.
- [29] H. Dai, "Carbon nanotubes: opportunities and challenges," *Surface Science*, vol. 500, no. 1–3, pp. 218–241, 2002.
- [30] P. P. Zhang, X. X. Zhang, H. X. Sun, R. H. Liu, B. Wang, and Y. H. Lin, "Pd-CNT-catalyzed ligandless and additive-free heterogeneous Suzuki-Miyaura cross-coupling of arylbromides," *Tetrahedron Letters*, vol. 50, no. 31, pp. 4455–4458, 2009.
- [31] X. Chen, Y. Hou, H. Wang, Y. Cao, and J. He, "Facile deposition of Pd nanoparticles on carbon nanotube microparticles and their catalytic activity for Suzuki coupling reactions," *Journal of Physical Chemistry C*, vol. 112, no. 22, pp. 8172–8176, 2008.
- [32] W. E. Alvarez, B. Kitiyanan, A. Borgna, and D. E. Resasco, "Synergism of Co and Mo in the catalytic production of single-wall carbon nanotubes by decomposition of CO," *Carbon*, vol. 39, no. 4, pp. 547–558, 2001.
- [33] V. M. Irurzun, Y. Tan, and D. E. Resasco, "Sol-gel synthesis and characterization of Co-Mo/silica catalysts for single-walled carbon nanotube production," *Chemistry of Materials*, vol. 21, no. 11, pp. 2238–2246, 2009.
- [34] N. Bejenaru, C. Lancelot, P. Blanchard et al., "Synthesis, characterization, and catalytic performances of novel CoMo hydrodesulfurization catalysts supported on mesoporous aluminas," *Chemistry of Materials*, vol. 21, no. 3, pp. 522–533, 2009.
- [35] Y. Fan, G. Shi, H. Liu, and X. Bao, "Selectivity enhancement of Co-Mo/Al₂O₃ FCC gasoline hydrodesulfurization catalysts via incorporation of mesoporous Si-SBA-15," *Fuel*, vol. 90, no. 5, pp. 1717–1722, 2011.
- [36] Q. X. Jia, T. M. McCleskey, A. K. Burrell et al., "Polymer-assisted deposition of metal-oxide films," *Nature Materials*, vol. 3, no. 8, pp. 529–532, 2004.
- [37] Q. Lin, Y. Xu, E. Fu et al., "Polymer-assisted chemical solution approach to YVO₄:Eu nanoparticle networks," *Journal of Materials Chemistry*, vol. 22, pp. 5835–5839, 2012.
- [38] X. S. Shen, G. Z. Wang, X. Hong, and W. Zhu, "Shape-controlled synthesis of palladium nanoparticles and their SPR/SERS properties," *Chinese Journal of Chemical Physics*, vol. 22, no. 4, pp. 440–446, 2009.

Research Article

Mechanical and Thermal Characteristics of Bio-Nanocomposites Consisting of Poly-L-lactic Acid and Self-Assembling Siloxane Nanoparticles with Three Phases

Masatoshi Iji and Naoki Morishita

Green Innovation Research Laboratories, NEC Corporation, 34 Miyukigaoka, Tsukuba, Ibaraki 305-8501, Japan

Correspondence should be addressed to Masatoshi Iji, m-iji@bk.jp.nec.com

Received 10 February 2012; Accepted 29 March 2012

Academic Editor: Guifu Zou

Copyright © 2012 M. Iji and N. Morishita. This is an open access article distributed under the Creative Commons Attribution License, which permits unrestricted use, distribution, and reproduction in any medium, provided the original work is properly cited.

Biopolymer nanocomposites (bio-nanocomposite) consisting of poly-L-lactic acid (PLLA) and siloxane nanoparticles with three phases, a high-density siloxane phase (plural cores), an elastomeric silicone phase, and a caprolactone oligomer phase, were developed to increase the mechanical properties of PLLA. The nanoparticles, average size of 13 nm, were self-assembled by aggregation and condensation of an organosiloxane with three units: isocyanatepropyltrimethoxysilane (IPTS), polymethylpropylloxysiloxane (PMPS), and a caprolactone oligomer (CLO), which form each phase. The bio-nanocomposite was produced using PLLA and the nanoparticles. Bending and tensile testing showed that the use of these nanoparticles (5 wt% in PLLA) greatly increases the tenacity (breaking strain) of PLLA while maintaining its relatively high breaking (maximum) strength. The elongation of the nanocomposite was more than twice that of PLLA while the elasticity modulus and breaking (maximum) strength were comparable to those of PLLA. The nanoparticles also increased the impact strength of PLLA. The use of the nanoparticles almost did not show adverse affect on the thermal resistance of PLLA. The nanocomposite's heat resistance indicated by the glass transition temperature and heat distortion temperature was fairly kept. The decomposition temperature of the nanocomposite somewhat increased.

1. Introduction

Polymer nanocomposites, usually consisting of polymers and nanometer-sized particles, have gathered high attentions because of their attracting characteristics [1]. In particular, inorganic nanometer-sized particles (nanoparticles) are mainly used as reinforcing fillers because they improve key characteristics of these composites at a relatively low content [2, 3]. For example, clay nanoparticles [4], metal oxide nanoparticles such as silica [5] and titania nanoparticles [6], and carbon nanotubes [7] increase the mechanical properties, especially the elasticity modulus, of many kinds of polymer composites. However, currently available nanoparticles insufficiently improve the tenacity (elongation at breaking point) of nanocomposites, which is necessary if nanocomposites are used in durable products such as electronic

equipments and automobiles. This is mainly because these nanoparticles lack rubber-like elasticity although they have an affinity for a polymer matrix. Adding a typical elastomer such as rubber or plasticizer (e.g., a long chain alkyl ester) with a high affinity for a polymer matrix, however, reduces the breaking strength and elasticity modulus of the composite due to their lack of rigidity [8, 9].

Nanoparticles with multiplephases, a high-density phase (core) with rigidity and outside phases with rubber-like elasticity and affinity for matrix polymers, should improve the tenacity of nanocomposites without degrading their breaking strength. Metal oxide nanoparticles are typically formed by hydrolysis and condensation reactions of organic metal compounds, mainly silicon alkoxides [10–14] and perhydropolysilazane [15], in solvents or polymers, that is,

a sol-gel method. However, the formation of multiple-phased nanoparticles using these organic metal compounds is difficult due to their limited chemical structures. Moreover, the use of conventional surface treatment agents such as organic metal alkoxides to uniformly form multiple phases on nanoparticles while preventing their coagulation is practically difficult because such treatment is an extremely complex process.

Poly-L-lactic acid (PLLA), a representative mass-produced biopolymer made of biomass (starch), is attractive for use in environmentally sensitive applications because its use prevents petroleum exhaust and reduces plastic waste due to its biodegradability after disposal. Although it has a relatively high breaking strength, its tenacity is extremely inadequate for it to be used in a variety of applications including durable products like those mentioned previously because of its stiff structure, which is due to the hard crystalline region. Studies on PLLA nanocomposites have focused on the usual nanoparticles such as clay and calcium carbonate ones [8, 16, 17]. However, to the best of the authors' knowledge, the use of multiphased nanoparticles to increase the tenacity of PLLA has not been reported.

We briefly reported self-assembling siloxane nanoparticles with three phases and a biopolymer nanocomposite (bio-nanocomposite) consisting of PLLA as a biopolymer and the nanoparticles that improve the tenacity of PLLA [18]. The nanoparticles consist of a high-density siloxane phase (plural cores), an elastomeric silicone phase, and a caprolactone oligomer phase. Self-assembly by aggregation and condensation of an organosiloxane with three units forms each phase. Testing showed that the use of the nanoparticles greatly increases the tenacity (breaking strain) of PLLA while maintaining its relatively high breaking strength.

In this paper, we report the detailed characterization of the nanoparticles with three phases and the mechanical and thermal characteristics of the bio-nanocomposite consisting of PLLA and the nanoparticles. The nanoparticles' outside and inside structures and size distribution were investigated. The influence of using the nanoparticles on PLLA's bending, tensile and impact strengths, heat resistance, and thermal decomposition resistance was revealed.

2. Experiment

2.1. Materials. Polymethylmethoxysiloxane (PMMS) (methoxy/methyl molecular ratio: 1/1, siloxane number: 8.0; Shin-etsu Kagaku Co., Japan; KC-89S), isocyanatepropyltrimethoxysilane (IPTS) (Azumax Co., Japan; SII645), and ϵ -caprolactone (Daicel Co., Japan; PLCCE) were used to produce the tested organosiloxanes. The analytical reagents, acetone, n-propanol, butanol, hexane, pyridine, tetrahydrofuran, dimethylsulfoxide (DMS) hydrogen chloride, methane sulfonic acid, thin octylate, and ammonium solution (28%), were obtained commercially and used as received. The poly-L-lactic acid (PLLA) (Mn: 900,000; TE-4000) was provided by Unitika Co. (Japan). The silica nanoparticles (average diameter: 12 nm; AEROJIL 200) were provided by Nippon Aerojil Co. (Japan).

2.2. Synthesis of Organosiloxanes. Organosiloxane with three units, isocyanatepropyltrimethoxysilane (IPTS), polymethylpropyloxysiloxane (PMPS), and a caprolactone oligomer (CLO), was prepared as follows.

PMPS was prepared by replacing the methoxy groups of polymethylmethoxysiloxane (PMMS) with propyloxy groups. PMMS (14.7 g, 25 mmol), n-propanol (45.0 g, 750 mmol), methane sulfonic acid (0.096 g, 10 mmol), and hexane (100 mL) were mixed and heated at 80°C for 5 hours in a nitrogen atmosphere while removing the formed methanol. After the reaction, the methane sulfonic acid was neutralized by adding pyridine (0.079, 10 mmol), and the resulting salt was removed using a paper filter. The remaining propanol was removed by evaporation. Almost all (more than 90%) methoxy was replaced by propyloxy, as determined by hydrogen-nuclear magnetic resonance (H-NMR) (Bruker Co., USA; BRUKER AVANCE 400; 400-MHz operation). (¹H-NMR [CDCl₃ (ppm)]: 0.14–0.27 (m, 24 H, Si-CH₃), 0.87–0.93 (m, 30 H, Si-OCH₂CH₂CH₃), 1.37–1.47 (m, 20 H, Si-OCH₂CH₂CH₃), 3.67–3.78 (m, 20 H, Si-OCH₂CH₂CH₃)).

The CLO was prepared by polymerizing ϵ -caprolactone by using butanol as an initiator; ϵ -caprolactam (22.8 g, 200 mmol), butanol (5.0 g, 67 mmol), and thin octylate (0.081 g, 0.020 mmol) were mixed for 10 hours at a room temperature. The unreacted materials were removed by evaporation. The resulting CLO had a molecular weight (Mn) of 550 as measured using a gel permeation chromatography (GPC) analyzer (Shimadzu Co., Japan; 10A-VP, standard material: Polystyrene, solvent: THF). The CLO was confirmed to be soluble in melted PLLA at 180°C.

The PMPS and CLO were then combined. PMPS (5.4 g, 6.0 mmol), CLO (3.3 g, 6.0 mmol), methanesulfonic acid (0.0058 g, 0.60 mmol), and toluene (20 mL) were mixed, and the resulting propanol was removed by evaporation. The methane sulfonic acid in the solution was neutralized by adding pyridine (0.047 g, 0.60 mmol), and the resulting salt was removed using a paper filter. The unreacted PMPS and CLO in the resulting compound were removed with a column with polystyrene particles. The reaction of the hydroxyl in the CLO with the propyloxy in PMPS was mostly completed (more than 90%), as determined by H-NMR. (¹H NMR [CDCl₃ (ppm)]: 0.14–0.27 (m, 24 H, Si-CH₃), 0.87–0.98 (m, 27 H, Si-OCH₂CH₂CH₃), 0.96 (t, 3 H, CH₃CH₂CH₂CH₂OCO-), 1.37–1.47 (m, 18 H, Si-OCH₂CH₂CH₃), 1.41 (m, 9 H, - (OCH₂CH₂CH₂CH₂CH₂CO)_n-OCH₂CH₂CH₂CH₃), 1.52–1.68 (m, 16 H, - (OCH₂CH₂CH₂CH₂CH₂CO)_n-OCH₂CH₂CH₂CH₃), 2.32 (m, 7 H, - (OCH₂CH₂CH₂CH₂CH₂CO)_n-), 3.67–3.78 (m, 18 H, Si-OCH₂CH₂CH₃), 3.85 (t, 2 H, Si-OCH₂CH₂CH₂CH₂CH₂CH₂OCO-), 4.09 (m, 7 H, - (OCH₂CH₂CH₂-CH₂CH₂CO)_{n-1}-OCH₂CH₂CH₂CH₃)).

The resulting compound consisting of PMPS and CLO was connected with IPTS, to produce the organosiloxane with IPTS, PMPS, and CLO. To promote reaction with the isocyanate in the IPTS, an adequate amount of the propyloxy group in the PMPS-CLO compound was changed to silanol by mixing the compound (3.8 g, 2.0 mmol),

diluted hydrogen chloride (pH 2.5, 1.5 g), and acetone (30 mL) for one hour. The hydrogen chloride in the solution was neutralized by adding sodium hydroxide (0.42 g, 10 mM), and then the water was removed by adding magnesium sulfate (50 g), which was recovered using a paper filter. The acetone was removed by evaporation. Approximately 13% of the propyloxy was changed to silanol, as determined by H-NMR. (^1H NMR [CDCl_3 (ppm)]: 0.14–0.27 (m, 24 H, Si- CH_3), 0.87–0.98 (m, 24 H, Si- $\text{OCH}_2\text{CH}_2\text{CH}_3$), 0.96 (t, 3 H, $\text{CH}_3\text{CH}_2\text{CH}_2\text{CH}_2\text{OCO}$ -), 1.37–1.47 (m, 15 H, Si- $\text{OCH}_2\text{CH}_2\text{CH}_3$), 1.41 (m, 9 H, $-(\text{OCH}_2\text{CH}_2\text{CH}_2\text{CH}_2\text{CH}_2\text{CO})_n-\text{OCH}_2\text{CH}_2\text{CH}_2\text{CH}_3$), 1.52–1.68 (m, 16 H, $-(\text{OCH}_2\text{CH}_2\text{CH}_2-\text{CH}_2\text{CH}_2\text{CO})_n-\text{OCH}_2\text{CH}_2\text{CH}_2\text{CH}_3$), 2.32 (m, 7 H, $-(\text{OCH}_2\text{CH}_2\text{CH}_2\text{CH}_2\text{CH}_2\text{CO})_n-$), 3.67–3.78 (m, 15 H, Si- $\text{OCH}_2\text{CH}_2\text{CH}_3$), 3.85 (t, 2 H, Si- $\text{OCH}_2\text{CH}_2\text{CH}_2\text{CH}_2\text{CH}_2\text{OCO}$ -), 4.09 (m, 7 H, $-(\text{OCH}_2\text{CH}_2\text{CH}_2\text{CH}_2\text{CH}_2\text{CO})_{n-1}-\text{OCH}_2\text{CH}_2\text{CH}_2\text{CH}_3$), 5.05–5.78 (br, 1 H, Si-OH)). The amount of silanol was almost the same as that of the isocyanate in the IPTS. The resulting PMPS-CLO compound containing the silanol (3.4 g, 2.0 mmol), ITMS (0.51 g, 2.5 mmol), and thin octylate (0.0081 g, 0.0020 mmol) was mixed in a nitrogen atmosphere at room temperature for 24 hours. The unreacted IPTS and PMPS-CLO compound in the final compound was removed using the same column. The reaction ratio of IPTS with the PMPS-CLO compound was 90%, as determined by H-NMR. (^1H NMR [CDCl_3 (ppm)]: 0.14–0.27 (m, 24 H, Si- CH_3), 0.62 (m, 2 H, Si- $\text{CH}_2\text{CH}_2\text{CH}_2$ -), 0.87–0.98 (m, 24 H, Si- $\text{OCH}_2\text{CH}_2\text{CH}_3$), 0.96 (t, 3 H, $\text{CH}_3\text{CH}_2\text{CH}_2\text{CH}_2\text{OCO}$ -), 1.37–1.47 (m, 15 H, Si- $\text{OCH}_2\text{CH}_2\text{CH}_3$), 1.41 (m, 9 H, $-(\text{OCH}_2\text{CH}_2\text{CH}_2\text{CH}_2\text{CH}_2\text{CO})_n-\text{OCH}_2\text{CH}_2\text{CH}_2\text{CH}_3$), 1.52–1.68 (m, 16 H, $-(\text{OCH}_2\text{CH}_2\text{CH}_2\text{CH}_2\text{CH}_2\text{CO})_n-\text{OCH}_2\text{CH}_2\text{CH}_2\text{CH}_3$), 1.60 (m, 2 H, Si- $\text{CH}_2\text{CH}_2\text{CH}_2$ -), 2.32 (m, 7 H, $-(\text{OCH}_2\text{CH}_2\text{CH}_2\text{CH}_2\text{CH}_2\text{CO})_n-$), 3.08 (m, 2 H, Si- $\text{CH}_2\text{CH}_2\text{CH}_2$ -), 3.55 (m, 9 H, Si- OCH_3), 3.67–3.78 (m, 15 H, Si- $\text{OCH}_2\text{CH}_2\text{CH}_3$), 3.85 (t, 2 H, Si- $\text{OCH}_2\text{CH}_2\text{CH}_2\text{CH}_2\text{CH}_2\text{OCO}$ -), 4.09 (m, 7 H, $-(\text{OCH}_2\text{CH}_2\text{CH}_2\text{CH}_2\text{CH}_2\text{CO})_{n-1}-\text{OCH}_2\text{CH}_2\text{CH}_2\text{CH}_3$), 5.45 (s, 1 H, NH)).

As references, an organosiloxane with IPTS and PMPS units and an organosiloxane with PMPS and CLO units were prepared using each unit and the methods described previously.

Moreover, the structures of these resulting organosiloxanes: the organosiloxane with IPTS, PMPS, and CLO units, the organosiloxane with IPTS and PMPS units, the organosiloxane with PMPS and CLO units, and the PMPS alone were measured by GPC as previously described to determine molecular weights and element analysis to determine the contents of carbon, hydrogen, and nitrogen (Elementar Co., Germany; vario MICRO cube, Burning furnace: 950°C, Reducing furnace: 550°C, Helium: 200 mL/min, Oxygen: 25–30 mL/min). The molecular weights and element contents are listed in Table 1, indicating that they mostly agreed with the calculated values.

2.3. Formation of Nanoparticles. Three-phased nanoparticles were formed by aggregation and condensation of the

organosiloxane with three units (IPTS, PMPS, and CLO) in two steps. The stepwise reactions were ascertained by H-NMR analysis for methoxy, propyloxy, and silanol.

The first step was core formation through hydrolysis and condensation of the methoxy in the IPTS unit. The organosiloxane with three units (1.9 g, 1.0 mmol), water (1.8 g, 100 mmol), ammonium solution (28%, 1.6 g), and tetrahydrofuran (THF, 10 mL) were mixed for 24 hours at room temperature. About 90% of the methoxy was consumed by hydrolysis, but the increase in silanol resulting from the methoxy was barely detected, demonstrating that most of the silanol formed siloxane bonds. Reaction of the propyloxy in the PMPS unit did not occur. The THF, water, and ammonia were removed by evaporation.

The second step was elastomeric silicone phase formation in the nanoparticles through hydrolysis and condensation of the propyloxy in the PMPS unit by heating at a high temperature in DMS, which has a higher boiling point (189°C). DMS (200 mL) was added to the resulting nanoparticles after the first step, followed by heating at 180°C for 20 minutes. After this step, there was almost complete (more than 90%) hydrolysis and condensation of the propyloxy in the nanoparticles.

The reference particle consisting of cores and elastic silicone phase (average diameter: 10 nm) was formed using the organosiloxane with IPTS and PMPS through the first step as aforementioned. The reference particle consisting of elastic silicone and CLO phases (average diameter: about 100 nm) was formed using the organosiloxane with PMPS and CLO through the second step as previously mentioned.

2.4. Production of Bio-Nanocomposites. A bio-nanocomposite consisting of PLLA and the three-phased nanoparticles was prepared as follows. After the first step (core formation), the THF, water, and ammonia were removed by evaporation. The resulting nanoparticles (5.0 g) were mixed with PLLA (95.0 g) in chloroform (500 mL), followed by removal of the solvent by evaporation. The resulting composite was extruded at 180°C for 10 minutes using a screw-type mixer (Thermo Electron Co., Germany; Mini Lab Haake Rheomex CTW5) and molded by pressing while heating at 180°C for 10 minutes at 100 kg/cm², followed by crystallization of the PLLA in the composite by heating at 100°C for 4 hours.

As references, PLLA composites containing the commercial silica nanoparticles, the two-phased nanoparticles, or the organosiloxane with PMPS and CLO were prepared using the method described previously. The two-phased nanoparticles (average diameter: 10 nm) were formed using the organosiloxane with IPTS and PMPS units through the core formation step as previously mentioned (the first step).

2.5. Measurements of Nanoparticles and Bio-Nanocomposites. The three-phased nanoparticles were observed with a scanning electron microscope (SEM) (Hitachi High-Technologies Co., Japan; HD-2300). Their size distribution and average diameter were measured with a light scattering analyzer (Microtrac Co., Japan; Nanotracer UPA-UT151).

To investigate the inside structure of the nanoparticles, the amounts of silicon and carbon in the nanoparticles were

TABLE 1: Molecular weights and element content of organosiloxanes.

Organosiloxane	Molecular weight (Mn)	Element content ratio (wt%)
	Measured/calculated	Measured/calculated
PMPS ⁽¹⁾	904/1062	C: 42.5/42.9 H: 8.8/8.9 N: <0.3/0
IPTS ⁽²⁾ + PMPS + CLO ⁽³⁾	1449/1695	C: 47.2/47.4 H: 8.6/8.6 N: 0.5/0.8
IPTS + PMPS	1083/1225	C: 41.5/41.1 H: 8.6/8.4 N: 0.6/1.1
PMPS + CLO	1433/1532	C: 48.9/49.9 H: 8.8/9.5 N: <0.3/0

⁽¹⁾ Polymethylpropyloxysiloxane.

⁽²⁾ Isocyanatepropyltrimethoxysilane.

⁽³⁾ Caprolactone oligomer.

determined using an SEM energy dispersive X-ray analyzer (SEM-EDX) (Hitachi High-Technologies Co., Japan; HD-2300).

The mechanical characteristics of the bio-nanocomposite, reference composites, and PLLA were measured by bending and tensile testing in accordance with JIS K 7171 using a bending and tensile testing instrument (Instron Co., USA; INSTRON 5567). The test pieces of the molded resin samples in the bending test were 2 mm thick, 40 mm long, and 25 mm wide. The test pieces in tensile testing were 1.2 mm thick, 70 mm long, and 4 mm wide. Furthermore, Izod-impact testing was conducted in accordance to JISK7110 using an impact testing instrument (Toyo Seiki CO., Japan; Universal Impact Tester C1). The test pieces with notch were 3.0 mm thick, 40 mm long, and 25 mm wide.

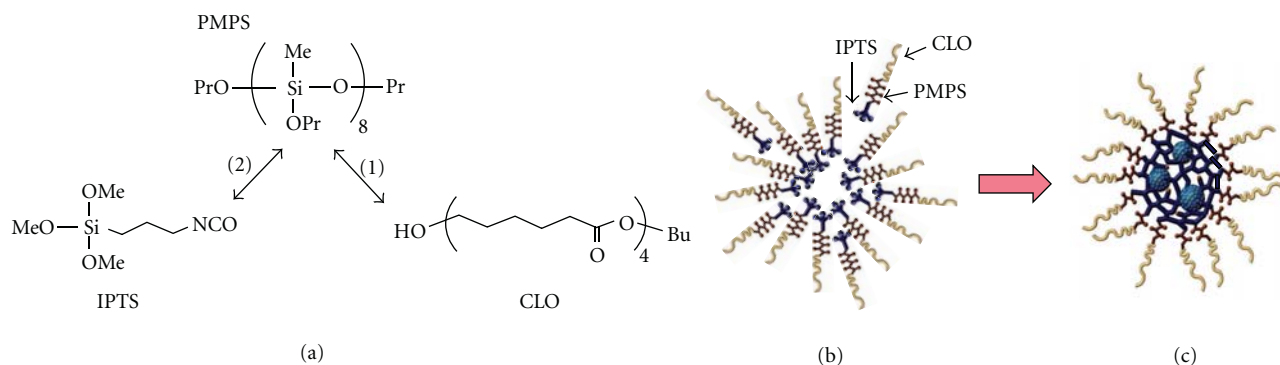
To evaluate thermal properties of the bio-nanocomposites and PLLA, their glass transition temperature (T_g) and melting temperature were measured by using differential scanning calorimetry (DSC) analysis of the samples (Perkin Elmer Co, USA; Perkin Elmer DSC-7 differential scanning calorimeter). The same thermal history as before the measurement was created by heating each sample from -20 to 220°C at a scanning rate of 20°C per minute, then keeping it at 220°C for 5 minutes, and finally quenching it to room temperature. Furthermore, heat distortion temperature of the molded resin samples was measured in accordance with JIS K 7191-2 using a heat distortion temperature measurement (Ueshima Seisakusho CO., Japan, TM-4126). The test pieces were 3.2 mm thick, 40 mm long, and 25 mm wide. The measurement was conducted by heating at a scanning rate of 2 centigrade per minute and loading at 1.8 MPa and 0.45 MPa. Thermal gravimetric analysis (TGA: Seiko Instruments Inc., Japan, EXSTAR 6000) of the resin samples was conducted in nitrogen by heating at 10 centigrade per minute.

3. Results and Discussions

3.1. Self-Assembly of Three-Phased Nanoparticles and Their Characterization. Scheme 1 illustrates the process used to prepare the organosiloxane with three units and the assumed self-assembly of the nanoparticles with three phases through aggregation and condensation of the organosiloxane, which consists of three units: isocyanatepropyltrimethoxysilane (IPTS), polymethylpropyloxysiloxane (PMPS), and a caprolactone oligomer (CLO).

IPTS was selected to form the high-density siloxane phase (plural cores) because it contains methoxy groups, which are highly polar and reactive, at a high molecular ratio, and thus preferentially aggregates and condensates, producing a rigidly cross-linked (high-density) siloxane network that forms more than one core in the particle. PMPS was selected to form the elastomeric silicone phase with an appropriate (nanometer) size around the cores because it contains propyloxy groups, which have moderate polarity and reactivity, at a low molecular ratio in an adequate-length siloxane chain (siloxane number: 8.0). Its use produces a loosely cross-linked (relatively low-density) siloxane network after the core formation. The CLO was selected to form the outside phase due to its low polarity compared with those of IPTS and PMPS and its high affinity for the PLLA matrix (it is highly soluble in melted PLLA). The organosiloxane was synthesized by mixing PMPS with CLO at a molecular ratio of 1 : 1 and then mixing the resulting compound with IPTS at a molecular ratio of 1 : 1.

The organosiloxane with three units dissolved in a solvent aggregated and formed the nanoparticles with three phases due to condensation by using water and a base catalyst (Schemes 1(b) and 1(c)). To avoid confusing the formation of the high-density siloxane cores with the formation of the elastomeric silicone phase around them, we initiated



SCHEME 1: Preparation of organosiloxane with three units (a) and self-assembly of three-phased nanoparticles through aggregation (b) and condensation (c) of organosiloxane.

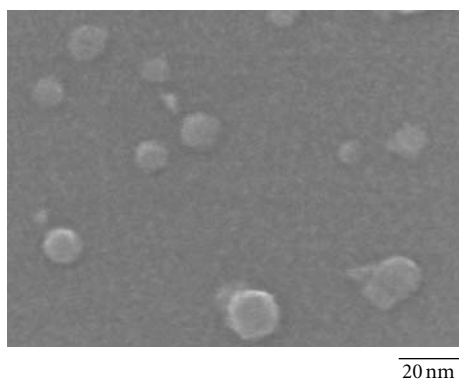


FIGURE 1: Observation of three-phased nanoparticles using scanning electron microscope.

two-step condensation of the organosiloxane by taking advantage of the higher reactivity of the methoxy groups in the IPTS unit than that of the propoxy groups in the PMPS unit. The first step was core formation through hydrolysis and condensation of the methoxy groups in the IPTS unit. The second step was elastomeric silicone phase formation through hydrolysis and condensation of the propoxy groups in the PMPS unit by heating.

As shown in Figure 1, the formed nanoparticles were observed with a scanning electron microscope (SEM). The size distribution, measured by light scattering analysis, indicated a relatively narrow size range, with an average diameter of 13 nm (Figure 2).

The inside structures of the nanoparticles were investigated by scanning electron microscopy and energy dispersive X-ray (SEM-EDX) analysis. Figure 3 shows the result for the amounts (intensities) of silicon and carbon that were detected along the cross section of a representative single nanoparticle in the nanoparticles shown in Figure 1. The amount of silicon originating from the IPTS and PMPS units was remarkably higher at several points around the center. This indicates that the nanoparticle had plural high-density siloxane cores formed mainly from the IPTS unit and that, around the cores, there was a relatively low-density siloxane

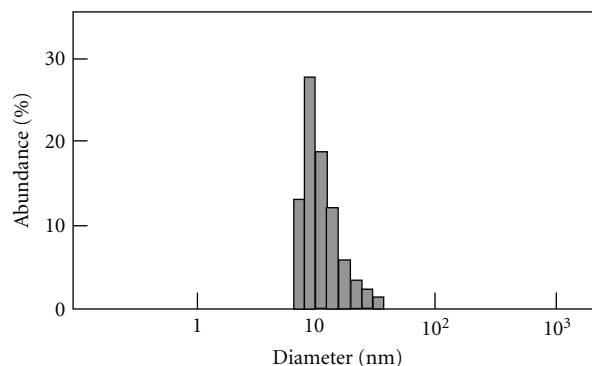


FIGURE 2: Size distribution of three-phased nanoparticles.

phase formed mainly from the PMPS unit. The amount of carbon, which originated from all the units, especially the CLO unit, did not significantly vary throughout the particle. This indicates that there was a relatively high concentration of carbon in the outer layer of the particle, meaning that the CLO unit formed the outside phase fairly well.

From these results, it seems reasonable that three-phased nanoparticles can be formed by self-assembly of the organosiloxane with three units, as shown in Schemes 1(b) and 1(c). The IPTS unit mainly performs the aggregation of the organosiloxane. The aggregated IPTS unit mainly forms the high-density cross-linked siloxane phase (plural cores) through preferential hydrolysis and condensation reactions of its methoxy groups. After the core formation, the PMPS unit mainly forms the middle phase, the relatively low-density cross-linked siloxane network (elastomeric silicone) around the cores through hydrolysis and condensation reactions of its propoxy groups. The CLO unit mainly forms the outside phase of the nanoparticles after the organosiloxane has aggregated because of its position and relatively low polarity.

3.2. Mechanical and Thermal Properties of Bio-Nanocomposite with Three-Phased Nanoparticles. Using PLLA and the three-phased nanoparticles at 5 wt%, we prepared a bio-nanocomposite to measure its mechanical and thermal properties.

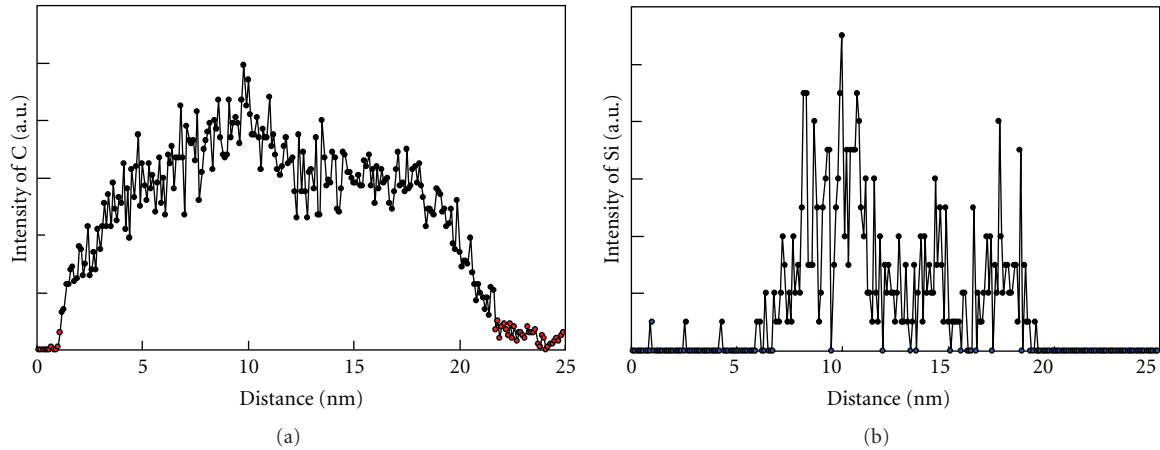


FIGURE 3: Analysis of silicon and carbon in three-phased nanoparticle by SEM-EDX: intensities of silicon (a) and carbon (b) detected along cross section of nanoparticle (The particle diameter: 23 nm).

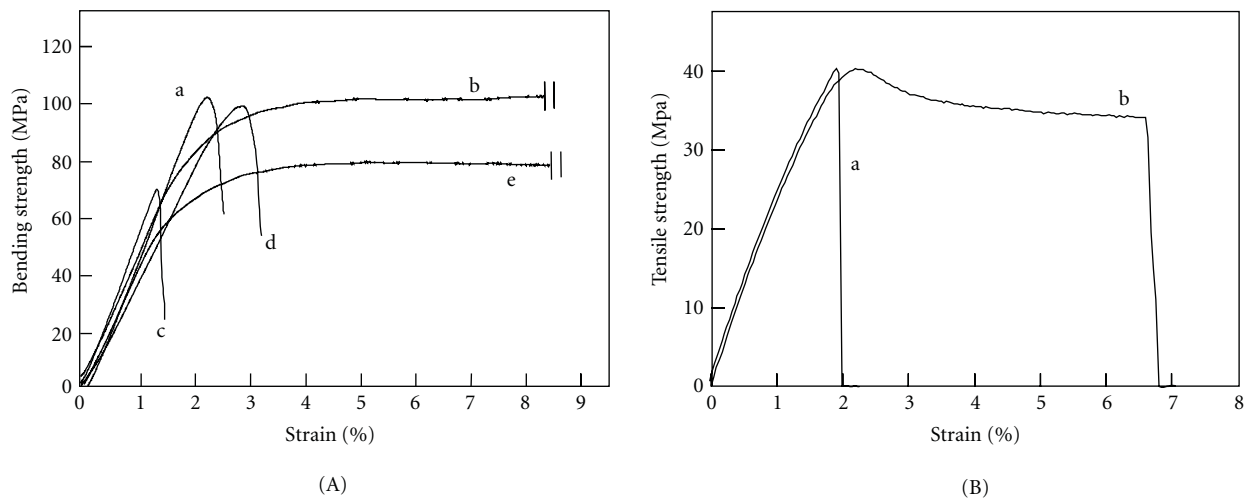


FIGURE 4: Flexural (A) and tensile (B) testing of bio-nanocomposite: (a) PLLA, (b) bio-nanocomposite consisting of PLLA and three-phased nanoparticles (5 wt%), (c) nanocomposite consisting of PLLA and silica nanoparticles (5 wt%), (d) nanocomposite consisting of PLLA and two-phased nanoparticles with cores and elastomeric silicone phase (5 wt%), and (e) composite consisting of PLLA and organosiloxane with PMPS and CLO (5 wt%).

As shown in bending and tensile tests of Table 2 and Figures 4(A) and 4(B), the three-phased nanoparticles greatly increased the PLLA's tenacity without degrading its high breaking strength. The elongation of the nanocomposite was more than twice that of PLLA while the elasticity modulus and breaking (maximum) strength were comparable to those of PLLA.

As references, PLLA composites containing commercial silica nanoparticles, two-phased nanoparticles (cores and elastomeric silicone phase), or the organosiloxane consisting of PMPS and CLO units were prepared using the method described previously. The composite containing the commercial silica nanoparticles, average diameter 12 nm, showed a slight increase in the modulus, but its strength and elongation were less than those of PLLA (Figure 4(A) (c)). The two-phased nanoparticles, average diameter of 10 nm, were formed using the organosiloxane with IPTS and PMPS

TABLE 2: Strength properties of bio-nanocomposite consisting of PLLA and three-phased nanoparticles (5 wt%).

	PLLA	Bio-nanocomposite with nanoparticles
Bending		
Strength (MPa)	100	99
Elastic modulus (GPa)	4.6	4.2
Strain (%)	2.2	9.7
Tensile		
Strength (MPa)	40	40
Elastic modulus (GPa)	2.1	1.8
Strain (%)	1.9	5.0
Izod impact strength (KJ/m ²)	4.3	5.1

TABLE 3: Thermal properties of bio-nanocomposite consisting of PLLA and three-phased nanoparticles (5 wt%).

	Glass transition temperature (°C)	Heat distortion temperature (°C) load: 0.45 MPa/1.80 MPa	Decomposition temperature (°C) /10% weight loss
PLLA	63	124/66	337
Bio-nanocomposite with nanoparticles	59	119/64	344

units through the same core formation step described previously. The composite containing the nanoparticles showed only a slight increase in elongation compared with that of PLLA (Figure 4(A) (d)). The composite containing the organosiloxane with PMPS and CLO (PMPS might be cross-linked when mixing with PLLA during heating) showed substantial increase in elongation compared with that of PLLA, but its strength and modulus were less (Figure 4(A) (e)). These mean that each phase in the three-phased nanoparticles is necessary to increase the PLLA's tenacity while maintaining its breaking strength and modulus.

These results suggest that the mechanism of the improved tenacity due to the use of the three-phased nanoparticles is as follows. During the initial period of the bio-nanocomposite deformation, the nanoparticles create a high elasticity modulus and maximize the strength because of their core rigidity and the high affinity of the outside CLO phase for the PLLA matrix. This idea is supported by the results that the reference organosiloxane with PMPS and CLO, not forming cores and also, the nanosilica, which aggregated in the PLLA composites due to its low affinity with PLLA, did not maintain such a high modulus and strength, simultaneously. In the middle and final periods of the deformation, the three-phased nanoparticles elongated the composite due to the rubber-like elasticity of the elastomeric silicone phase derived from PMPS and the plasticity of the outside CLO phase. While the nanosilica and the reference two-phased particles without the CLO phase did not perform such elongation of the PLLA composites, the organosiloxane with PMPS and CLO elongated the composite, which can support the proposed mechanism.

As listed in Table 2, Izod impact strength of the bio-nanocomposite consisting of PLLA and the three-phased nanoparticle was higher than that of PLLA (20%), indicating that the nanoparticles has a function to increase the strength. However, the effect was limited comparing with usual typical elastomers such as rubber or plasticizer [8]. It is mainly due to the nanoparticles' rigid cores, which can retard the role of the elastomeric phase in the nanoparticles as an impact absorber.

Furthermore, we have cleared the influence of adding the three-phased nanoparticles on the heat resistance of PLLA as listed in Table 3. The glass transition temperature and heat distortion temperature of the bio-nanocomposite consisting of PLLA and the nanoparticles slightly decreased comparing with PLLA, but these levels were fairly kept. Adding typical elastomers such as rubber or plasticizer reduces heat resistance of the composites [8]. However, the nanoparticles maintained the heat resistance of PLLA because of their

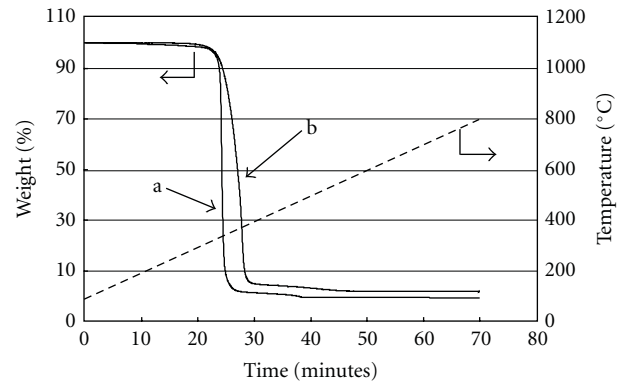


FIGURE 5: Thermal gravimetric analysis of bio-nanocomposite: (a) PLLA and (b) bio-nanocomposite consisting of PLLA and three-phased nanoparticles: 5 wt% (in N₂, 10°C/min).

cores' rigidity to retard the resin's deformation during heating as aforementioned.

The decomposition temperature of the bio-nanocomposite with PLLA and the nanoparticles somewhat increased comparing with PLLA (Table 3, Figure 5). The result was mainly caused by the formation of the cores with high-density cross-linking structures in the nanoparticles, which are resistant to the thermodegradation of the nanocomposites.

4. Conclusion

We reported on a bio-nanocomposite consisting of PLLA and self-assembling siloxane nanoparticles with three phases: a high-density cross-linked siloxane phase (plural cores), an elastomeric silicone phase around the cores, and an outside CLO phase with a high affinity for the PLLA matrix. These nanoparticles were self-assembled by aggregation and condensation of the organosiloxane with three units that, respectively, form each phase. The bio-nanocomposite was produced by mixing PLLA and the nanoparticles in a solvent and removing it. These nanoparticles increased the tenacity of the PLLA and its impacting strength. Bending and tensile test indicated that the elongation of the bio-nanocomposite consisting of PLLA and the nanoparticles was more than twice that of PLLA while the elasticity modulus and breaking (maximum) strength were comparable to those of PLLA. The izod impact strength of the bio-nanocomposite increased by 20 percent comparing with PLLA. The use of the nanoparticles almost did not show adverse affect on the thermal

resistance of PLLA. The heat resistance indicated by the glass transition temperature and heat distortion temperature of the bio-nanocomposite slightly decreased comparing with PLLA, but these levels were fairly kept. The decomposition temperature of the bio-nanocomposite somewhat increased. From these results, the bio-nanocomposite using the three-phased nanoparticles will be used in durable product applications and other new applications. These nanoparticles can also be applied to various other brittle polymers by modifying the structure of the outside phase to achieve a high affinity with these polymers.

Acknowledgments

The authors are grateful to Mr. Hiroyuki Kai, University of California, Berkeley, and Dr. Ryouta Yuge, NEC Corporation for their help with the production, observation, and analysis of the nanoparticles. The authors do not have any direct financial relation with the commercial identity mentioned in the paper.

References

- [1] E. Manias, "Nanocomposites: stiffer by design," *Nature Materials*, vol. 6, no. 1, pp. 9–11, 2007.
- [2] F. Hussain, M. Hojjati, M. Okamoto, and R. E. Gorga, "Review article: polymer-matrix nanocomposites, processing, manufacturing, and application: an overview," *Journal of Composite Materials*, vol. 40, no. 17, pp. 1511–1575, 2006.
- [3] J. Jordan, K. I. Jacob, R. Tannenbaum, M. A. Sharaf, and I. Jasiuk, "Experimental trends in polymer nanocomposites—a review," *Materials Science and Engineering A*, vol. 393, no. 1–2, pp. 1–11, 2005.
- [4] A. Usuki, N. Hasegawa, and M. Kato, "Polymer-clay nanocomposites," *Advances in Polymer Science*, vol. 179, pp. 135–195, 2005.
- [5] P. Rosso, L. Ye, K. Friedrich, and S. Sprenger, "A toughened epoxy resin by silica nanoparticle reinforcement," *Journal of Applied Polymer Science*, vol. 100, no. 3, pp. 1849–1855, 2006.
- [6] Z. Evgeni, T. Roza, M. Narkis, and S. Arnon, "Particulate multi-phase polymeric nanocomposites," *Polymer Composites*, vol. 27, no. 4, pp. 425–430, 2006.
- [7] M. Moniruzzaman and K. I. Winey, "Polymer nanocomposites containing carbon nanotubes," *Macromolecules*, vol. 39, no. 16, pp. 5194–5205, 2006.
- [8] T. Li, L. S. Turng, S. Gong, and K. Erlacher, "Polylactide, nanoclay, and core-shell rubber composites," *Polymer Engineering and Science*, vol. 46, no. 10, pp. 1419–1427, 2006.
- [9] M. Shibata, Y. Someya, M. Orihara, and M. Miyoshi, "Thermal and mechanical properties of plasticized poly(L-lactide) nanocomposites with organo-modified montmorillonites," *Journal of Applied Polymer Science*, vol. 99, no. 5, pp. 2594–2602, 2006.
- [10] C. S. Ha and W. Cho, "Microstructure and interface in organic/inorganic hybrid composites," *Journal of Polymer Advanced Technologies*, vol. 11, pp. 145–150, 2000.
- [11] Y. Chujo and T. Saegusa, "Organic polymer hybrids with silica gel formed by means of the sol-gel method," *Advances in Polymer Science*, vol. 100, pp. 10–29, 1991.
- [12] R. Tamaki and Y. Chujo, "Synthesis of polystyrene and silica gel polymer hybrids utilizing ionic interactions," *Chemistry of Materials*, vol. 11, no. 7, pp. 1719–1726, 1999.
- [13] G. Z. Li, L. Wang, H. Toghiani, T. L. Daulton, K. Koyama, and C. U. Pittman, "Viscoelastic and mechanical properties of epoxy/multifunctional polyhedral oligomeric silsesquioxane nanocomposites and epoxy/ladderlike polyphenylsilsesquioxane blends," *Macromolecules*, vol. 34, no. 25, pp. 8686–8693, 2001.
- [14] G. M. Kim, H. Qin, X. Fang, F. C. Sun, and P. T. Mather, "Hybrid epoxy-based thermosets based on polyhedral oligosilsesquioxane: cure behavior and toughening mechanisms," *Journal of Polymer Science B*, vol. 41, no. 24, pp. 3299–3313, 2003.
- [15] A. Yamano and H. Kozuka, "Preparation of silica coatings heavily doped with spiropyran using perhydropolysilazane as the silica source and their photochromic properties," *Journal of Physical Chemistry B*, vol. 113, no. 17, pp. 5769–5776, 2009.
- [16] L. Petersson and K. Oksman, "Biopolymer based nanocomposites: comparing layered silicates and microcrystalline cellulose as nanoreinforcement," *Composites Science and Technology*, vol. 66, no. 13, pp. 2187–2196, 2006.
- [17] L. Jiang, J. Zhang, and M. P. Wolcott, "Comparison of polylactide/nano-sized calcium carbonate and polylactide/montmorillonite composites: reinforcing effects and toughening mechanisms," *Polymer*, vol. 48, no. 26, pp. 7632–7644, 2007.
- [18] M. Iji, N. Morishita, and H. Kai, "Self-assembling siloxane nanoparticles with three phases that increase tenacity of poly L-lactic acid," *Polymer Journal*, vol. 43, no. 1, pp. 101–104, 2011.

Research Article

The Overall Effects of AlN Nanoparticle Addition to Hybrid Magnesium Alloy AZ91/ZK60A

Muralidharan Paramsothy,¹ Jimmy Chan,² Richard Kwok,² and Manoj Gupta¹

¹Department of Mechanical Engineering, National University of Singapore, 9 Engineering Drive 1, Singapore 117576

²CTO Office, Singapore Technologies Kinetics Ltd (ST Kinetics), 249 Jalan Boon Lay, Singapore 619523

Correspondence should be addressed to Manoj Gupta, mpegm@nus.edu.sg

Received 5 December 2011; Accepted 11 February 2012

Academic Editor: Hongmei Luo

Copyright © 2012 Muralidharan Paramsothy et al. This is an open access article distributed under the Creative Commons Attribution License, which permits unrestricted use, distribution, and reproduction in any medium, provided the original work is properly cited.

A hybrid magnesium alloy nanocomposite containing AlN nanoparticle reinforcement was fabricated using solidification processing followed by hot extrusion. The nanocomposite exhibited similar grain size to the monolithic hybrid alloy, reasonable AlN and intermetallic nanoparticle distribution, nondominant (0 0 0 2) texture in the longitudinal direction, and 17% higher hardness than the monolithic hybrid alloy. Compared to the monolithic hybrid alloy, the nanocomposite exhibited higher tensile yield strength (0.2% TYS) and ultimate tensile strength (UTS) without significant compromise in failure strain and energy absorbed until fracture (EA) (+5%, +5%, -14% and -10%, resp.). Compared to the monolithic hybrid alloy, the nanocomposite exhibited unchanged compressive yield strength (0.2% CYS) and higher ultimate compressive strength (UCS), failure strain, and EA (+1%, +6%, +24%, and +6%, resp.). The overall effects of AlN nanoparticle addition on the tensile and compressive properties of the hybrid magnesium alloy is investigated in this paper.

1. Introduction

Compared to aluminium, magnesium is the lightest structural metal (35% lighter) used in many engineering applications today [1, 2]. Commercially available magnesium alloys are suitable for actual or potential use regarding weight-critical applications in the automotive, aerospace, civil infrastructure, building and construction, defence, biomedical, and sports/recreational industries [1, 3]. In the World War 2 era, Mg-Zn alloy parts were economically manufactured and heavily used in aircraft [3]. Soon after the world war, Mg-Al alloys were also economically developed with specific metallurgical advantages over Mg-Zn alloys [3]. At present, Mg-Y and Mg-RE (Rare Earth) alloys are in development for even more specific metallurgical advantages but at generally higher cost compared to Mg-Zn and Mg-Al alloys [1]. Regardless of cast or wrought forms, Mg-Zn and Mg-Al alloys each still remain as the main classes of Mg alloys commercially in use. In the wrought form, the Mg alloys have good strength and ductility. However, wrought Mg-Zn and Mg-Al

alloy nanocomposites have often demonstrated simultaneously higher strength and ductility compared to the monolithic alloys [4–14]. Additionally, friction stir processed Mg-Al nanocomposites have also demonstrated higher hardness and strength than the corresponding monolithic alloys [15–18]. Based on much of the existing representative research literature on solidification processed magnesium alloy nanocomposites, good nanoparticle distribution can be achieved in the magnesium matrix and better mechanical properties can be achieved due to the addition of nanoparticles [4–18]. However, it is the addition of oxide- or carbon-based nanoparticles to magnesium alloys as opposed to nitride-based nanoparticle addition that most of the research literature currently discusses. In the context of magnesium composite processing, the magnesium-oxygen strong affinity and magnesium-carbon weak affinity (comparative to each other) are both well known. On the other hand, what is not known is the affinity between magnesium and nitrogen concerning effects in magnesium nanocomposite processing (let alone solidification processing).

Accordingly, one of the primary aims of this study was to simultaneously increase tensile strength and ductility of AZ91/ZK60A hybrid magnesium alloy with AlN nanoparticles. Another aim of the present study was to evaluate the compressive properties of AZ91/ZK60A/AlN hybrid alloy nanocomposite. Disintegrated melt deposition (DMD) [19, 20] followed by hot extrusion was used to synthesize the AZ91/ZK60A/AlN hybrid alloy nanocomposite.

2. Experimental Procedures

2.1. Materials. In this study, AZ91 (nominally 8.30–9.70 wt.% Al, 0.35–1.00 wt.% Zn, 0.15–0.50 wt.% Mn, 0.10 wt.% Si, 0.030 wt.% Cu, 0.005 wt.% Fe, 0.002 wt.% Ni, 0.02 wt.% others, balance Mg) and ZK60A (nominally 4.80–6.20 wt.% Zn, 0.45 wt.% Zr, balance Mg), both alloys supplied by Tokyo Magnesium Co. Ltd. (Yokohama, Japan) were used as matrix material. 3 parts AZ91 were mixed with 1 part ZK60A by mass to metallurgically downgrade AZ91. The intention of this mixing was to decrease the nominal aluminium content of AZ91 by 2 wt.%. AZ91 and ZK60A blocks were sectioned to smaller pieces. All oxide and scale surfaces were removed using machining. All surfaces were washed with ethanol after machining. AlN nanoparticles (99% purity, spherical, 10–20 nm size) supplied by Nanostructured & Amorphous Materials Inc (TX, USA) were used as the reinforcement phase.

2.2. Processing. Monolithic AZ91/ZK60A hybrid alloy (nominal aluminium content of AZ91 decreased by 2 wt.%) was cast using the DMD method [19, 20]. This involved heating AZ91 and ZK60A blocks to 750°C in an inert Ar gas atmosphere in a graphite crucible (A12 designated size of top OD: 171 mm, bottom OD: 121 mm, height: 210 mm) using a resistance heating furnace. The crucible was equipped with an arrangement for bottom pouring. Upon reaching the superheat temperature, the molten slurry was stirred for 2.5 min at 460 rpm using a twin blade (pitch 45°) mild steel impeller to facilitate the uniform distribution of heat. The impeller was coated with Zirtex 25 (86% ZrO₂, 8.8% Y₂O₃, 3.6% SiO₂, 1.2% K₂O and Na₂O, and 0.3% trace inorganics) to avoid iron contamination of the molten metal. The melt was then released through a 10 mm diameter orifice at the base of the crucible. The melt was disintegrated by two jets of argon gas oriented normal to the melt stream located 265 mm from the melt pouring point. The argon gas flow rate was maintained at 25 lpm. The disintegrated melt slurry was subsequently deposited onto a metallic substrate located 500 mm from the disintegration point. An ingot of 40 mm diameter was obtained following the deposition stage. To form the AZ91/ZK60A/1.5 vol% AlN hybrid alloy nanocomposite, AlN nanoparticle powder was isolated by wrapping in Al foil of minimal weight (<0.50 wt.% with respect to AZ91 and ZK60A total matrix weight) and arranged on top of the AZ91 and ZK60A alloy blocks (see Figure 1), with all other DMD parameters unchanged. All billets were machined to 35 mm diameter and hot-extruded using 20.25:1 extrusion ratio on a 150 ton hydraulic press. The extrusion temperature was 350°C. The billets were held at 400°C for 60 min in a

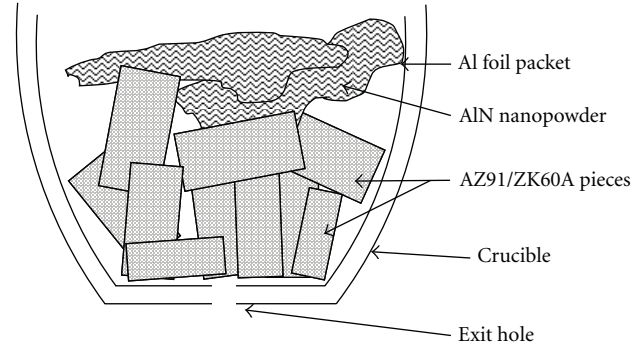


FIGURE 1: Arrangement of raw materials in crucible before casting for AZ91/ZK60A/AlN nanocomposite.

furnace prior to extrusion. Colloidal graphite was used as a lubricant. Rods of 8 mm were obtained.

2.3. Heat Treatment. Heat treatment was carried out on all extruded sections at 200°C for 1 hour using a resistance heating furnace. This selection of temperature and time was made in order to relax the monolithic AZ91/ZK60A hybrid alloy (nominal aluminium content of AZ91 decreased by 2 wt.%) without recrystallization softening. The recrystallization temperature of AZ61 magnesium alloy (as the nearest matching alloy in terms of composition) following 20% cold work after 1 hour is 288°C [1]. Prior to heat treatment, the sections were coated with colloidal graphite and wrapped in aluminum foil to minimize reaction with oxygen present in the furnace atmosphere.

2.4. Microstructural Characterization. Microstructural characterization studies were conducted on metallographically polished monolithic and nanocomposite extruded samples to determine grain characteristics. Hitachi S4300 Field-Emission SEM (FESEM) was used. Image analysis using Scion software was carried out to determine the grain characteristics. Thin foils were prepared from the monolithic and nanocomposite extruded samples for transmission electron microscopy (TEM) using disc punch-out and ion-milling for nanoparticle distribution observation (regarding localized effects). Goniometer XRD studies were conducted using CuK_α radiation ($\lambda = 1.5406 \text{ \AA}$) with a scan speed of 2°/min in an automated Shimadzu LAB-X XRD-6000 diffractometer to determine intermetallic phase(s) presence and dominant textures in the transverse and longitudinal (extrusion) directions (regarding globalised effects).

2.5. Hardness. Microhardness measurements were made on polished monolithic and nanocomposite extruded samples. Vickers microhardness was measured with an automatic digital Shimadzu HMV Microhardness Tester using 25 gf-indenting load and 15 s dwell time.

2.6. Tensile Testing. Smooth bar tensile properties of the monolithic and nanocomposite extruded samples were determined based on ASTM E8M-05. Round tension test

TABLE 1: Results of grain characteristics and microhardness of AZ91/ZK60A and AZ91/ZK60A/AlN nanocomposite.

Material	AlN (vol.%)	Grain characteristics ^a		Microhardness (HV)
		Size (μm)	Aspect ratio	
AZ91/ZK60A	—	4.5 ± 0.9	1.4	137 ± 4
AZ91/ZK60A/ 1.5 vol% AlN	1.50	4.2 ± 0.8	1.4	$160 \pm 8 (+17)$

^aBased on approximately 100 grains.

() Brackets indicate % change with respect to corresponding result of AZ91/ZK60A.

samples of 5 mm diameter and 25 mm gauge length were subjected to tension using an MTS 810 machine equipped with an axial extensometer with a crosshead speed set at 0.254 mm/min.

2.7. Compressive Testing. Compressive properties of the monolithic and nanocomposite extruded samples were determined based on ASTM E9-89a. Samples of 8 mm length (l) and 8 mm diameter (d) where $l/d = 1$ were subjected to compression using a MTS 810 machine with 0.005 min^{-1} strain rate.

3. Results

3.1. Macrostructural Characteristics. No macropores or shrinkage cavities were observed in the cast monolithic and nanocomposite materials. No macrostructural defects were observed for extruded rods of monolithic and nanocomposite materials.

3.2. Microstructural Characteristics. Microstructural analysis results revealed that grain size and aspect ratio remained statistically unchanged in the case of nanocomposite as shown in Table 1 and Figures 2(a) and 2(b). Grain size refers to diameter of the grain assuming it is circular in shape. AlN nanoparticle reinforcement and fine intermetallic particle distributions in the nanocomposite were reasonably uniform as shown in Figure 2(c).

Texture results are listed in Table 2 and shown in Figure 3. In monolithic and nanocomposite materials, the dominant texture in the transverse and longitudinal directions was (1 0 -1 1). Here, extrusion did not result in the (0 0 0 2) plane being intensely parallel to the extrusion direction (as we have previously reported) [6–14].

3.3. Hardness. The results of microhardness measurements are listed in Table 1. The nanocomposite exhibited higher hardness than the monolithic material.

3.4. Tensile Behavior. The overall results of ambient temperature tensile testing of the extruded materials are shown in Table 3 and Figure 4(a). The strength of AZ91/ZK60A/1.5 vol% AlN was higher compared to monolithic AZ91/ZK60A, without significant compromise in failure strain and energy absorbed until fracture (EA). EA was determined by

TABLE 2: Texture results of AZ91/ZK60A and AZ91/ZK60A/AlN nanocomposite based on goniometer X-ray diffraction.

Material	Section ^a	Plane	Average
			(I/I_{max}) ^b
AZ91/ZK60A	T	1 0 -1 0 prism	0.46
		0 0 0 2 basal	0.20
		1 0 -1 1 pyramidal	1.00
	L	1 0 -1 0 prism	0.33
		0 0 0 2 basal	0.66
		1 0 -1 1 pyramidal	1.00
AZ91/ZK60A/ 1.5 vol% AlN	T	1 0 -1 0 prism	0.32
		0 0 0 2 basal	0.18
		1 0 -1 1 pyramidal	1.00
	L	1 0 -1 0 prism	0.35
		0 0 0 2 basal	0.72
		1 0 -1 1 pyramidal	1.00

^aT: transverse, L: longitudinal.

^b I_{max} is XRD maximum intensity from either prism, basal or pyramidal planes.

TABLE 3: Results of tensile testing of AZ91/ZK60A and AZ91/ZK60A/AlN nanocomposite.

Material	0.2% TYS (MPa)	UTS (MPa)	Failure Strain (%)	Energy absorbed, EA (MJ/m ³) ^a
AZ91/ZK60A	225 ± 4	321 ± 4	16.1 ± 0.3	49 ± 1
AZ91/ZK60A/ 1.5 vol% AlN	236 ± 6 (+5)	336 ± 4 (+5)	13.8 ± 1.0 (-14)	44 ± 4 (-10)

^aEnergy absorbed until fracture, that is, area under the engineering stress-strain curve until the point of fracture (obtained using EXCEL software).

() Brackets indicate % change with respect to corresponding result of AZ91/ZK60A.

TABLE 4: Results of compressive testing of AZ91/ZK60A and AZ91/ZK60A/AlN nanocomposite.

Material	0.2% CYS (MPa)	UCS (MPa)	Failure Strain (%)	Energy absorbed, EA (MJ/m ³) ^a
AZ91/ZK60A	106 ± 5	508 ± 17	19.5 ± 1.7	83 ± 9
AZ91/ZK60A/ 1.5 vol% AlN	107 ± 12 (+1)	541 ± 19 (+6)	24.1 ± 6.5 (+24)	$88 \pm 7 (+6)$

^aEnergy absorbed until fracture, that is, area under the engineering stress-strain curve until the point of fracture (obtained using EXCEL software).

() Brackets indicate % change with respect to corresponding result of AZ91/ZK60A.

computing the area under the stress-strain curve up to the point of fracture.

3.5. Compressive Behavior. The overall results of ambient temperature compressive testing of the extruded materials are shown in Table 4 and Figure 4(b). Comparing AZ91/ZK60A/1.5 vol% AlN to monolithic AZ91/ZK60A, yield strength was unchanged and ultimate strength, failure strain, and EA were each higher.

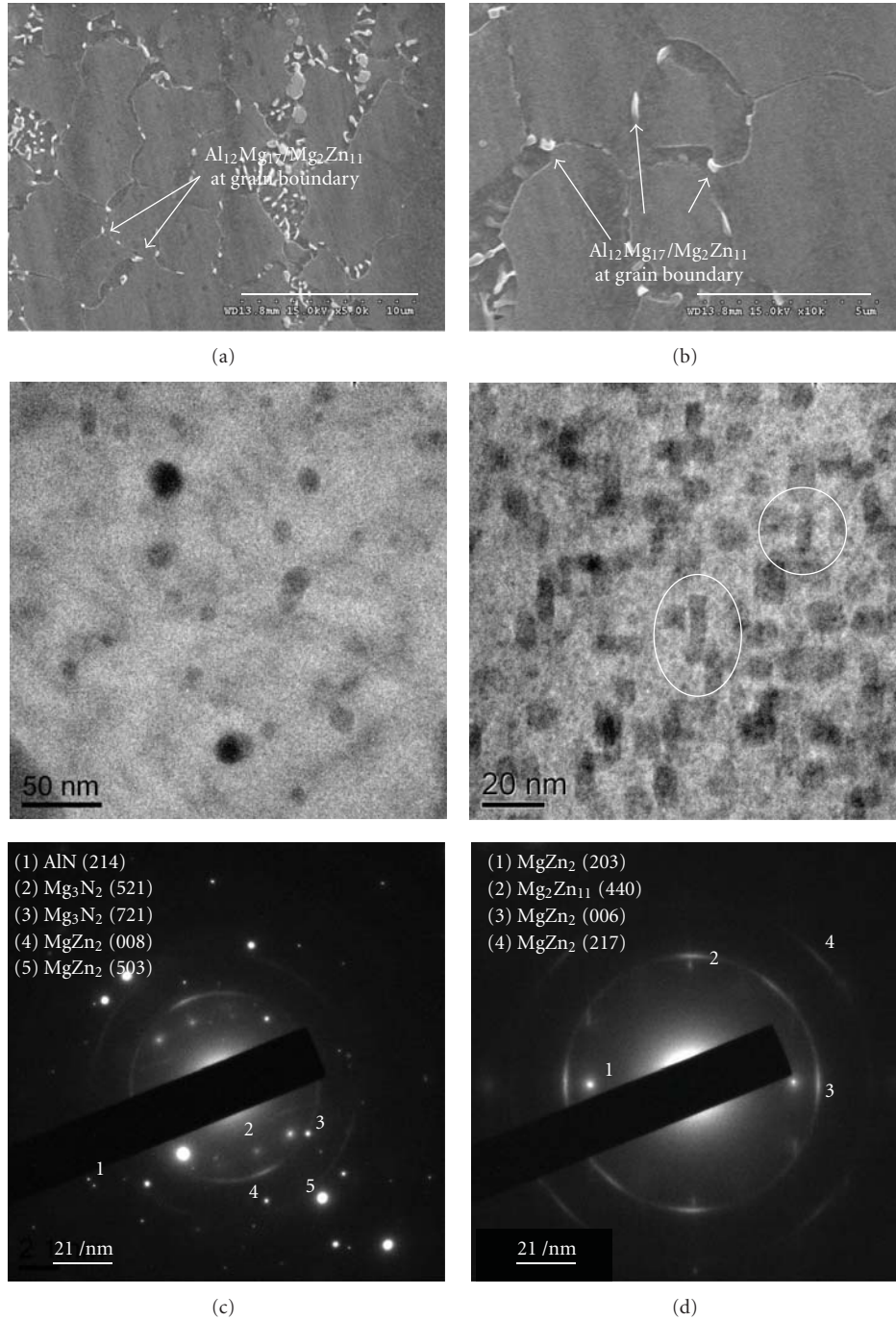


FIGURE 2: Representative FESEM micrographs showing grain size in monolithic AZ91/ZK60A and AZ91/ZK60A/AlN nanocomposite: (a) lower magnification and (b) higher magnification. (c) Representative TEM micrograph (including SAED pattern) showing the presence of individual nitride nanoparticles and fine intermetallic particles in AZ91/ZK60A/AlN nanocomposite. (d) Representative TEM micrograph (including SAED pattern) showing the presence of individual Mg-Zn rod-shaped nanoparticles in AZ91/ZK60A/AlN nanocomposite. Phases present but not labeled in the SAED patterns include Mg and Mg-Al phases only.

4. Discussion

4.1. Synthesis of Monolithic AZ91/ZK60A and AZ91/ZK60A/AlN Nanocomposite. Synthesis of monolithic and nanocomposite materials, the final form being extruded rods, was successfully accomplished with no detectable metal oxidation or reaction between graphite crucible and melts. The inert

atmosphere used during DMD was effective in preventing oxidation of the Mg melt. No stable carbides of Mg or Al formed due to reaction with graphite crucible.

4.2. Microstructural Characteristics. Microstructural characterization of extruded samples is discussed in terms of (a)

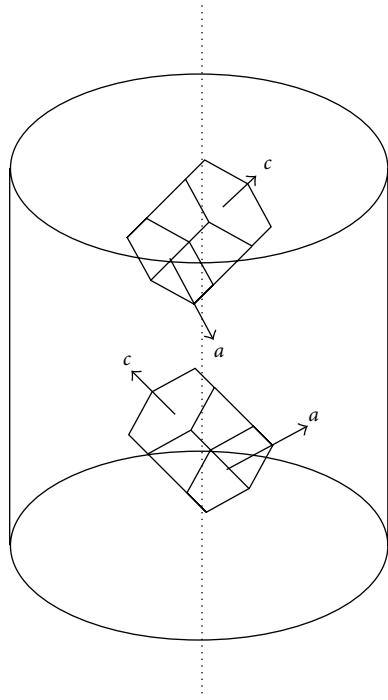


FIGURE 3: Schematic diagram showing textures of monolithic AZ91/ZK60A and AZ91/ZK60A/AlN nanocomposite based on goniometer X-ray diffraction. In each case, vertical axis (dotted line) is parallel to extrusion direction. Each cell is made up of 2 HCP units having 1 common (0 0 0 2) basal splane.

grain characteristics and (b) AlN and intermetallic nanoparticle reinforcement distribution.

Nearly equiaxed grains were observed in monolithic material and nanocomposite as shown in Table 1 and Figures 2(a) and 2(b). Grain size was statistically unchanged in the case of nanocomposite, suggesting the inability of AlN nanoparticles to serve as either nucleation sites or obstacles to grain growth during solid state cooling. It was observed that $\text{Al}_{12}\text{Mg}_{17}$ and $\text{Mg}_2\text{Zn}_{11}$ intermetallic particles decorated the grain boundaries in the monolithic material and nanocomposite. Goniometer X-ray diffraction (XRD) analysis revealed the presence of $\text{Al}_{12}\text{Mg}_{17}$ and $\text{Mg}_2\text{Zn}_{11}$ phases [4, 11]. This was possibly due to near-homogenous (as opposed to total homogenous) mixing of AZ91 and ZK60A constituent alloys since the mixing time at 750°C before spray deposition was only a few minutes. $\text{Al}_{12}\text{Mg}_{17}$ and $\text{Mg}_2\text{Zn}_{11}$ intermetallic phases are commonly found in the individual AZ91 and ZK60A alloys, respectively [1].

The reasonably uniform distribution of AlN and intermetallic nanoparticles as shown in Figure 2(c) can be attributed to (a) minimal gravity-associated segregation due to judicious selection of stirring parameters [21], (b) good wetting of AlN nanoparticles by the alloy matrix [11, 22–24], (c) argon gas disintegration of metallic stream [25], and (d) dynamic deposition of composite slurry on substrate followed by hot extrusion. In the nanocomposite, selected area electron diffraction (SAED) in TEM revealed the (a) partial reaction of AlN with the Mg alloy matrix to form Mg_3N_2

(see Figure 2(c)) and (b) the occurrence of Mg-Zn nanorods (not observed in the monolithic alloy, see Figure 2(d)). Regarding the occurrence of Mg-Zn nanorods, the Mg-Zn intermetallic phase(s) precipitation was possibly regulated at nanoscale due to the presence of well-dispersed AlN nanoparticles. Dissolved Zn possibly segregated at the liquid-AlN nanoparticle interface enabling Mg-Zn intermetallic phase manipulation at the nanoscale. This is similar to possible dissolved Zn segregation at the liquid-SiC nanoparticle interface enabling nanoscale MgZn_2 precipitation as recently reported [26]. With a reasonably uniform AlN distribution throughout the AZ91/ZK60A matrix, the nanoparticle-matrix interface area was ample for effectively regulated segregation of 4.80–6.20 wt.% Zn (or 1.21–1.59 vol. % Zn) as nanoscale Mg-Zn precipitates. This was similar to that reported recently for selected ZK60A nanocomposites [12–14].

4.3. Mechanical Behavior

4.3.1. Hardness. A significant increase in microhardness by 17% was observed in the nanocomposite when compared to monolithic material as listed in Table 1. This was consistent with earlier observations made on $\text{Mg}/\text{Al}_2\text{O}_3$, AZ31/ C_{60} and AZ31/MWCNT nanocomposites [16, 17, 27–29]. The increase in hardness of the nanocomposite in the present study can be attributed to (a) reasonably uniform distribution of harder AlN nanoparticles in the matrix and (b) higher constraint to localized matrix deformation during indentation due to the presence of nanoparticles [27, 28].

4.3.2. Tensile and Compressive Behavior. The tensile and compressive strengths of monolithic material and nanocomposite are listed in Tables 3 and 4 (and shown in Figures 4(a) and 4(b)), respectively. 0.2% TYS and UTS were enhanced by 5% each in AZ91/ZK60A/1.5 vol% AlN compared to monolithic material. In comparison of compressive strengths, 0.2% CYS and UCS of AZ91/ZK60A/1.5 vol% AlN were unchanged and higher by 6%, respectively, compared to monolithic material. However, the compressive stress detected at any given strain was lower for AZ91/ZK60A/1.5 vol% AlN compared to monolithic AZ91/ZK60A as shown in Figure 4(b). The tensile strength increase in AZ91/ZK60A/1.5 vol% AlN compared to monolithic AZ91/ZK60A can be attributed to the following well-known factors (pertaining to reinforcement): (a) dislocation generation due to elastic modulus mismatch and coefficient of thermal expansion mismatch between the matrix and reinforcement [28–31], (b) Orowan strengthening mechanism [30–32], and (c) load transfer from matrix to reinforcement [28, 30]. The lower compressive strength of AZ91/ZK60A/1.5 vol% AlN compared to monolithic AZ91/ZK60A can be attributed possibly to compressive shear buckling of brittle Mg-Zn nanorods in AZ91/ZK60A/1.5 vol% AlN as illustrated in Figure 5. The compressive shear buckling of Mg-Zn nanorods induces a slightly lower limit on the factors pertaining to reinforcement (as just described).

In both AZ91/ZK60A/1.5 vol% AlN and monolithic AZ91/ZK60A, 0.2% TYS was about 2.21 and 2.12 times the 0.2% CYS, respectively. Here, the tensile/compressive yield

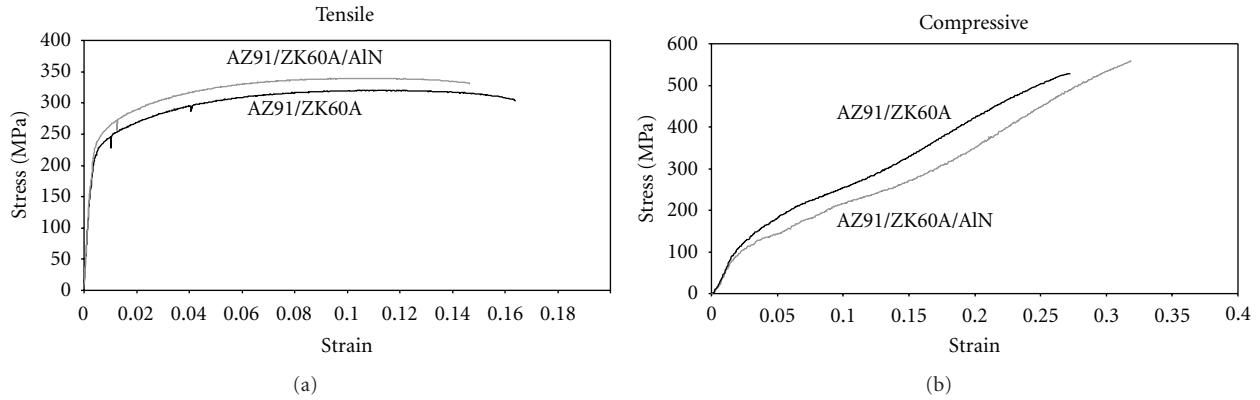


FIGURE 4: Representative: (a) tensile and (b) compressive stress-strain curves of monolithic AZ91/ZK60A and AZ91/ZK60A/AlN nanocomposite.

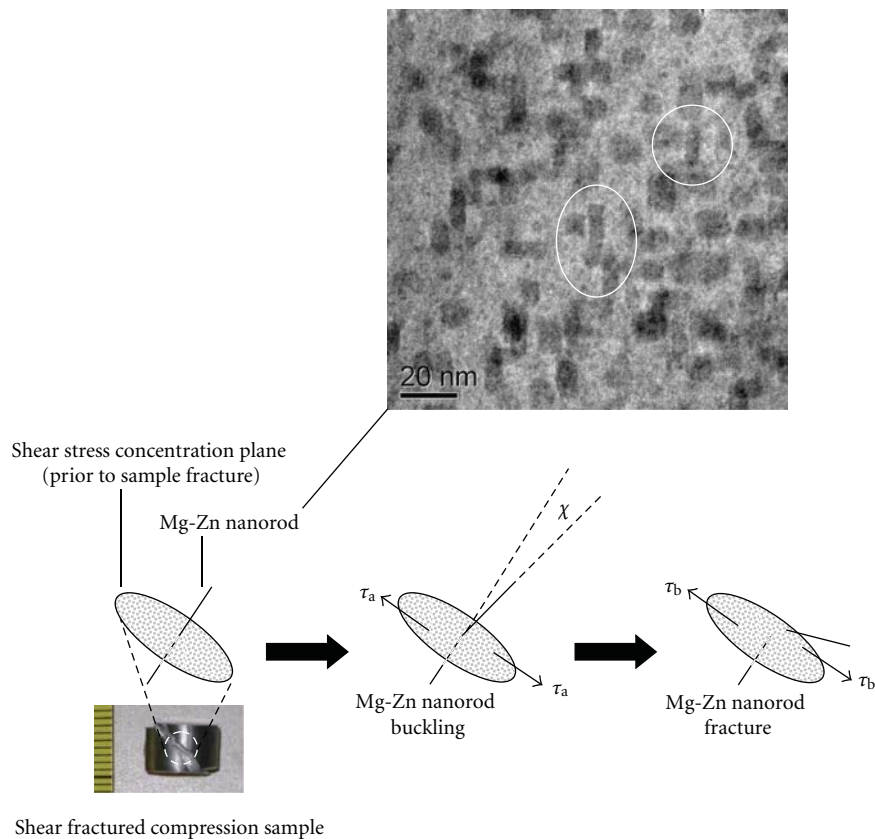


FIGURE 5: Schematic diagram illustrating compressive shear buckling of brittle Mg-Zn nanorod (circled in TEM micrograph) in AZ91/ZK60A/AlN nanocomposite. τ_a and τ_b represent planar shear stresses where $\tau_a < \tau_b$. χ (exaggerated) represents very low angular deflection of the brittle Mg-Zn nanorod during buckling.

stress anisotropy (0.2% TYS/0.2% CYS) was present despite the crystallographic texture exhibited where $\{1\ 0\ 1\ -2\}$ $\{1\ 0\ 1\ -1\}$ -type twinning was activated along the c -axis of the HCP unit cell in Figure 3 with comparatively similar ease in both tension and compression along the c -axis, based on the 45° angle between the c -axis and the vertical axis [33, 34]. The tensile/compressive yield stress anisotropy (0.2% TYS/0.2% CYS) can be attributed generally to half the

strain rate used (less strain hardening) in compressive testing compared to tensile testing. The tensile/compressive yield stress anisotropy was slightly higher for AZ91/ZK60A/1.5 vol% AlN compared to monolithic AZ91/ZK60A (2.21 compared to 2.12, resp.). This was similar to that observed in the case of selected ZK60A nanocomposites compared to monolithic ZK60A [12–14]. This can be attributed possibly to compressive shear buckling of brittle Mg-Zn nanorods as

illustrated in Figure 5. The brittle Mg-Zn nanorod is prone to buckling followed by fracture within the AZ91/ZK60A matrix during compressive deformation unlike during tensile deformation.

The tensile and compressive failure strains of monolithic material and nanocomposite are listed in Tables 3 and 4 (and based on stress-strain curves shown in Figures 4(a) and 4(b)), respectively. Compared to monolithic material, tensile failure strain was slightly compromised (−14%) in AZ91/ZK60A/1.5 vol% AlN. Compared to monolithic material, compressive failure strain was higher (+24%) in AZ91/ZK60A/1.5 vol% AlN. Both trends in failure strain of AZ91/ZK60A/1.5 vol% AlN compared to monolithic AZ91/ZK60A can be attributed to the presence of Mg-Zn nanorods (not observed in monolithic AZ91/ZK60A) in AZ91/ZK60A/1.5 vol% AlN (see Figure 2(d)). Regarding the trend in tensile failure strain, it has been shown in previous studies that the nanoparticles provide sites where cleavage cracks are opened ahead of the advancing crack front. This cleavage crack opening dissipates the stress concentration that would otherwise exist at the crack front and alters the local effective stress state from plane strain to plane stress in the neighbourhood of the crack tip [27, 35]. However, stress concentrations around the sharp ends of the Mg-Zn nanorods could not be effectively diffused by the surrounding near-spherical AlN or Mg-Al intermetallic nanoparticles. The trend in tensile failure strain can also be attributed to the partial reactivity between AlN nanoparticles and the Mg alloy matrix where Mg_3N_2 was formed (see Figure 2(c)). Regarding the trend in compressive failure strain, compressive shear buckling of Mg-Zn nanorods within the AZ91/ZK60A matrix (see Figure 5) aided in dispersing localized stored energy during compressive deformation. This allowed AZ91/ZK60A/1.5 vol% AlN to globally absorb relatively large amounts of strain energy during compressive deformation [12, 36]. Here, Mg-Zn nanorod buckling within the AZ91/ZK60A matrix is a compressive toughening mechanism.

5. Conclusions

- (i) Monolithic AZ91/ZK60A and AZ91/ZK60A/1.5 vol% AlN nanocomposite can be successfully synthesized using the DMD technique followed by hot extrusion.
- (ii) Compared to monolithic AZ91/ZK60A, tensile strength of AZ91/ZK60A/1.5 vol% AlN was enhanced. This can be attributed to well-known factors pertaining to reinforcement. Compared to monolithic AZ91/ZK60A, compressive strength of AZ91/ZK60A/1.5 vol% AlN was decreased. This can be attributed possibly to compressive shear buckling of Mg-Zn nanorods in the nanocomposite.
- (iii) Compared to monolithic AZ91/ZK60A, tensile and compressive failure strains of AZ91/ZK60A/1.5 vol% AlN were slightly compromised and enhanced, respectively. The slight compromise in tensile failure strain can be attributed to (a) stress concentrations around the sharp ends of the Mg-Zn nanorods not

being effectively diffused by the surrounding near-spherical AlN or Mg-Al intermetallic nanoparticles and (b) partial reactivity between AlN nanoparticles and the Mg alloy matrix where Mg_3N_2 was formed. The enhancement in compressive failure strain can be attributed to compressive shear buckling of Mg-Zn nanorods in the AZ91/ZK60A matrix.

Acknowledgments

The authors wish to acknowledge National University of Singapore (NUS) and Temasek Defence Systems Institute (TDSI) for funding this research (TDSI/09-011/1A and WBS no. R265000349).

References

- [1] M. M. Avedesian and H. Baker, *ASM Specialty Handbook: Magnesium and Magnesium Alloys*, ASM International, Nov- elty, Ohio, USA, 1999.
- [2] J. G. Kaufman, *Introduction to Aluminium Alloys and Tempers*, ASM International, Materials Park, Ohio, USA, 2000.
- [3] E. F. Emley, *Principles of Magnesium Technology*, Pergamon Press, Oxford, UK, 1966.
- [4] M. Paramsothy, S. F. Hassan, N. Srikanth, and M. Gupta, “Enhancing tensile/compressive response of magnesium alloy AZ31 by integrating with Al_2O_3 nanoparticles,” *Materials Science and Engineering A*, vol. 527, no. 1-2, pp. 162–168, 2009.
- [5] M. Paramsothy, S. F. Hassan, N. Q. Bau, N. Srikanth, and M. Gupta, “Selective enhancement of tensile/compressive strength and ductility of AZ31 magnesium alloy via nano- Al_2O_3 reinforcement integration method alteration,” *Materials Science Forum*, vol. 618, pp. 423–427, 2009.
- [6] M. Paramsothy, S. F. Hassan, N. Srikanth, and M. Gupta, “Simultaneous enhancement of tensile/compressive strength and ductility of magnesium alloy az31 using carbon nanotubes,” *Journal of Nanoscience and Nanotechnology*, vol. 10, no. 2, pp. 956–964, 2010.
- [7] M. Paramsothy, J. Chan, R. Kwok, and M. Gupta, “Carbon nanotube addition to simultaneously enhance strength and ductility of hybrid AZ31/AA5083 alloy,” *Materials Sciences & Applications*, vol. 2, pp. 20–29, 2011.
- [8] M. Paramsothy, J. Chan, R. Kwok, and M. Gupta, “The synergistic ability of Al_2O_3 nanoparticles to enhance mechanical response of hybrid alloy AZ31/AZ91,” *Journal of Alloys and Compounds*, vol. 509, no. 28, pp. 7572–7578, 2011.
- [9] M. Paramsothy, J. Chan, R. Kwok, and M. Gupta, “Enhanced mechanical response of hybrid alloy AZ31/AZ91 based on the addition of Si_3N_4 nanoparticles,” *Materials Science and Engineering A*, vol. 528, no. 21, pp. 6545–6551, 2011.
- [10] M. Paramsothy, J. Chan, R. Kwok, and M. Gupta, “TiC nanoparticle addition to enhance the mechanical response of hybrid magnesium alloy,” *Journal of Nanotechnology*, vol. 2012, Article ID 401574, 2012.
- [11] M. Paramsothy, J. Chan, R. Kwok, and M. Gupta, “The effective reinforcement of magnesium alloy ZK60A using Al_2O_3 nanoparticles,” *Journal of Nanoparticle Research*, vol. 13, no. 10, pp. 4855–4866, 2011.
- [12] M. Paramsothy, J. Chan, R. Kwok, and M. Gupta, “Addition of CNTs to enhance tensile/compressive response of magnesium alloy ZK60A,” *Composites Part A*, vol. 42, no. 2, pp. 180–188, 2011.

- [13] M. Paramsothy, J. Chan, R. Kwok, and M. Gupta, "Enhanced mechanical response of magnesium alloy ZK60A containing Si_3N_4 nanoparticles," *Composites Part A*, vol. 42, no. 12, pp. 2093–2100, 2011.
- [14] M. Paramsothy, J. Chan, R. Kwok, and M. Gupta, "Adding TiC nanoparticles to magnesium alloy ZK60A for strength/ductility enhancement," *Journal of Nanomaterials*, vol. 2011, Article ID 642980, 2011.
- [15] Y. Morisada, H. Fujii, T. Nagaoka, and M. Fukusumi, "Effect of friction stir processing with SiC particles on microstructure and hardness of AZ31," *Materials Science and Engineering A*, vol. 433, no. 1-2, pp. 50–54, 2006.
- [16] Y. Morisada, H. Fujii, T. Nagaoka, and M. Fukusumi, "Nanocrystallized magnesium alloy—uniform dispersion of C_{60} molecules," *Scripta Materialia*, vol. 55, no. 11, pp. 1067–1070, 2006.
- [17] Y. Morisada, H. Fujii, T. Nagaoka, and M. Fukusumi, "MWCNTs/AZ31 surface composites fabricated by friction stir processing," *Materials Science and Engineering A*, vol. 419, no. 1-2, pp. 344–348, 2006.
- [18] C. J. Lee, J. C. Huang, and P. J. Hsieh, "Mg based nano-composites fabricated by friction stir processing," *Scripta Materialia*, vol. 54, no. 7, pp. 1415–1420, 2006.
- [19] L. M. Tham, M. Gupta, and L. Cheng, "Influence of processing parameters during disintegrated melt deposition processing on near net shape synthesis of aluminium based metal matrix composites," *Materials Science and Technology*, vol. 15, no. 10, pp. 1139–1146, 1999.
- [20] M. Gupta, M. O. Lai, and S. C. Lim, "Regarding the processing associated microstructure and mechanical properties improvement of an Al-4.5 Cu alloy," *Journal of Alloys and Compounds*, vol. 260, no. 1-2, pp. 250–255, 1997.
- [21] L. M. Tham, M. Gupta, and L. Cheng, "Influence of processing parameters during disintegrated melt deposition processing on near net shape synthesis of aluminium based metal matrix composites," *Materials Science and Technology*, vol. 15, no. 10, pp. 1139–1146, 1999.
- [22] B. Q. Han and D. C. Dunand, "Microstructure and mechanical properties of magnesium containing high volume fractions of yttria dispersoids," *Materials Science and Engineering A*, vol. 277, no. 1-2, pp. 297–304, 2000.
- [23] N. Eustathopoulos, M. G. Nicholas, and B. Drevet, *Wettability at High Temperatures*, Vol. 3, Pergamon Materials Series, Pergamon, New York, NY, USA, 1999.
- [24] J. D. Gilchrist, *Extraction Metallurgy*, Pergamon Press, New York, NY, USA, 3rd edition, 1989.
- [25] M. Gupta, M. O. Lai, and C. Y. Soo, "Effect of type of processing on the micro structural features and mechanical properties of Al-Cu/SiC metal matrix composites," *Materials Science and Engineering A*, vol. 210, no. 1-2, pp. 114–122, 1996.
- [26] M. De Cicco, H. Konishi, G. Cao et al., "Strong, ductile magnesium-zinc nanocomposites," *Metallurgical and Materials Transactions A*, vol. 40, no. 12, pp. 3038–3045, 2009.
- [27] S. F. Hassan and M. Gupta, "Effect of particulate size of Al_2O_3 reinforcement on microstructure and mechanical behavior of solidification processed elemental Mg," *Journal of Alloys and Compounds*, vol. 419, no. 1-2, pp. 84–90, 2006.
- [28] S. F. Hassan and M. Gupta, "Effect of different types of nano-size oxide participates on microstructural and mechanical properties of elemental Mg," *Journal of Materials Science*, vol. 41, no. 8, pp. 2229–2236, 2006.
- [29] S. F. Hassan and M. Gupta, "Enhancing physical and mechanical properties of Mg using nanosized Al_2O_3 particulates as reinforcement," *Metallurgical and Materials Transactions A*, vol. 36, no. 8, pp. 2253–2258, 2005.
- [30] Z. Száraz, Z. Trojanová, M. Cabbibo, and E. Evangelista, "Strengthening in a WE54 magnesium alloy containing SiC particles," *Materials Science and Engineering A*, vol. 462, no. 1-2, pp. 225–229, 2007.
- [31] L. H. Dai, Z. Ling, and Y. L. Bai, "Size-dependent inelastic behavior of particle-reinforced metal-matrix composites," *Composites Science and Technology*, vol. 61, no. 8, pp. 1057–1063, 2001.
- [32] D. Hull and D. J. Bacon, *Introduction to Dislocations*, Butterworth-Heinemann, Oxford, UK, 4th edition, 2002.
- [33] T. Laser, C. Hartig, M. R. Nürnberg, D. Letzig, and R. Bormann, "The influence of calcium and cerium mischmetal on the microstructural evolution of Mg–3Al–1Zn during extrusion and resulting mechanical properties," *Acta Materialia*, vol. 56, no. 12, pp. 2791–2798, 2008.
- [34] J. Bohlen, S. B. Yi, J. Swiostek, D. Letzig, H. G. Brokmeier, and K. U. Kainer, "Microstructure and texture development during hydrostatic extrusion of magnesium alloy AZ31," *Scripta Materialia*, vol. 53, no. 2, pp. 259–264, 2005.
- [35] S. F. Hassan and M. Gupta, "Development of nano- Y_2O_3 containing magnesium nanocomposites using solidification processing," *Journal of Alloys and Compounds*, vol. 429, no. 1-2, pp. 176–183, 2007.
- [36] S. Namilae and N. Chandra, "Role of atomic scale interfaces in the compressive behavior of carbon nanotubes in composites," *Composites Science and Technology*, vol. 66, no. 13, pp. 2030–2038, 2006.